ANSYS

SVS FEM

Your partner in computing

Proceedings of

21th SVSFEM ANSYS Users' Group Meeting and Conference 2013

12th – 14th of June 2013, Hotel Fontana in Luhačovice, Czech Republic

ISBN: 978-80-905525-0-0

http://aum.svsfem.cz

Content

USING FEM FOR BUTTON ACTUATING OF AUTOMOTIVE KEY 5

Matěj Bartecký[1], Michal Šofer[2]

VIBRATION ANALYSIS OF COOLING FAN GRID ON BOBCAT TELEHANDLER 12

Vladislav Drobný

PARAMETRIC STUDY OF A CAVITATING VALVE FOR CONTROL OF OXIDIZER FLOW IN A HYBRID ROCKET ENGINE 19

Petr Dvořák*, Rob Tijsterman**

STOCHASTIC NUMERICAL MODEL OF ELECTRODYNAMICS AND APPLICATION ON HV TEST 37

Pavel Fiala, Michael Hanzelka, Ivo Běhunek

STRESS ANALYSIS PERFORMED BY FINITE ELEMENT SIMULATION OF THE STRAIN GAUGE MEASUREMENT IN ANSYS 46

Vladimír Goga

FULLWAVE ELEKTROMAGNETICKÁ ANALÝZA UHLÍKOVÝCH KOMPOZITŮ S OHLEDEM NA JEJICH MIKROSTRUKTURU A ANIZOTROPII 58

Stanislav Goňa

INCREASING THE RESISTANCE TO INTERNAL EXPLOSION OF THE STRUCTURE OF A BROWN COAL TRAY 71

Petr Horyl, Petr Jahn

ZKOUŠKY NELINEÁRNÍCH MATERIÁLOVÝCH MODELŮ BETONU V PROSTŘEDÍ SYSTÉMU LS-DYNA 82

Hradil P. , Salajka V.

ANALÝZA OCEĽOVÝCH NÁDRŽÍ 84

Norbert Jendželovský, Ľubomír Baláž

MODELOVANIE VODOJEMOU POMOCOU MKP 93

Norbert Jendželovský

COMPARISON OF ACCURACY OF THE MODELS FOR ANALYSIS OF ELECTROMAGNETIC WAVES PROPAGATION IN MULTILAYER MATERIAL 102

Radim Kadlec, Pavel Fiala, Michael Hanzelka

FAST NPSH3 ANALYSIS USING TBR AND BATCH PROCESSING 110

Tomáš Krátký[A], Milan Sedlář[A], Luděk Bartoněk[B]

FEM MODEL OF SURFACE ACOUSTIC WAVE SENSOR WITH SENSITIVE LAYER 118

Vladimír Kutiš*, Gabriel Gálik*, Ivan Rýger[+], Juraj Paulech*, Justín Murín*, Juraj Hrabovský*, Tibor Lalinský+

SOLAR PANEL FOR PARKING SPOT – COUPLED CFD AND STRUCTURAL STUDY 126

Juraj Paulech, Jakub Jakubec, Vladimír Kutiš, Emil Mojto

SIMULATION OF MOTORCYCLE HELMET IMPACT BY ECE 22-05 133

Jan Popl, Jan Vyčichl, Michal Micka, Jitka Jírová

ZTRATA STABILITY OCELOVÉ KONSTRUKCE 142

Zdeněk Poruba, Jan Szweda

ANALÝZA PONORENÝCH PILOT 154

Ľubomír Prekop

DESIGN OPTIMIZATION OF RECIPROCATING COMPRESSOR PULSATION SUPPRESION DEVICE IN ACCORDANCE WITH API 618........ 162

Kirill Solodyankin*, Jiří Běhal

ANALYSIS THE CEILING PLATE COBIAX........ 175

Katarína Tvrdá

Slovak University of Technology Bratislava, Department of Structural Mechanics

NUMERICAL MODELING OF THE BEHAVIOUR OF A FLEXIBLE CLAMP AT GRIPPING OF A RAIL........ 183

Tadeáš Volf, Jan Vyčichl

d. Material properties........ 186

THE OBTAINING OF BICYCLE HELMET'S MODEL FOR NUMERICAL ANALYSIS 191

Jan Vyčichl, Ondřej Krupička, Martin Šudřich

INVESTIGATION OF HYDRODYNAMIC PUMP PARAMETERS WITH APPLICATION OF THE PARTIAL WETTABILITY BOUNDARY CONDITION 199

Lukáš Zavadil, Sylva Drábková

USING FEM FOR BUTTON ACTUATING OF AUTOMOTIVE KEY

MATĚJ BARTECKÝ[1], MICHAL ŠOFER[2]
[1]Continental Automotive Czech Republic s.r.o
[2]VŠB-TU Ostrava, Fakulta strojní, Katedra pružnosti a pevnosti, michal.sofer@vsb.cz

Abstract:

The subject of this paper is solving the proces of pressing button of automotive key in enviroment of software ANSYS. Physical model includes hyperelastic material, nonlinear spring and prescribed boundery condition of structural analysis. The main reason of this work was to obtain actuating forces of automotive key and also stress and strain level of ruber membrane.

Keywords: Ansys,FEM, hyperelasticity, automotive key

1 Úvod

Jedním z kritérií při vývoji automobilního klíče je síla potřebná pro aktivaci jednotlivých tlačítek. Výsledná síla je pro každé tlačítko záměrně rozdílná, přičemž musí být dostatečně velká, aby nemohlo dojít k samovolné aktivaci nebo naopak aby uživatel nemusel klíč aktivovat příliš vysokou silou. Tuto vlastnost lze značně ovlivnit konstrukcí klíče stejně jako použitými materiály. Nejvýznaměji však tuto vlastnost ovlivňuje právě pryžová membrána umístěná pod pohledovým tlačítkem. Z tohoto důvodu je vhodné analýzu zaměřit právě na tuto membránu a na její deformační chování.

2 Materiál a metodika

Úloha stanovení reakčních sil společně s příslušnou sktrukturální analýzou byla řešena vytvořením konečnoprvkového modelu založeného na 3D geometrii, která byla zpracována v příslušném CAD software. Geometrie byla podrobena určitým zjednoušením, zejména v oblasti plastového tlačítka, které slouží pouze k přenosu síly na pryžovou membránu. Tlačítko bylo diskretizováno skořepinovými prvky shell181 s lineární bázovou funkcí a šesti stupni volnosti v každém uzlu. U pryžové membrány je snaha vytvořit co nejregulérnější mapovanou síť tvořenou prvkem solid185 taktéž s lineární bázovou funkcí a základními třemi stupni volnosti v každém uzlu. Pro řešení nestlačitelného materiálu, jaký je použit právě u této membrány, přibývá další stupeň volnosti, konkrétně hydrostatický tlak, který je zaveden do interních uzlů elementů. Element formulace *„mixed u-p“* řeší potíže s objemovou nestlačitelností tedy poissonova konstanta blízká nebo rovna 0,5. Kde finální matice tuhosti má tvar:

$$\begin{bmatrix} K_{uu} & K_{up} \\ K_{pu} & K_{pp} \end{bmatrix} \begin{Bmatrix} \Delta u \\ \Delta \bar{P} \end{Bmatrix} = \begin{Bmatrix} \Delta F \\ 0 \end{Bmatrix} \quad (1)$$

Kde:

Δu = přírůstek posuvů

$\Delta\bar{P}$ =přírůstek hydrostatického tlaku

Poslední částí systému je elektronický spínač, jež je popsán rovněž skořepinovými prvky shell181, které pouze reprezentují pozici a kontaktní plochu spínače. Tuhost sepnutí je řešena separátně pomocí combin39 elementů. V tomto případě reprezentují nelineární chování sepnutí spínače. Viz. graf 1.

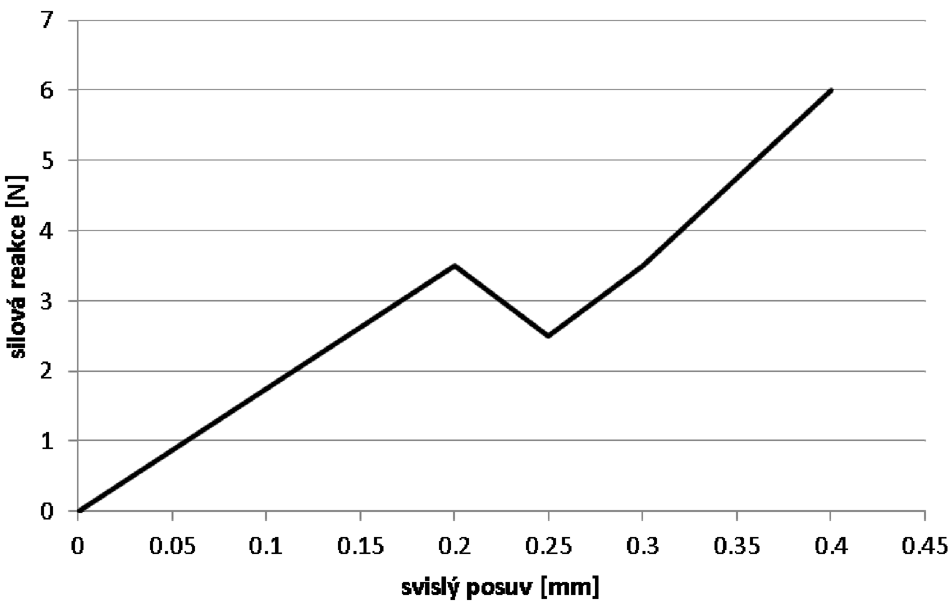

Graf 1 závislost síly na posuvu spínače

Materiál spinače a tlačítka byl definován jako lineární izotropní. Viz tab 1.

vlastnost	hodnota	jednotky
hustota	2900	kg/m^3
E	4600	MPa
μ	0.3	-----

Tab. 1 Materiálové vlastnosti použité pro spínač, tlačítko

Materiál membrány je hyperelastický a z tohoto důvodu bylo nutné stanovení vhodného kostitutivního vztahu a jemu příslušných koeficientů. Vzhledem k naměřeným infomacím a povaze úlohy (předpokládané maximální poměrné prodloužení 100%) byly spočteny konstanty pro 2 parametrický Mooney-Rivlin a pro Yeoh model.

2 parametrický Mooney-Rivlin

$$\sigma = \frac{\partial W}{\partial \lambda} = 2\left(C_1 + \frac{C_2}{\lambda}\right)(\lambda - \lambda^{-2}) \tag{2}$$

Kde:

C_1 - konstanta

C_2 - konstanta

λ - první hlavní poměrné protažení

Yeoh

$$\sigma = 2 \cdot \left(\lambda_1 - \frac{1}{\lambda_1^2}\right) \cdot \left[C_{10} + 2 \cdot C_{20} \cdot \left(\lambda_1^2 + \frac{2}{\lambda_1} - 3\right) + 3 \cdot C_{30} \cdot \left(\lambda_1^2 + \frac{2}{\lambda_1} - 3\right)^2\right] \tag{3}$$

Kde:

C_{10} - konstanta

C_{20} - konstanta

C_{30} - konstanta

λ_1 - první hlavní poměrné protažení

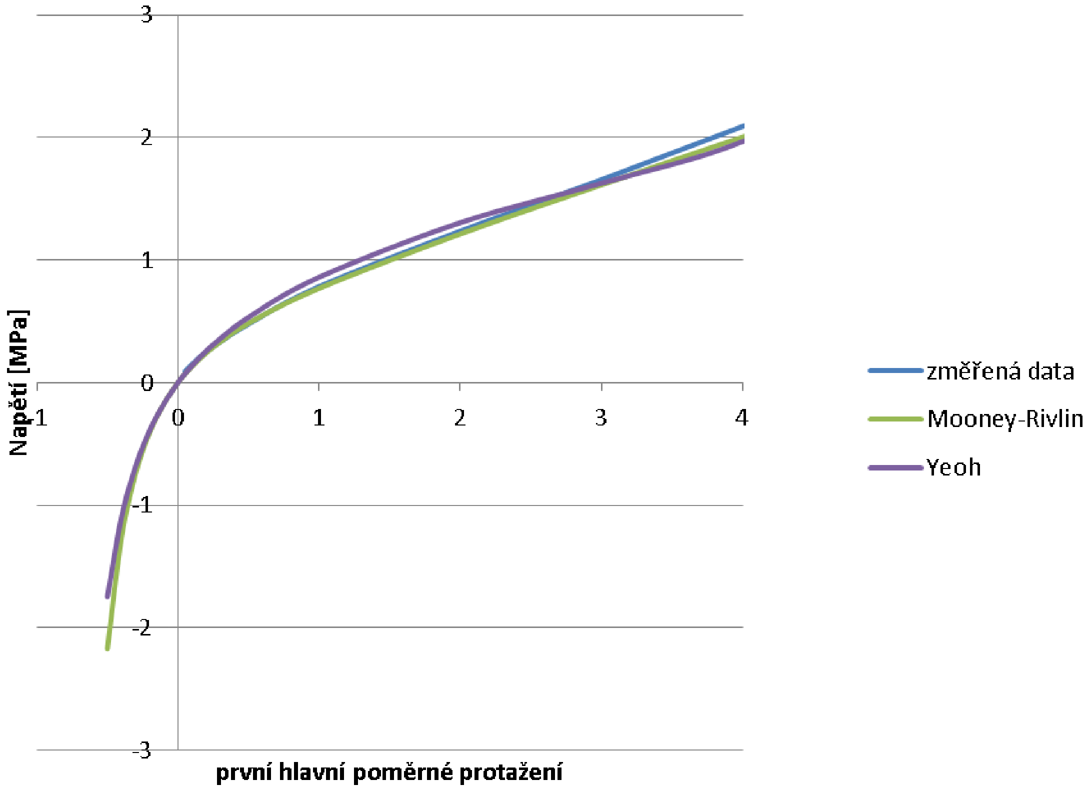

Graf 2 průběh napětí na poměrném protažení

Vzhledem k omezeným naměřeným informacím pouze tahová, tlaková zkouška ANSYS doporučuje použití Yeoh modelu.

Tab . 2 konstanty konstitutivního vztahu Yeoh C10,C20,C30

C10	C20	c30
0.255887	-0.00265	4.06E-05

Stanovení okrajových podmínek řešení odpovídá reálnému umístění v kompletu klíče tak, že membrána je po svém obvodu vetknuta a tlačítko koná vertikání pohyb směrem do kontaktu s membránou, následně celou membránu deformuje až do kontaktu se spínačem. Následně se celý systém posouvá (membrána deformuje) proti síle pružiny až do konečného sepnutí spínače, které je znázorněno na grafu 1 prudkým poklesem reakční síly (posunutí spínače 0,2mm).

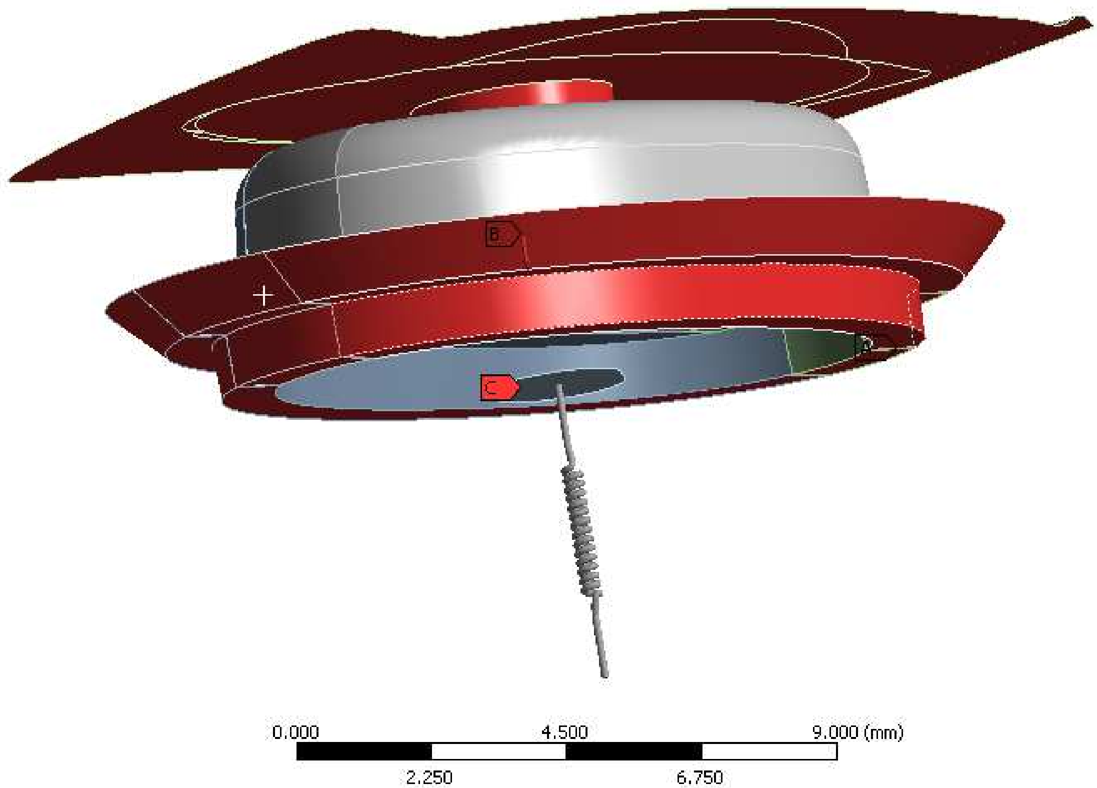

Obr.1 3D geometrie + okrajové podmínky

3 Výsledky

Následující graf uvádí průběh deformací v zadaném rozsahu posuvu tlačítka spolu s průběhem síly nutným pro aktivaci spínače.

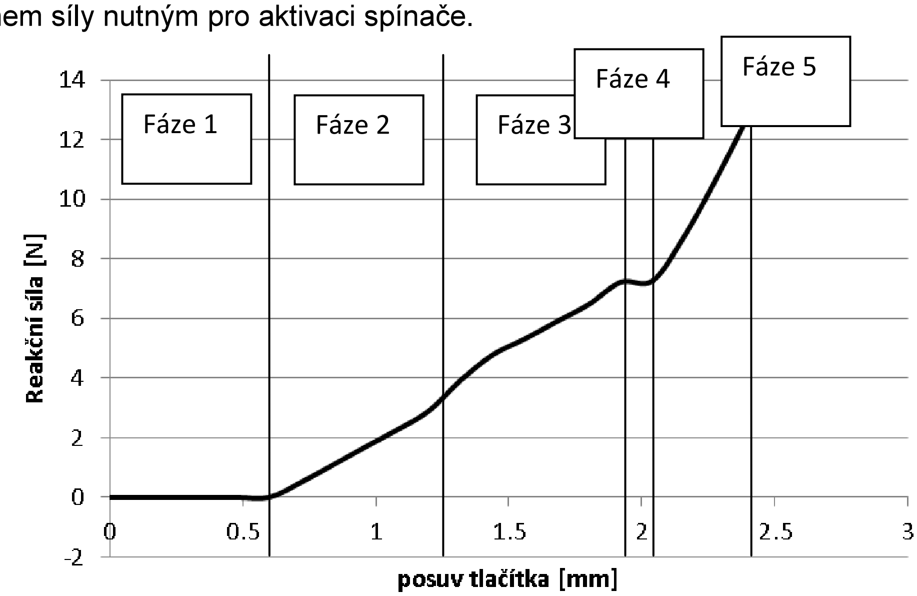

Graf 3 průběh napětí na poměrném protažení

Průběh lze rozdělt do 5 fází. V první fázi se tlačítko posouvá do kontaktu s membránou a reakční složka je nulová po kontaktu je vidět téměř lineární nárůst síly (Fáze 2) do okamžiku kontaktu membrány s tlačítkem, kdy je membrána stlačována mezi spínačem a tlačítkem a zároveň docházi k posuvu (Fáze 3) až do sepnutí spínače, které se projeví náhlým poklesem zatížení (Fáze 4) dále pak roste reakční síla až do poškození (spínače, PCB, membrány, tlačítka).

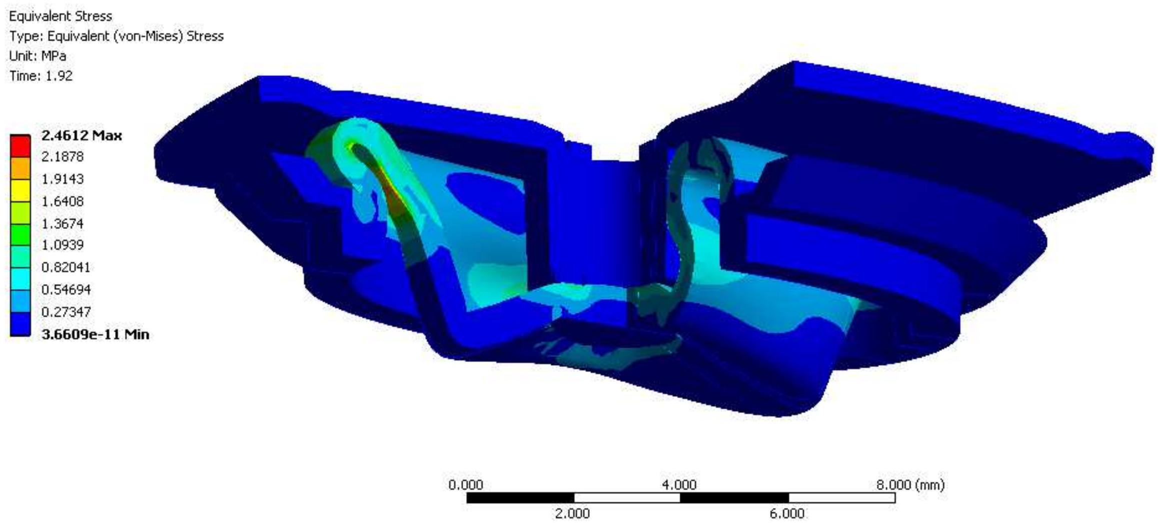

Obr. 2 deformovaný tvar a HMH napětí v okamžiku sepnutí spínače

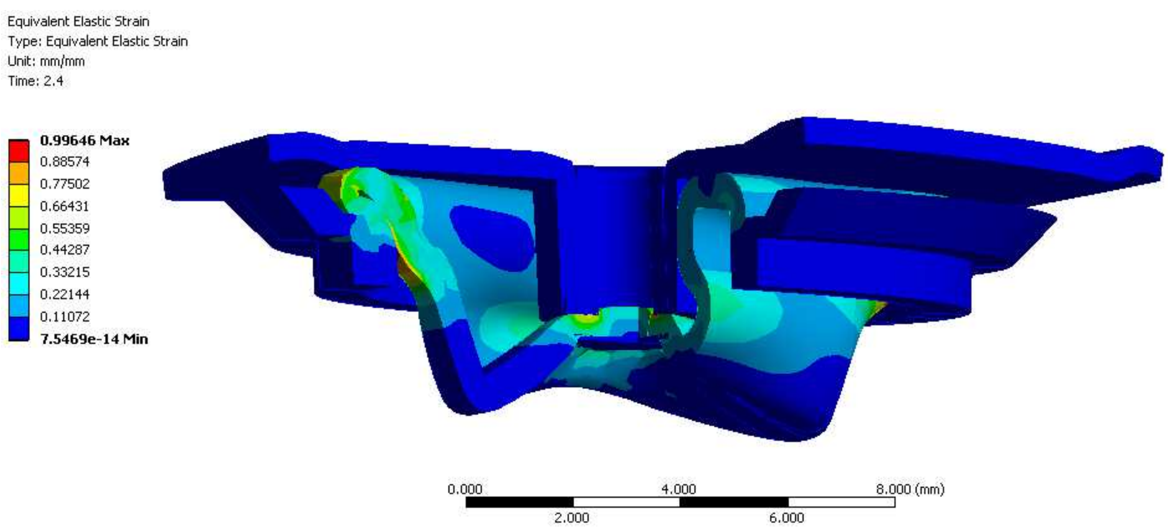

Obr. 3 deformovaný tvar a HMH prodloužení na konci testu

4 Závěr

Byla provedena nelineární struktuární analýza části konstrukce automobilového klíče. Výsledkem je průběh reakční síly nutné pro sepnutí spínače. Popsán je zároveň průběh spínání spínače automobilového klíče a jeho důvody řešení. Dalším směrem vývoje by měla být optimalizace tvaru pryžové membrány za účelem snížit hodnoty poměrných prodloužení a tím zamezit kontaktu samotné membrány se sebou.

Literatura:

[1] ANSYS release 14 documentation
[2] Li Q, Zhao J C, Zhao B 2009 Fatigue life prediction of a rubber mount based on test of material properties and finite element analysis *Engineering Failure Analysis* 16: 2304-2310

[3] www.polymerfem.com

Kontakt:
Kopanská 1713;74401;Frenštát pod Radhoštěm

Poděkování:
Tento článek byl vytvořen s podporou Centra excellence – IT4Innovations reg. č. CZ.1.05/1.1.00/02.0070

VIBRATION ANALYSIS OF COOLING FAN GRID ON BOBCAT TELEHANDLER

VLADISLAV DROBNÝ
Doosan Bobcat Engineering s.r.o.

Abstract: The paper deals with vibration analysis of a fan grid, where during development testing several cracks have been observed. Ansys Random vibration analysis was performed to locate problematic areas and to analyze current design with suggestions for improvements. Model was tuned to match full experimental measurements on real machine.

Keywords: Random vibration fatigue, PSD, Model validation by experiment

1 Machine introduction

Tested machine was Bobcat Telehandler with 130HP engine as showed in Image 1. The blue arrow points out to the fan grid location in the machine.

Image 1 – Bobcat Telehandler

The fan grid is placed in the top front section of the engine basket and is mounted with 4 x M8 screws to the fan shroud. The subassembly is mounted with 6 x M8 screws to the cooler body, details see in the Image 2.

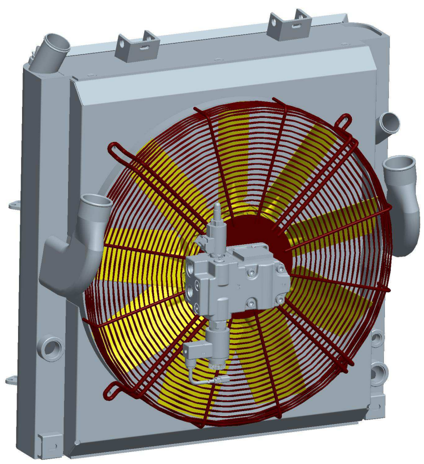

Image 2 – Detail of cooling fan grid

2 Measurement

2.1 PSD profile measurement

Measurement was performed on running engine without hydraulic load, where RPM sweep from low idle to high idle was measured. Pulse LanXI module with 3-axis accelerometer was used for data acquisition. Image 3 shows measuring point located on the bolted connection between shroud and cooler body. To get PSD data from the sweep, several postprocessing operations had to be applied. To obtain one composite profile, final averaged response was divided into RPM bins and each of them was multiplied by statistically evaluated participation of particular engine RPM range.

Then raw PSD data were reduced to decrease number of sampling points and prepared as separate XML file that was directly loaded into Ansys using PSD tabular data import. The PSD tabular data import provides simple way to define PSD points for all three measured directions from one file. It hardly saves time spent defining PSD profile and allows quick switch to another PSD profile.

On Image 4 there is a collection of reduced PSD profiles (black line) together with original measured PSD data (red line) in all 3 measured directions.

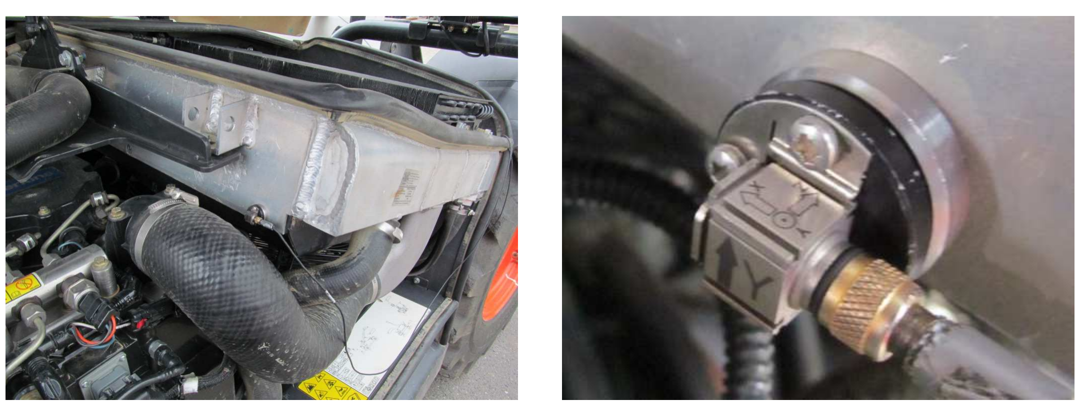

Image 3 – PSD data gathering, measurement on fixation screw (left), accelerometer axes orientation (right)

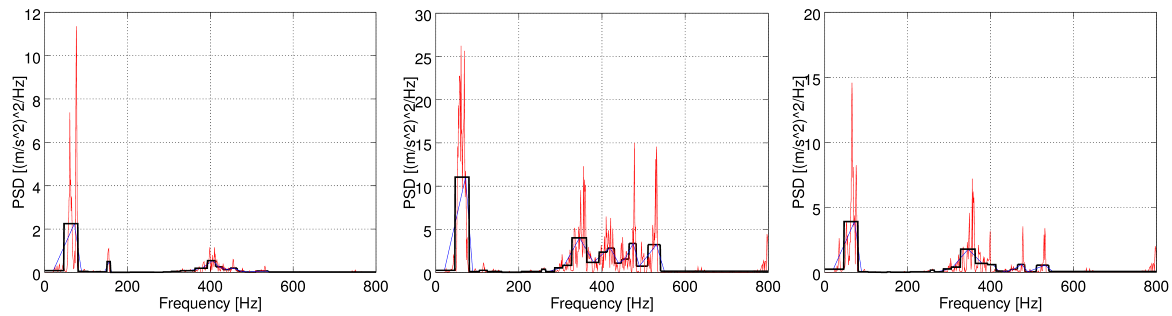

Image 4 – PSD profile for accelerometer's x, y, z axes

2.2 Modal behavior measurement

To get the best vibrational correlation with measured data, Ansys model was tuned to match the experimental modal analysis results. Correlation between measured and calculated eigenfrequencies is summarised in Table 1.

Table 1 Correlated modal frequencies and measured modal damping

	Eigenmodes						
measured data frequency [Hz]	21	35.7	69.5	78	90.5	110	115
damping [%]	5.2	5	6.3	0.9	0.7	0.7	1.8
Ansys model frequency [Hz]	21.16	39.64	69.68	80.58	87.2	108.13	118.75

Postprocessing software MEscopeVES was used for evaluation of the mode shapes and to find modal damping coefficients (Image 5). Due to mode dependency of the experimentally examined damping coefficients, it was preferable to use Ansys APDL command *mdamp* in Random vibration. Appropriate damping coeffitients on observed modes were set up based on results from Table 1. Modal properties were identified up to 120 Hz. Modes on higher frequencies were taken into account with constant damping of 1%. Except damping defined by *mdamp* command, all other damping coefficients available in Ansys were set to zero value.

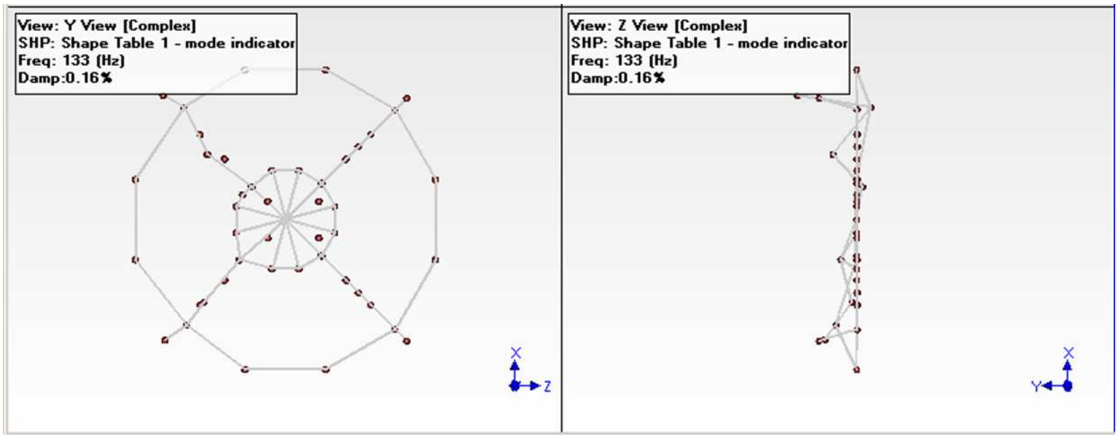

Image 5 – Mode identification in MEscopeVES

3 Ansys model

Ansys Workbench environment was used to solve the project. In the early stage there was started with linebody model of the grid and with shroud plate modelled by shell elements.

3.1 Linebody model of the grid

This element type was chosen because it was promising simple wire modelling in Design Modeler with significantly low number of elements. The modal behavior was tuned on this model, where sufficient correlation with measured data was obtained as shows Table 1.

Ansys unfortunatelly does not offer direct possibility to get stresses from linebodies in Random vibration analysis, as it is possible for static structural analysis using Beam tool. The procedure to obtain this information seemed to be too complicated because of the necessity of data extraction from /AUX3 results file. I decided to solve the grid modelled by solid elements even though it led to dramatic increase of computing time and disc space requirements.

3.2 Solid model of the grid

To sucesfully mesh the grid with solid elements, there was selected Advanced size Function on Curvature with min. element size of 1.5 mm. This settings provided satisfactory mesh made from tetrahedrons. The shroud was meshed using shell elements with element size of 8 mm. Both linebody model and solid model results produced the same response as measured data.

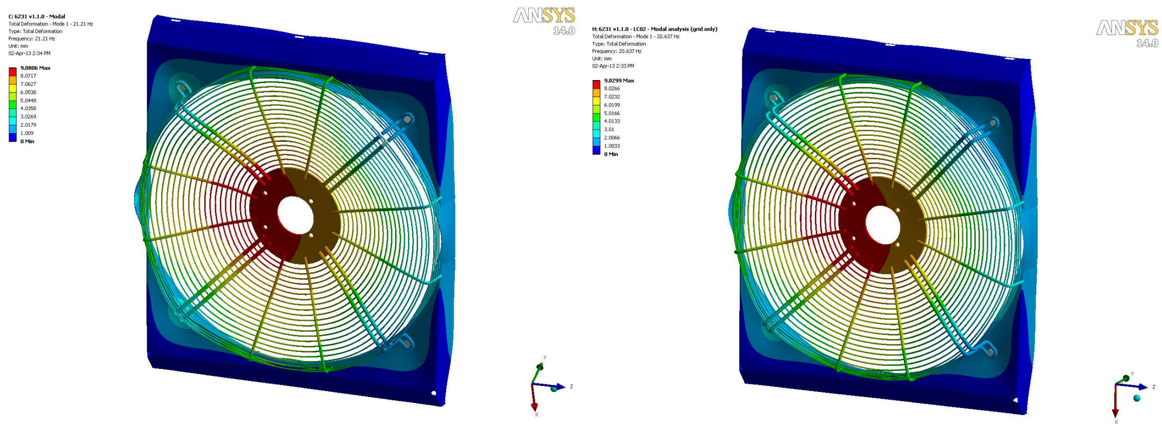

Image 6 – First mode on 21 Hz for linebody model (left) and for solid model (right)

4 Random vibration

Random vibration module in Ansys allows to insert the PSD load only in global coordinate system. The original global coordinate system was located to follow the machine's main directions. It had to be transformed to align the axis coordinate system of testing accelerometer. Additionally, two coordinate systems had to be created for inserting the loads. First coordinate system oriented in new global axis represents fan motor mass point location. Second coordinate system with directions of original machine coordinate system is used for gravity preload.

The vibration calculation chain in Workbench consists of static structural block with gravity preload, modal analysis and random analysis. The random analysis is excited in all three directions and is damped using above described *mdamp* command. The modal analysis was set up to include modes up to 515 Hz, so 75 modes were found and solved.

5 Results

Based on real wire cracks during the field durability tests, design changes of current fan grid concept were initiated. Although the cracks are mostly influenced by the welding technique, there were found vibrational issues, which had to be also eliminated. Image 7 shows damage on fan grid after durability test.

The FEA results highlighted two locations that represent areas with high stress concentration. The area with the highest stress exactly corresponds to cracked area in durability test. Focused areas are following:

1. Radial wire - area where real cracks during durability test occured
2. Double wire - bent edge on main supporting double wire

Image 7 – Wire damage location during Durability test

5.1 Radial wire

The stress map in this detail together with Response PSD graph is shown on Image 8. There are three resonance peaks in the range between 70 – 80 Hz. This is the most used engine excitation frequency during machine operation as it is very close to high idle RPM. The all known engine and fan excitation frequencies are:

- Engine excitation frequencies: 30 – 80 Hz
- Fan excitation frequencies: 180 – 420 Hz

The fan excitation frequencies are negligable compared to the engine excitation in this case. The Response PSD curve is plotted only up to 100 Hz for better clarity.

Image 8 – Response PSD on radial wire

The Equivalent stress maximum is located on the weld, thus stress estimation method Structural Hot Spot Stress (Hobbacher, 2007) was used. The value of 1-sigma Random vibration von-Mises stress assessed using hot spot method in selected critical area is 90.3 MPa.

To improve this detail, the grid resonance should be removed from engine excitation frequency. This could be primary done by stiffening the construction around the radial wires.

5.2 Double wire

The second detailed area (Image 9) with high stress shows significantly lower stress compared to radial wire. The dominant frequency on this response is under the engine low idle. Moreover the stress resistance on parent material is higher compared to the welds. For these reasons, discussed detail doesn't apparently affect the life of this component. The value of 1-sigma Random vibration von-Mises stress in critical area is about 75 MPa.

This mode has to be taken into account when tuning the structure. By stiffening the structure, this mode could be excited by low idle frequencies.

Image 9 – Response PSD on double wire

1 Conclusion

There were performed detailed modal and random vibration analyses together with the real structure tests. In the machine development phase, the FE analysis helped to confirm insuffitient durability robustness of the fan grid. The analysis explained that the low life level is caused by structural resonance excited by engine high idle firing frequency. The final summary shows the values of 1-sigma Random vibration von-Mises stresses.

Table 2 1-sigma von-Mises stress values

location	von-Mises stress [MPa]	material detail
Radial wire	90.3	weld
Double wire	75	parent material

In order to fullfil the Bobcat durability requirements, stress levels of the welded details have to be reduced. Assuming that the real structure behavior follows the same Woehler curve as analysed design, the structural hot spot stress in the weld should be less than 43 MPa. This assumption is valid for the same excitation frequency which is the highest 1st order one. Depending on the dominant excitation frequency in the new design, the maximum allowable stress level should be corrected.

References

HOBBACHER A., 2007. *Recommendations for Fatigue Design of Welded Joints and Components*. International Institute of Welding, doc. XIII-2151-07/XV-1254-07, Paris.

Contact address:
Ing. Vladislav Drobný, Ph.D.
Doosan Bobcat Engineering s.r.o.
Za Pivovarem 600
263 12 Dobříš
vladislav.drobny@doosan.com

PARAMETRIC STUDY OF A CAVITATING VALVE FOR CONTROL OF OXIDIZER FLOW IN A HYBRID ROCKET ENGINE

PETR DVOŘÁK*, ROB TIJSTERMAN**
*Institute of Aerospace Engineering, Brno University of Technology, **Moog Bradford of The Netherlands

Abstract: Part of a collaborative European effort to advance throttleable hybrid rocket technology, Bradford Engineering is developing a cavitating flow control valve. In order to improve performance of the valve Brno University of Technology has performed extensive numerical simulation campaign resulting in new valve design. The paper describes design considerations of the cavitating valve as well as characterization of the valve performance by experimental and numerical means. Furthermore, numerical parametric study is performed together with experimental evaluation of the optimized design.

Keywords: cavitation, control valve, oxidizer, hybrid engine

5 Introduction

Both unmanned and manned missions to extra-terrestrial bodies require reliable means to perform soft and precise landing on the surface of a planet. One of the few concepts to allow for deceleration and controlled soft landing is a hybrid rocket engine (Ball, 2007). Unfortunately, such a technology has not been available within Europe so far (Parissenti, 2011).

To develop a deeply-throttleable hybrid engine is the primary objective of FP7 European Commission funded project SPARTAN (SPAce exploration Research for Throttleable Advanced eNgine). This effort is in agreement with International Space Exploration Coordination Group and ESA development guidelines (Wilson, 2005; ISECG, 2009). The three-year long project has commenced 1st March 2011. It is coordinated by Thales Alenia Space Italia S.p.A. and incorporates both commercial and academic partners from seven European countries.

During course of the project, hybrid propulsion technology based on HTPB (hydroxyl-terminated polybutadiene) solid propellant fed by hydrogen peroxide as an oxidiser has been selected. Outcome of the project, the SPARTAN demonstrator is going to employ four of these rocket engines ensuring vertical deceleration from 30m/s to 2m/s , which is considered to be a nominal landing condition. The demonstration mission profile is designed so as to reproduce the Mars landing dynamic requirements. To achieve this goal, the engines need to be capable of operation with 10:1 thrust ratio.

In hybrid engine, modulation of thrust is achieved by controlling the oxidizer inflow to the combustion chamber. The standard valves with a flow characteristic dependent on the pressure drop over the valve are not adequate for this application: a rocket engine firing downstream of the valve not only produces combustion-induced oscillations in the oxidizer pressure, it also has to be reliably controlled during the start-up transient phase. This implies a back-pressure independent valve – cavitating venturi solution was therefore developed, fulfilling this criteria.

This approach is not new. In fact, cavitating valve designs have been used in throttleable rocket engines at least since the Apollo program, where they were used for thrust modulation of the Lunar Module Descent Engine (Cherne, 1967). Most recently, cavitating valves were used in the Mars Science Laboratory SkyCrane (Udomkesmalee, 2005).

The major design issue for the cavitating valve was limiting the pressure drop over the valve. Initial development tests were immensely successful, but for the issue of pressure recovery. This necessitated the need to look into the design of the venturi section in detail and consequently Institute of Aerospace Engineering, Brno University of Technology, was invited to provide numerical simulation support of the process.

The paper describes both experimental and numerical characterization of the most promising initial design. This step is used for validation of the numerical setup as well. Subsequently, numerical parametric study is performed to identify better-performing design in terms of pressure drop across the valve needed for it to operate in fully cavitating mode. Finally, the best candidate design is manufactured and characterized experimentally, thereby providing further validation of the numerical code.

1 Valve design overview

The valve is based on a pintle in nozzle configuration, whereby a moveable pintle is inserted into a venturi nozzle. The mass flow through the valve is directly controlled by variation of the pintle position with respect to the nozzle.

By applying Bernoulli's principle for incompressible flow between valve inlet and valve throat, the basic performance relation of a cavitating venturi is obtained:

$$m = c_d\, A_t\, \mathrm{sqrt}(2\, \rho\, (p_i - p_v)) \qquad (1)$$

where A_t stands for throat area [m^2], c_d for coefficient of discharge [-], m for mass flow rate [kg/s], p_i for inlet pressure [Pa], p_v denotes outlet pressure [Pa] and ρ is for density [kg/m^3]. For the above relation to hold true, the pressure at the valve outlet must be sufficiently low to ensure that the liquid is cavitating in the valve throat.

Modulation of mass flow rate is achieved through variation of throat area. In contrast to non-cavitating valves, where mass flow rate is a function of pressure drop over the valve, for a cavitating venturi the mass flow rate is a function of the square root of the difference in pressure at valve inlet and vapour pressure of the liquid medium. Given that the temperature of the liquid remains relatively constant, so does the vapour pressure. The mass flow rate through a cavitating valve in a particular configuration is effectively a function of the inlet pressure.

The baseline oxidizer, hydrogen peroxide, was deemed too troublesome to handle for development test purposes. Instead, water was selected for testing. From a theoretical performance viewpoint, influence of the medium on the performance of the valve is governed by the density and vapour pressure.

The influence of vapour pressure is minor. For hydrogen peroxide 87.5 % at 20 °C vapour pressure is ~400 Pa (van Laar, 1910), compared to ~2350 Pa (Wagner, 1993) for water. At the nominal operating pressure of 65 bar, this results in m_{H2O2} / m_{H2O} = sqrt((6500000 – 400) /

(6500000 – 2350)) = 1.00015, or a change of 0.015 % in the mass flow rate. This is effectively negligible.

The density has a significant effect on the performance of the valve however. With a density of 1376 kg/m^3 at 20 °C for hydrogen peroxide against 998 kg/m^3 of water (Linstrom), the mass flow rate will increase sqrt(1376 / 998) = 1.17 or 17 % with respect to that measured in a water based test.

The valve is designed such that pintles and nozzles are easily exchangeable. This offers flexibility in flow control range by modifying the throat diameter. It also allows modification of flow rate control ability by altering pintle shape.

Initially, a pair of pintles was produced, as depicted in Figure 1. One of the pintles was manufactured with a conical tip with half-angle 10 °, while the other featured a parabolic contour. The latter was expected to give a desirable linear control characteristic.

A pair of nozzles was also produced (Figure 2). One of the nozzles was manufactured with a strictly converging-diverging section. Both nozzles have a convergent half-angle of 22 ° and converge to a throat 2.6 mm in diameter. The divergent for nozzle 1 has a half-angle of 15 ° and immediately follows the convergent. The divergent for nozzle 2 has a half-angle of 20 ° and is separated from the convergent by an 8.2 mm long straight section. Both nozzles were equipped with pressure ports to enable pressure measurements on different locations inside the nozzles.

Pintle **1**

Pintle **2**

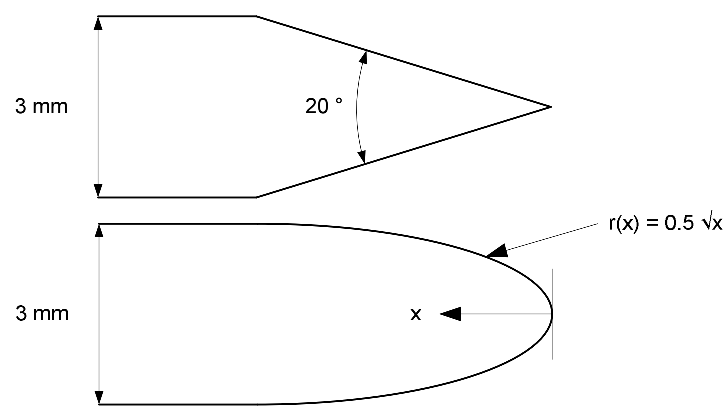

Figure 1 Pintle geometry comparison

Nozzle **1**

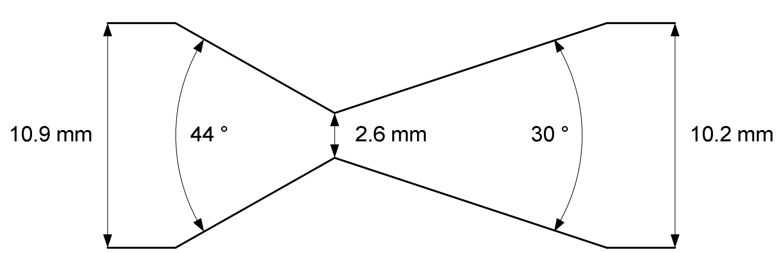

Figure 2 Nozzle geometry comparison

The operational scenario for the valve foresees cavitation over the entire flow range.

1 Experimental setup

The test setup consists of a 25 litre pressurized water reservoir feeding a test section

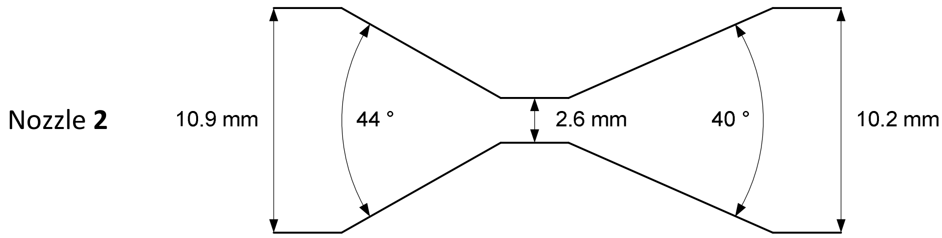

containing the device under test. Pressure is supplied in the form of nitrogen from a standard 200bar 50l gas cylinder. The pressure is regulated before being supplied to the reservoir. Water is discharged into a container which is open to atmosphere. The facility is sized based on a flow rate of 0.6 kg/s to be maintained over 30 seconds at a nominal supply pressure of 65 bar. Monitoring equipment consists of upstream and downstream pressure transmitters and inline Coriolis flow meter upstream of the test section. The test setup schematic is given in Figure 3.

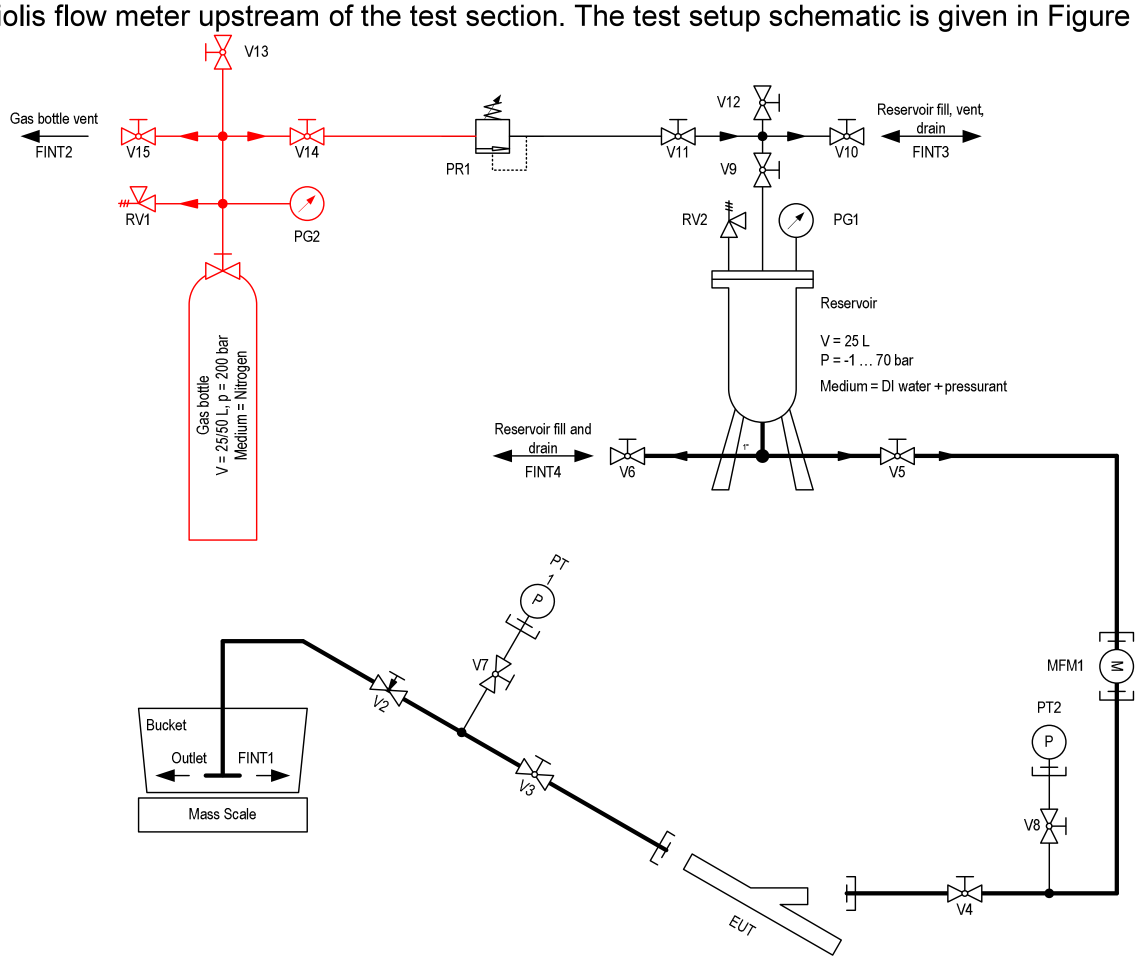

Figure 3 Schematic of the test setup

The test procedure consists of setting the valve stroke to a specific value, then pressurizing the valve, with back pressure controlled by a downstream valve, and enabling flow through the valve. This procedure is performed for pintle positions of 0.70 mm, 1.75 mm, 3.50 mm, 5.25 mm, and 7.00 mm open as illustrated in Figure 6. For each pintle position, flow rates and pressures have been measured and recorded for a number of back pressures ranging from 2 to 60 bar. Data points have been gathered in the direction of increasing pintle position starting from the smallest pintle position. Hysteresis from the pintle drive mechanism is thereby eliminated.

2 Numerical setup

Initial definition of the problem contained four combinations of boundary condition geometries (pintle with conical and parabolic contours combined with two convergent divergent nozzle variants) with five blockage configurations each, totalling in 20 required simulation combinations. For each combination, study of behaviour based on differing pressure drop across the valve was required.

Therefore, the simulation was decided to be treated as 2D, axi-symmetric problem to allow for rapid solution turnaround and swift reaction to Bradford Engineering requirements. Furthermore, the baseline computations were treated as steady-state to mimic the real stabilised flow at constant boundary conditions.

Spatial discretization of the domain was performed within the Ansys ICEM environment to obtain fully structured meshes for the respective geometry configurations. Typically the mesh (Figure 4) consists of approximately 150 000 cells. Compared to the first simulation campaign (Dvorak, 2012; 2013), the near-wall modelling was improved, aiming for y+ lower than 5 to support the Enhanced Wall Treatment of the k-epsilon turbulence model. However, no significant deviation of results has been observed compared to the original unrefined meshes (y+ up to 80).

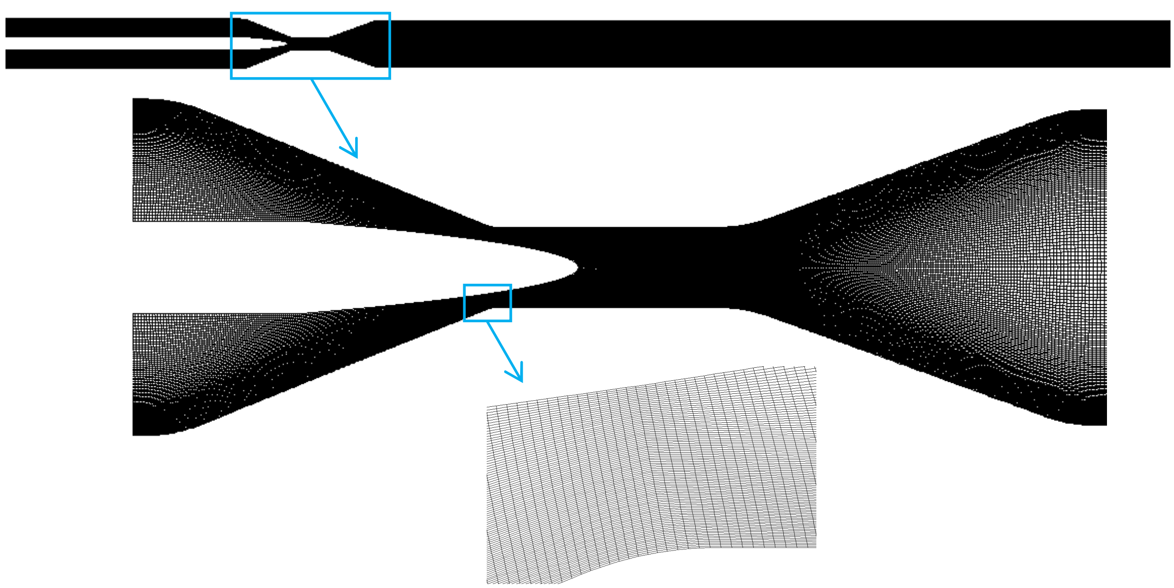

Figure 4 Fully structured computational grid

During the simulation, incompressible Reynolds-Averaged Navier-Stokes equations are solved in their steady state form in the frame of Ansys Fluent 14.5 pressure-based solver. The partial differential equations are treated by finite-volume method. Coupled iterative approach to solve the system of algebraic equations is deployed. Second order upwind scheme is selected to discretize the convective as well as diffusion terms of the governing equations. Green-Gauss Node Based method is used to treat the gradient data.

The simulation is isothermal at 293.15K. The cavitating multiphase flow is modelled by a mixture model of water and water vapour. Computations with hydrogen peroxide are part of the on-going work as a support to further stages of experimental characterization of the valve. Comparison of the material properties for the considered temperature is given in Table 1.

Table 1 Material properties used in CFD code

Material	Liquid density [kg/m^3]	Liquid viscosity [kg/m-s]	Vapour density [kg/m^3]	Vapour viscosity [kg/m-s]
H_20	998	0.001003	0.0256	1.26e-06
H_2O_2 87.5%	1376	0.001300	0.0030	9.40e-06

To consider the cavitation phenomena, mass transfer mechanism is defined from water-liquid phase to water vapour phase. The code is modelling bubble dynamics with generalized form of Rayleigh-Plesset equation (Brennen, 1995; Franc, 2007), deploying Schnerr-Sauer (Schnerr, 2001) cavitation model with the parameters set as detailed in Table 2. Parameters for hydrogen peroxide are given for reference only and are not considered in the frame of this setup.

Table 2 Schnerr-Sauer cavitation model parameters

Material	Vaporisation pressure [Pa]	Bubble Number Density [-]
H_20	2350	1e+13
H_2O_2 87.5%	400	1e+13

Turbulence is accounted for by standard k-ε model with Enhanced wall treatment deployed as recommended by (Ansys, 2010) in favour of widely used RNG k-ε formulation (Blejchar, 2006; Frölich, 2010; Rautova among others). Stability of the deployed model proved to be superior to other models for the given application.

Surfaces of the pintle and nozzle are modelled by no-slip wall boundary condition. The domain is fed by pressure-inlet boundary condition with constant value of absolute pressure (62 bar) to account for pressure regulator droop and piping pressure losses of the experimental setup (Tijsterman, 2012). Outlet is modelled as pressure-outlet with defined constant value of gauge pressure. The computational cases are initialized gradually with outlet pressure values ranging from 60 bar to 24 bar in steps not higher than 2 bar. The axisymmetric computational domain with boundary condition specification is depicted in Figure 5. Five various valve openings were simulated, representing the pintle strokes used during the experimental investigation as given in Figure 6.

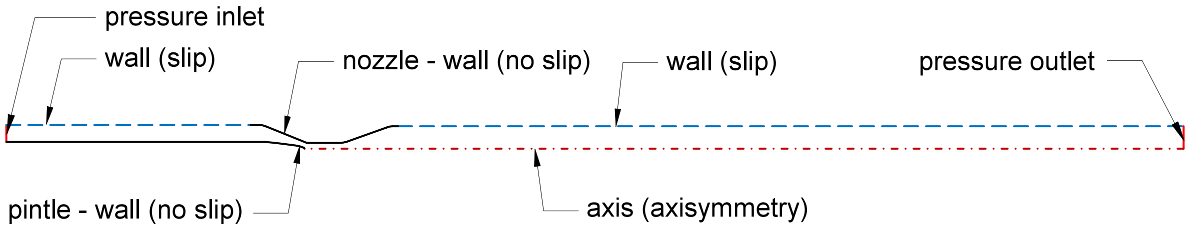

Figure 5 Simulation domain boundary condition assignment

Mass-flow-rate at the outlet as well as the pressures averaged across inlet and outlet boundaries are monitored during the computation in addition to the residual values in order to assess the stability and convergence of the computation.

Flow variables across the domain are initialized with the hybrid routine and solved. Typically, the solution arrives at a stable state within 5000 iterations.

Following a check of convergence and stability of the solution, parameters of each simulated case are extracted. Several cases with higher pressure drops across the domain displayed instabilities/oscillations in the outlet pressure values, however mass flow rate was not affected by this. The oscillatory behaviour seems to be in agreement with observations of (Bily, 2011) and is also mentioned by (Oprea, 2011). Switching the simulation code into double precision mode did not affect this phenomena, it is therefore probably result of the physics-modelling rather than round-off error. However this issue concerns only minority of the cases and the integral values of interest are not affected, therefore no further attention was paid to the phenomena.

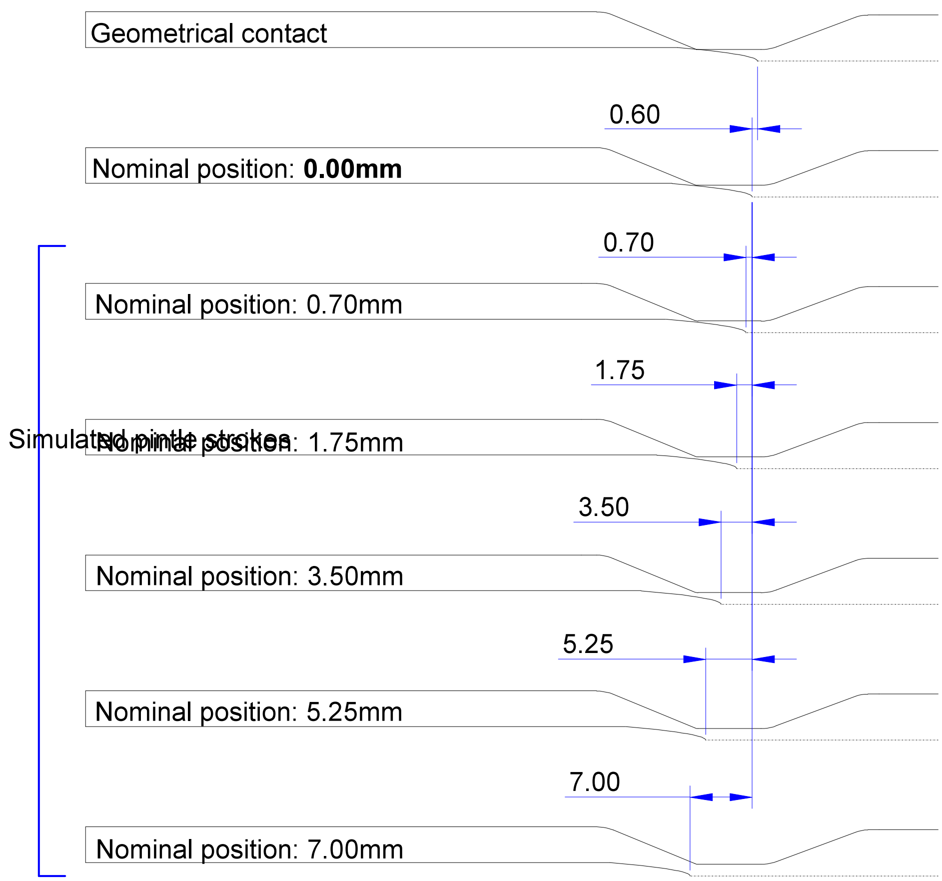

Figure 6 Respective geometrical variants: valve pintle stroke

3 Results and discussion

This chapter contains description of the succesive steps taken during redesign of the original geometry as detailed in section 1. It features comparison of experimental and numerical results for the original nozzle and the nozzle after redesign.

6.1 Initial characterization

The following nozzle-pintle combinations were subjected to both experimental and numerical evaluation:

- Nozzle 1 + Pintle 1
- Nozzle 1 + Pintle 2
- Nozzle 2 + Pintle 2

The Nozzle 2 + Pintle 1 combination was not measured, nor simulated, while it was apparent during the tests that Pintle 2 provides better performance – most importantly it provides the linear stroke-mass flow rate behaviour.

As the nozzle 2 / pintle 2 configuration clearly outperformed all other variants in all aspects (Tijsterman, 2012), only data characterizing this combination are presented further.

Mass flow rate of the nozzle 2 / pintle 2 combination as a dependency of pressure drop over the valve is presented in Figure 7, from both experiment and numerical study.

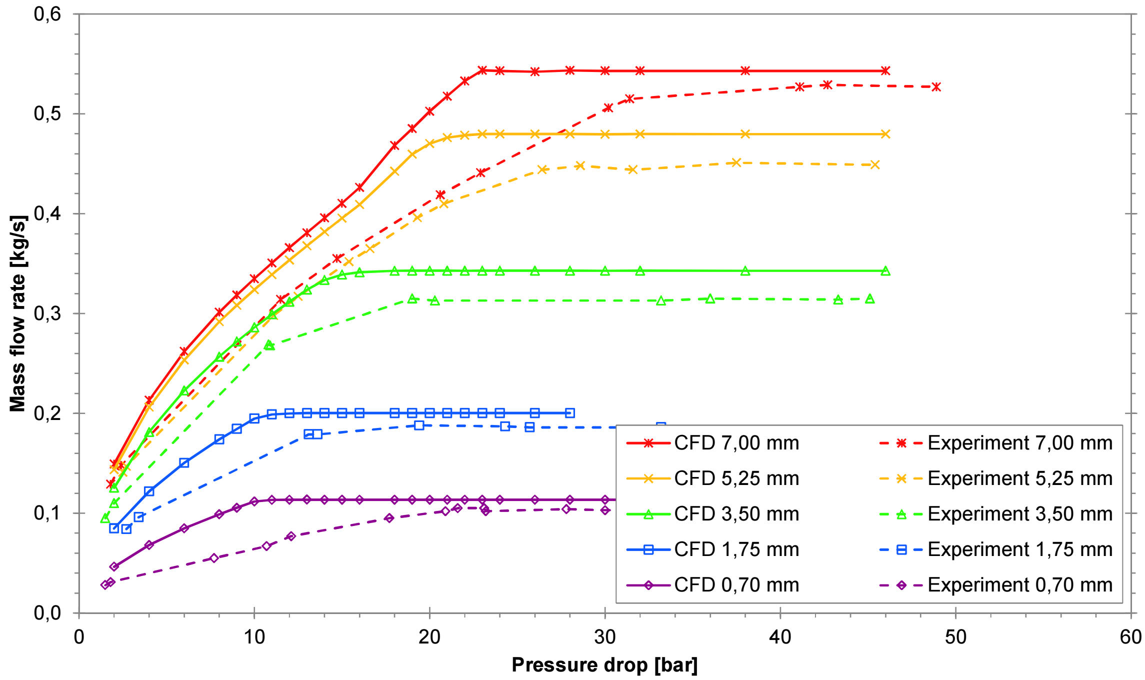

Figure 7 Nozzle 2/Pintle 2 performance as provided by CFD and experiment

The results display very good agreement in qualitative terms. Quantitatively, numerical simulation predicts the valve to enter the cavitating mode of operation at slightly more favourable values than measured experimentally, however the difference is tolerable and consistent across the whole simulation space. The discrepancy might be caused both by simplifications in simulation domain and numerical code as well as by inaccuracies during the measurement and manufacturing of the physical components.

Comparison of the obtained numerical results with computation performed by Lazzarin (Lazzarin, 2012) at the University of Padua seems to be favourable. The code used was Ansys CFX and for the two evaluated configurations (100% and 50% opening) differences in forces acting on pintle were 3.5% for both cases. Differences in mass flow rates were 4% and 9%, respectively. This is considered a good agreement between the numerical codes.

The pressure drop required to achieve back-pressure independence is larger than initially expected – approximately 30 bar for the 7mm stroke case compared to 10 bar anticipation. Given the differences between nozzle 1 and nozzle 2 this is most likely a nozzle design issue. In particular, the changes in flow direction are smaller for nozzle 2 than for nozzle 1, due to the inclusion of a straight section in nozzle 2. Therefore, the current effort to minimize pressure drop needed for the valve to operate in cavitating mode is aimed at redesign of nozzle 2.

6.2 Parametric study

During the initial experimental and numerical characterization (section 6.1) the two original nozzle designs were found to provide unsatisfactory performance with respect to pressure drop needed for the valve operation in fully cavitating mode. To facilitate the redesign process, numerical parametric study was requested to explore the available design space, optimizing the geometric design of the valve within the constraints imposed by an acceptable valve envelope.

This approach proved advantageous in terms of resources and time scale, while enabling to evaluate far more designs than physical experimentation would.

Nozzle 2 + pintle 2 combination was considered the baseline for the study. Opening of the valve was selected to be 100% = 7mm nominal pintle stroke according to Figure 6.

The parametric study considered three basic parameters:

- nozzle divergence angle
- nozzle straight section length
- nozzle divergence section transition radii

The design space was explored by decoupled approach - "One parameter at a time" – primarily due to the fact that objective function (minimization of pressure drop for the valve to operate in cavitation mode) could not be easily fed into a more sophisticated optimization routine.

5.2.1 Nozzle divergence angle

First parameter to be studied was the divergence angle. Nine geometry variants were prepared to study the response of the flow to the varying nozzle divergence. Figure 8 depicts several significant variants.

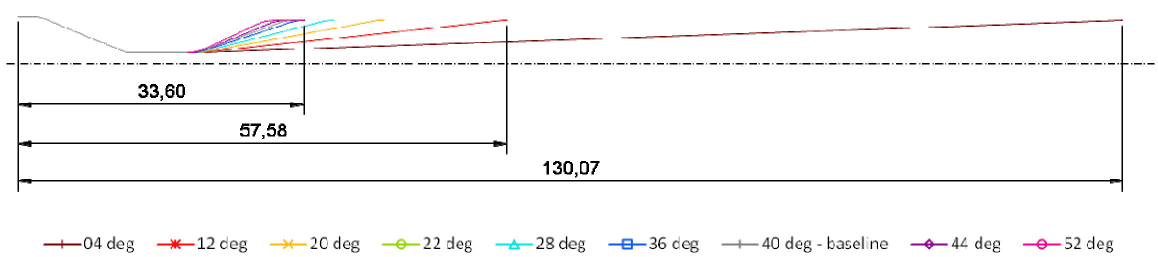

Figure 8 Nozzle divergence angle study geometry variants

For illustration, overall valve length as a consequence of the divergence angle is compared to the baseline value (33,6mm). Default radii (5mm) were used where applicable. 22 degrees divergence angle case was designed so as to minimize the divergence angle while being able to fit into the original nozzle outer dimensions (when attached directly to the convergent section).

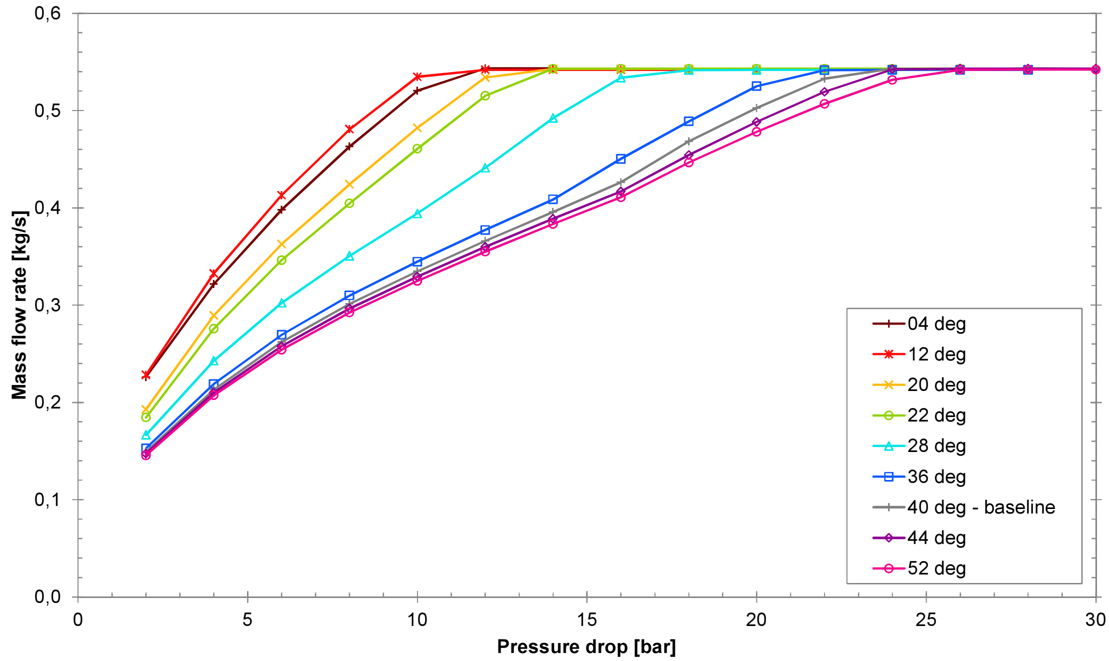

Figure 9 Nozzle divergence angle study results

As illustrated by Figure 9, there is a strong correlation between the divergence angle and pressure recovery of the valve. Performance of the original nozzle could be clearly increased by lowering the divergence angle. However, lowering the divergence angle has a limit – pressure recovery improves till about 10°, for smaller angles the recovery decreases.

5.2.2 Nozzle straight section length

Second investigated parameter is the length of the straight section. Three lengths of straight section were simulated for each of the three nozzle divergence angles (4, 22 and the original 40 degrees), thus 9 geometry configurations in total.

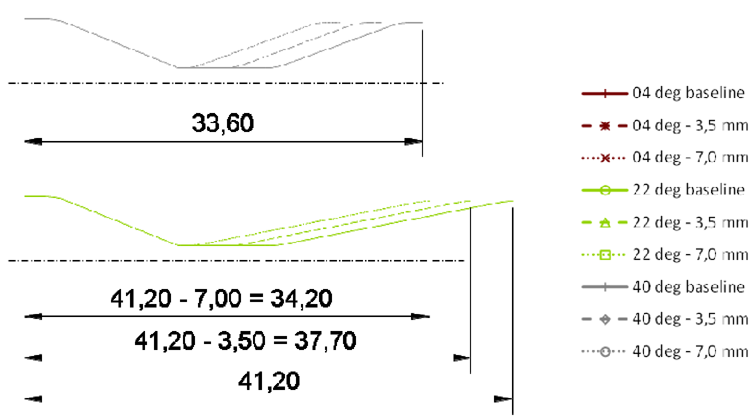

Figure 10 Straight section length study illustration

In Figure 10 , the cases are denoted by change of the straight section length as compared to the baseline nozzle 2. Default radii (5mm) were used where applicable.

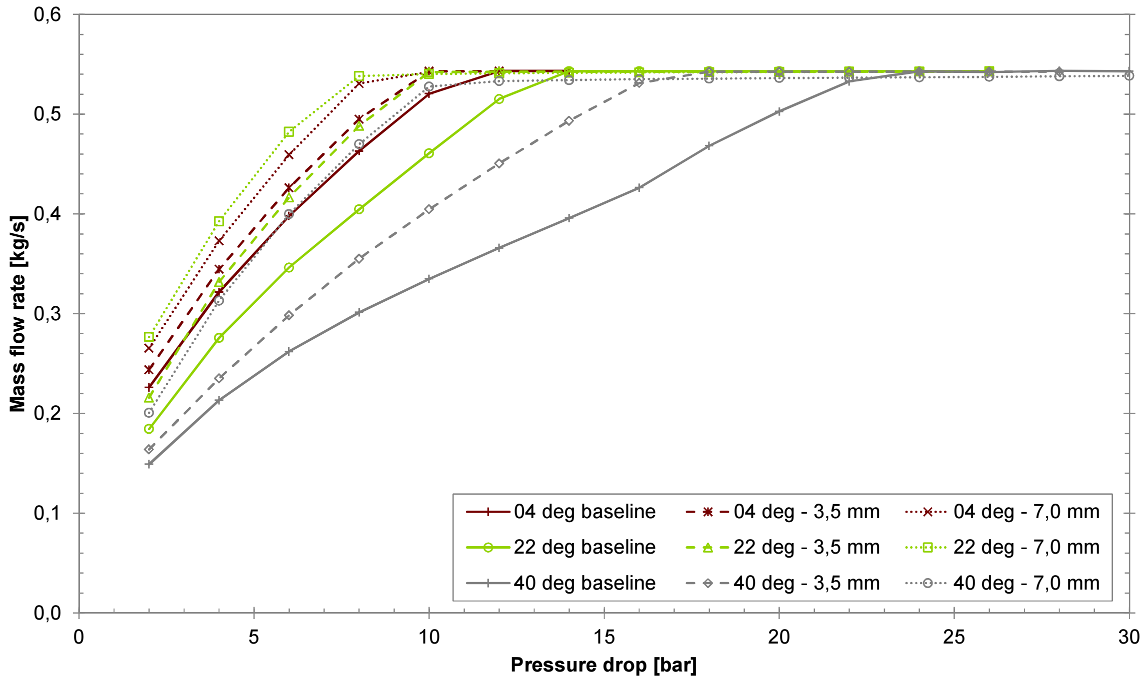

Figure 11 Straight section length study results

Benefit of the shortened straight section is most evident for the higher divergence angles and less pronounced for small angles. Nozzle with 22deg divergence angle and short (negligible) straight section outperforms other candidates.

5.2.3 Nozzle divergence section transition radii

The third considered parameter was the transition radius between different nozzle sections. Three different radii were investigated for each of the three nozzle divergence angles (4, 22 and the original 40 degrees).

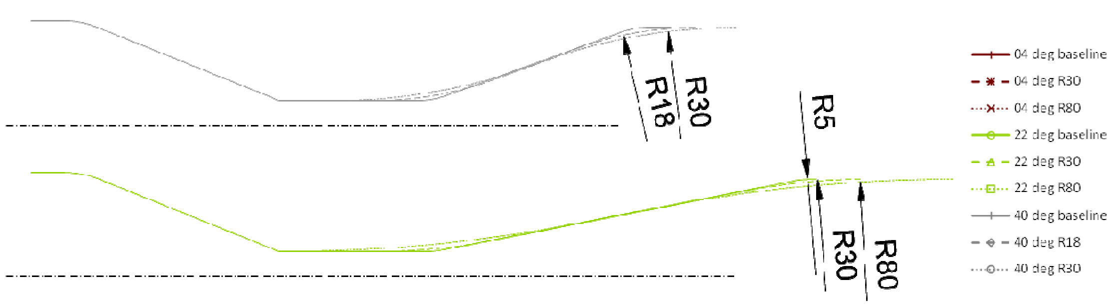

Figure 12 Straight section length study illustration

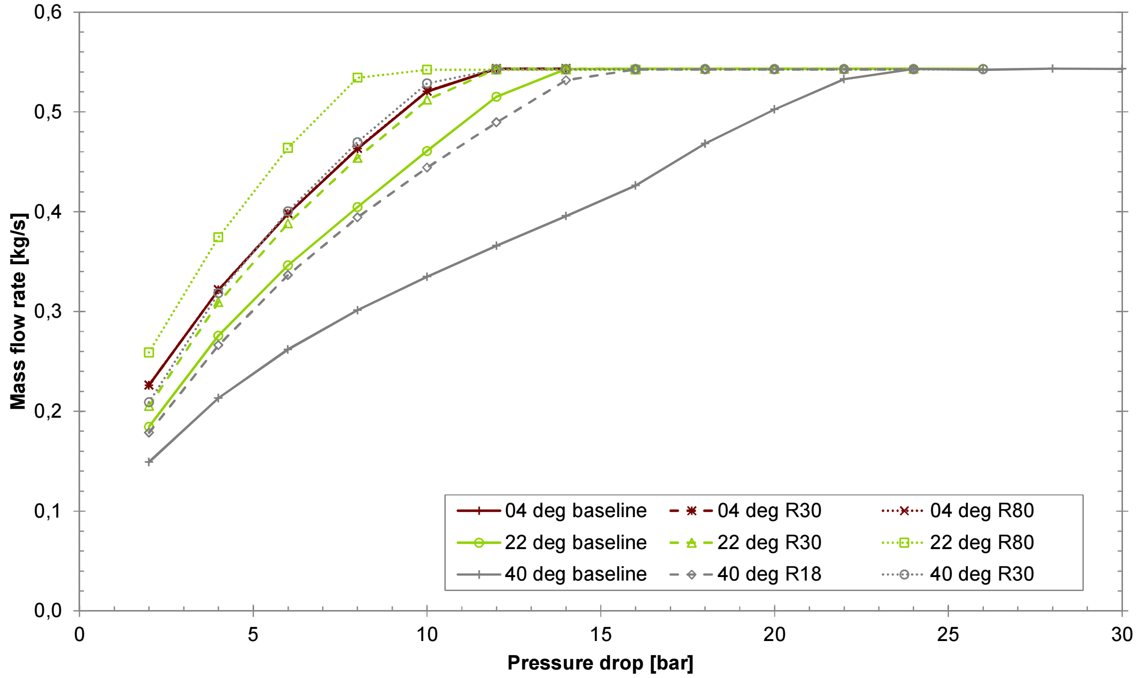

Figure 13 Transition radii study results

Again, radii influence is most pronounced for the 40deg divergence angle, whereas it is negligible in case of the 4deg nozzle. Nozzle with 22deg divergence angle and 80mm transition radii outperforms other candidates.

5.2.4 Parametric study best candidate

The performed study brings insight into sensitivity of the nozzle design to variation of three basic parameters. All investigated parameters were found to have significant impact on the nozzle performance. Among the investigated configurations, the 22deg divergence nozzle design with eliminated straight section requires the lowest pressure drop to operate in cavitation mode as illustrated by Figure 14.

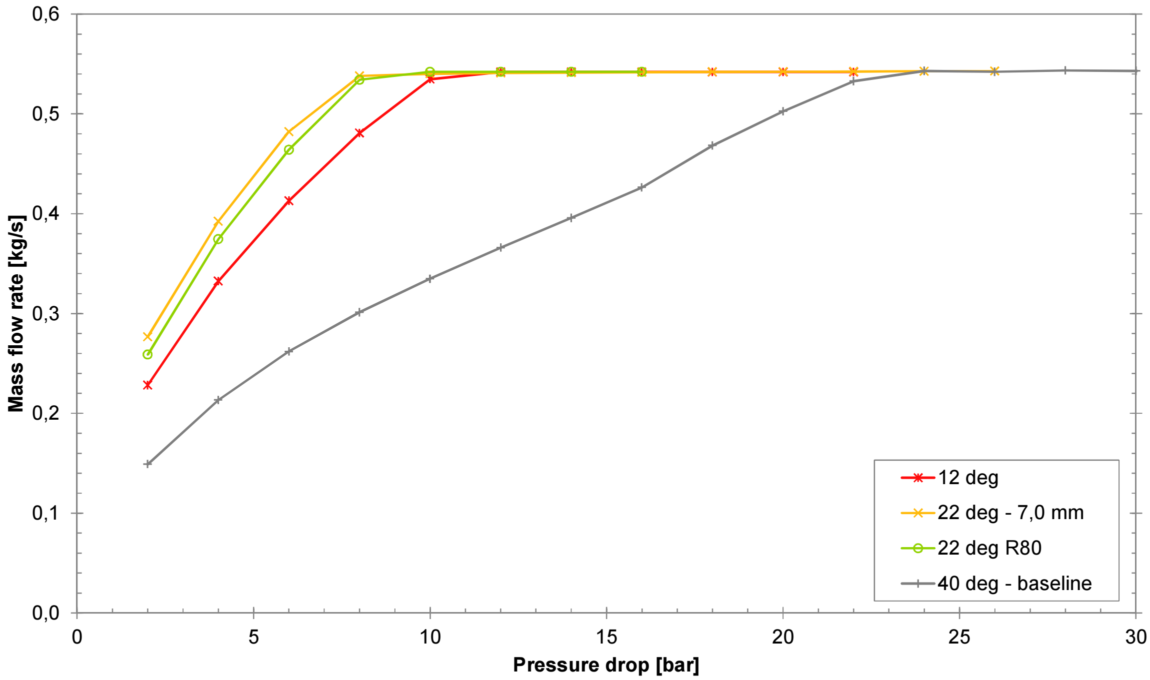

Figure 14 Parametric study best results comparison

The selected best candidate most probably does not represent the global optimum available in the whole design space. Slightly lower divergence angle in combination with eliminated straight section and possibly increased transition radii might perform better. However, the difference is anticipated to be marginal. Furthermore, such a solution would require the valve envelope dimensions to be elongated.

It was found that the pressure drop for the valve to operate in fully cavitating mode is in strong correlation with the mass flow rate through the valve in non-cavitating mode. Therefore in future investigations this parameter could be used as an objective function. This brings considerable computational and post/pre-processing time savings, as only one computation is needed to evaluate each design in contrast to the present 12+ computations. The aforementioned objective function formulation would also enable deployment of automated optimization routine.

5.2.5 Practical implementation

Due to the practical considerations of a new valve design, the proposed parametric study best candidate geometry was further modified. Two variants were promoted into the test phase, Nozzle 3 and Nozzle 4, as compared in Figure 15.

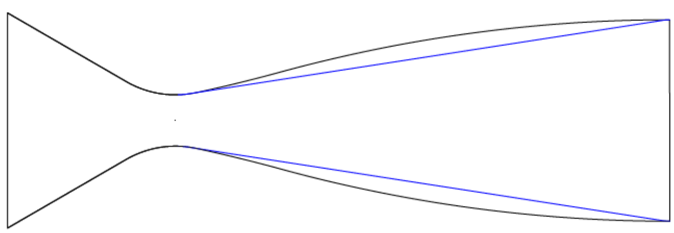

Figure 15 Comparison of geometry: Nozzle 3 (black) vs. Nozzle 4 (blue)

Both of the variants were subjected to numerical evaluation. These results are compared to the parametric study best candidate (22deg – 7mm) and the baseline nozzle 2 design in Figure 16.

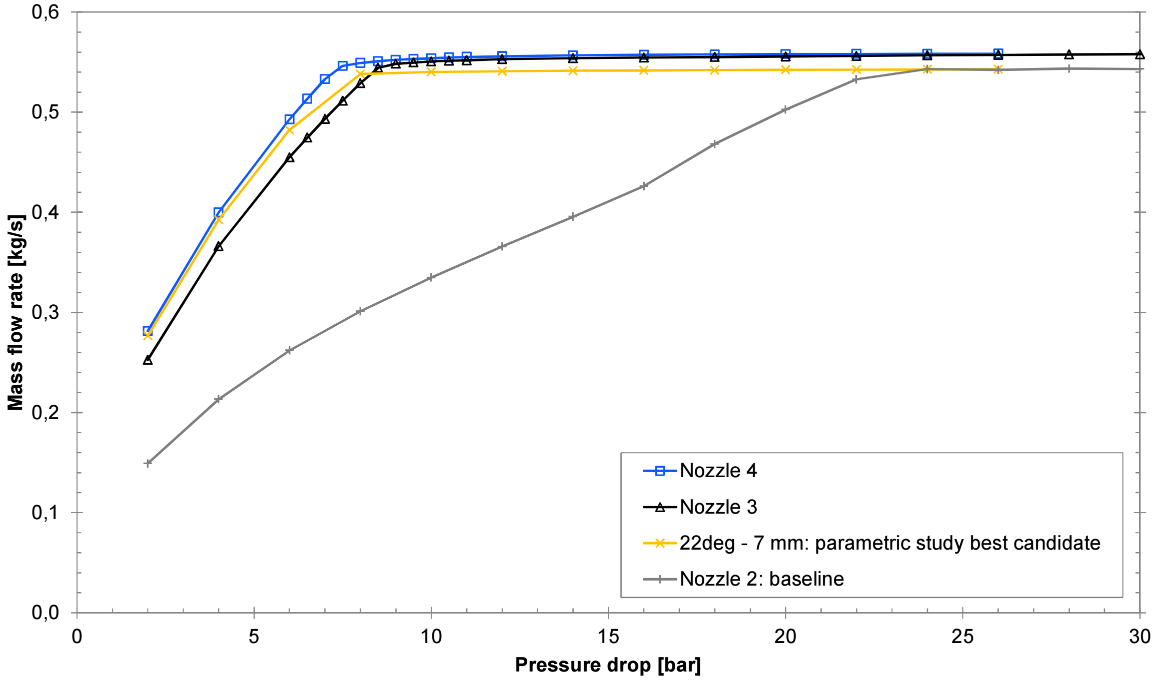

Figure 16 Nozzle design performance comparison

The best performing design, Nozzle 4 is compared to the baseline Nozzle 2 for all pintle strokes in Figure 17.

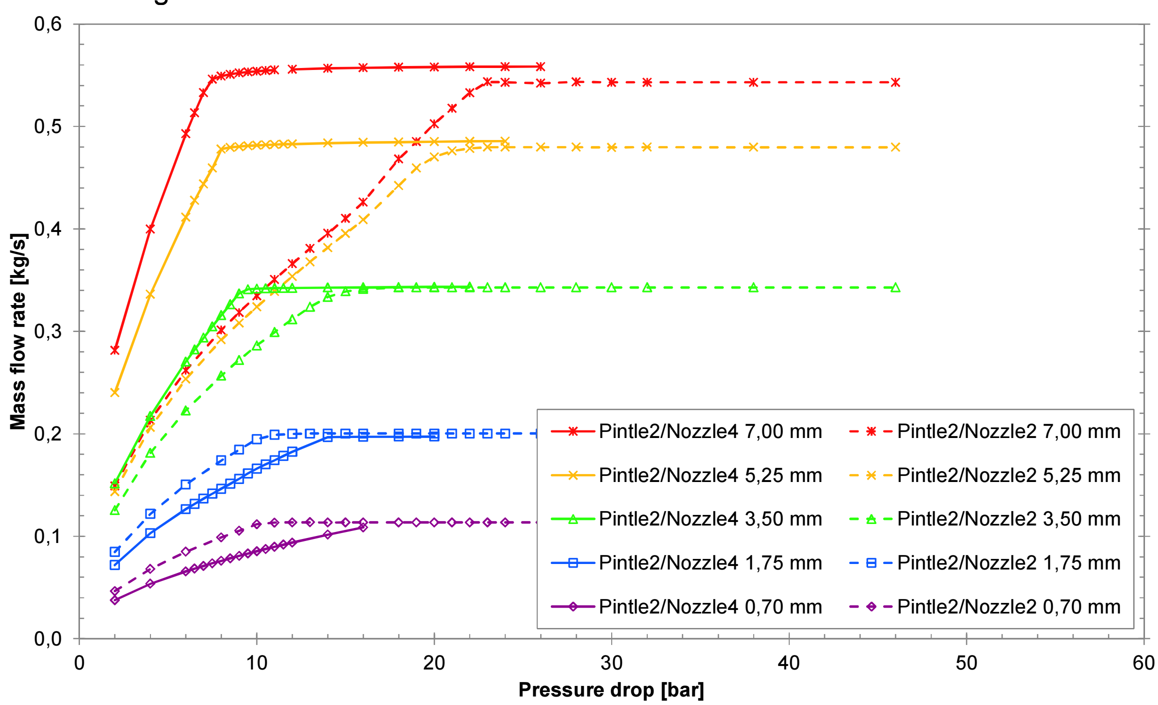

Figure 17 Nozzle 4 vs. Nozzle 2 performance comparison

The simulation foresees improvement of pressure drop needed for the valve to cavitate of nearly 20 bar for the fully opened valve. The nozzle 4 is predicted to perform slightly worse for the small openings however.

6.3 Final comparison

Nozzle 4 has been subjected to the experimental test procedure as described in section 3 and initial data have been extracted. The data are sparse, therefore it is hard to draw definitive conclusion on the valve performance and fidelity of the numerical simulation. However, the valve seems to have improved approximately by the values predicted numerically, as can be seen from Figure 18.

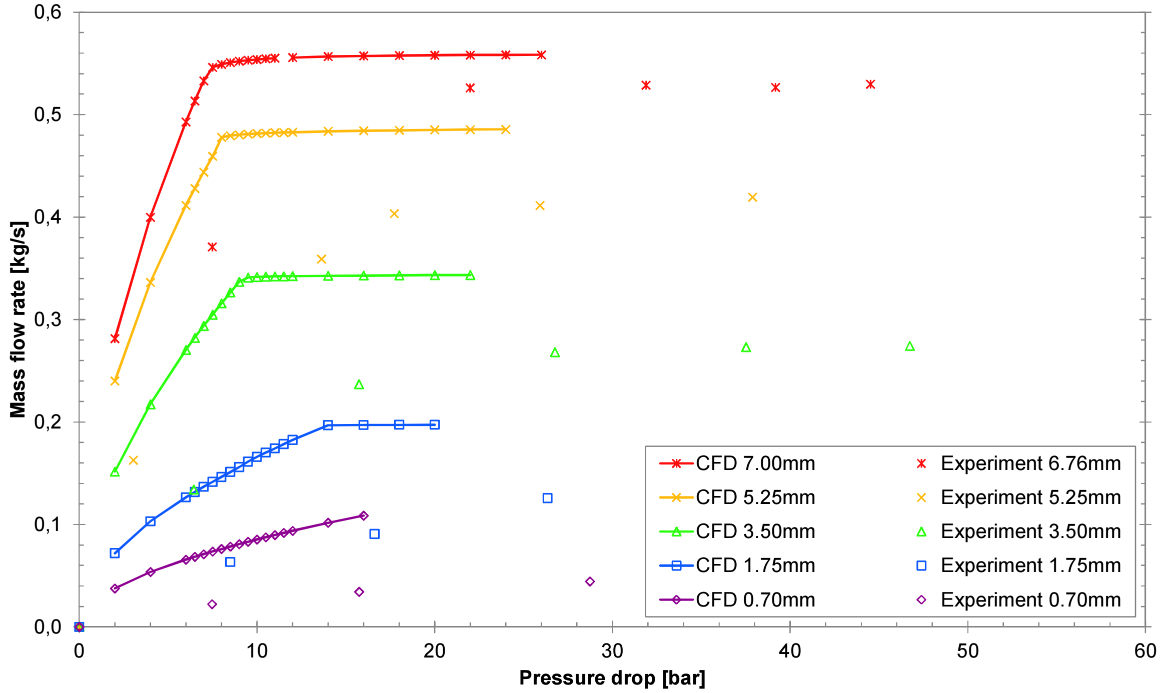

Figure 18 Pintle 2/Nozzle 4: numerical and experimental evaluation

4 Conclusion

Flow control valve has been designed to modulate oxidizer flow for hybrid rocket engine. The cavitating venturi concept of the valve proved to fulfil the challenging requirements of the application. This has been confirmed both by experimental and numerical evaluation of the various geometry configurations considered.

Reasonable agreement between the experiment and numerical simulation has been found, enabling the CFD to be used during optimization of the valve geometry, in order to lower the pressure drop needed for the valve to operate in fully cavitating mode.

The first experimental results of the optimized nozzle seem to be favourable, however more detailed investigation is needed to perform conclusive comparison with the numerical setup and with the baseline nozzle.

As part of the future work, experimental and numerical characterization of the valve with hydrogen peroxide as a working media will be performed to enable the valve to be flight tested in the Spartan lander demonstrator.

Acknowledgements

The research leading to these results has received funding from the EC FP7 project SPARTAN (SPA.2010.2.1-04 GA n. 262837).

References

ANSYS, 2010. ANSYS 13 Help. FLUENT Documentation. 13th ed. Ansys, Inc. Canonsburt, USA.

BALL, A., GARRY, J., LORENZ, R., KERZHANOVICH, V., 2007. Planetary Landers and Entry Probes. Cambridge, United Kingdom: Cambridge University Press. 978-0-521-82002-8.

BILY, D., KOZUBKOVA, M., 2011. Dynamics Behaviour of The Cavitation Field. *Journal of Applied Science in the Thermodynamics and Fluid Mechanics*, 9(2).

BLEJCHAR, T., 2006. Matematicke modelovani nestacionarniho proudeni, kavitace a akustickych projevu v hydraulickem ventilu. Doctoral thesis. Advisor: Kozubkova, M. Ostrava University of Technology, Faculty of Mechanical Engineering. Ostrava, Czech Republic.

BRENNEN, C., 1995. Cavitation and Bubble Dynamics. New York, USA. Oxford engineering science series. 44. 0-19-509409-3.

DVORAK, P., 2013. Spartan Flow Control Valve: Computational support of the cavitating venturi development. LU02-2013-SPA.AD. Brno University of Technology, Faculty of Mechanical Engineering. Brno, Czech Republic.

DVORAK, P., HRADIL, J., 2012. Numerical Simulation of Cavitation Valve Flow. In: Polonyiova, L., ed. *Techsoft Ansys User Meeting 2012 conference proceedings.* Praha, Czech Republic: Techsoft Engineering, pp. 33-39.

FRANC, J.-P., 2007. The Rayleigh-Plesset equation: a simple and powerful tool to understand various aspects of cavitation. In: D'Agostino, L. and Salvetti, M. V., eds. *Fluid Dynamics of Cavitation And Cavitating Turbopumps.* Udine, Italy: Springer.

FRÖLICH, K., 2010. Modeling of cavitating flow. Master thesis. Advisor: Rudolf, P. Brno University of Technology, Faculty of Mechanical Engineering. Brno, Czech Republic.

CHERNE, J., 1967. Mechanical Design of the Lunar Module Descent Engine. TRW Systems.

ISECG, 2009. Annual Report: 2009. International Space Exploration Coordination Group. Europe.

LAZZARIN, M., 2012. Pintle CFD Simulation. SPA-DII-RPT-0003. University of Padua. Padua, Italy.

LINSTROM, P., MALLARD, W. NIST Chemistry WebBook. NIST Standard Reference Database. 69.

OPREA, A., BULTEN, N., 2011. Cavitation Modelling using RANS approach. *Warwick Innovative Manufacturing Research Centre 3rd International Cavitation Forum 2011.* Warwick, UK: University of Warwick.

PARISSENTI, G., PESSANA, M., 2011. Throttleable Hybrid Engine for Planetary Soft Landing. *4th European Conference for Aerospace Sciences (EUCASS) proceedings*.

RAUTOVA, J., KOZUBKOVA, M. Matematicke Modelovani Proudeni Stlacitelne Kapaliny s Kavitaci. In: Tucek, A., ed. *Techsoft & SVS FEM Ansys User Meeting 2009 proceedings*.

SCHNERR, G., SAUER, J., 2001. Physical and Numerical Modeling of Unsteady Cavitation Dynamics. *Fourth International Conference on Multiphase Flow, New Orleans, USA*.

TIJSTERMAN, R., 2012. Breadboard Model Flow Control Valve Test Sequence 1 Test Report. SPAR-FCV-BE-RP-0001. Moog Bradford. Heerle, The Netherlands.

UDOMKESMALEE, S., HAYATI, S., 2005. Mars Science Laboratory Focused Technology Program Overview. *IEEE Aerospace Conference, Big Sky, Montana*.

VAN LAAR, J., 1910. The Vapor Pressure of Binary Mixtures. *Z. Phys. Chem.*, 72(723).

WAGNER, W., PRUSS, A., 1993. Vapour pressure of water at temperatures between 0 and 360°C. *J. Phys. Chem. Reference Data*, 22, 783-787.

WILSON, A., 2005. ESA Achievements. More than thirty years of pioneering space activity. BR-250. 3rd. Noordwijk, The Netherlands: ESA Publications. 92-9092-493-4.

Contact address:
Ing. Petr Dvořák
Institute of Aerospace Engineering,
Faculty of Mechanical Engineering,
Brno University of Technology
Technicka 2, 616 69 Brno, Czech Republic
dvorak.p@fme.vutbr.cz
+420 541 143 687

STOCHASTIC NUMERICAL MODEL OF ELECTRODYNAMICS AND APPLICATION ON HV TEST

PAVEL FIALA, MICHAEL HANZELKA, IVO BĚHUNEK

Brno university of technology, Faculty of electrical engineering and communication, Department of theoretical and experimental electrical engineering, Czech Republic

Abstract: The article presents the transient task numerical modelling of the electrodynamic process in gas with a pulsed electric field. Within the numerical model, non-linear electric properties of gas are respected and, by the help of a non-deterministic stochastic model, the possibility of an electric charge generation is analyzed. The authors examine the problem of electric charge probability evaluation on 3-D spark gap model; on the basis of testing the tip-tip disposition, a comparison of individual instances of the probability function evaluation is provided. The model was appliyed on the high voltage (HV) apparatus test.

Keywords: Numerical modelling, stochastic, non-linear, material, discharge, electric field, probabilistic function, HV test, PCB design.

1 INTRODUCTION

The origins of research in the field of single-shot processes modelling date back deep into the past century. Then, the related problems were solved through the use of experimental methods as applied by Nikola Tesla, the Nestor of electrical engineering www[1], www[2]. For the solution of the pulse process in an electromagnetic field, models based on the conversion of a physical model into a mathematical one can be classified as stochastic. From the perspective of a macroscopic physical model, the concerned tasks mostly involve a high number of relations of the system elements, with the possibility of description comprising only several external parameters and functions of the system. The models can be further solved as stochastic or deterministic. For numerical models based on finitary methods, it is easier to utilize the stochastic approach Enokizono M., Tsutsumi H.,1994 in the first approximation. This article uses the example of a 2-D model to present the algorithm and parameters of a stochastic model of a discharge generation in an air spark gap, Figure 1. The related experiments on a test circuit are indicated in Fig. 2.

Figure 1. A simple electrical spark gap, 3-D model

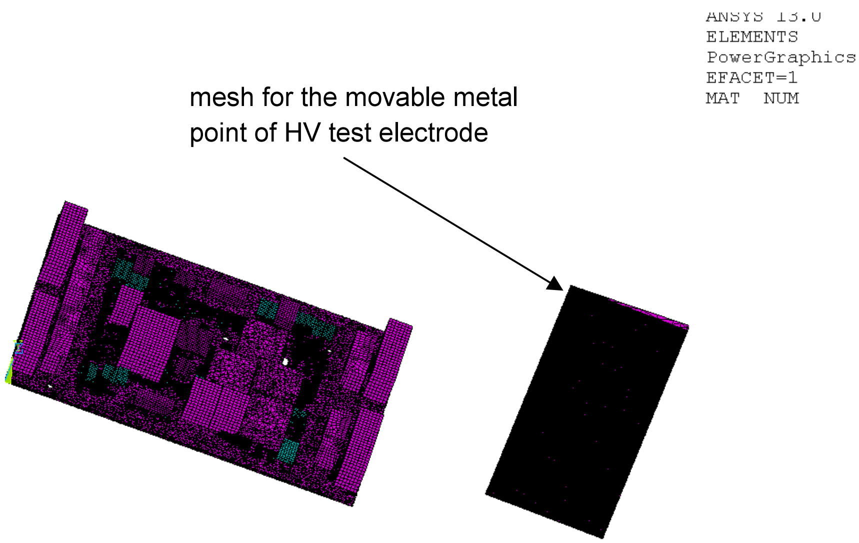

Figure. 2 A HV test PCB circuits for a electrodanamic test, 3D analysis

2 STOCHASTISATION OF THE MODEL: THE STOCHASTIC/DETERMINISTIC APPROACHES

One of the many techniques of "stochastisation" is focused on the change of input parameters of a deterministic model consisting of the stochastic (probabilistic) processes. The solution of the final model has a random process character (stochastic approach). A simple differential equation can be written in the form

$$\frac{dx}{dt} = a\left(x,\ldots z,t\right). \tag{1}$$

Stochastic form of the equation with the member added to the right-hand side can be written as $b(t,X(t),\ldots.Z(t))\ \xi(t)$

$$\frac{d}{dt}X(t) = a\left(X(t),\ldots Z(t),t\right) + b\left(X(t),\ldots Z(t),t\right)\,\xi(t), \tag{2}$$

where the symbol x(t) describes the stochastic process of the main function change. The solution of this equation will include the stochastic process X(t). Another stochastisation technique is based on deterministic solution of the relation (2) for the non-trivial function with discontinuities in the time domain. Modification of the model (2) is performed by changing

$$dX(t) = a\left(X(t),\ldots Z(t),t\right)dt + b\left(X(t),\ldots Z(t),t\right)\,\xi(t)\,dt, \tag{3}$$

and, after that, the part $\xi(t)\,dt$

$$dW(t) = \xi(t)\,dt, \tag{4}$$

where dW(t) is known as the Wiener process W(t) incrementation. The function can be explained as Brown movement. Then, the model changes the formula. Then, the stochastic differential equation from relation (3) can be writen as

$$dX(t) = a\left(X(t),\ldots Z(t),t\right)dt + b\left(X(t),\ldots Z(t),t\right)\,dW(t), \tag{5}$$

and the next step for the description of the time domain is in the form

$$X(t) = X_{T_0} + \int_{T_0}^{T} a\left(X(t),\ldots Z(t),t\right)dt + \int_{T_0}^{T} b\left(X(t),\ldots Z(t),t\right)\,dW_t, \tag{6}$$

The above-stated model (6) can be further solved by means of well-known methods. One of the promising techniques is based on utilizing cognitive functions and system in solving the stochastic system of partial differential equations. In the following sections of this study, the stochastic approach tested within article P.Fiala, M. Friedl will be analyzed.

3 THE NUMERICAL MODEL

As it was already discussed in study Enokizono M., Tsutsumi H.,1994, the model is formulated for a quasi-stationary electric field from reduced Maxwell´s equations Stratton J.A. , 1961,

$$\operatorname{div}\varepsilon\,\boldsymbol{E} = q\,,\ \operatorname{div}\boldsymbol{J} = -\frac{\partial q}{\partial t} \tag{7}$$

$$\operatorname{div}(\gamma\,\boldsymbol{E}) = -\frac{\partial q}{\partial t} \tag{8}$$

where $\boldsymbol{E}$ is the electric field intensity, $\boldsymbol{J}$ is the current density vector, ε is the permittivity, γ the conductivity, and q the electric charge. After modification, the equations from (7) become

$$\operatorname{div}\left(\gamma\,\boldsymbol{E} + \frac{\partial(\varepsilon\,\boldsymbol{E})}{\partial t}\right) = 0 \tag{9}$$

If the formulation of electric intensity vector by the help of potential φ is respected,

$$\boldsymbol{E} = -\operatorname{grad}\varphi \tag{10}$$

then the model according to expression (9) can be written as

$$\mathrm{div}\left(\gamma\,\mathrm{grad}\,\varphi + \frac{\partial(\varepsilon\,\mathrm{grad}\,\varphi)}{\partial t}\right) = 0 \tag{11}$$

In expression (11), the partial derivative includes the formulation ε grad φ. If we assume time independence of the environment macroscopic characteristic – permittivity ε, the form can be written in a manner consistent with paper Enokizono M., Tsutsumi H.,1994

$$\mathrm{div}\left(\gamma\,\mathrm{grad}\,\varphi + \varepsilon\,\mathrm{grad}\frac{\partial\varphi}{\partial t}\right) = 0 \tag{12}$$

This form, in the dynamical modelling of an electric field shock wave, does not include the effect of permittivity variation. Conversely, conductivity γ, or electrical resistivity ρ as its reversed value, is shown in Figure 3.

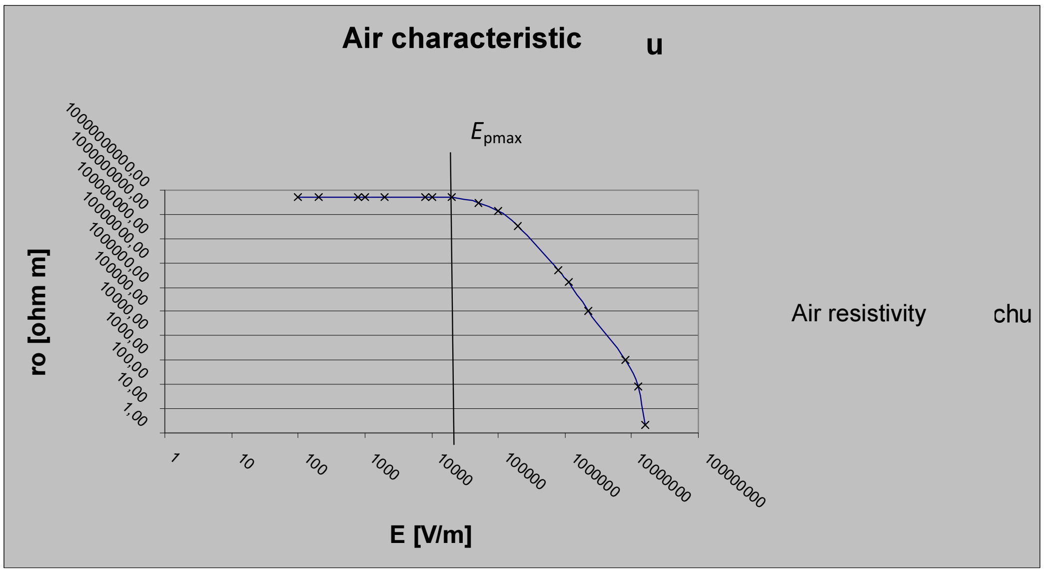

Figure 3. Characteristics of the electrical resistivity dependence on electric field intensity

If we assumed the dependence of electrical permittivity ε on time variation and the module of electric intensity ***E***, model (5) could be employed to describe more exactly the processes related to an electric discharge. The time behaviour of electric potential variation was preset with parameters of 1.2/50 μs, Figure 3.

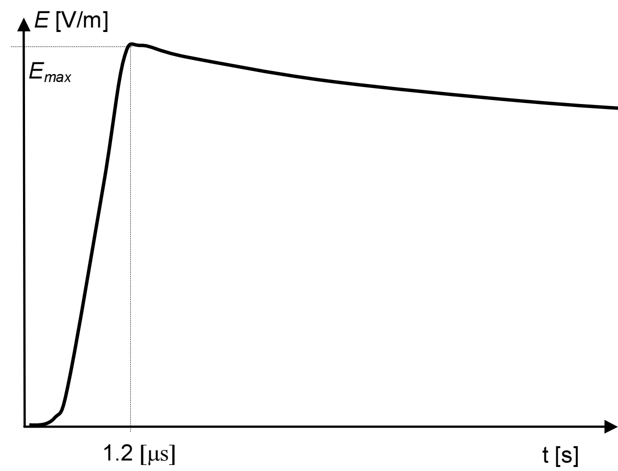

Figure 4. The electric potential time behaviour in model (11)

4 A 3-D stochastic model

If we apply the probabilistic function for the 2-D stochastic model based on relation (12)

$$P_{i,j} = \left(\frac{E_{i,j}}{E_{\mathrm{br,max}}} \right)^{\eta} \quad (13)$$

where E_{ij} is the electric intensity module of the numerical model element solved by means of the finite element method (FEM), η relates the growth probability with the local electric field, $E_{\mathrm{br,max}}$ is the electric intensity module of the electric discharge. The time behaviour of electric potential φ or electric module intensity E according to Figure 4, in which we tested the model behaviour for $E_{\mathrm{max},1}$=3kV/cm, $E_{\mathrm{max},2}$=100 kV/cm. The probability function (13) consists of two basic functions and is indicated in Fig. 5.

For example, for entering the waveform of intensity of electric field E (electric potential φ) P. Fiala, 2003, P. Fiala, 2007, from the behaviour described in Figure 3 $E_{br,\mathrm{max}}$=30kV/cm for the normal electric strenght, $E_{br,\mathrm{max}}$=300/cm for the tangential electric strenght. The 3D test model distribution of electric field E for the non-uniform mesh of the 3-D spark gap model elements is shown in Figure 6.

The distribution of changed characteristics of conductivity γ in the 3-D stochastic model based on the transient process modelling is showen in Figure 6. Figure 7 shows probability P distribution in the PCB tested model as a function of electric field E intensity according to the characteristics from Figure 5. Thus, the entire transient process was modelled according to the time behaviour of the exciting electric intensity E from Figure 4. Also, it was determined that the described probabilistic function from Enokizono M.; Tsutsumi H.,1994 has certain drawbacks for the 3-D numerical model; therefore, we used (for example) the double Gauss probabilistic function, Figure 5. This algorithm of stochastic model solution reveal oneself as a powerfull tool. Figures 8 and 9 shows probability P distribution in the PCB HV test model in different scale of displaying a function of electric field E intensity distribution. Figure 10 indicates the model complemented with a known value of specific conductivity γ.

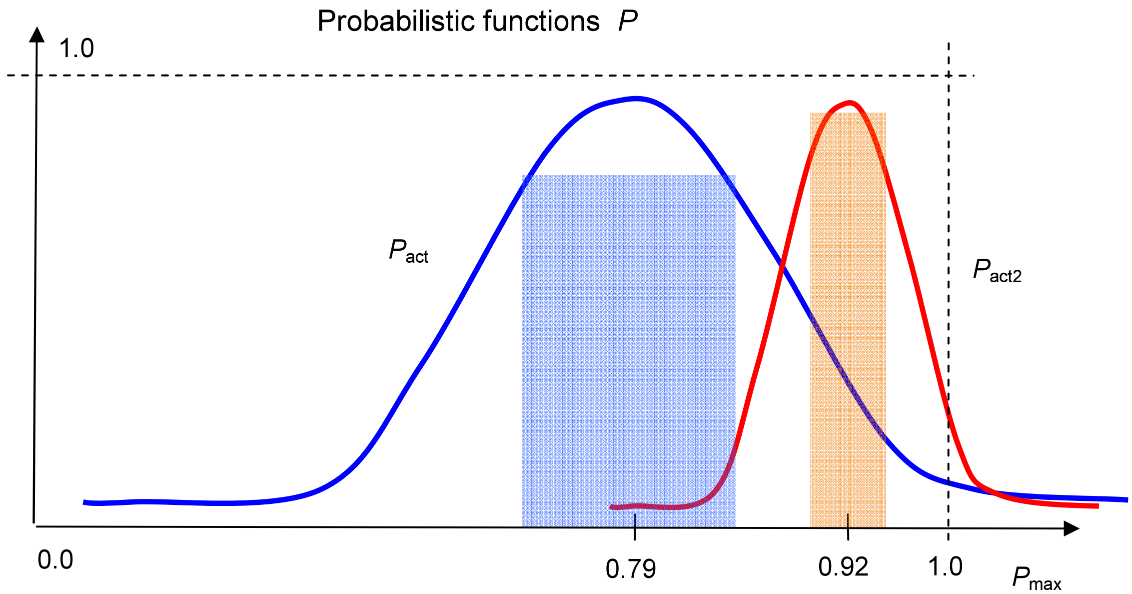

Figure 5. Used a double Gauss probabilistic function, P_{act}, P_{act2}

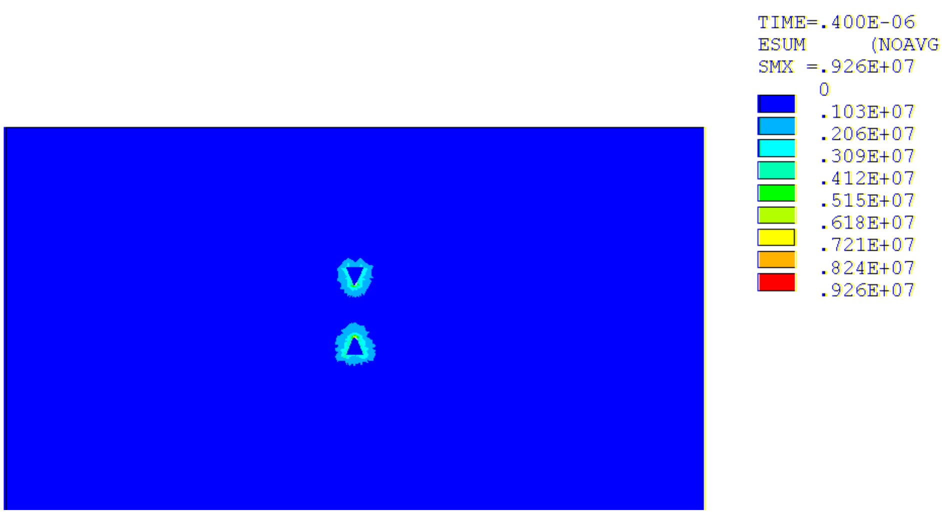

Figure 6. The spark gap model module of electric intensity distribution *E, t*= 0.4μs

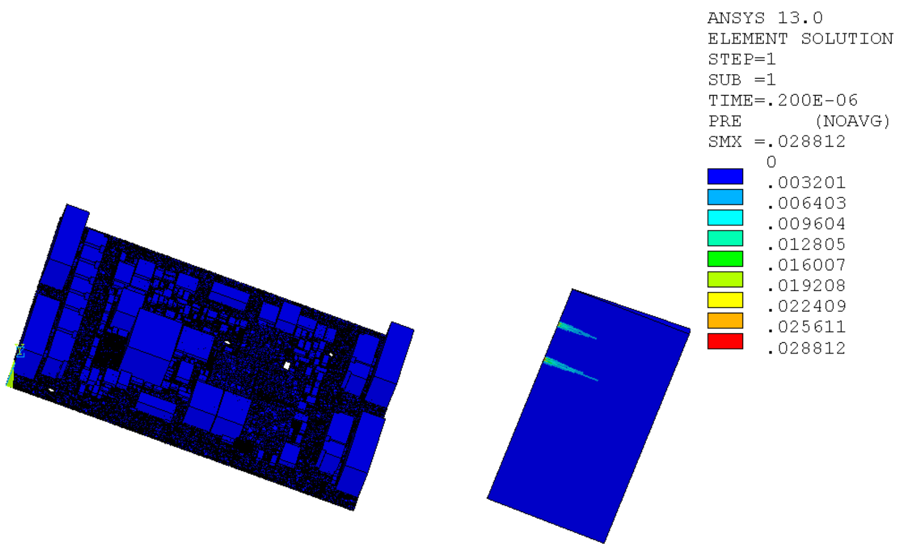

Fig.7 The distribution of probability P, t= 0.2μs

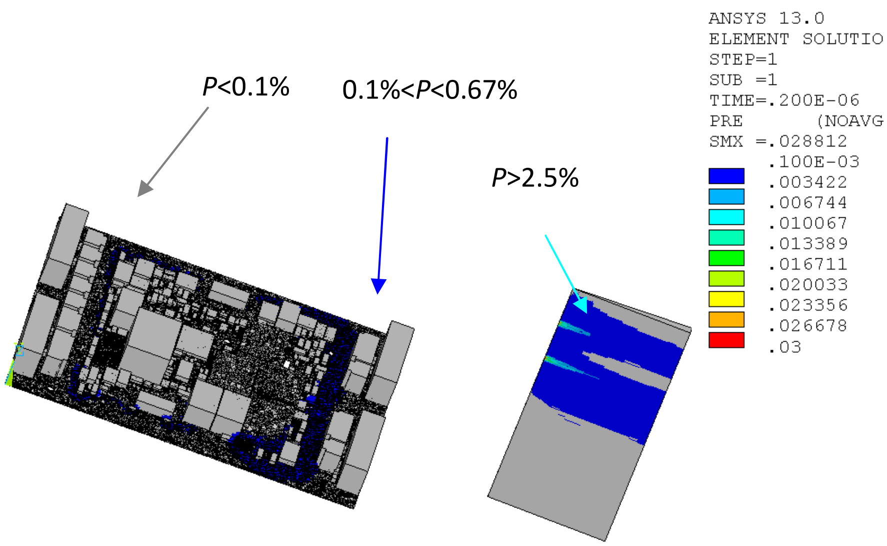

Fig.8 The distribution of the probability function P, t= 0.2μs: the probability function P at the start of the electric discharge

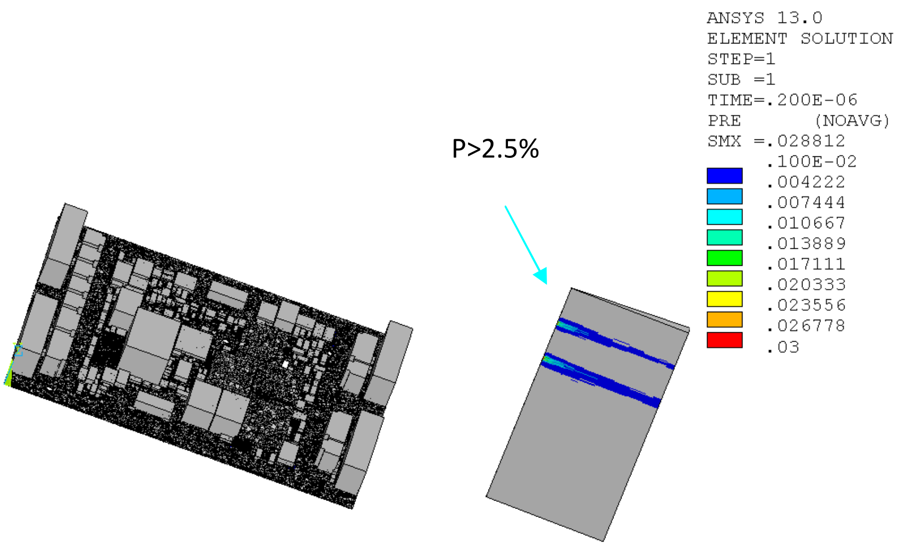

Fig.9 The distribution of the probability function P, t= 0.2μs: the probability function P at the start of the electric discharge

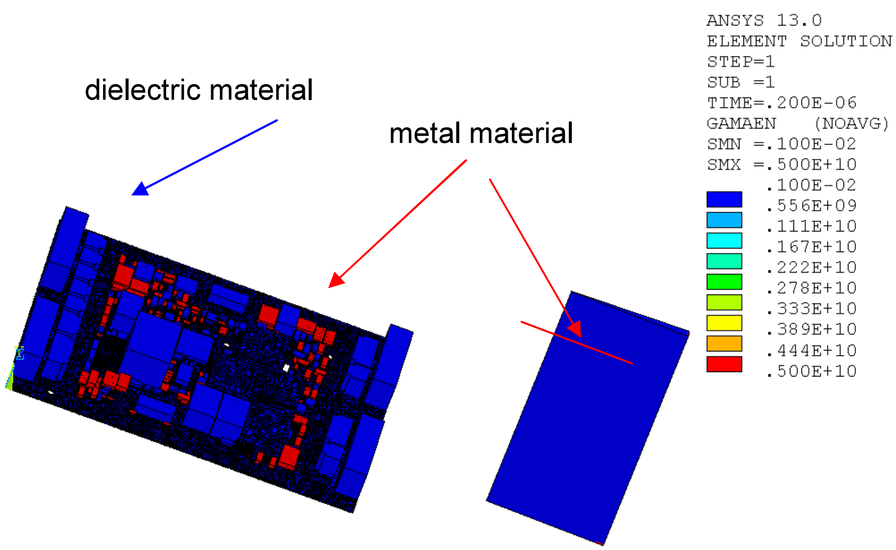

Fig.10 The distribution of conductivity γ , t = 0.2μs

5 CONCLUSION

The tests conducted by the help of a 3-D numerical model designed for the modelling of the HV electric discharge stochastic process PCB electronic design proved that the quality of the assembled numerical model, uniform distribution, and boundary conditions setting are aspects of fundamental importance to the modelling procedure, Kikuchi H., 2001. The stochastic model algorithm was tested on the design of a preliminary module having an architecture of intermediate complexity. We selected one probability function and applied it to the tested stochastic model of the electronic module.

Acknowledgements, The funding of the project was supported by Ministry of Education, Youth and Sports of the CR, and by institutional resources from the related Research Design project of the BUT Grant Agency FEKT-S-10-13, GACR 13-09086S and project from Education for Competitiveness Operative Programme CZ.1.07.2.3.00.20.0175 and CZ.1.07/2.3.00/30.0005.

References

P. Fiala, 2003, *Finite Element Method Analysis of a Magnetic Field Inside a Microwave Pulsed Generator*, 2nd European Symposium on Non-Lethal Weapons, May 13-15, Ettlingen, SRN.

P. Fiala, P. Drexler, 2007, *MEASUREMENT METHODS OF PULSED POWER GENERATORS*, 4nd European Symposium on Non-Lethal Weapons May 21-23, Ettlingen, SRN.

Enokizono M.; Tsutsumi H.,1994, *Finite element analysis for discharge phenomenon*, Magnetics, IEEE Transactions on , vol.30, no.5, pp.2936-2939, ISSN : 0018-9464

Kikuchi H., 2001, *Electrohydrodynamics in dusty and dirty plasmas, gravito-electrodynamics and EHD*, Kluwer academic publishers, Dordrecht/Boston/London, ISBN 0792368223, 9780792368229

Stratton J.A. , 1961, *Theory of electromagnetic field*. SNTL Praha , In Czech.

www[1], http://www.rastko.rs/projekti/tesla/delo/10761

www[2],http://books.google.cz/books?id=QclcZw7I4yMC&pg=PA112&lpg=PA112&dq=Nikola+Tesla+discharge&source=bl&ots=s1VLwDeNNX&sig=bqNGiCHEwHagK4PnlOSgWgqnbYg&hl=cs&ei=SEGoTd6TCoebOpW0scwJ&sa=X&oi=book_result&ct=result&resnum=2&ved=0CCIQ6AEwAQ#v=onepage&q=Nikola%20Tesla%20discharge&f=false

P.Fiala, M. Friedl, *Stochastic models of electrodynamics*, PIERS 2011, Progress In Electromagnetics Research Symposium Proceedings, Suzhou, China, Sept. 12-16, 2011, pp. 91-96, Suzhou , China, 2011.

Drexler,P. Fiala, P., *Methods for high-power EM pulse measurement*, IEEE SENSORS JOURNAL Volume:7 Issue: 7-8 , 1006-1011, JUL-AUG 2007

Contact address:
assoc.prof. Ing.Pavel Fiala, Ph.D.,
Ing. Michael Hanzelka, MBA
Ing. Ivo Behunek, Ph.D.
Brno university of technology, Faculty of electrical engineering and communication, Department of theoretical and experimental electrical engineering Technicka 12, 616 00 Brno, Czech Republic
fialap@feec.vutbr.cz, michael.hanzelka@daccee.eu, behunek@feec.vutbr.cz

STRESS ANALYSIS PERFORMED BY FINITE ELEMENT SIMULATION OF THE STRAIN GAUGE MEASUREMENT IN ANSYS

VLADIMÍR GOGA
Institute of Power and Applied Electrical Engineering, Faculty of Electrical Engineering and Information Technology, Slovak University of Technology, Ilkovičova 3, 81219 Bratislava

Abstract: This article presents finite element simulation of how the strain gauge works during stress analysis. Principle of strain gauge measurement was simulated for solid body loaded in tension. Strain gauge was modeled as solid part with mechanical and electrical properties. Model of strain gauge was supplemented with special elements to create Wheatstone bridge. Other simulation presents the measurement with strain gauge rosette to determine the state of plane stress in thin solid structure. Results from plane stress simulations were compared with experimental measurement. All finite element simulations were performed using software ANSYS.

Keywords: finite element simulation, strain gauge, stress analysis, plane stress

1 Introduction

Strain gauge is device used to measure the mechanical strains of solid bodies. Principle of strain gauge measurement is a change of the electrical resistance of the material due its deformation. Strain gauge is actually an electric wire of negligible cross section compared to its length and therefore the deformation is most pronounced precisely along its length (sensitive direction). Uniaxial strain gauge is shown in Image 1a.

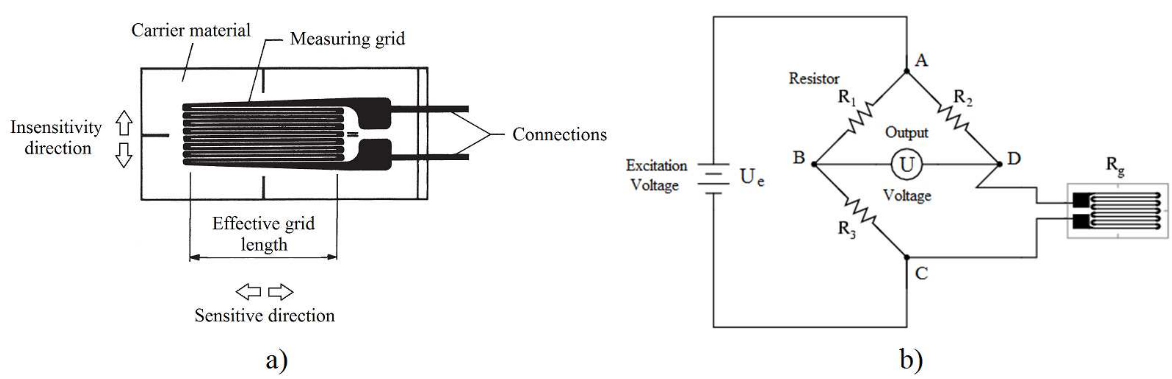

Image 10 – Strain gauge: a) uniaxial gauge, b) quarter Wheatstone bridge

Metallic foil strain gauges are commonly used. This type of strain gauge consists of a grid of wire filament (resistor) of approximately 25 μm thickness, bonded directly to the strained surface by a thin layer of epoxy resin. Typical material for wire filament is a constantan (coppernickel alloy). Strain gauge is attached to the surface of the measured structure with special glue, so that the surface deformation is transferred on the strain gauge. Surface deformation causes a very small change of the strain gauge resistance. To measure resistance change, the strain gauge is connected to the Wheatstone bridge.

Wheatstone bridge is an electrical circuit used to measure an unknown electrical resistance. Image 1b shows the quarter bridge which is used for measurement with single strain gauge. Excitation voltage U_e of the Wheatstone bridge is 1-10 V. Output voltage U is zero if gauge resistance R_g is equal to the resistance of others resistors R (resistors R_1, R_2, R_3 have the same resistance R). Resistance change ΔR_g due to gauge deformation caused nonzero output voltage (Hoffman, 1989):

$$U = \frac{1}{4} GF \cdot U_e \cdot \varepsilon \quad \Rightarrow \quad \varepsilon = \frac{4 \cdot U}{GF \cdot U_e} \tag{1}$$

where U – is output voltage [V], U_e – is excitation voltage [V], ε – is strain [-] and GF – is gauge factor [-].
This resistance change ΔR_g is related to the strain by the quantity known as the gauge factor GF. Gauge factor for metallic strain gauge is typically around 2 and nominal resistance of resistors and strain gauge is 120 or 350 Ω. Gauge factor is defined as follows (Hoffman, 1989):

$$GF = \frac{\Delta R_g / R_g}{\Delta L / L} = \frac{\Delta R_g / R_g}{\varepsilon} \tag{2}$$

where ΔR_g – is gauge resistance change [Ω], R_g – is nominal gauge resistance [Ω], ΔL – is change in length [m] and L – is original length [m].
Finally, uniaxial tension/compression stress σ in elastic region of deformation is calculated by using Hooke's law (where E – is Young's modulus [Pa]):

$$\sigma = E \cdot \varepsilon \quad \Rightarrow \quad \sigma = E \frac{4 \cdot U}{GF \cdot U_e} \tag{3}$$

The accuracy of the strain gauge measurement is affected by several factors of which the most unfavorable is temperature sensitivity. Therefore half and full bridge is used instead quarter bridge (Hoffman, 1989). Half and full bridge can also increase value of output voltage.

2 Finite element model of the strain gauge

Geometry model of the strain gauge is represented just by solid wire filament with square cross section area (S = 20×20 μm) and mid-length 42,6 mm (effective grid length is 3 mm). Wire was meshed with element SOLID5. This element has a 3-D magnetic, thermal, electric, piezoelectric, and structural field capability with limited coupling between the fields (ANSYS, 2012). Material of the strain gauge wire is constantan with properties: Young's modulus 162 GPa, Poisson's ratio 0,33 and resistivity ρ_C = 500 nΩ·m (Hoffman, 1989). Desired resistance R for strain gauge is 120 Ω. For resistivity ρ_C = 500 nΩ·m, the length of constantan wire L_C was calculated from:

$$R = \rho_C \frac{L_C}{S} \quad \Rightarrow \quad L_C = \frac{R \cdot S}{\rho_C} = 96 \text{ mm} \tag{4}$$

But length of our model is just L = 42,6 mm. Therefore new resistivity for the model had to be determined:

$$\rho = \frac{R \cdot S}{L} = 1126,76 \text{ n}\Omega \cdot \text{m} \tag{5}$$

Ratio of lengths and resistivities must be equal: $96 / 42,6 = 1126,76 / 500 = 2,2535$.

a. Resistivity of the strain gauge

New resistivity ρ was controlled by electric simulation. Boundary condition at the ending surfaces was voltage 0 V and 5 V (U_e = 5 V). Current I passes through the wire is from Ohm's law (resistance of the wire R = 120 Ω):

$$I = \frac{U}{R} = 0,041667 \text{ A} \tag{6}$$

Voltage distribution along the wire is shown in Image 2. For resistivity ρ = 1126,76 nΩ·m was current 0,04121 A, what means wire resistance was 121,33 Ω. Resistivity has been modified to ρ = 1114,5 nΩ·m when current was 0,041665 A. Resistivity of the wire is then 120,005 Ω. Final resistivity for other simulations was therefore chosen ρ = 1114,5 nΩ·m.

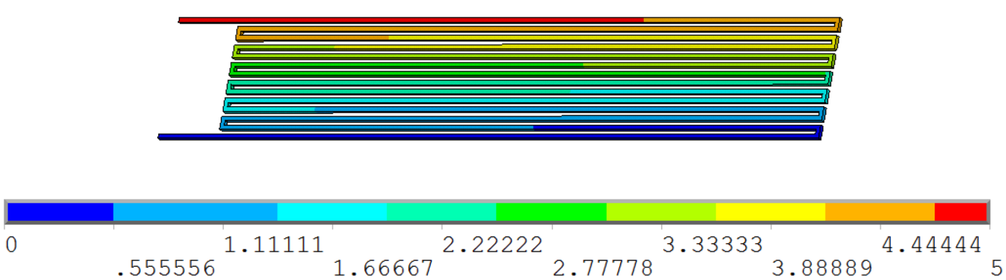

Image 2 – Voltage result [V] in strain gauge model (U_e = 5 V)

Next control of the strain gauge finite element model was simulated the Wheatstone quarter bridge connection. Three resistors were created from element CIRCU124 (ANSYS, 2012) with nominal resistance 120 Ω. Wheatstone bridge circuit is shown in Image 3. Excitation voltage in circuit was 2,5 V. Wire resistance was not exactly 120 Ω (but 120,005 Ω) therefore measured output voltage was not zero, but 0,03 mV, see Image 3. This value must be subtracted from measured output voltage in next simulations. This value of voltage can be considered as zero balance value U_0.

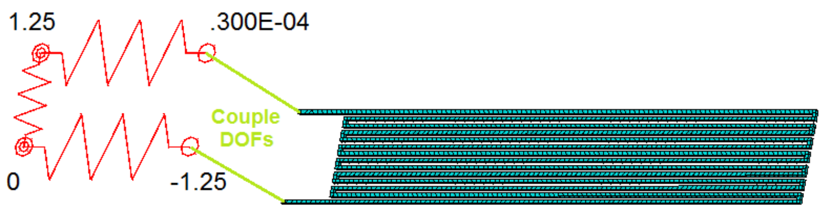

Image 3 – Output voltage [V] for unloaded strain gauge finite element model (quarter bridge)

b. Simulation of the strain gauge measurement

Strain gauge measurement was simulated for tensile test. Sample was loaded by uniaxial pressure p from 0 to 100 MPa. Applied pressure represents tensile stress in the sample. Dimensions of the sample: 23×2×1 mm. Sample material was steel with Young's modulus E = 210 GPa and Poisson's ratio 0,3. Wire of strain gauge has no significant influence on the strength of the sample therefore the Young's modulus of wire was 1 Pa and Poisson's ratio 0,499. Resistivity of wire was ρ = 1114,5 nΩ·m. Volume of tension sample was meshed with element SOLID285 (ANSYS, 2012). Complex finite element model is shown in Image 4.

For every load case structural analysis was performed first. Geometry of the finite element model was then updated to deformed configuration and electric analysis was done. Excitation voltage was U_e = 2,5 V and zero balance voltage was U_0 = 0,03 mV. Observed variable was measured voltage U_m. Longitudinal strain and stress was calculated from output voltage $U = U_m - U_0$ using Eqv. (1) and (3). Results are in Table1. Gauge factor was considered GF_1 = 2. Image 5 shows plot results of longitudinal stress and strain for load case p = 40 MPa.

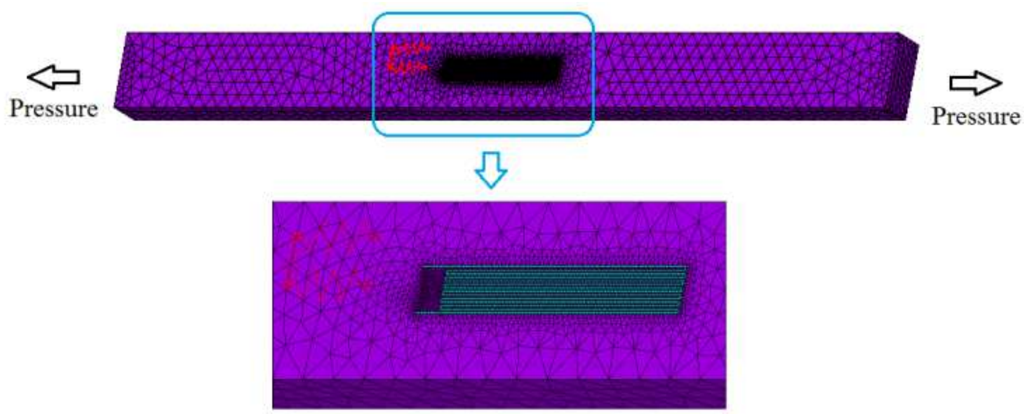

Image 4 – Finite element model of the tensile sample with strain gauge

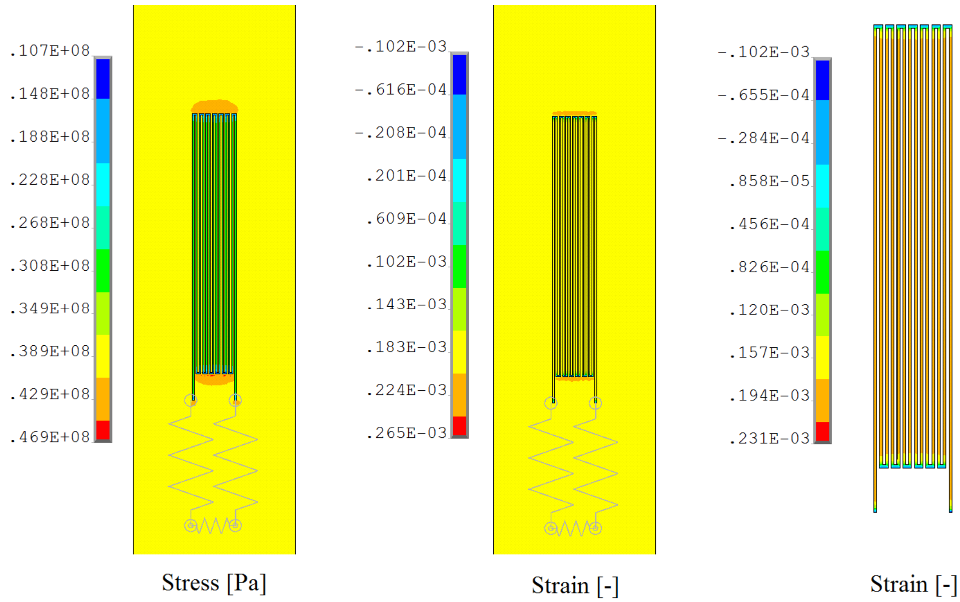

Image 5 – Longitudinal stress and strain for load case p = 40 MPa (GF_1 = 2)

Table 3 Results from simulation: voltage, strain and stress (GF_1 = 2)

p [MPa]	U_m [mV]	U [mV]	$\varepsilon \times 10^{-3}$ [-]	σ [MPa]	$\Delta\sigma$ [MPa]	$\Delta\sigma$ [%]
0	0,03000	0	0	0	0	0
20	0,14706	0,11706	0,09365	19,7	0,3	1,7
40	0,26412	0,23412	0,18730	39,3	0,7	1,7
60	0,38118	0,35118	0,28094	59,0	1,0	1,7
80	0,49824	0,46824	0,37459	78,7	1,3	1,7
100	0,61531	0,58531	0,46825	98,3	1,7	1,7

Percentage difference between applied pressure and stress result for each load case was 1,7 %. This error was caused by gauge factor GF_1. If the stresses are equal to applied pressure it is possible to calculate new gauge factor GF from Eqv. (3). New gauge factor GF = 1,967, see Table 2.

Table 2 Gauge factor GF for equal stress and applied pressure

p [MPa]	20	40	60	80	100
σ [MPa]	20	40	60	80	100

U [mV]	0,11706	0,23412	0,35118	0,46824	0,58531
GF [–]	1,967	1,967	1,967	1,967	1,967

3 Plane stress analysis

Plane stress is a special case of general three-dimensional stress state at a point of structure under mechanical loading. Plane stress is typical in many engineering problems where the stresses are induced in a thin plate or on the free surface of a structural element. A point of thin-walled structure can be represented as a rectangular planar element in the *x-y* plane. This element in the state of plane stress has three nonzero stress components: two normal stresses σ_x, σ_y and one shear stress τ_{xy} (from static equilibrium $\tau_{xy} = \tau_{yx}$) as shown in Image 6a. Stress components σ_x, σ_y and τ_{xy} change with the angle φ of rotation of the element into new coordinate system. In new coordinate system, there are maximum σ_1 and minimum σ_2 normal stresses called principal stresses and zero shear stress in the element, see Image 6b. Principal stresses lie in principal directions. Maximum shear stress τ_{max} occurs when the element is rotated from principal directions about angle 45°, see Image 6c. For this orientation of element, there are except maximum shear stress τ_{max} also two nonzero normal stresses with the same average stress value σ_{ave}. More detail about plane stress can be found in (Bauchau, 2009 and Ugural, 2011).

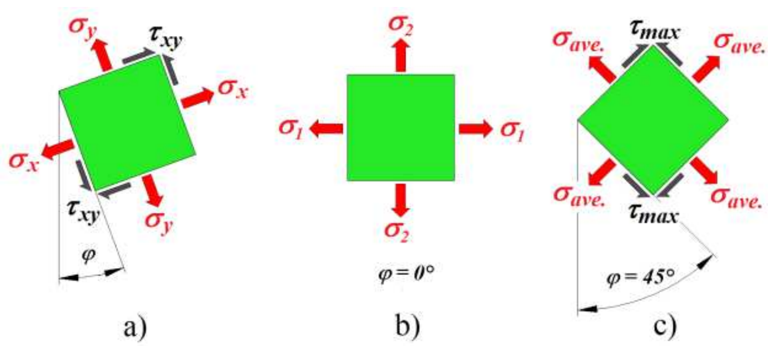

Image 6 – Element in the state of plane stress:
a) *x-y* coordinate system, b) principal directions, c) direction of maximum shear stress

Three stress components in plane stress state produce in *x-y* plane deformation given by extensional strains ε_x and ε_y and shear strain γ_{xy}. Relation between stress and strain in elastic region of deformation is given by generalized Hooke's law (where E is Young's modulus and ν is Poisson's ratio):

$$\begin{bmatrix} \varepsilon_x \\ \varepsilon_y \\ \gamma_{xy} \end{bmatrix} = \frac{1}{E} \begin{bmatrix} 1 & -\nu & 0 \\ -\nu & 1 & 0 \\ 0 & 0 & 2(1+\nu) \end{bmatrix} \begin{bmatrix} \sigma_x \\ \sigma_y \\ \tau_{xy} \end{bmatrix} \Leftrightarrow \begin{bmatrix} \sigma_x \\ \sigma_y \\ \tau_{xy} \end{bmatrix} = \frac{E}{1-\nu^2} \begin{bmatrix} 1 & \nu & 0 \\ \nu & 1 & 0 \\ 0 & 0 & \frac{1-\nu}{2} \end{bmatrix} \begin{bmatrix} \varepsilon_x \\ \varepsilon_y \\ \gamma_{xy} \end{bmatrix} \tag{7}$$

To determine the state of plane stress, it is necessary measure not only two extensional strains, but also shear strain, with respect to some given *x*-*y* coordinate system. However, there is not direct way to measure the shear strain (Bauchau, 2009). The solution of this problem is to make three independent measurements of extensional strains at a point on the surface of structure. The most obvious approach is to place three strain gauges together in a rosette with each gauge oriented in a different direction and with all of them located as close together as possible to approximate a measurement at a point (Bauchau, 2009). Strain gauges in rosette are typically oriented at fixed angle 45° (rectangular rosette) or 60° (delta rosette) with respect to each other.

Image 7 shows measurement with rectangular strain gauge rosette. Gauge *A* is rotated relative to the principal axis 1 of the angle φ. Directions of gauges *A* and *C* represents *x*-*y* coordinate system of the element. From measured strains ε_A, ε_B, ε_C we can determine strain components for element in *x*-*y* coordinate system (Hoffman, 1989):

$$\varepsilon_x = \varepsilon_A \;\; ; \;\; \varepsilon_y = \varepsilon_C \;\; ; \;\; \gamma_{xy} = 2\varepsilon_B - \varepsilon_A - \varepsilon_C \tag{8}$$

Now, it is possible calculate stresses in the element in *x*-*y* coordinate system using generalized Hooke's law using Eqv. (7). Principal stresses $\sigma_{1,2}$, maximum shear stress τ_{max} and angle φ between principal directions and *x*-*y* coordinate system and the equivalent von Mises stress σ_{Mises} are then calculated from:

$$\begin{aligned} &\sigma_{1,2} = \frac{(\sigma_x + \sigma_y)}{2} \pm \sqrt{\left(\frac{\sigma_x - \sigma_y}{2}\right)^2 + \tau_{xy}^2} && \tan(2\varphi) = \frac{2\tau_{xy}}{\sigma_x - \sigma_y} \\ &\tau_{max} = \pm\sqrt{\left(\frac{\sigma_x - \sigma_y}{2}\right)^2 + \tau_{xy}^2} = \pm\frac{(\sigma_1 - \sigma_2)}{2} && \sigma_{Mises} = \sqrt{\sigma_1^2 - \sigma_1\sigma_2 + \sigma_2^2} \end{aligned} \tag{9}$$

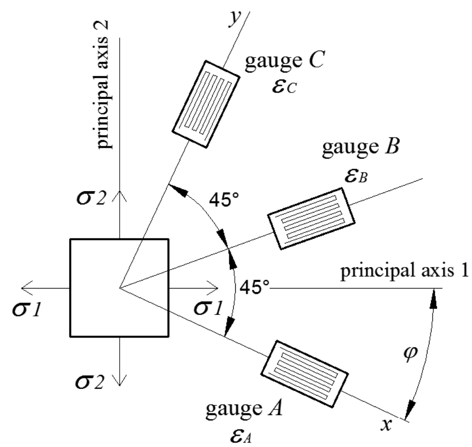

Image 7 – Rectangular strain gauge rosette

a. Testing specimen

Plane stress was investigated in the center of specimen shown in Image 8a. Specimen was loaded in tension by force *F* as shown in Image 8b. Parameters for plane stress test:

- shape and dimensions (in millimeters) of the specimen are shown in Image 8a;
- thickness of the specimen: t = 1 mm;
- material: aluminum (E = 70 GPa, ν = 0.33);
- applied force: F = 200, 400, 600 N.

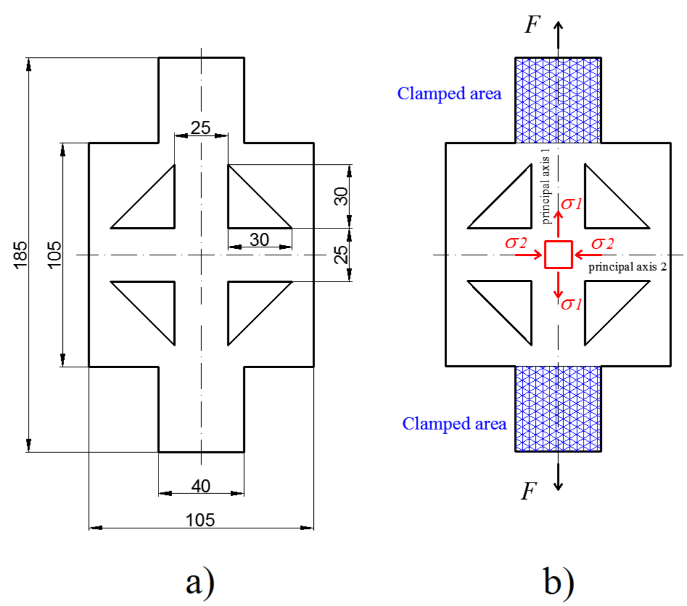

Image 8 – Specimen: a) shape with dimensions,
b) loaded of the specimen and expected state of stress

b. Standard static structural analysis

The first simulation was performed standard static structural analysis. Results from simulation for applied load F = 400 N are shown in Image 9. All results are in Table 3.

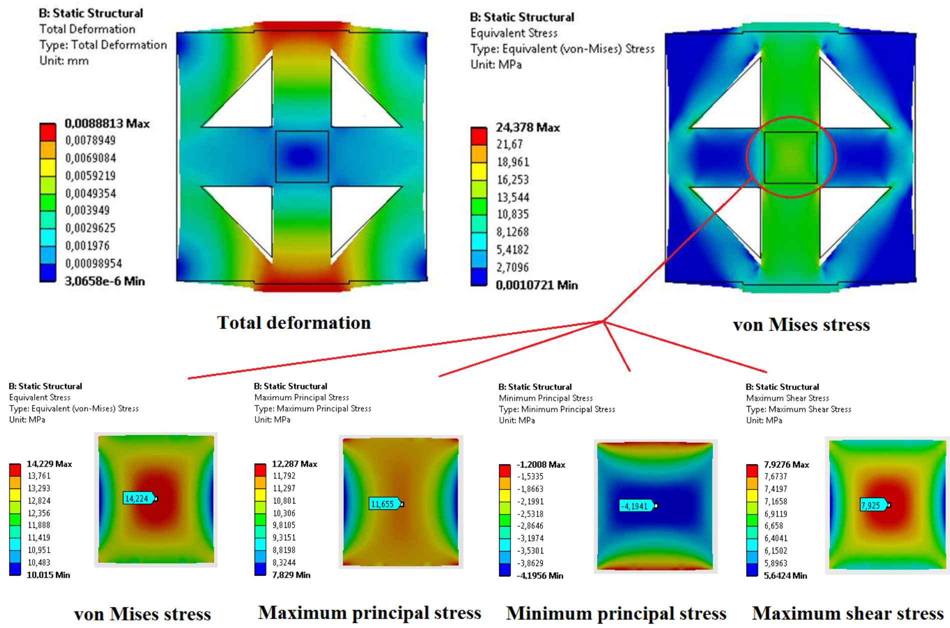

Image 9 – Plot results for load case F = 400 N

c. Simulation of strain gauge rosette measurement

Rectangular strain gauge rosette was modeled in the center of specimen to determine three individual extensional strains. Orientation of the rosette is shown in Image 10. Gauge A is rotated from principal axis 2 about angle φ = –20°. Specimen was modeled as three-dimensional body and each gauge was modeled as individual shell element with own local coordinate system (dimensions 1×0.5 mm, thickness 0.001 mm). Results of this simulation were extensional strains of individual gauges ε_A, ε_B, ε_C (strain in X axis of local coordinate system, see Image 10). Stress quantities were calculated from the strain results using Eqv. (7), (8) and (9). All results are presented in Table 3.

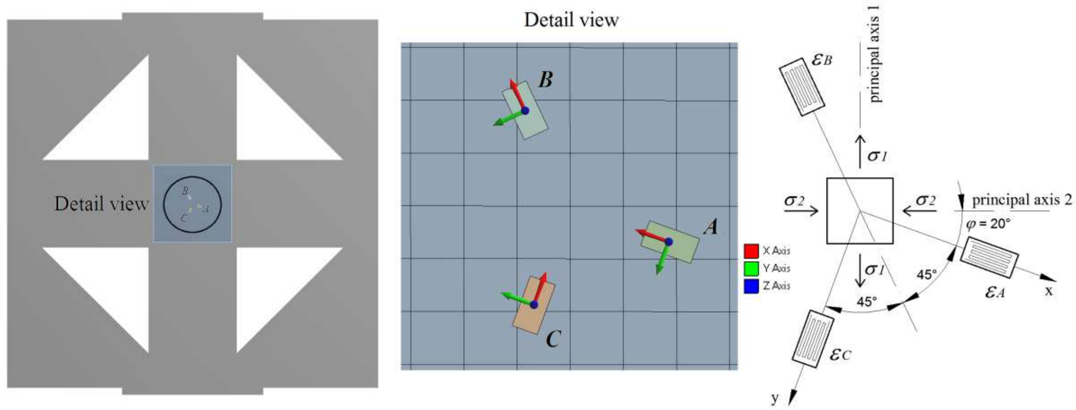

Image 10 – Model and orientation of the strain gauges

d. Experimental measurement

Real specimen was subjected to testing. Three gauges were attached on the specimen. Orientation of gauges is the same as in previous finite element simulation, see Image 11. Measured strains and calculated stresses are in Table 3. Devices used for experimental measurements: universal tensile testing machine, load cell, strain gauges, measuring amplifier, PC with software to acquisition and visualization of measuring data.

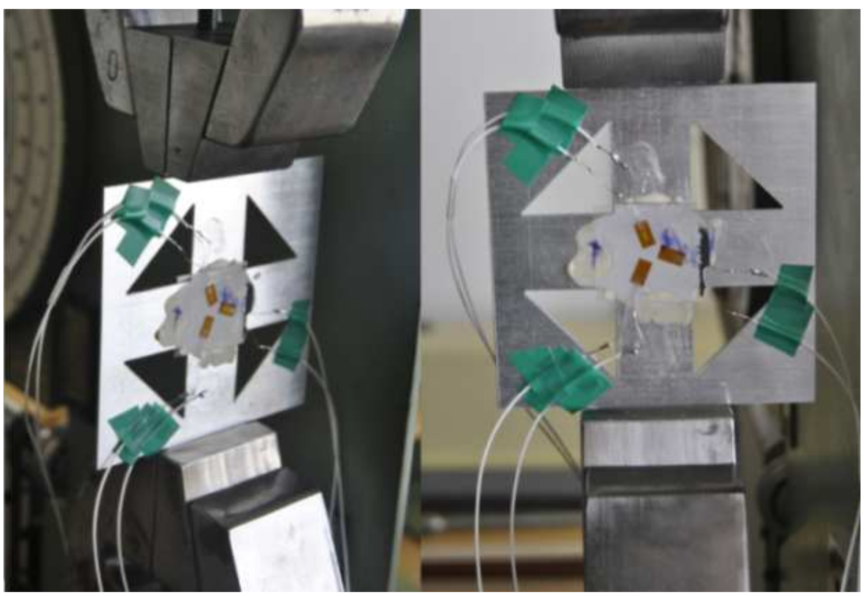

Image 11 – Experimental measurement: specimen with strain gauges

Table 3 Results from simulations and measurements

F	ε_A	ε_B	ε_C	σ_x	σ_y	τ_{xy}	σ_1	σ_2	τ_{max}	σ_{Mises}	φ
[N]	[μm/m]	[μm/m]	[μm/m]	[MPa]	[MPa]	[MPa]	[MPa]	[MPa]	[MPa]	[MPa]	[°]
Static structural analysis											
200	-	-	-	-	-	-	5.0	-2.0	4.0	7.1	-
400	-	-	-	-	-	-	11.7	-4.2	7.9	14.2	-
600	-	-	-	-	-	-	17.5	-6.3	11.9	21.3	-
FEA of strain gauge rosette measurement											
200	-39.6	65.7	74.9	-1.2	4.9	2.5	5.8	-2.1	3.9	7.1	-20
400	-79.1	131.4	149.8	-2.3	9.7	5.1	11.6	-4.2	7.9	14.1	-20
600	-118.7	197.1	224.7	-3.5	14.6	7.6	17.3	-6.3	11.8	21.2	-20
Experimental measurement											
200	-40.4	61.6	68.6	-1.4	4.3	2.5	5.3	-2.3	3.8	6.8	-20.5
400	-80.8	123.2	137.2	-2.8	8.7	5.0	10.6	-4.7	7.6	13.5	-20.5
600	-121.2	184.8	205.8	-4.2	13.0	7.5	15.8	-7.0	11.4	20.3	-20.5

4 Conclusion

Simulation of strain gauge measurement was performed using finite element method in software ANSYS. Strain gauge was modeled as a wire and its resistivity was calculated and adjusted according to the simulation. Finite element model of tensile sample with strain gauge was created and loaded by uniaxial pressure. Results from simulations were output voltage in quarter Wheatstone bridge and strains and stresses in the sample were then calculated. Finite element method was also used for simulation of measurement with strain gauge rosette to determine the state of plane stress. Percentage errors of von Mises stress results from the simulations are less than 6 % in view of the experimental measurement.

References

ANSYS Help, 2012

BAUCHAU O.A., CRAIG J.I., „Structural Analysis: With Applications to Aerospace Structures" Publisher: Springer, ISBN 978-90-481-2515-9, 2009

HOFFMANN K., „An Introduction to Measurements using Strain Gages“, Darmstadt: Hottinger Baldwin Messtechnik GmbH, 1989

UGURAL A.C., FENSTER S.K., „Advanced Mechanics of Materials and Applied Elasticity“, Publisher: Prentice Hall, ISBN 978-0-13-707920-9, 2011

Acknowledgement
This work was supported by: Slovak Research and Development Agency under the contracts APVV-0450-10, Grant Agency KEGA - grant No. 015STU-4/2012 and grant VEGA No. 1/0534/12.

Contact address:
Ing. Vladimír Goga, PhD.
Institute of Power and Applied Electrical Engineering, Faculty of Electrical Engineering and Information Technology, Slovak University of Technology, Ilkovičova 3, 81219 Bratislava
e-mail: vladimir.goga@stuba.sk

FULLWAVE ELEKTROMAGNETICKÁ ANALÝZA UHLÍKOVÝCH KOMPOZITŮ S OHLEDEM NA JEJICH MIKROSTRUKTURU A ANIZOTROPII

STANISLAV GOŇA

FAI UTB Zlín, Nad Stráněmi 4511, 760 05 Zlin

Abstract: This paper describes FEM high frequency electromagnetic analysis of composite materials consisting from the epoxy and long carbon fibers with respect to their anizotropy. The result of the analysis is the transmission coefficient (resp. shielding effectiveness) of the composite for the plane electromagnetic wave with linear polarization in the frequency range 100 MHz to 18 GHz. Main concern of the paper is focused to the transformation of electromagnetic material properties (namely tenzor of high frequency conductivity) from the local system connected with fibers to the global Cartesian system. An example of the high frequency electromagnetic analysis for two composite samples having different structure and orientation of carbon fibers is given in the paper. Shielding effectiveness of these samples is compared with an analytical model, which is valid at the low frequency region.

Keywords: carbon fiber composites, high frequency conductivity, anizotropy, shielding effectiveness

1 Úvod

Vysokofrekvenční elektromagnetická analýza kompozitů byla v minulosti nejčastěji prováděna pomocí momentové metody (Chin,1998) nebo analytických přístupů připodobňující uhlíkový kompozit k přenosovému vedení (Holloway,2006), a to z důvodu limitaci paměti a výpočetního výkonu stolních počítačů. V posledních 10 letech je prakticky možné provádět vysokofrekvenční analýzu uhlíkových kompozitů také pomocí komerčně dostupných fullwave simulačních nástrojů (Ansys, Cst microwave studio případně dalších), a to i na běžných stolních PC s pamětí řádově do 4 GB.

V programu Ansys je přitom možná analýza vysokofrekvenčních vlastností kompozitů s uvažováním jejich anizotropie od verze Ansys 11 (z roku 2007). Předchozí verze byly omezeny na izotropní vysokofrekvenční materiálové modely.

Tento příspěvek popisuje fullwave elektromagnetickou analýzu vlastností uhlíkových kompozitů CFC (Carbon Fiber Composites) s dlouhými uhlíkovými vlákny. Tyto kompozity nacházejí nejčastěji uplatnění v leteckém průmyslu jako potahové materiály semikompozitních letounů. Nověji se objevují také v automobilovém průmyslu. Každý kompozit se sestává z řady vrstev (v angličtině označovaných jako plies) s tloušťkou cca. 100 až 150 mikrometrů. V každé vrstvě jsou vlákna orientována buď jedním směrem (Obr. 1) nebo jsou provedeny ve formě struktury utkané ve formě mřížky (Obr. 2). Druhé provedení je častější neboť zaručuje potřebnou mechanickou stabilitu. Nicméně pro zjednodušení analýzy je v praxi dostatečné uvažovat náhradu struktury z Obr. 2 pomocí dvou vrstev (plies) orientovaných ve směru 0 a 90 stupňů.

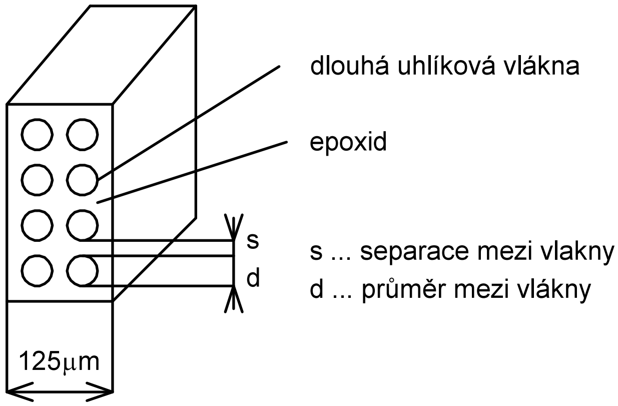

Obrázek 11 - Jedna vrstva (ply) uhlíkového kompozitu s vlákny orientovanými v jednom směru (unidirectional carbon fiber composite with long carbon fibers)

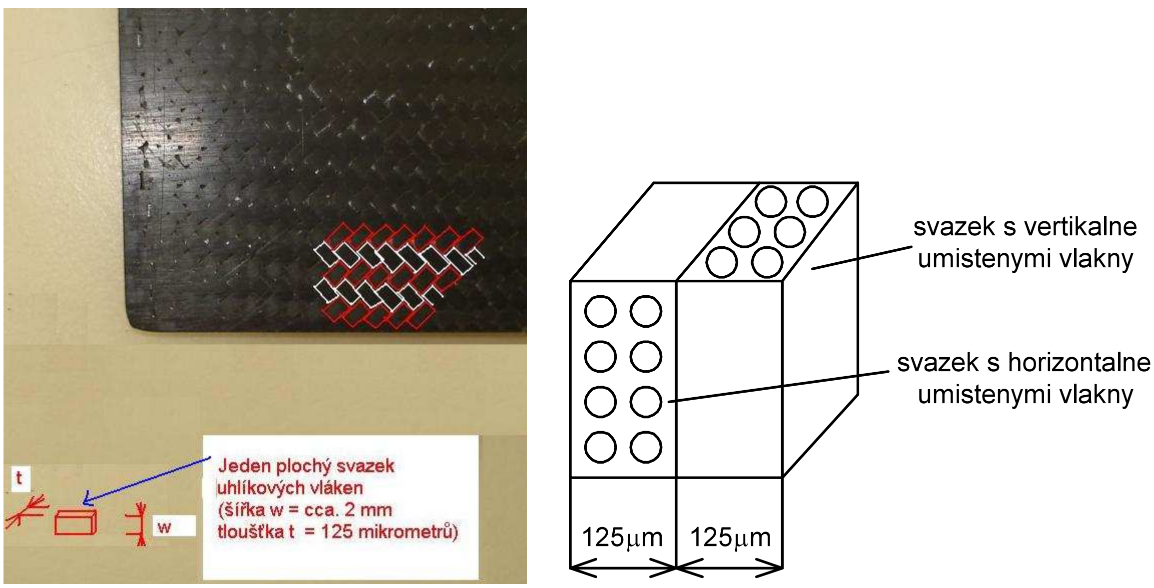

Obrázek 2 - *Vlevo) Jedna vrstva (ply) uhlíkového kompozitu s vlákny orientovanými ve tvaru mřížky. Vpravo) Náhrada takovéto vrstvy pomocí dvojce vrstev*

CFC kompozity používané v praxi mají většinou alespoň 8 vrstev s typickou tloušťkou okolo 125 mikrometrů. Orientace vláken v jednotlivých vrstvách přitom ovlivňuje výslednou dosažitelnou stínící účinnost (Mehdipour,2008). Příklad takového kompozitu, který je také dále analyzován v tomto článku je uveden v Obr. 3.

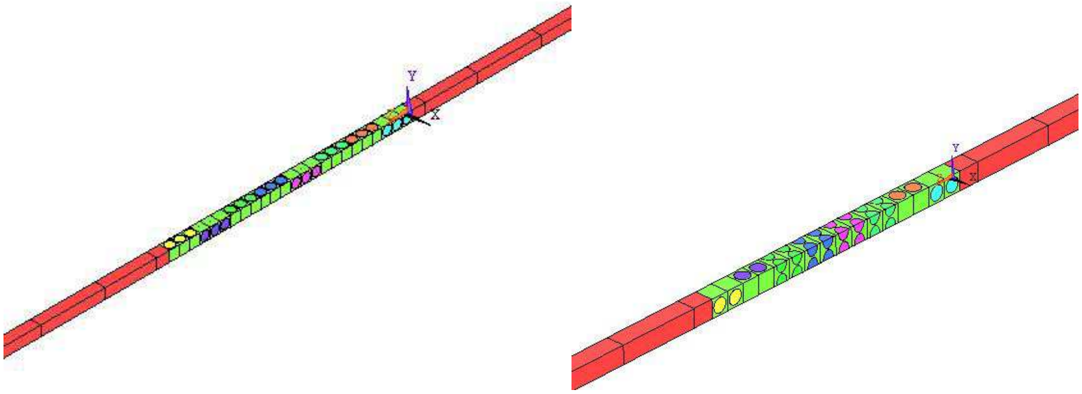

Obrázek 3 - Příklad CFC kompozitu s 8 vrstvami a rozdílnou orientací vláken v jednotlivých vrstvách. Vlevo 00,90,90,0,90,90,0,90 stupňů. Vpravo 00,90,45,-45,-45,45,90,0. Počet vláken je zmenšen oproti realitě. Objemy jsou barevně odlišeny (zelená = epoxid, červená = vzduch, ostatní bravy představují uhlíkvá vlákna v jednotlivých vrstvách)

2 Materiál a metody

Vysokofreveční elektromagnetická analýza v programu Ansys pokrývá řadu problémů z oblasti mikrovlnné techniky, antén a problémů týkajících se vedení či vyzařování elektromagnetických vln, a to při užití elementů HF118, 119 nebo HF120. Určitou speciální částí této oblasti je analýza periodiických struktur, tj. struktur které mají 1D, 2D nebo 3D periodicitu. V tomto případě probíhá analýza na ohraničené oblasti, tzv. základní peridické buňce. Viz. Obr.4. Hranice této buňky jsou přitom na souřadnících <-a/2;a/2> pro směr x, a <-a/2;a/2> pro směr y. Na hranicích buňky je nutné pomocí příkazu CPCYC aplikovat tzv. Periodickou okrajovou podmínku. Tato podmínka se aplikuje na stupeň volnosti AX, který má pro vysokofrekvenční problémy význam složky Hertzova vektoru (na rozdíl od nízkofrekvenčního elektromagnetismu, kde má AX význam magnetického vektrorového potenciálu.

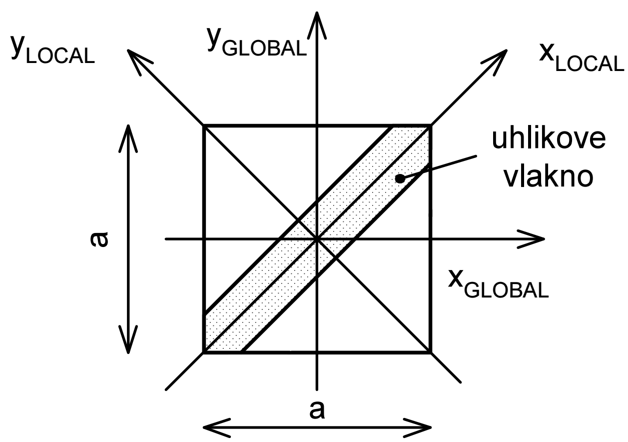

Obrázek 4 - Základní buňka kompozitu (2D pohled, řez jedním z vláken)

Uvnitř peridocié buňky se nachází uhlíkové vlákno danou oreintací vzhledem k ose x_{global}. Uhlíkové vlákno má relativní permitivitu $[\varepsilon_r]$ a $[\gamma]$, kde $[\varepsilon_r]$ a $[\gamma]$ jsou tensory relativní permitivity a vysokofrekveční vodivosti vlákna. Celkově lze vlákno popsat jediným materiálovým parametrem, a to komplexní permitivitou

$$[\varepsilon_{r\_complex}] = [\varepsilon_r] - j\frac{[\gamma]}{\omega\,\varepsilon_0} \tag{1}$$

$$[\varepsilon_{r\_LOCAL}] = \begin{bmatrix} \varepsilon_{rxx} & 0 & 0 \\ 0 & \varepsilon_{ryy} & 0 \\ 0 & 0 & \varepsilon_{rzz} \end{bmatrix} \tag{2}$$

$$[\gamma_{\_LOCAL}] = \begin{bmatrix} \gamma_{xx} & 0 & 0 \\ 0 & \gamma_{yy} & 0 \\ 0 & 0 & \gamma_{zz} \end{bmatrix} \tag{3}$$

Pro zjednodušení budeme předpokládat, že permitivita uhlíkového vlákna je izotropní, to jest $\varepsilon_r = \varepsilon_{rxx} = \varepsilon_{ryy} = \varepsilon_{rzz} = 3.3$. Naopak vlákna budou anizotropní, kde $\gamma_{yy} = \gamma_{zz} = 0.1 S/m$ a $\gamma_{xx} = 17000 S/m$ jsou složky vodivosti vlákna v lokálním souřadném systému.

Vysokofrekvenční analýza vlastností kompozitních materiálů se většinou omezuje na výpočet koeficeintu odrazu a koeficientu prostupu dané periodické strutury. Například kompozitů uvedených v Obr. 3. V takovém případě je vzorek kompozitu umístěn v tzv. TEM vlnovodu, který je buzen z jedné strany mikrovlnný port číslo 1, a na druhé straně je vyhodnocován komplexní přenos S_{21} do přizpůsobeného portu číslo 2. Celý TEM vlnovod je z obou stran ukončen tzv. přizůsobenou vrstvou PML. Celá situace je schematicky zachycena na Obr. 5. Vzdálenost portů 1 a 2 od testované struktury by měla být taková, aby bylo možné předpokládat, že na portu 1 a 2 existuje pouze rovinná elektromagnetická vlna, a vyšší spektrální složky elektrické intezity dopadající vlny je možné zanedbat. Vzhledem k tomu, že základní periodická buňka analyzovaných kompozitů má velmi malý rozměr (řádově jednotky mikrometrů), tak je nutné jenom velmi malá separace mezi portem a strukturou (řádově desítky mikrometrů). V příkladech uvedených dále je použita hodnota h_{wg}=100 mikrometrů.

Co se týká vrstvy PML, tak její tloušťka je většinou volena jako 0.25 vlnové délky ve vzduchu. Nicméně na nížkých kmitočtech by měl TEM vlnovod v části PML příliš extrémní stranový poměr (aspect ratio,a tak je možné veliksot této vrstvy zmenšit až na cca. 0.01 vlnové délky ve vzduchu) při zachování stability a správnosti vypočtených koeficientů S_{11} a S_{21}.

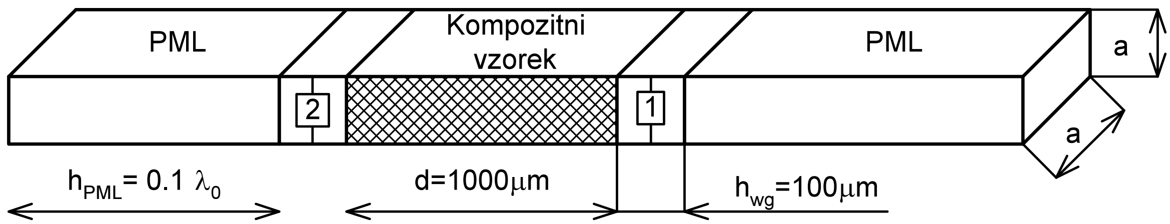

Obrázek 5 – TEM vlnovod s analyzovaným kompozitním vzorkem

Model na Obr. 5 je buzen pomocí planewave portů, schematicky zobrazených v Obr. 5 čísly 1 a 2. Na portu číslo jedna byla uplatněna vertikální polarizace, tj. vektor elektrické intenzity dopadající vlny měl orientaci ve svislém směru. Předmětem analýzy byl výpočet výkonového koeficientu přenosu (power transmission coefficient) T v decibelech.

$$T[dB] = 10\log_{10}\left(\frac{P_2}{P_1}\right) \tag{4}$$

kde P_1 a P_2 jsou činné výkony dodané do portu 1 a absorbované v portu 2. SE je výkonová stínící účinnost kompozitního materiálu (vložný útlum) platná pro buzení kompozitu rovinnou elektromagnetickou vlnou.

Samotná analýza probíhá pomocí standardní harmonické vysokofrekvenční analýzy v prostředí Ansys Classic (tj. ANTYPE,HARMIC) pro požadovaný rozsah frekvencí. Následný výpočet koeficientu odrazu a prostupu je realizován voláním makra FSSPARM.MAC.

3 Teorie – transformace vodivosti

V oblasti elektromagnetismu, jak nízkofrekvenčního tak vysokofrekvenčního mají Maxwellovy rovince formálně stejný star ve všech souřadných systémech. Nicméně při přechodu z jednoho souřadného sytému do jiného se odpovídajícím způsobem (Johnosn, 2010) transformují materiálové vlastnosti prostředí, tj. permitivita a permebilita.

$$\left[\varepsilon_{GLOBAL}\right]=\left[Jac\right]\left[\varepsilon_{LOCAL}\right]\left[Jac\right]^{T} \tag{5}$$

kde Jac je Jakobian zobrazení, v našem případě transformace souřadnic z lokálních na globální.

$$\begin{bmatrix} x_{GLOBAL} \\ y_{GLOBAL} \\ z_{GLOBAL} \end{bmatrix}=\begin{bmatrix} \cos(\varphi) & -\sin(\varphi) & 0 \\ \sin(\varphi) & \cos(\varphi) & 0 \\ 0 & 0 & 1 \end{bmatrix}\begin{bmatrix} x_{LOCAL} \\ y_{LOCAL} \\ z_{LOCAL} \end{bmatrix} \tag{6}$$

Po aplikaci vztahu (4) dostaneme následující maticový součin

$$\left[\varepsilon_{r\_GLOBAL}\right]=\begin{bmatrix} -\sin(\varphi) & -\cos(\varphi) & 0 \\ \cos(\varphi) & -\sin(\varphi) & 0 \\ 0 & 0 & 1 \end{bmatrix}\begin{bmatrix} \varepsilon_{rxx} & 0 & 0 \\ 0 & \varepsilon_{ryy} & 0 \\ 0 & 0 & \varepsilon_{rzz} \end{bmatrix}\begin{bmatrix} -\sin(\varphi) & -\cos(\varphi) & 0 \\ \cos(\varphi) & -\sin(\varphi) & 0 \\ 0 & 0 & 1 \end{bmatrix}^{T} \tag{7}$$

Zjednodušením a aplikací na tensor vodivosti lze psát

$$\left[\gamma\right]_{GLOBAL}=\begin{bmatrix} \cos^{2}(\varphi)\gamma_{11}+\sin^{2}(\varphi)\gamma_{22} & \sin(\varphi)\cos(\varphi)(\gamma_{11}-\gamma_{22}) & 0 \\ \sin(\varphi)\cos(\varphi)(\gamma_{11}-\gamma_{22}) & \sin^{2}(\varphi)\gamma_{11}+\cos^{2}(\varphi)\gamma_{22} & 0 \\ 0 & 0 & \gamma_{33} \end{bmatrix} \tag{8}$$

kde γ_{11}, γ_{22}, γ_{33} jsou složky tenzoru vodivosti v lokálním souřadném systému, tj. systému spojeném s vlákny. Vodivost γ_{11} je podélná vodivost ve směru osy vlákna. Vodivosti γ_{22} a γ_{33}

jsou vodivosti ve směru kolmém na osu vlákna. Úhel φ udává pootočení lokálního souřadného systému (pootočení vlákna) vzhledem k globálnímu systému CSYS,0.

4 Výsledky

V rámci tohoto článku byla provedena vysokofrekvenční elektromagnetická analýza dvou kompozitních vzorků, schematicky vyobrazených v obrázku 3. Celková tloušťka kompozitu byla h = 1 mm. Kompozit se skládal z osmi vrstev. Každá vrstva s tloušťkou h1 = 125 mikrometrů byla tvořena 16 vlákny. Průměr vlákna byl d = 6.75 mikrometru (hodnota změřená optickým mikroskopem Leica). Separace mezi vlákny byla s = 1.06 mikrometru. Kombinace průměr vlákna a separace odpovídala objemové koncentraci vláken p = 58.7 %.

$$p = \frac{\frac{\pi d^2}{4}}{(d+s)^2} \qquad (9)$$

Model kompozitu z Obr. 3, je zobrazen v Obr. 6. Tento model byl vytvořen pomocí v jazyce APDL v prostředí Ansys Classic. Síťování modelu bylo provedeno částečně lokálně pomocí LESIZE (vrstva PML) a částečně globálně pomocí ESIZE. Hustota sítě v oblasti vláken a epoxidu byla přitom ESIZE,d/6,6 kde *d* je průměr vlákna. Jako typ elementů byl použit tetrahedrální element HF119 s lineární aproximací. Celý model se sestával zhruba z 400 000 elementů. Poblíž první a poslední vrstvy (ply) se nacházel pomocný objem s větší hustotou sítě, aby byly správně modelovány vyšší spektrální složky intezity elektrického pole.

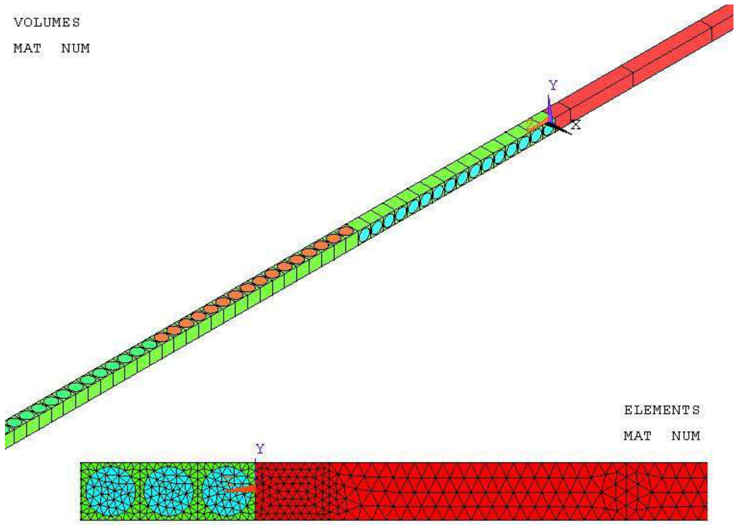

Obr. 6 Detail části geometrického a FEM modelu kompozitu 00,90,90,0,90,90,0,90 v prostředí Ansys Classic (červená odpovídá vzduchu, zelená epoxidu, ostatní barvy odpovídají uhlíkovým vláknům v příslušných vrstvách)

Pro model z Obr. 6 byla voláním makra FSSPARM.MAC vypočtena stínící účinnost pro pásmo 100 MHz až 18 GHz. Výsledky tohoto výpočtu jsou uvedeny v Obr. 7. Na nízkých kmitočtech tato stínící účinnost dosahuje hodnoty okolo 62dB. Pro vyšší kmitočty řádově nad 1GHz stínící účinnost monotónně roste a na nejvyšším kmitotu 18 GHz dosahuje hodnoty okolo 190 dB. Mezi LF aproximací a FEM modelem je na nejvyšším pracovním kmitočtu 18 GHz velmi malý rozdíl, neboť perioda buňky kompozitu je mnohem menší než je délka vlny.

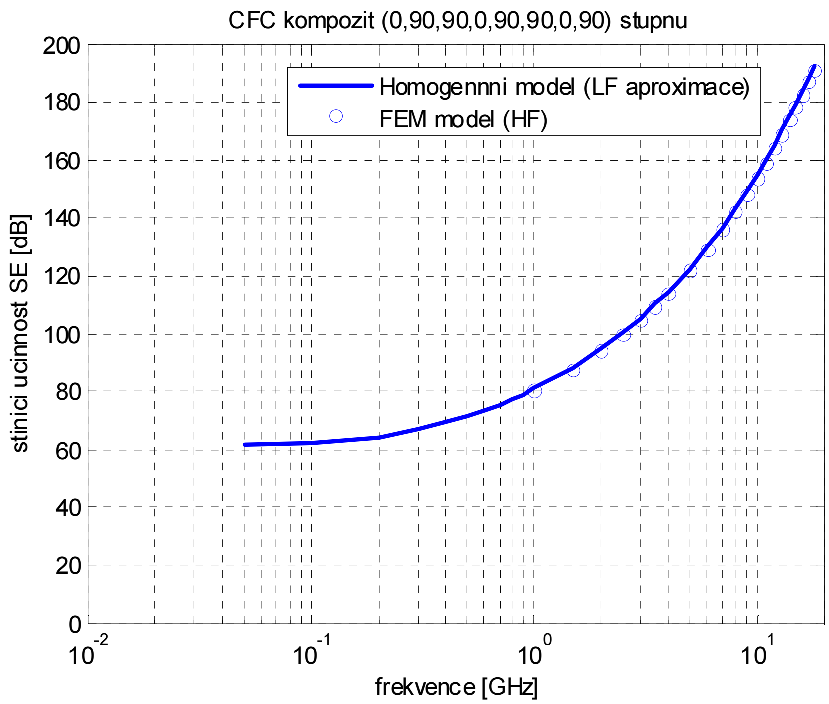

Obr. 7 Srovnání stínící účinnosti vypočtené pomocí program Ansys (FEM model, HF) a homogennního modelu (křivka LF aproximace) pro kompozit s orientací vláken 0,90,90,0,90,90,0,90.

Druhý analyzovaný vzorek kompozitu je schematicky vyobrazen v Obr. 3 vpravo. Tento vzorek se setával z 8 vrstvev (plies). Každá vrstva měla tloušťku 125 mikronů a obsahovala celkem Nz=16 vláken s průměrem d= 6.75 mikrometru. Objemová koncentrace vláken byla zvolena o něco menší než u prvního vzorku a činila p = 46.7 %.

Fyzická podélná vodivost uhlíkových vláken tak byla o něco větší, a to 21413 S/m.

Vytváření solid modelu tohoto 8 vrstvého kompozitu bylo provedeno opět v prostředí Ansys Classic, kde byl pro tento účel napsán skript pro vytvoření odpovídající geometrie. Příklad takového modelu je ve zjednodušené podobě uveden v Obr. 8. Je vidět, že ve vrstvách šikmo orientovaných, se v periodické buňce nachází jedno celé vlákno společně s malými výřezy, dvou vláken které zasahují z buněk okolních.

Konečně v posledním obrázku je uvedeno srovnání vypočtené stínící účinnosti tohoto vzoru (00,90,45,-45,-45,45,90) s nízkofrekvenčním modelem. Podobně jako u prvního vzorku je shoda velmi dobrá. Díky jiné skladbě vrstev je však výsledná stínící účinnost menší a na kmitočtu 18 GHz dosahuje asi 160 dB.

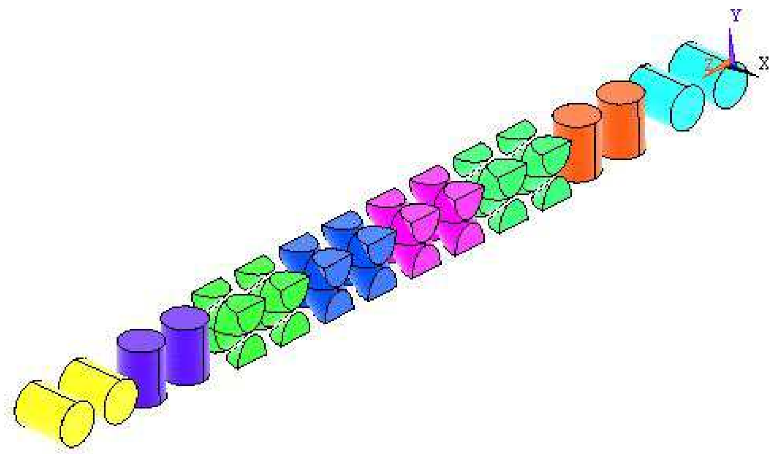

Obr. 8 Detail části geometrického a FEM modelu kompozitu 00,90,45,-45,-45,45,90, v prostředí Ansys Classic zobrazující objemy odpovídající uhlíkovým vláknům. Pro účely zobrazemí byl model zjednodušen, kde místo plného počtu vláken ve vrsvtvě jsou zobrazena pouze 2 vlákna v každé vrstvě s cílem prezentovat objemvy, které odpovídaly jednotlivým vláknům pro dané vrstvy. Síťování model bylo provedeno s hustotou cca. ESIZE,d/6,6, tj. 6 elementů HF119 na průměr vlákna.

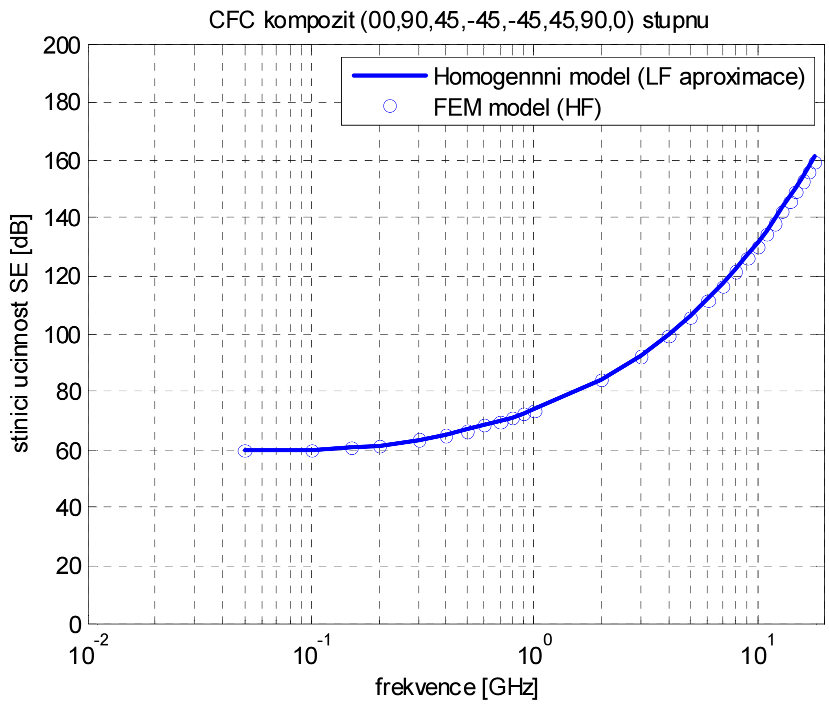

Obr. 9 Srovnání stínící účinnosti vypočtené pomocí program Ansys (FEM model, HF) a homogennního modelu (křivka LF aproximace) pro kompozit s orientací vláken 00,90,45,-45,-45,45,90.

5 Závěr

Tento příspěvek prezentoval vypočtené výsledky stínící účinnosti dvou v praxi se vyskutících kompozitních materiálů s 8 vrstvami a celkovou tloušťkou 1 mm. Výsledky vypočtené pomocí fullwave elektromagnetické analýzy byly srovnány s nízkofrekvenčním modelem (tzv. homogenním ekvivalentem). Díky malému rozměru peridocické buňky ve srovnání s délkou vlny je shoda obou modelů velmi dobrá i nejvyšším pracovním kmitočtu18 GHz.

Celé modelování těchto kompozitů v prostředí Ansys Classic vyžadovalo pečlivou přípravu skriptu pro vytvoření geometrie, a korektní modelování vysokofrekveční vodivosti pro jednotlivé vrstvy kompozititního materiálu. Tato vysokofrekvenční vodivost byla vypočtena podle teroretických vztahů uvedených v tomto příspěvku, které představují transformaci tenzoru vodivosti z lokálního systému spojeného s vlákny do globálního kartzského souřadného systému.

Správnost uvedené transformace byla ověřena srovnáním s výsledky uvedenými v jiném příspěvku, který však byl limitován na tzv. homogenní ekvivalent kompozitu, platný přesně pro nízké kmitočty.

Literatura

CHIN H. K., CHU H. C., CHEN C. H., 1998. Propagation modeling of periodic laminated composite structures. *IEEE Trans. on EMC,* 1998, ročník 40, číslo 3, 218-224. ISSN 0018-9375

HOLLOWAY C. L., SARTO M. S, JOHANSSON M., 2005. Analyzing Carbon-Fiber Composite Materials With Equivalent-Layer Models. *IEEE Trans. on electromagnetic compatibility*, ročník 47, číslo 4, Nov. 2005, pp. 833 – 844. ISSN 0018-9375.

MEHDIPOUR A., TRUEMAN C. W., SEBAK A. R., ROSCA I. D, 2008. Shielding Effectiveness Analysis of Multilayer Carbon-Fiber Composite Materials Ve sborníku *Název sborníku a konference XXIX General Assembly of the International Union of Radio Science (URSI 2008)*, Chicago, 10-15.8.2008. ISSN 0074-9516. ISBN nepřiřazeno.

PICHE A., BENNANI A., PERRAUD R., ABBOUD T., BEREUXV, F., PERES G., SRITHAMMAVANHV V. 2009. Electromagnetic modeling of multilayer carbon

fibers composites. *Sborník konference International Symposium on Electromagnetic Compatibility - EMC Europe*, Athény, Řecko, 11-12.6. 2009. Athény, stránky. ISBN 978-1-4244-4107-5 (Print).

JOHNSON S. G., 2010. Co-ordinate transformateion & Invariance in Electromagnetism. *Notes for course on MIT,* Dostupné z www.math.mit.edu/~stevenj.

Kontaktní adresa:
Ing. Stanislav Goňa
FAI UTB Zlín, Nad Stráněmi 4511, 76005 Zlín
Email: gona@fai.utb.cz

INCREASING THE RESISTANCE TO INTERNAL EXPLOSION OF THE STRUCTURE OF A BROWN COAL TRAY

PETR HORYL, PETR JAHN
VSB - Technical University of Ostrava, Varroc Lighting Systems s.r.o.

Abstract: This article deals with increasing the resistance of the steel structure of a brown coal tray to internal explosion. The steel tray is welded to the supporting structure of the heating plant. The paper focuses on changing the existing design to increase its resistance to internal explosion. Because internal explosion of brown coal dust takes only a few milliseconds, an explicit method was used. The explicit dynamic module from ANSYS Workbench 13 was used for the solution of this difficult nonlinear dynamic problem.

Keywords: Brown Coal Tray, Internal Explosion, Explicit Dynamic Module

1 Introduction

The subject is a concrete solution tray which is welded to the structure of the plant. The length is 11 m, width is 6 m and depth is 9.6 m, with a volume of 400 m^3 of brown coal. The mass of the silo is 43,500 kg. The silo is welded on the top circuit to the supporting construction (see Image 1). The aim of computer modeling was to determine whether an internal explosion of coal dust causes this weld to break, followed by tearing of the container structure and its collapse.

The tank walls have a thickness of 10 mm and are reinforced by rolled profiles of type I, U and sheets. The tray is reinforced by a collar all around the upper and middle part welded from two I180 profiles.

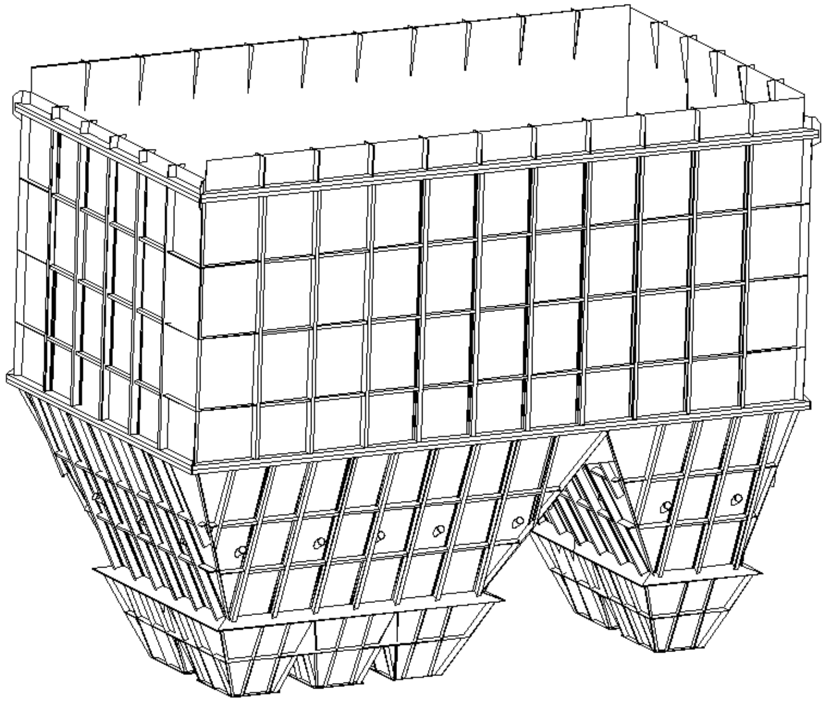

Image 12 – Tray structure

Because internal explosion of brown coal dust takes only a few milliseconds, an explicit method was used. Explicit time integration is more accurate and efficient for simulations involving large deformations, large strains and material nonlinear behavior. The explicit method is conditionally stable. There must be some limit on the maximum size of the time step. Ansys [ANSYS Explicit STR, 2009] recommends the Courant-Friedrichs-Levy condition for the size of the time step. This condition implies that the time step will be limited such that a stress wave cannot travel further than the smallest characteristic element dimension in the mesh, in a single step. The time step criterion for solution stability is

$$\Delta t \leq f\left(\frac{h}{c}\right)_{\min} \tag{1}$$

where Δt is the time increment, f is the stability time step factor (0.9 by default), h is the characteristic dimension of an element and c is the local material sound speed in an element. The element characteristic dimension, h, is calculated as follows in Table 1.

Table 4 Elements characteristic dimensions

Type of element	Characteristic dimension, h,
Quad shell	The square root of the shell area
Tri shell	The minimum distance of any node to its opposing element edge

Beam	The length of the element

2 Loading from Eurocode 1

According to Eurocode 1 – Actions on structure (CSN EN 1991-1-7, 2007), the stack was assessed as a construction, which falls within the class consequence CC3, as when the coal-dust explodes, there can be subsequent failures. This refers to the risk to persons from the falling tank or damage to other equipment and great material damage. A crucial parameter for evaluating explosion pressure is an index K_{ST} – the deflagration index dust cloud. This is determined experimentally and gives the behavior of the explosion in a limited space. Larger deflagration index values mean internal explosions with higher pressures and shorter time waveforms. The deflagration index value K_{St} for brown coal is 18,000 kN/m^2.m/s. For this index value we obtained from the Eurocode standard a maximum load pressure pmax = 0.8 MPa. The highest values of dust explosion pressure are achieved within a time span of 20 ms to 50 ms.

3 Computer model

A stack model for dynamic simulation of the internal explosion was created using the drawings in the Ansys Workbench 13.0 (see Image 2).

The body model consists of areas that are reinforced by straight lines defined by the properties of objects by type and size of reinforcements. The computer model is designed from 630 parts.

For the modeling of a coal-dust explosion in a coal storage, procedures were used according to Eurocode 1 – Actions on structure (CSN EN 1991-1-7, 2007). The aim is to verify the design using nonlinear dynamic analysis in the "Explicit Dynamics" ANSYS Workbench 13.0. The worst case load condition occurs when pouring coal into the tray. The assumption is that when pouring is complete, with eight full hoppers of brown coal, the coal dust concentration will be enough to cause a blast. In this case the pressure wave reaches the largest possible area and causes the greatest damage. The pressure load acts on the inner surface reservoir. The course load is plotted in Image 3.

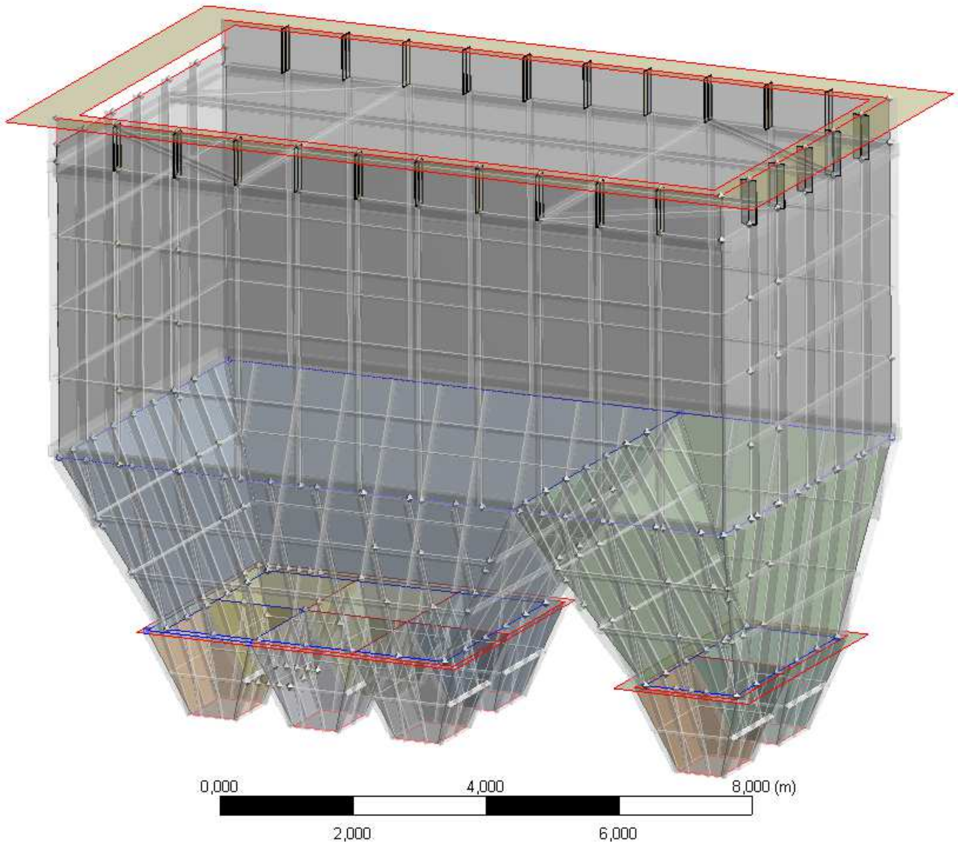

Image 2 – Computer model created in Ansys Design Modeler

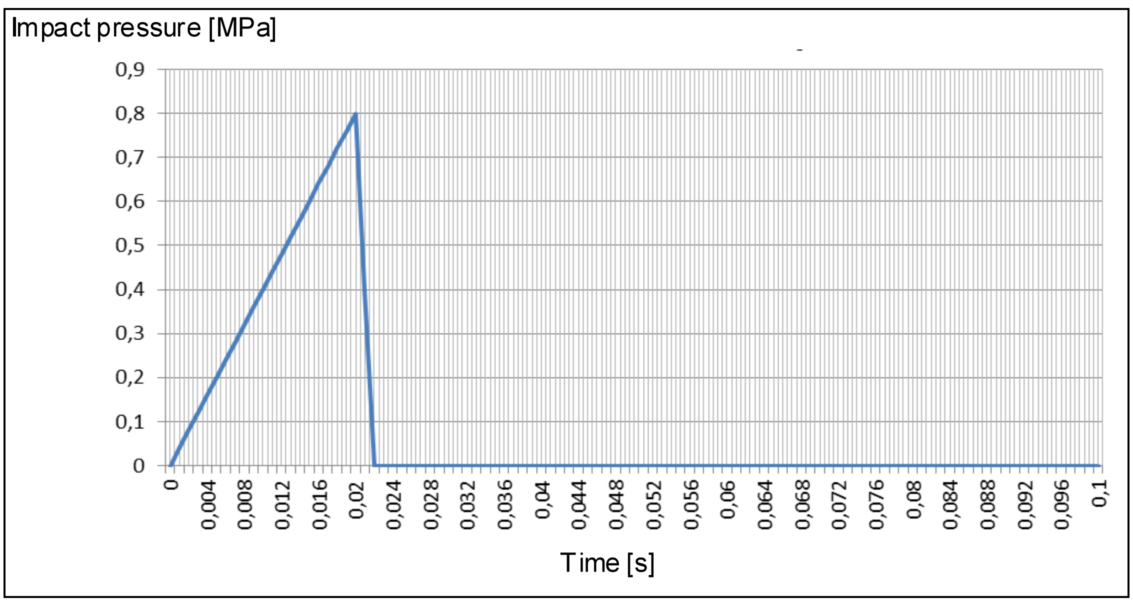

Image 3 – The course of the pressure load

6.4 Mesh

The mesh consists of the shell and the beam elements. Shell elements were used for creating the sheath. Profiles that stiffen the sheath container, beam elements are formed elements. The mesh is made up of 21,627 elements, containing 28,376 nodes. The maximum size of the shell elements is 160 mm. The generated mesh is shown in Image 4. The mesh quality was verified by a quality metric system. The quality of the mesh elements is plotted in Image 5. The x-axis describes the quality elements and the y-axis plots the percentage of these elements. The quality of the elements is in the range from 0 to 1 and is determined by the ratio of volume to the edge length of the element. A value of 1 reflects a perfect cube or square, while a value of 0 means that the element has zero volume [Ansys Explicit, 2009]. In our case, the quality elements in all parts of the tank are very good and we can expect good results.

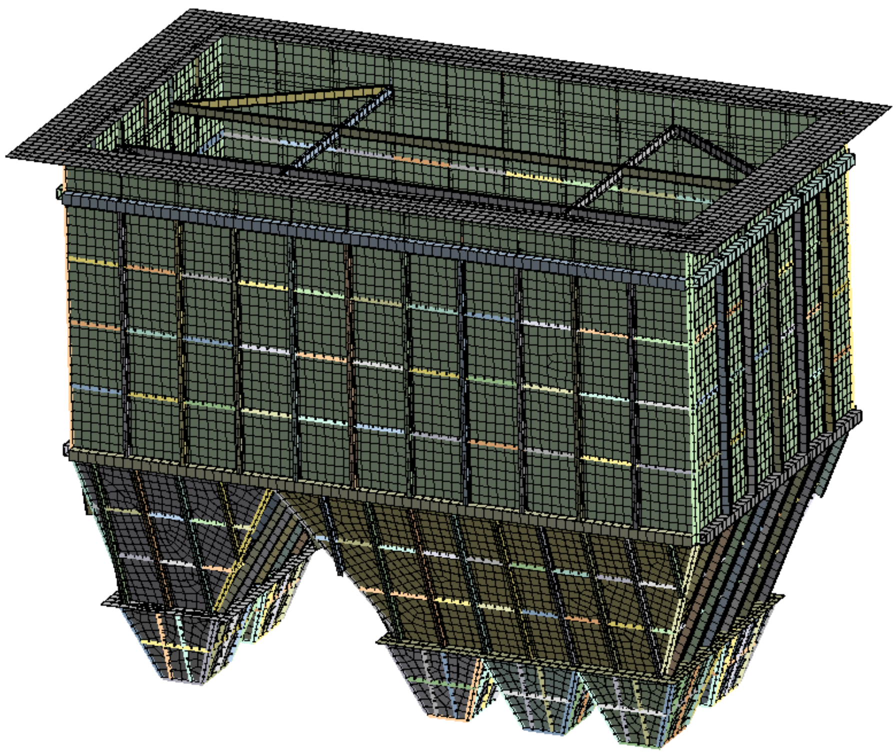

Image 4 – Silo mesh

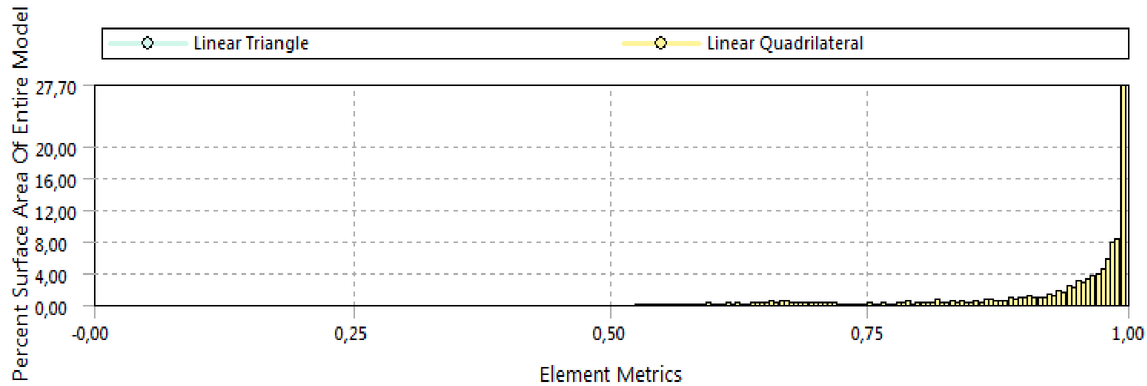

Image 5 – Mesh quality

6.5 Boundary conditions, contact

The computer model was applied to the following boundary conditions. The tray is welded to the perimeter of the structure. Therefore, the model is loaded into a special part. This simply replaced the bearing structure of the building. The welded joint has been replaced by a "bonded - breakable" type contact [ANSYS, 2010]. So there is hard contact with the possibility of a breach. Breach of contact is limited to a maximum value of normal and shear stresses in contact elements. Our case was set to stress the ultimate strength of the material CSN 11523 to 510 MPa for the maximum normal stress, and 335 MPa for the maximum shear stress. Breach of contact occurs when these values are exceeded and this will result in the tearing of the tray from the structure. Another boundary condition is the pressure load from the blast. This load, with a maximum pressure of 0.8 MPa and the process shown in Figure 3, was applied to all the internal walls in addition to the hoppers. The boundary condition is evident from Image 7. The influence of the tray's own weight has been taken into account. This influence is not negligible, because the entire stack mass is 43,500 kg.

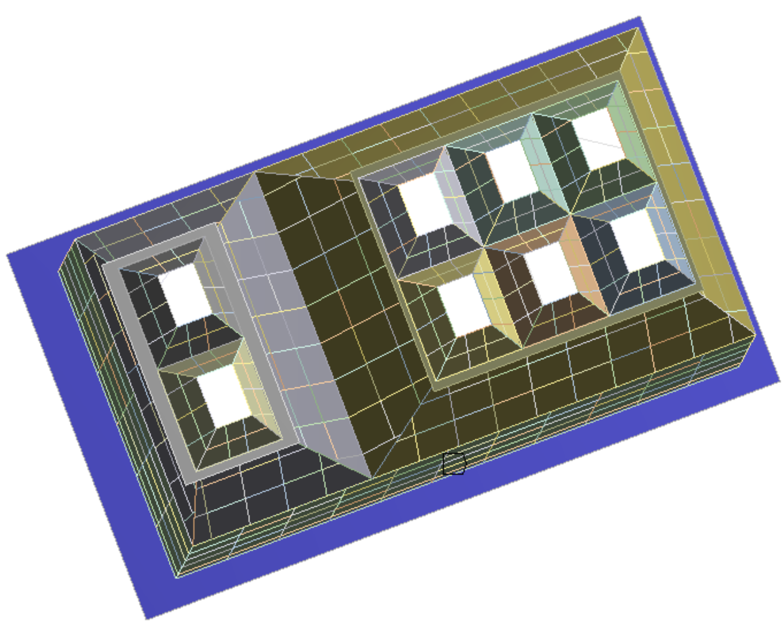

Image 6 –Fixed connection on upper part of silo jacket

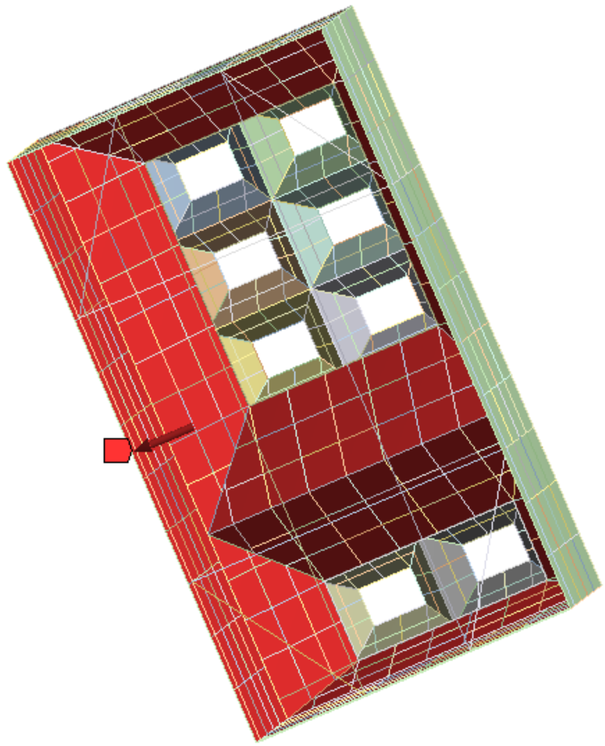

Image 7 – Pressure loading on internal walls, red areas

6.6 Material properties

All parts of the tray are made of material CSN 11 523, which is normally steel with higher carbon content. The material properties are in Table 2.

Table 2 Material properties

Material CSN	Yield stress [MPa]	Ultimate stress [MPa]	Young's modulus [GPa]	Poisson's ratio [1]
11523	355	510	200	0.3

To calculate this dynamic task we used the Johnson Cook material model [Özel, 2007]. This is a material model which describes the stress as a result of deformation, strain rate and thermal effects. The following equation expresses the stress flow.

$$\bar{\sigma} = [A + B(\bar{\varepsilon})^n]\left[1 + C\ln\left(\frac{\bar{\dot{\varepsilon}}}{\bar{\dot{\varepsilon}}_0}\right)\right]\left[1 - \left(\frac{T - T_0}{T_m - T_0}\right)^m\right] \quad (2)$$

where parameter A is initial yield stress, B hardening constant. The equivalent plastic strain speed $\bar{\dot{\varepsilon}}$ is normalized to a reference strain speed, $\bar{\dot{\varepsilon}}_0$,T_0 is room temperature, T_m is melting temperature, and the temperature values are constants. While the parameter n is the hardening exponent, parameter m is the thermal softening exponent and C is the reference strain rate. The Johnson

Cook model [Özel, 2007] is a numerically robust constitutive material model, which is often used in computer simulations. Table 3 shows the constants needed for the Johnson Cook model.

Table 3 Description of Johnson Cook material model [Varmint, 2012]

Initial yield stress **A**	250 [MPa]
Hardening constant **B**	712 [MPa]
Reference strain rate **C**	0.01 [1]
Hardening exponent, parameter **n**	0.196 [1]
Thermal softening exponent **m**	1.1164 [1]
Melting temperature **Tm**	1500 deg

4 Results

First, a calculation was performed on the resistance of the original tray design against an internal explosion of coal dust. It was found that the tearing supporting weld is already carrying a pressure value p1 = 0.6 MPa at the time of 0.015 s, i.e. before reaching the maximum pressure value. At the moment of tear, we observed extreme values of permanent plastic deformation, as shown in Image 8. The original design is not able to withstand the full explosion, so we proceeded to make design changes.

The first change (Image 9, red lines) strengthens the walls under the weld with two new rings created from profile 2 x U180. The tray was also reinforced inside, doubling the existing internal reinforcement. In this case, there was an increase in the marginal value of the pressure to p2 = 0.7 MPa.

The second change (Image 10, red lines) consisted in changing the internal stiffeners formed from profiles of type I160. For this structure, the longitudinal and transverse reinforcements were taken away and moved into the center of the tray with a spacing of 1 m. The pressure load which led to a structural collapse was now down to p3 = 0.58 MPa.

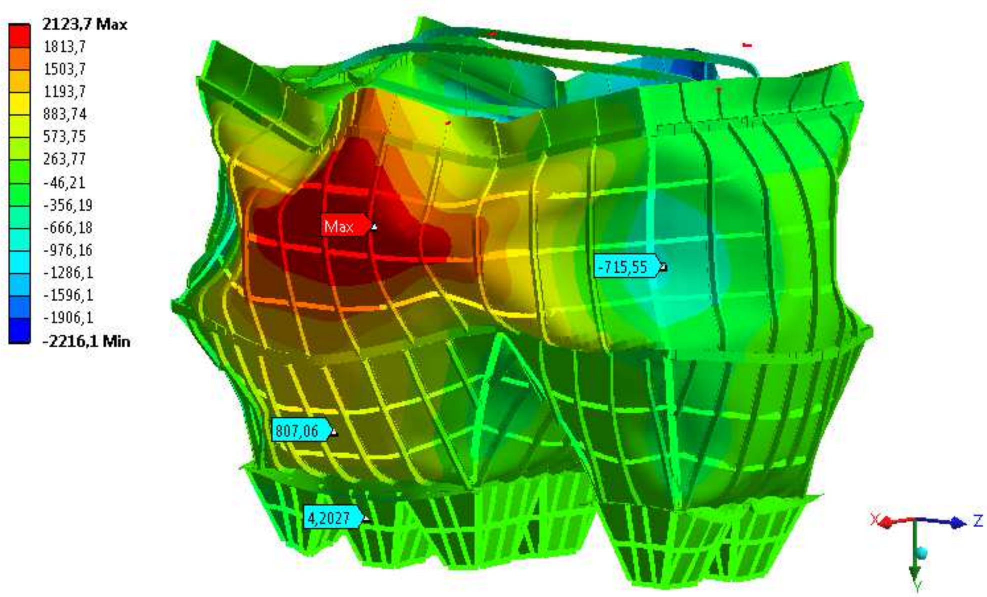

Image 8 – Permanent plastic deformation of silo jacket [mm]

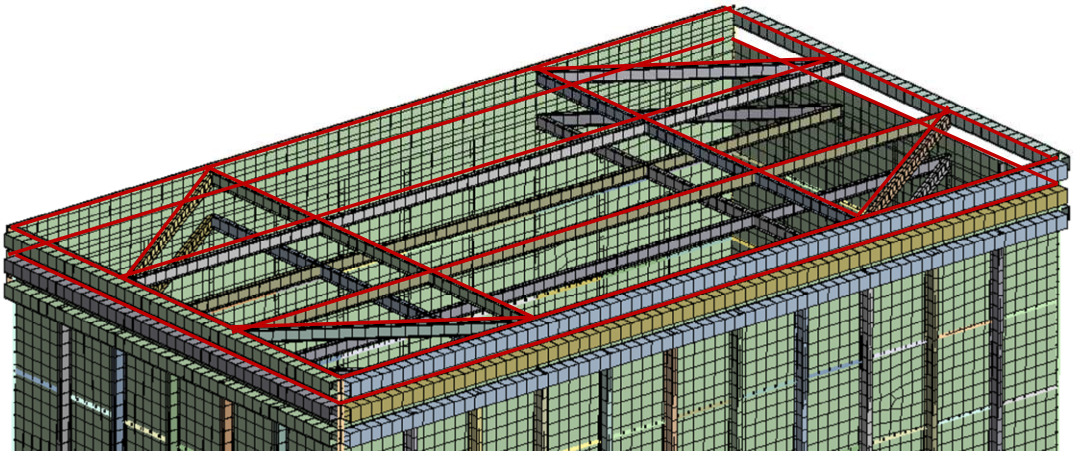

Image 9 – The first design modification, red lines

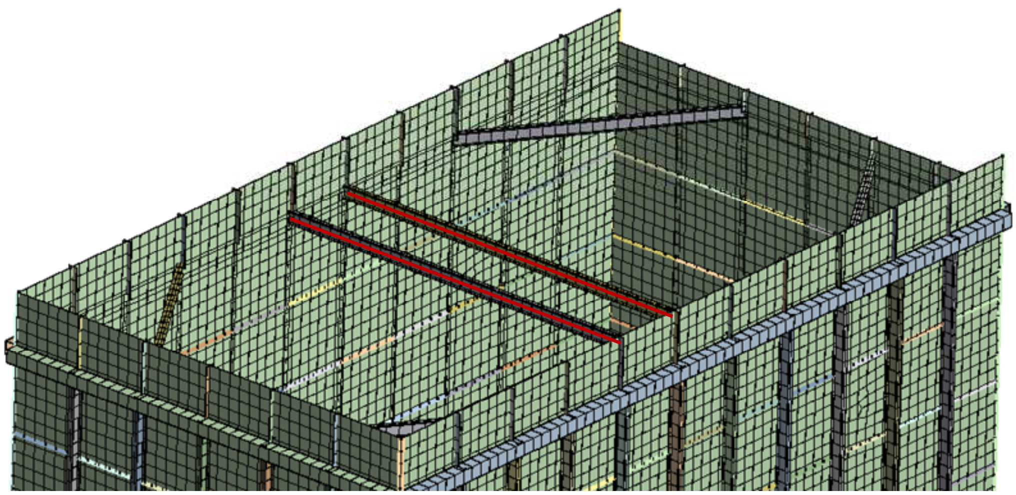

Image 10 – The second design modification, red lines

The third treatment consisted of a structural change in the wall thickness by increasing it from 10 mm to 14 mm. The value of the pressure load which led to a structural collapse fell to p4 = 0.62 MPa. Calculations showed that the coal tray was not able to withstand the full value of the pressure from the blast without a full collapse. Standard Eurocode 1 in this case requires the building of a safety exhaust system with a defined cross-section and defined activation pressure. An exhaust system was designed with an area of 10.5 m^2, with an activation pressure of 40 kN/m^2. Based on these facts, the calculation was carried out for a control tank pressure of 50 kN/m^2 load, i.e. 0.05 MPa. The level of safety of the so-called partial load factor $\gamma F = 50/40 = 1.25$. The results of the last calculation showed that maximum displacement during the dynamic action does not exceed the elastic limit. The maximum displacement is only 38 mm and after dynamic action this completely disappeared (see Image 11). In the supporting weld the yield stress was not exceeded at any point.

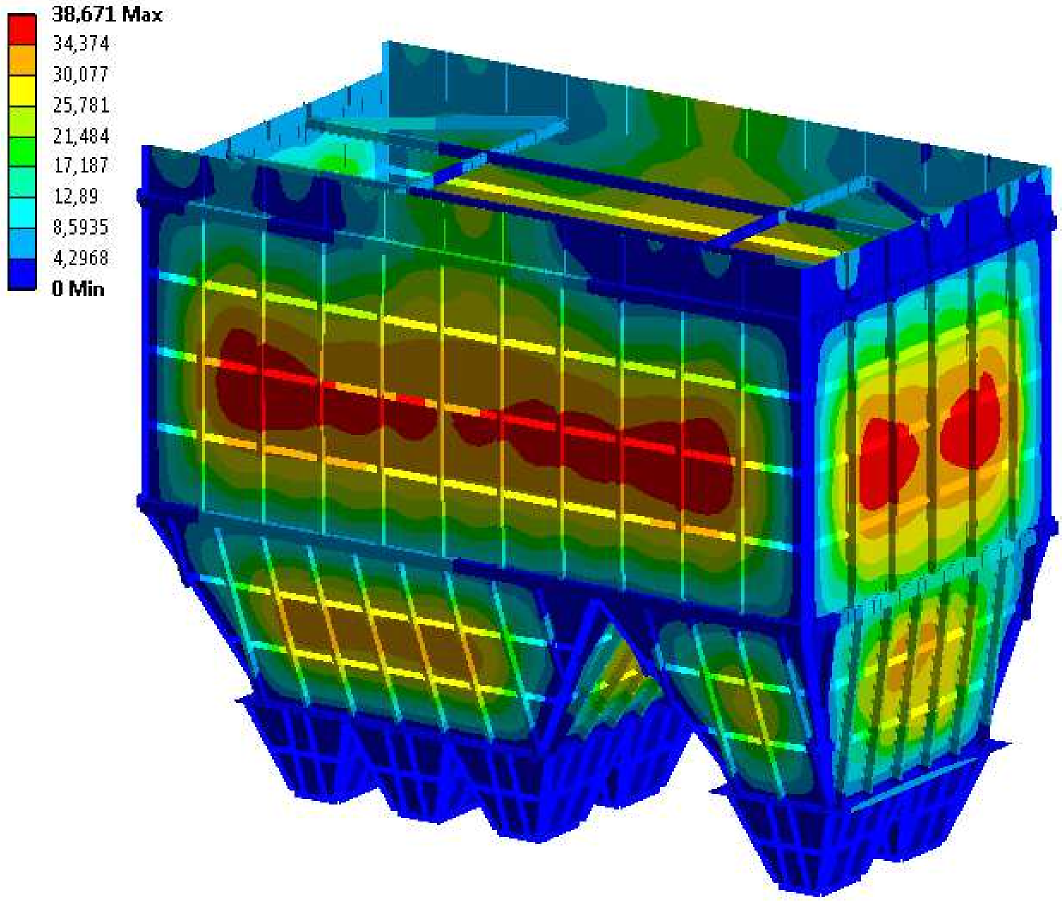

Image 11 – Maximum elastic deflection in [mm]

5 Conclusion

Calculations have shown that the structure of a brown coal tray, even after design modifications, is not able to transfer the full value of the pressure from the explosion of coal dust. A new exhaust system with a construction area of about 10.5 m^2 and the activation pressure of 40 kN/m^2 must be added. Final dynamic calculations showed that, for the maximum value of the internal pressure of the exhaust system, which is expected to be around 50 kN/m^2, the designed tray complies. This is achieved only when the elastic deformation and stress do not exceed the maximum allowed value.

References

ANSYS Explicit STR [online]. c2009 [cit. 2009-10-01]. Available from http://www.ansys.com/solutions/servicesandsupport/training/ansysexplicit

ANSYS, INC. ANSYS Academic Research, Release 13.0 Help System, Theory reference. 2010

CSN EN 1991-1-7, Eurocode 1: Actions on structure - Part 1-7: General actions - Accidental actions, 2007, 64 p.

ÖZEL T, KARPAT Y., 2007 Identification of constitutive material model parameters for high-strain rate metal cutting conditions using evolutionary computational algorithms. *Materials and Manufacturing Processes* [online], vol. 22, no. 5-6 [cit. 2012-01-25]. Available from http://ie.rutgers.edu/resource/research_paper/paper_07-019.pdf. ISSN 1042-6914.

VARMINT A., 1990. Johnson-Cook Plasticity [online], last revision 10. 2. 2012 [cit. 2012-02-05]. Available from http://www.varmintal.com/aengr.htm

Acknowledgement
This paper has been supported by a grant from the Ministry of Education of the Czech Republic No. MSM6198910027.

Contact address:
Prof. Ing. Petr Horyl, CSc.
VSB-TU Ostrava, 17. listopadu 15, 708 33 Ostrava-Poruba

ZKOUŠKY NELINEÁRNÍCH MATERIÁLOVÝCH MODELŮ BETONU V PROSTŘEDÍ SYSTÉMU LS-DYNA

HRADIL P. , SALAJKA V.

Abstrakt: Hlavním účelem provedení zkoušek na železobetonových prvcích bylo kalibrování nelineárních materiálových modelů betonu při velmi rychlém nárůstu zatížení. Tento případ namáhání (konstrukcí) se uplatňuje například při nárazu vozidel do pilířů mostních konstrukcí nebo do záchytných systémů, které se na vozovky umisťují z důvodu zvýšení bezpečnosti a pomáhají chránit účastníky silničního provozu. Záchytné systémy jsou instalovány na krajnici nebo ve středním dělícím pásu. Úkolem záchytných systému je zadržet na komunikaci a přesměrovat neovládané vozidlo při zajištění přiměřené bezpečnosti cestujících a dalších uživatelů komunikace. Byl navržen zkušební experiment, který sledoval přírůstek napětí v čase až do porušení betonového prvku. Výpočet slouží k provedení zkoušek na skutečných betonových prvcích, které jsou zatěžovány náhle přiloženým zatížením. Ke kalibrování zkoušky betonových vzorků byl použit program LS-DYNA a materiálový model CSCM, který byl speciálně vytvořen k modelování záchytných systémů.

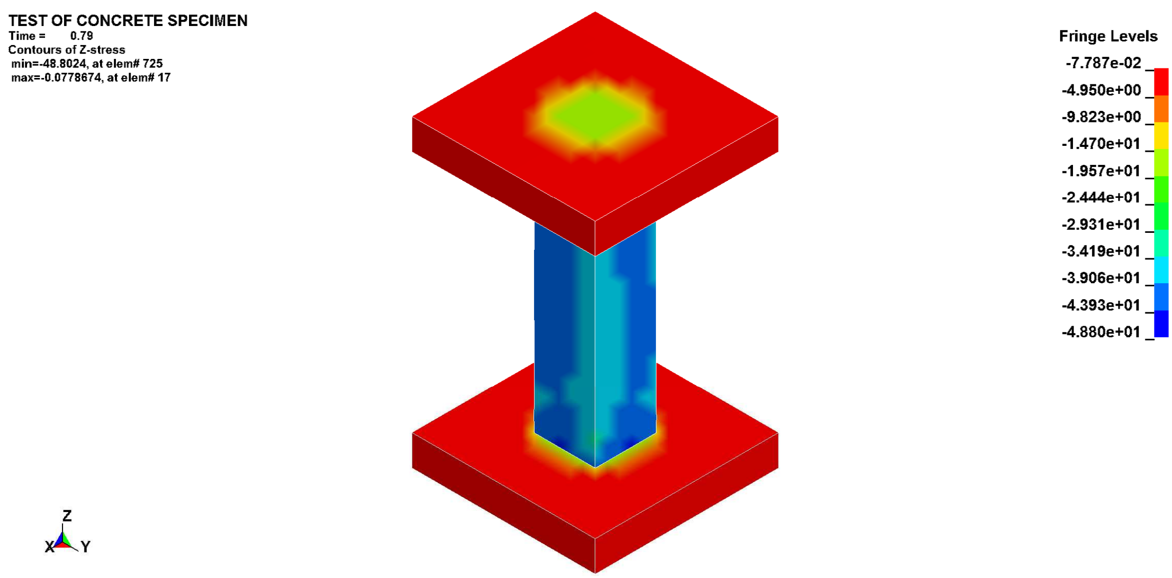

Obr. 1 Normálové napětí v betonovém prvku

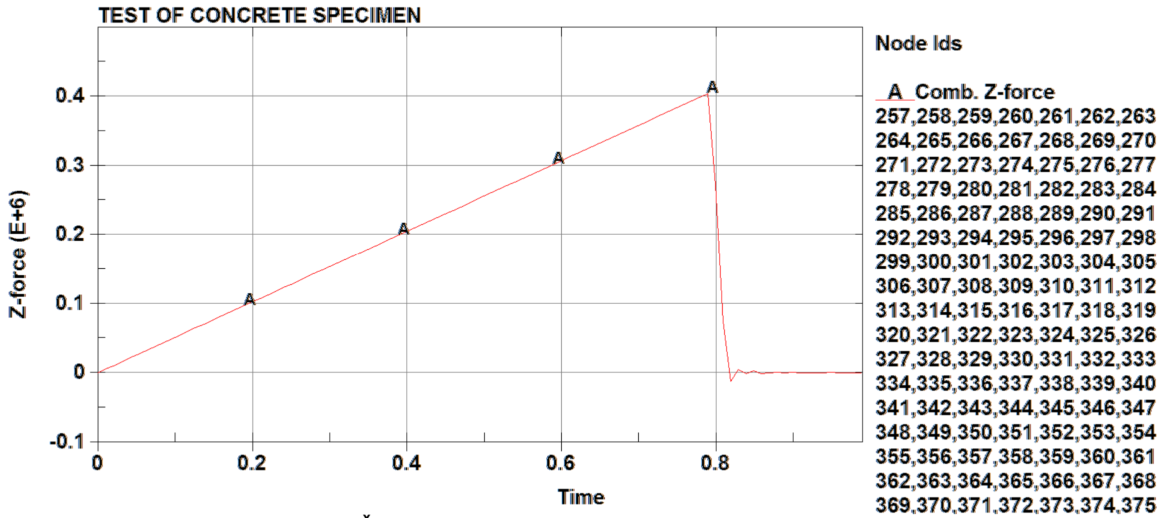

Obr. 2 Časový přírůstek normálové síly v betonovém vzorku

PODĚKOVÁNÍ

Tento výsledek byl získán za finančního přispění projektu GAP104/11/0703 - Použití progresivních materiálů u cyklicky namáhaných konstrukcí

LITERATURA

European Standard EN-1317 Test Vehicle Models, CM/E Group - Politecnico di Milano, Italy

Hradil, P., Salajka, V., Vymlátil, P: Posouzení stability systému mobilní protihlukové stěny, únor 2009

Kontaktní adresa

Ing. Petr Hradil, Ph.D., Vysoké učení technické v Brně, Fakulta stavební, Ústav stavební mechaniky, Veveří 95, 602 00 Brno, +420541147366., hradil.p@fce.vutbr.cz.
doc. Ing. Vlastislav Salajka, CS.c., Vysoké učení technické v Brně, Fakulta stavební, Ústav stavební mechaniky, Veveří 95, 602 00 Brno, +420541147365., salajka.v@fce.vutbr.cz

ANALÝZA OCEĽOVÝCH NÁDRŽÍ

NORBERT JENDŽELOVSKÝ, ĽUBOMÍR BALÁŽ

Katedra stavebnej mechaniky,Stavebná fakulta, STU v Bratislave

Abstract: This article presents the comparison of a numerical calculation and experimental measurement relating a cylindrical water tank.

Keywords: numerical analysis, cylindrical tank, FEM, ANSYS, experiment

1 Úvod

V tomto príspevku sa venujeme porovnaniu výpočtového modelu oceľovej valcovej nádrže vytvoreného pomocou MKP a výsledkom experimentálneho výskumu, ktorý sme urobili na našom pracovisku.

2 Numerický model

Valcová škrupina (oceľová nádrž na vodu) bola modelovaná pomocou MKP v systéme ANSYS. Vzhľadom k vzorke konštrukcie ktorú sme experimentálne merali bol vytvorený model, ktorý nezohľadňuje prelisy na plášti valca.

Parametre modelu podľa experimentálnej vzorky (oceľový sud):

Výška:	870 mm
Priemer:	560 mm
Hrúbka steny a dna:	1,1 mm
Materiál:	oceľ (E= 210GPa)
Náplň:	voda (γ=10 kN/m^3)

Predstavená vzorka bola skúšaná v troch krokoch:

1. Prázdny sud
2. Sud naplnený do polovice svojej výšky
3. Plný sud

V programe ANSYS sme vytvorili konečnoprvkový model valcovej nádrže (plechového suda) podľa preddefinovaných parametrov reálnej vzorky, ktorú sme mali možnosť skúšať. Priestorový model sme vytvorili ako 3D teleso rovnakých rozmerov ako je skutočný plechový barel. Na modelovanie steny a dna valcovej škrupiny sme použili škrupinový prvok SHELL43. Objem kvapalinovej oblasti je vytvorený osemuzlovým konečným prvkom FLUID30.

SHELL43 je štvoruzlový, trojrozmerný prvok, ktorý umožňuje v každom uzle definovať posuny a pootočenia UX, UY, UZ, ROTX, ROTY, ROTZ. Prvok je určený na namáhanie plastické s dotvarovaním a na veľké deformácie. Vďaka svojim dobrým ohybovým a membránovým vlastnostiam je predovšetkým vhodný na modelovanie tenkostenných konštrukcií.

FLUID30 je osemuzlový priestorový prvok v tvare šesťstenu, ktorý slúži na modelovanie tekutiny. Prvok existuje v dvoch variantoch. V základnom variante ide o prvok, ktorý ma v každom uzle len jeden parameter, a to tlak p. Tento prvok sa využíva na modelovanie kvapaliny bez kontaktu s poddajným telesom. V prípade interakcie s poddajným telesom musíme použiť variant prvku majúci v každom uzle štyri stupne voľnosti, a to tlak p a posunutia UX, UY, UZ. V kontaktných uzloch, na rozhraní kvapalina – teleso, musíme zviazať ich stupne voľnosti - posunutia. V uzloch, ktoré nie sú v kontakte s poddajným telesom, sa stupne voľnosti odpovedajúce posunutiam odoberú. Pre zadanie vlastnosti kvapaliny je dostačujúce zadať hustotu kvapaliny ρ a rýchlosť šírenia zvuku v kvapaline c, ktoré sú ovplyvňovane množstvom obsiahnutého vzduchu v kvapaline.

Dno nádrže je po obvode kĺbovo podopreté, plocha dna bola voľná.

2.1 Model č. 1 – Prázdny sud

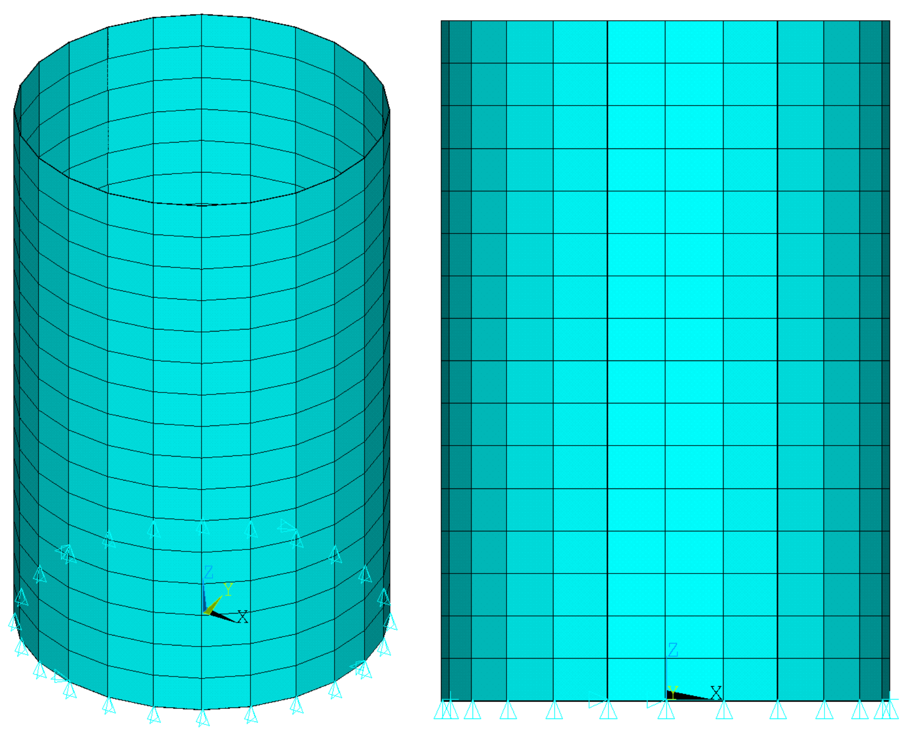

Obrázok 13 – Axonometria a pohľad z boku

2.2 Model č. 2 – Sud naplnený do polovice výšky

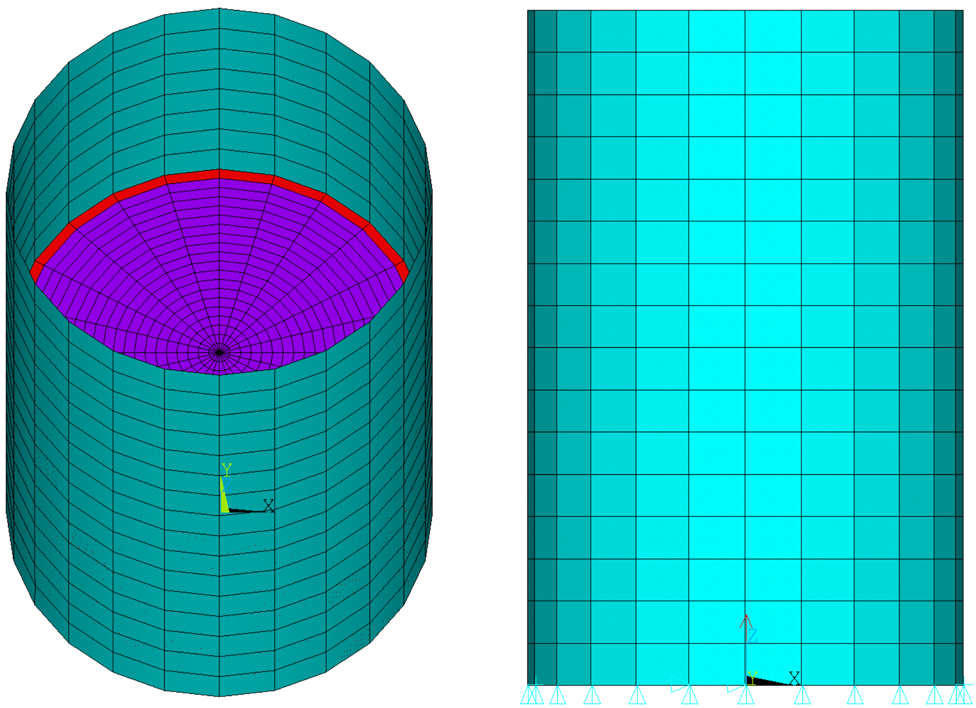

Obrázok 2–Axonometria a pohľad z boku

2.3 Model č. 3 – Plný sud

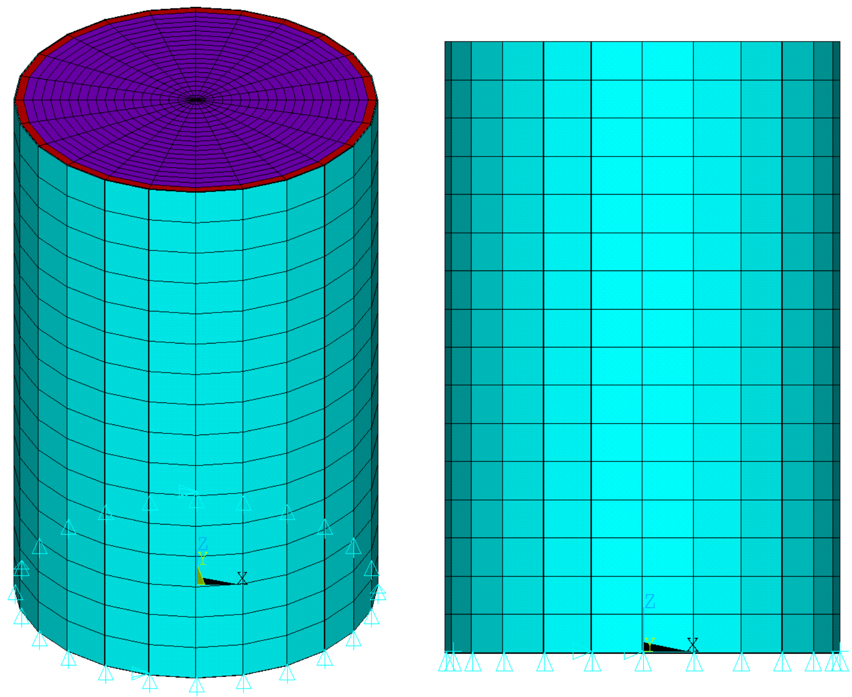

Obrázok 3 – Axonometria a pohľad z boku

3 Experimentálne overenie výsledkov analýzy

Pri meraní sme použili prenosnú meraciu aparatúru (obr. 4 až 7). Táto meracia aparatúra pozostáva z hardvéru a zo softvérového vyhodnocovacieho zariadenia. Na meranie zmien zrýchlení, využitím zotrvačných vlastností konštrukcie, sme použili päť piezoelektrických akcelerometrov od spoločnosti Brüel & Kjaer. Pri meraniach sme použili 16-kanálový A/D prevodník. Všetky akcelerometere mali nastavenú rovnakú vzorkovaciu frekvenciu - 10 000 vzoriek za 1 sekundu, pričom dĺžka meraného časového záznamu bola 5 sekúnd.

Obr. 4–Vzorka pre experiment

Obr. 5–Pripravený model

Obr. 6–Detail akcelerometra

Obr. 7 – zosilovač

Na vyhodnotenie výsledkov sme použili licencovaný program LabVIEW. Tento program funguje na princípe vytvorenia virtuálneho zariadenia pomocou vlastného programu s požadovanými vlastnosťami a nastaveniami, ktorým sme schopní vyhodnotiť údaje z experimentálnych meraní. Merania boli robené na troch modeloch M1 až M3 podľa množstva vody. V každom modeli bolo urobených 7 meraní. Na nasledujúcich obrázkoch (obr 8 a 9) uvádzame záznam zrýchlenia v čase a spektrum zrýchlení. Zdrojom údajov bol biely akcelerometer.

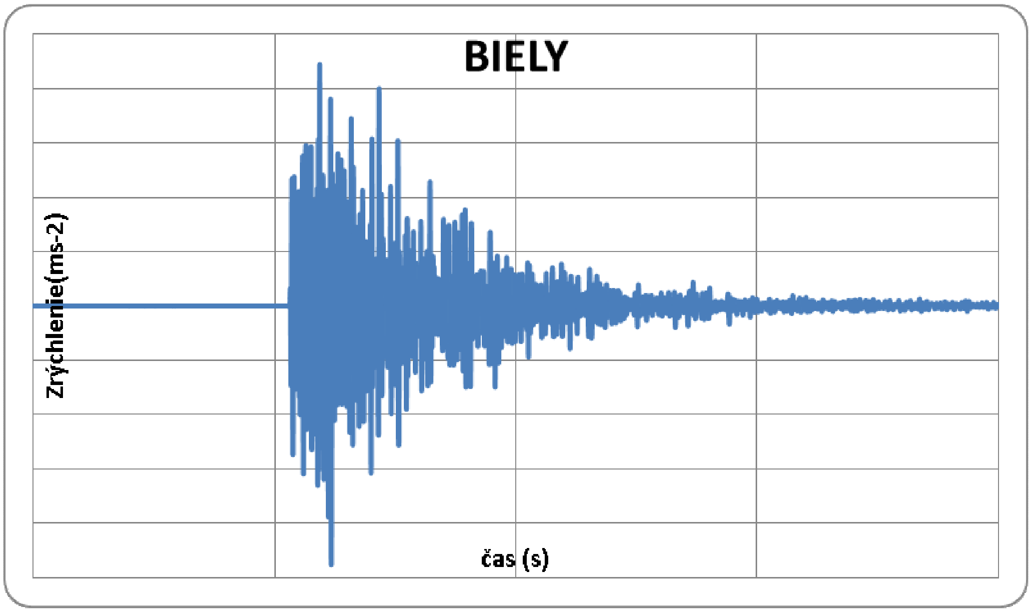

Obrázok 8– Záznam zrýchlenia pre plný sud

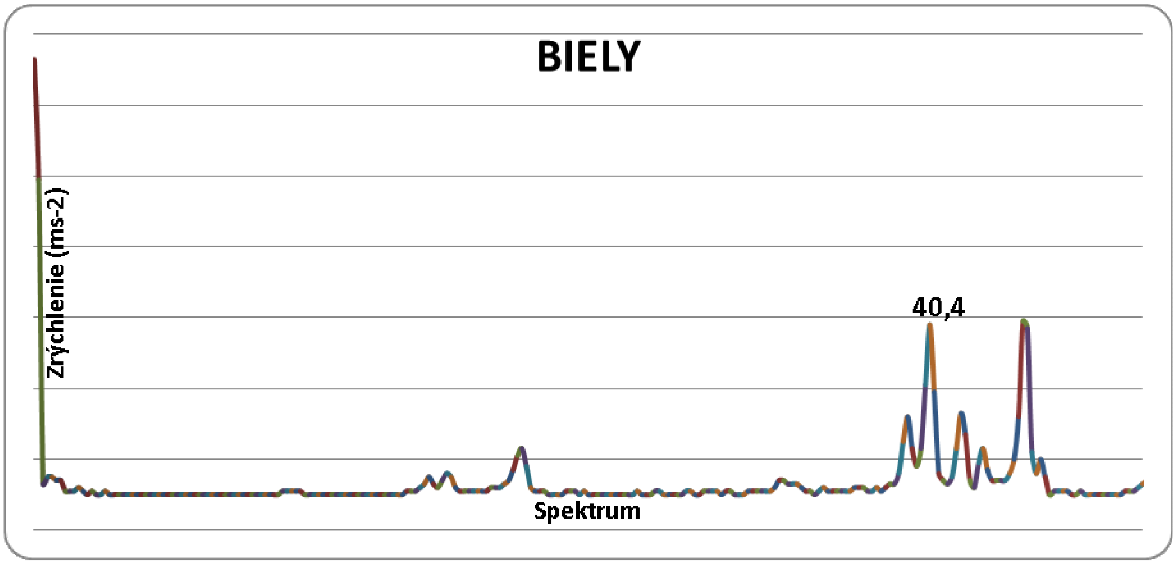

Obrázok 9 – Spektrum

4 Normový výpočet

Pomocou vzťahu (1) z americkej normy je možné získať vlastnú periódu valcových nádrží. Ním sme porovnávali dosiahnuté hodnoty frekvencií z numerického výpočtu a z experimentu.

$$T = C_t.(h_n)^{\frac{3}{4}} \qquad (2)$$

kde: T = perióda kmitania v sekundách

h_n = výška konštrukcie v metroch

C_t = súčiniteľ konštrukcie (C_t = 0,02 - 0,0448)

$$T = C_t.(h_n)^{\frac{3}{4}} \approx 0{,}0448 \cdot (0{,}85)^{\frac{3}{4}} \approx 0{,}0432 \Rightarrow VYHOVUJE \cdot PREDPOKLAD\,U$$

Výpočet vlastnej frekvencie:

$$f = \frac{1}{T} \quad \text{(Hz)} \qquad (2)$$

Podľa vzťahu (2) vieme prepočítať periódu T kmitania na vlastnú frekvenciu.

5 Zhodnotenie výsledkov

V tabuľke úvadzame porovnanie hodnôt prvých vlastných frekvencií resp. periód kmitania skúmaného modelu valcovej škrupiny.

Tabuľka 5Porovnanie výsledkov numerických a experimentálnych modelov

	ANSYS	**EXPERIMENT**	**VÝPOČET**
	frekvencia (Hz)	frekvencia (Hz)	frekvencia (Hz)
M1	20,99	21,80	23,14

M2	35,64	30,80	32,89
M3	41,48	40,40	56,49

Literatúra

SOKOL M., TVRDÁ K., 2011. *Dynamika stavebných konštrukcií.* Bratislava: Vydavateľstvo STU, 212 strán. ISBN 978-80-227-3587-2

ŠMERDA Z., 1974. *Výpočty železobetónových nádrží a zásobníku*. Praha: SNTL

VYSKOČ E., MISTRÍKOVÁ Z., 2001 *POROVNANIE VÝPOČTOVÝCH METÓD ŽELEZOBETÓNOVEJ KRUHOVÉJ NÁDRŽE*. Konferencia s medzinárodnou účasťou - Vysoké Tatry

Uniform building code – 1630.2.2 Structure period, 1997

Poďakovanie

Tento príspevok vznikol za finančnej podpory grantovej agentúry MŠ SR, ako projekt VEGA01/0629/12.

Kontaktná adresa:
Prof. Ing. Norbert Jendželovský,PhD., Katedra stavebnej mechaniky, Stavebná fakulta Slovenská technická univerzita v Bratislave, Radlinského 11, 813 68 Bratislava.
e-mail:norbert.jendzelovsky@stuba.sk

Ing. Ľubomír Baláž, Katedra stavebnej mechaniky, Stavebná fakulta
Slovenská technická univerzita v Bratislave, Radlinského 11, 813 68 Bratislava.
e-mail:lubomir.balaz@stuba.sk

MODELOVANIE VODOJEMOU POMOCOU MKP

NORBERT JENDŽELOVSKÝ
Katedra stavebnej mechaniky, Stavebná fakulta, STU v Bratislave

Abstract: This paper presents practical experience in the modeling of water tanks, in particular reinforced concrete water reservoirs and water towers. FLUID type elements are used for analisys interaction of water with the structure.

Keywords: numerical analysis, cylindrical tank, FEM, ANSYS

6 Úvod

V tomto príspevku sa venujeme modelovaniu železobetónových konštrukcií na uskladnenie vody. Jedná sa o vodojemy, ktoré su umiestnené tesne na zemi, ide o valcové rotačne symetrické škrupiny. Tiež o vežové vodojemy, kde samotná nádrž je v určitej výške nad terénom. Riešením statiky a dynamiky takýchto konštrukcií sa zaoberali viacerí autori, spomeňme aspoň (Kotrasová, 2009) a (Salajka – Mrózek,2007).

7 Základné predpoklady

Špecifikom tejto úlohy je interakcia vody s konštrukciou a modelovanie náplne vodojemu pomocou konečných prvkov. Pre dynamické riešenie stavebných konštrukcií MKP máme k dispozícii: maticu hmotnosti M, maticu tuhosti K a maticu tlmenia C. Matica hmotnosti sa skladá z hmotnosti konštrukcie a hmotnosti kvapaliny. Matica prídavnej hmotnosti kvapaliny má najvýraznejší vplyv na kmitanie analyzovanej konštrukcie.

Na modelovanie kvapaliny je možné v systéme Ansys zvoliť pre 2D úlohy konečné prvky FLUID29 a FLUID79. Pre priestorové úlohy s ktorými sa zaoberáme v článku sa používaju priestorové prvky FLUID30 a FLUID80. Prístup k riešeniu može byť Lagrangeovsky alebo Eulerovský. Ako uvádzajú autori (Salajka – Mrózek, 2007) pri Lagrangeovskom prístupe sa využíva prvok FLUID80, kde v modálnej analýze je veľké množstvo vlastných tvarov a autori doporučujú pri dynamických úlohách použiť radšej prvok FLUID30. Pri statickom riešení vychádzajú výsledky úplne zhodné bez ohľadu na použitý typ prvku FLUID. Na základe týchto odporúčaní sme sa viac venovali prvku typu FLUID30. Tento vychádza z Eulerovského pricípu a z diferenciálnej akustickej rovnice (1).

$$\frac{1}{c^2}\frac{\partial^2 p}{\partial t^2} = \nabla^2 p \,. \tag{3}$$

Kde c je rýchlosť šírenia zvuku vo vode a p je tlak.

Pri diskretizácii rovnice pre danú kvapalinovú oblasť a po zavedení väzby medzi kvapalinou a konštrukciou dostávame rovnicu, kde je nesymetrická matica hmotnosti. Pri riešení vlastných čísel, preto nie je možné použiť metódu iterácie podpriestoru, alebo Lancsosovu metódu, je potrebné zvoliť parameter „ unsymetric“.

Pri výstavbe modelu železobetónovej konštrukcie používame rôzne prvky z knižnice Ansys. Pre modelovanie škrupinových stien vodojemu ide najčastejšie o prvok SHELL43 a SHELL63. Prvok SHELL43 je štvoruholníkový. Má šesť stupňov voľnosti v každom uzle: posuny v smere x,y,z a rotácie okolo osi x,y,z. (obr.1) Využíva sa na modelovanie stien v kontakte s kvapalinou. Prvok SHELL63 je taktiež štvoruholníkový a využíva sa na modelovanie dosiek, ktoré sú v z jednej strany v kontakte s kvapalinou a z druhej sú uložené na základovej pôde. V realných vlastnostiach prvku je možné zadať elastickú tuhosť podložia (EFS). Má zhodnú geometriu a stupne voľnosti ako SHELL43.

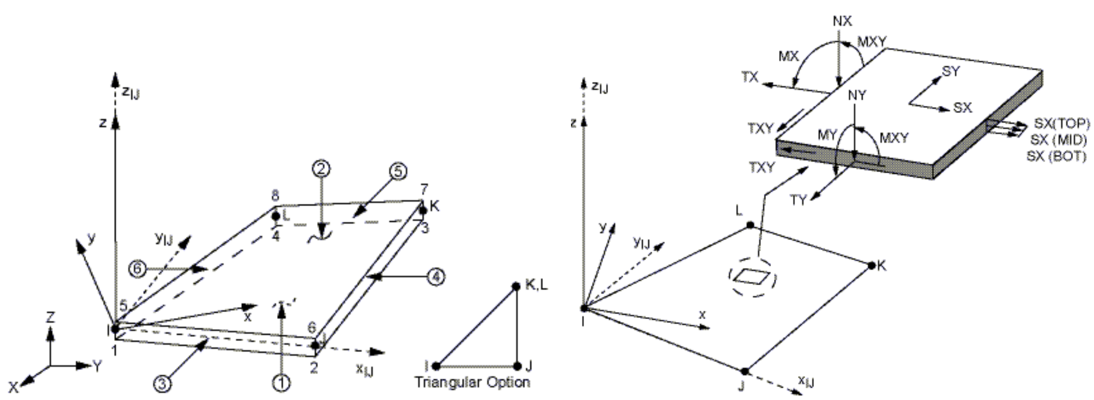

Obr. 14 – Element SHELL43

FLUID30 je trojrozmerný prvok pozostávajúci z 8 uzlov, pričom každý z nich má 4 stupne voľnosti: premiestnenie v smere x, y, z a tlak p (obr. 2). Premiestnenia sa však dajú aplikovať iba na prvky, ktoré sú na kontakte s poddajným telesom, kde treba tieto posuny prepojiť s premiestneniami telesa. Pre priradenie vlastností vody stačí zadať hustotu vody ρ a rýchlosť šírenia zvuku vo vode c. V princípe existuje prvok v dvoch variantoch - prvý je taký, že má za uzlový parameter iba tlak kvapaliny. Tento variant sa používa na modelovanie objemu vo vnútri kvapaliny. Na okraji kvapaliny v mieste interakcie s okolitou konštrukciou sa využíva druhý variant, keď uzlové parametre sú: tlak kvapaliny a 3 posuny ux, uy, uz.

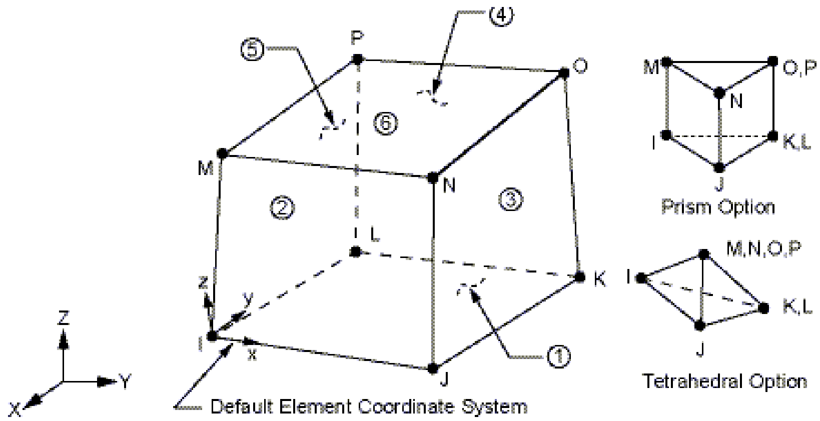

Obr. 2 – Element FLUID30

8 Statické riešenie nádrží

Prvým krokom v statickej analýze bol výpočet vnútorných síl nádrže s votknutým dnom. Tento výpočet sme realizovali tromi spôsobmi: analyticky, pomocou modelu v programe ANSYS využitím hydrostatického trojuholníka a nakoniec v programe ANSYS využitím prvkov FLUID30.

Pri analytickom spôsobe riešenia valcovej škrupiny sme vychádzali zo známej základnej diferenciálnej rovnice 4. rádu s konštantnými koeficientmi a pravou stranou:

$$\frac{d^4w}{dx^4} + 4\lambda w = \frac{r^2}{E_b t}\gamma(h-x)\,. \qquad (2)$$

Riešením diferenciálnej rovnice, dostávame funkcie pre výpočet priehybu w:

$$w = \frac{r^2}{E_b t}\gamma(h-x) - \frac{r^2}{E_b t}\gamma h(\xi_1 - \frac{1}{\lambda h}\xi_2) \qquad (3)$$

normálových síl:

$$N = r\gamma(h-x) - r\gamma h(\xi_1 - \frac{1}{\lambda h}\xi_2) \qquad (4)$$

priečnych síl:

$$V = \frac{\gamma h}{2\lambda(2\xi_4 - \frac{1}{\lambda h}\xi_1)} \qquad (5)$$

a pre výpočet ohybových momentov:
$$M = \frac{\gamma h}{(2\lambda^2)(\xi_3 - \frac{1}{\lambda h}\xi_4)} \qquad (6)$$

Výsledky týchto troch výpočtových modelov sme porovnali, čím sme si overili správnosť jednotlivých riešení. Porovnanie bolo urobené na kruhovej rotačne symetrickej nádrži zo železobetónu, kde sme uvažovali dokonalé votknutie stien do spodnej dosky. Polomer nádrže bol 16 metrov výška nádrže 8m, hrúbka stien t = 180mm. Modul pružnosti betónu sme uvažovali E_b = 30 GPa a Poissonovo číslo v_b = 0,2.

Na obr. 3 a 4 sú vykreslené grafy jednotlivých veličín po výške steny. Je zrejmé, že došlo k relatívnej zhode výsledkov medzi analytickým riešením (zelená), riešením MKP zaťaženie tlakom (modrá) a riešením MKP s použitím prvkov FLUID (červená).

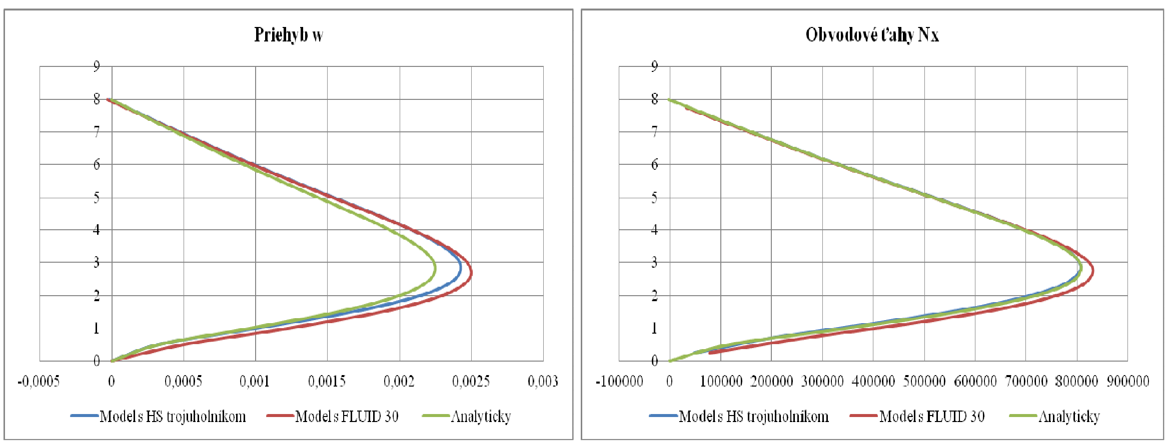

Obr. 3 – Priebeh priehybov a priebeh obvodových ťahov pri porovnaní 3 riešení

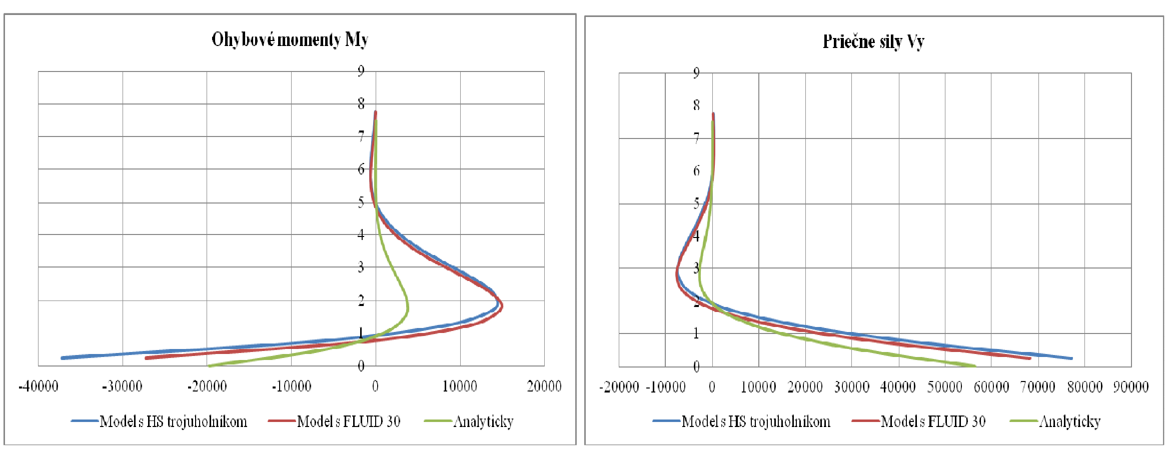

Obr. 4 – Priebeh ohybových momentov a priebeh priečnych síl pri porovnaní 3 riešení

9 Dynamika nádrží

Využitie prvkov FLUID v dynamike vodojemov prezentujeme na dvoch vežových vodojemoch, kde sa účinky hmoty, ktorá je v určitej výške, lepšie prejavia. Modelovanie železobetónovej konštrukcie prvého vodojemu bolo urobené na základe projektu vodojemu. Tento projekt je najlepšie zdokumentovaný v literatúre (Havelka 1956), odkiaľ je aj prebraný rez uvedený na obr. 5. Základy vodojemu tvorí kruhová doska priemeru 30,0m s rebrami. Zo základov vyrastá šesť mohutných železobetónových stĺpov. Tieto sú po výške zviazané skružami – železobetónovými medzikruhovými doskami. Po výške stredom medzi stĺpmi ide valcová konštrukcia, ktorej vnútro slúži na komunikáciu. Sú v nej umiestnené točité schody a technologické potrubie pre dopravu vody. Na stĺpoch je umiestnená kruhová doska so zosilujúcimi rebrami, ktorá drží samotnú nádrž. Nádrž je dvojkomorová. Objem vodojemu je 1200 m^3 a maximálna výška konštrukcie je 65 m nad terénom.

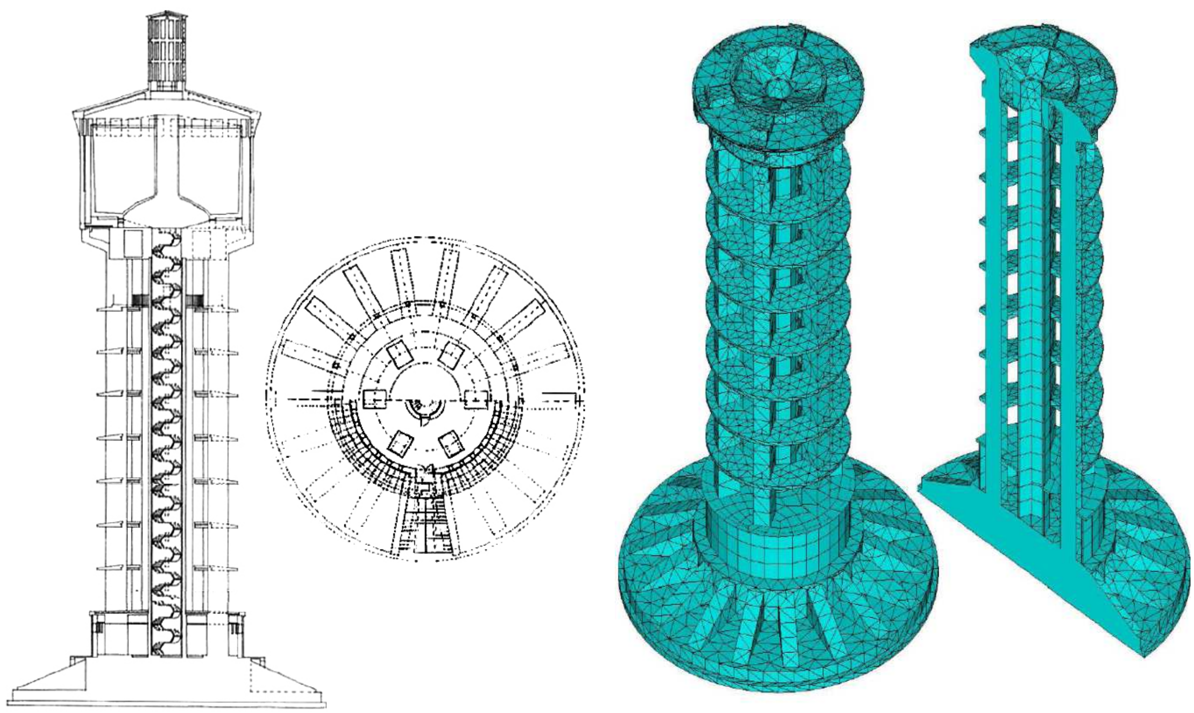

Obr. 5 – Zvislý rez a model podnože vežového vodojemu

Modelovanie spodnej časti železobetónovej konštrukcie bolo bez problémov, pozri obrázok 5. Ako najzložitejšiu časť konštrukcie na modelovanie môžeme označiť dvojkomorovú nádrž. Na jej modelovanie bol použitý prvok SHELL43. Hrúbka plášťa aj dna nádrže je 300 mm, stredná stena medzi nádržami je hrúbky 180 mm. Z geometrického hľadiska bolo náročné modelovanie kónického dna nádrže. (obr. 6)

V ďalšej časti modelovania sa prikročilo k modelovaniu kvapaliny t.j. vyplnili sme ňou objem dvojkomorovej nádrže. Kvapalina bola modelovaná prvkom FLUID30. Bolo použitých 3888 prvkov pre kvapalinu a celkovo sa model skladal z 37450 elementov.

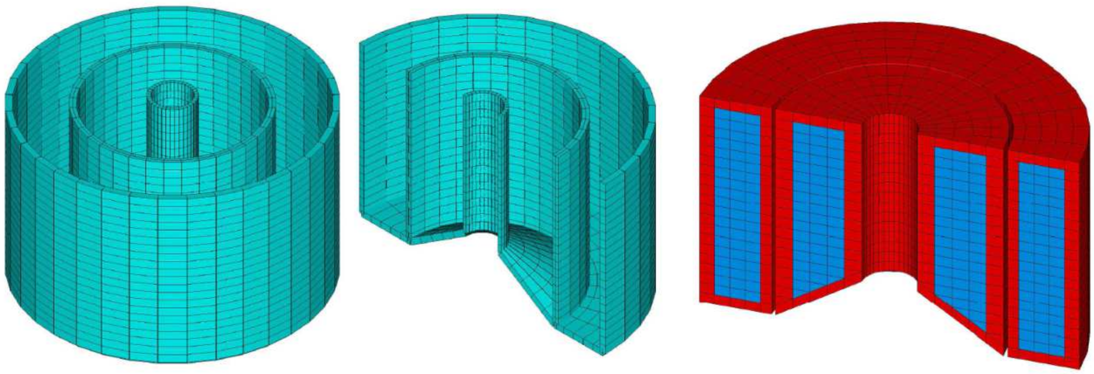

Obr, 6 – Modelovanie nádrže a náplne

Na obrázku 7 je výsledný model konštrukcie na ktorom sme zisťovali vlastné tvary a vlastné frekvencie.Prvý vlastný tvar prázdneho vodojemu bol 0,788 Hz, pri plnom vodojeme je vlastná frekvencia 0,905 Hz.

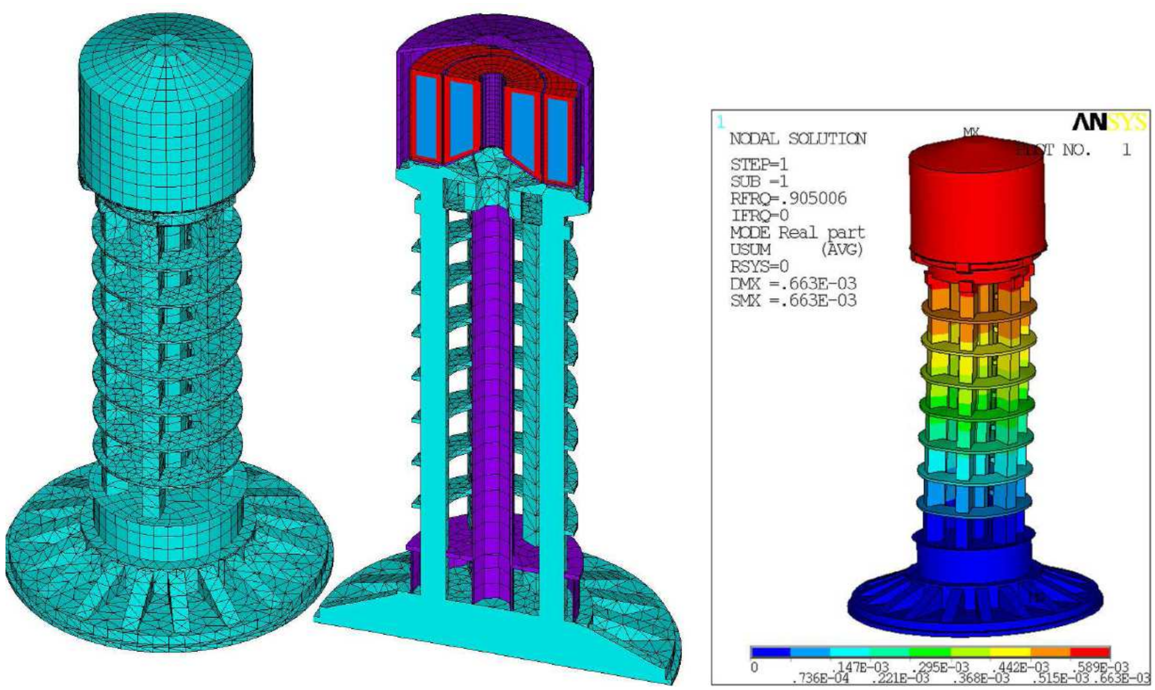

Obr. 7 – Výsledný model vežového vodojemu a prvý vlastný tvar

Druhým vežovým vodojemom bol novší železobetónový vodojem. Na obr. 8 je jeho silueta a geometria nádrže. Výška konštrukcie nad terénom je 58 m. Nádrž vodojemu v tvare obráteného kužela je na 1000 m^3 vody. Základová škára je 5m pod terénom.

Priemer základovej dosky je 20,4m, jej hrúbka je 1500 mm a je vystužená 10 rebrami. Dutý pilier je mierne kónicky, dole s priemerom 4,8 m a hrúbkou steny 600, ktorá sa po výške mení. V strednej časti je priemer 4,08 m hrúbka steny 250mm. Priemer kužela nádrže je 21700 mm, kónická výška je 5 400 mm, nasleduje zvislá časť 900mm. (obr.8) Z betónových panelov je strecha v sklone, ktorá je klbovo ulužená po obvovde a na stredový pilier. Vo vnútri piliera sú schody a vodárenská technológia.

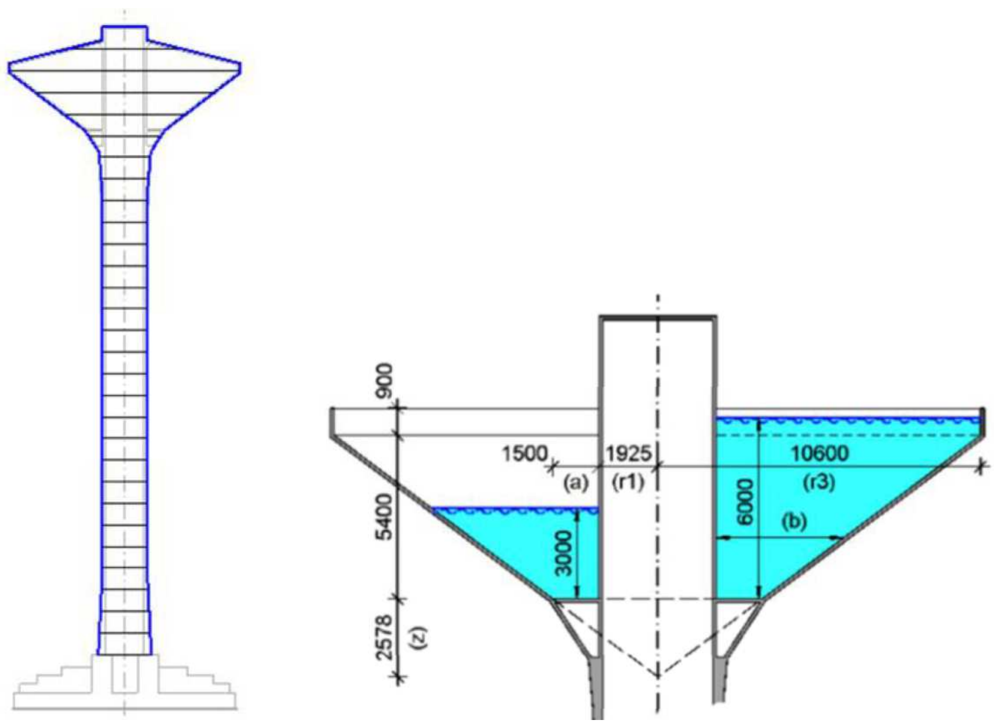

Obr. 8 – Silueta vežového vodojemu a geometria nádrže

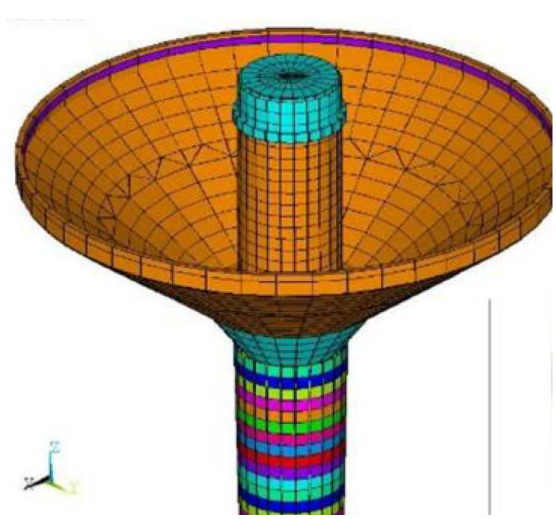

Obr. 9 – Horná časť modelu - nádrž

Modelovali sme vežový vodojem prázdny, s náplňou 250 m^3 a s plnou nádržou vody. Z bezpečnostneho hľadiska (požiarna voda) je minimálne množstvo 250 m^3. Na obrázku 10 uvádzame vlastné tvary konštrukcie pri plnej nádrži. Frekvencie sú nasledovné: f_1 = 0,27 Hz, f_2 = 2,49 Hz, f_3 = 5,96. Pri prázdnom vodojeme vlastné frekvencie nadobúdajú hodnoty: f_1 = 0,38 Hz, f_2 = 2,95 Hz, f_3 = 6,20 Hz.

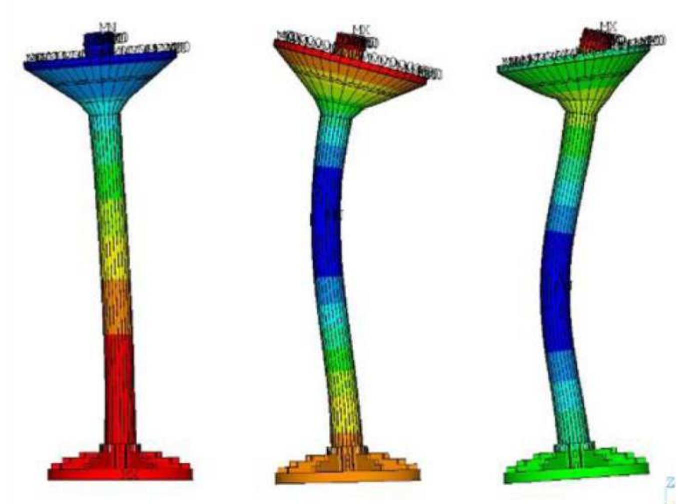

Obr. 10 – Vlastné tvary konštrukcie vodojemu pri plnej nádrži

10 Záver

V súlade so závermi článku [4] **môžeme potvrdiť veľmi dobrú zhodu výsledkov v statickom riešení. K tejto zhode dochádza pri porovnávaní analytického riešenia s klasickým zaťažením hydrostatickým trojuholníkom, prípadne keď použijeme prvky FLUID30 a FLUID80. V dynamickej oblasti pri modelovaní vežových vodojemov bol využitý len prvok FLUID30.**

Literatúra

HAVELKA, K.: Teória lineárnej redukcie plošných konštrukcií. Vydavateľstvo SAV, Bratislava, 1956.

JENDŽELOVSKÝ, N., SUMEC,J.: Stress – Strain Fields of the Reinforced Water Tower under Seismic Loads. In *9th International scientific conference VSU 2009*. Vol,1: Proceedings, Sofia, Bulgaria, 4.-5.6.2009. ISBN 978-954-331-023-4.

KOTRASOVÁ.K.: Influence of category of sub-soil on liquid storage circular tanks during Earthquake. In.: *XII. medzinárodní vědecká konference, Brno*, 2009. ISBN 978-80-7204-629-4, str.41 – 44.

SALAJKA. V., MRÓZEK,M,: Possible Solution to the Dynamic Response of Fluid Filled Tanks in the Ansysy system. In *15. Ansys User s Meeting Lednice* 2007.

RELEASE 11 Dokumentation for ANSYS, SAS IP, INC., 2007

Poďakovanie

Tento príspevok vznikol za finančnej podpory grantovej agentúry MŠ SR, ako projekt VEGA01/0629/12.

Kontaktná adresa:
Prof. Ing. Norbert Jendželovský,PhD., Katedra stavebnej mechaniky, Stavebná fakulta
Slovenská technická univerzita v Bratislave, Radlinského 11, 813 68 Bratislava.
e-mail:norbert.jendzelovsky@stuba.sk

COMPARISON OF ACCURACY OF THE MODELS FOR ANALYSIS OF ELECTROMAGNETIC WAVES PROPAGATION IN MULTILAYER MATERIAL

RADIM KADLEC, PAVEL FIALA, MICHAEL HANZELKA
Brno university of technology, Faculty of electrical engineering and communication, Department of theoretical and experimental electrical engineering, Czech Republic

Abstract: The authors report on an analytical solution of the propagation, reflection and refraction of broadband electromagnetic signals within multilayer optical materials. The presented solution is processed in the Matlab program, which is suitable for a specifically oriented detailed analysis of a general problem. The paper includes a theoretical analysis and references to the generated algorithms. Comparison of the parameter changes is supported by graphical outputs of the algorithms. Algorithms created in the Matlab environment are verified by means of programs based on the finite element method (FEM), namely the ANSYS program. Inhomogeneities and regions with different parameters generally appear even in the cleanest materials. During the electromagnetic wave passage through a material there occurs an amplitude decrease and a wave phase shift; these phenomena are due to the material characteristics such as conductivity, permittivity, or permeability. Any incidence of a wave on an inhomogeneity results in a change in its propagation. The change manifests itself in two forms, namely in the reflection and refraction. In addition to this process, polarization and interference may appear in these waves. The methods described in this paper are well-suited for the analysis of beam refraction to the other side from the perpendicular line during the passage through the boundary. This phenomenon occurs in metamaterials.

Keywords: Numerical modelling, accuracy analysis, electromagnetic waves propagation, metamaterial, reflection, refraction, layer, complex model.

11 Introduction

Generally, inhomogeneities and regions with different parameters appear even in the cleanest materials. During the electromagnetic wave passage through a material there occur an amplitude decrease and a wave phase shift, owing to the material characteristics such as conductivity, permittivity, or permeability. If a wave impinges on an inhomogeneity, a change of its propagation there occurs. This change materializes in two forms, namely in reflection and refraction. In addition to this process, polarization and interference may appear in the waves. It should be notify that in terms of the general theory is the frequency interval from 0 to 100 GHz (the area that deals with electricity and magnetism) and the interval 0.1 to 10 THz PHZ (studied in optics) no principled difference. The idea of a solid as the atomic structure of the opposite assumption connection environment, it is necessary to understand the material properties that describe the response of the environment, such as mean values of a sufficient number of atoms.

In the Matlab program, algorithms were created that simulate reflection and refraction in a lossy environment on the boundary between two dielectrics. The reflection and refraction are in accordance with Snell's law for electromagnetic waves as shown in Fig. 1. a). The form of Snell's law is as follows Stratton J.A. , 1961:

$$\frac{\sin\theta_0}{\sin\boldsymbol{\theta}_2} = \frac{\mathbf{k}_2}{\mathbf{k}_1} = \frac{\sqrt{\mathrm{j}\omega\mu_2\cdot(\gamma_2+\mathrm{j}\omega\varepsilon_2)}}{\sqrt{\mathrm{j}\omega\mu_1\cdot(\gamma_1+\mathrm{j}\omega\varepsilon_1)}}, \tag{1}$$

where **k** is the wave number, γ is the conductivity, ε the permittivity, μ the permeability, θ_0 angle of incidence and θ_2 angle of refraction. Relation (1) is defining for the boundary line between the dielectrics medium. Interpretation of the Fresnel equations and Snell´s laws is simple in the case of the refraction on boundary line between the dielectrics medium. In case of refraction in a lossy medium, according to relation (1), angle θ_2 depends on wave numbers $\mathbf{k}_1$ a $\mathbf{k}_2$, which are generally complex; then, in medium 2 an inhomogeneous wave is propagated.

This complicates the physical nature of the phenomena and brings qualitatively new phenomena. Areas of constant phase generally do not merge with areas of constant amplitude, then wave is not completely transverse. Areas of constant amplitude are parallel to the interface, but the same areas of phases are generally oblique to it. The resulting EMG waves are propagated in the coordinate system in the direction $\mathbf{u}_{n2}$. An electromagnetic wave is understood as the electric field strength and the magnetic field strength.

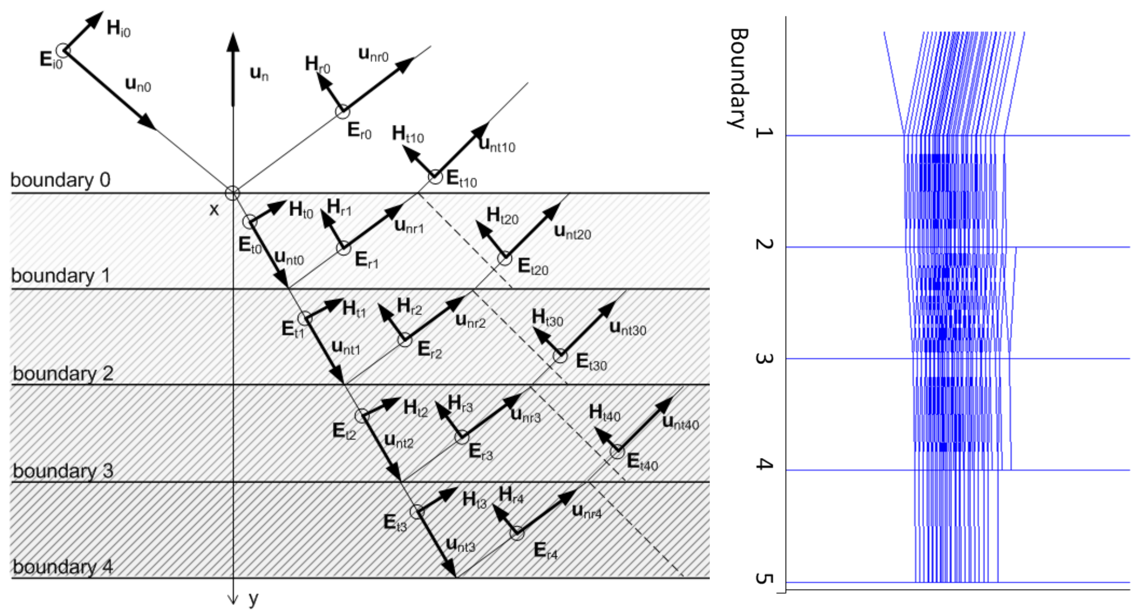

a) b)

Figure 1: Reflection and refraction of the electromagnetic waves on a layered medium for the TE wave: a) layout, b) in Matlab for 5000 cycles.

For simplicity, we will analyse separately the **E** vector parallel to the boundary (also known as TE wave) as indicated in Fig. 1.a) and the **H** vector parallel to the boundary (also known as TM wave). For the TE wave, electric field strength of the reflection and transmission beams is expressed according to the equation

$$\mathbf{E_r} = \mathbf{E_1}\mathrm{e}^{-\mathrm{j}k_1\,\mathbf{u_{n1}}\times\mathbf{r}}, \quad \mathbf{E_t} = \mathbf{E_2}\mathrm{e}^{-\mathrm{j}k_2\,\mathbf{u_{n2}}\times\mathbf{r}}, \tag{2}$$

where $\mathbf{E_1}$ is calculated from the intensity on boundary line $\mathbf{E_0}$ and reflection coefficient ρ_E, and $\mathbf{E_2}$ is calculated from the intensity on boundary line $\mathbf{E_0}$ and transmission factor τ_E. For numerical modelling, there is a suitable relation in the form:

$$\mathbf{E_r} = \frac{\mu_2 k_1 \cos\theta_0 - \mu_1 \sqrt{k_2^2 - k_1^2 \sin^2 \theta_0}}{\mu_2 k_1 \cos\theta_0 + \mu_1 \sqrt{k_2^2 - k_1^2 \sin^2 \theta_0}} \mathbf{E_0} \cdot e^{-j\mathbf{k}}$$

$$\mathbf{E_t} = \frac{2\mu_2 k_1 \cos\theta_0}{\mu_2 k_1 \cos\theta_0 + \mu_1 \sqrt{k_2^2 - k_1^2 \sin^2 \theta_0}} \mathbf{E_0} \cdot e^{-j\mathbf{k}_2} \qquad (3)$$

These relations are calculated from the basic variable and they facilitate an acceleration of the calculation process. We use atypical formulas for calculating the magnetic components:

$$\mathbf{H}_r = -\frac{\frac{\mu_2}{\mu_1}\mathbf{k}_1 \cos\theta_0 - \sqrt{\mathbf{k}_2^2 - \mathbf{k}_1^2 \sin^2\theta_0}}{\mu_2 \cos\theta_0 + \frac{\mu_1}{\mathbf{k}_1}\sqrt{\mathbf{k}_2^2 - \mathbf{k}_1^2 \sin^2\theta_0}} \frac{\mathbf{E}_0}{\omega} \cdot e^{-j\mathbf{k}}$$

$$\mathbf{H}_t = -\frac{2\mathbf{k}_2 \cos\theta_0}{\mu_2 \cos\theta_0 + \frac{\mu_1}{\mathbf{k}_1}\sqrt{\mathbf{k}_2^2 - \mathbf{k}_1^2 \sin^2\theta_0}} \frac{\mathbf{E}_0}{\omega} \cdot e^{-j\mathbf{k}} \qquad (4)$$

12 FEM MODEL OF MULTILAYR MATERIAL SAMPLE

In order to verify the properties of analytical model of an accurate evaluation of wave propagation in layered environment another model has been used. This numerical model utilizes finite element method (FEM) and following material properties: material 1 [$\varepsilon_r = 1$, $\mu_r = 1$ and $\gamma = 1.10^{-9}$ S/m], material 2 [$\varepsilon_r = 81$, $\mu_r = 0.999991$ and $\gamma = 1.10^{-9}$ S/m]. Layer thickness was x_v=20 mm and the frequency of the incident electromagnetic wave was f =1GHz. As a mathematical model, the enhanced wave equation for lossy environment has been used

$$\nabla^2 u + f\frac{\partial u}{\partial t} + g\frac{\partial^2 u}{\partial t^2} - f_c(x,y,z,t) = 0,\ \forall g(x,y,z) \neq 0, \forall f(x,y,z) \neq 0 \text{ in } \Omega \qquad (5)$$

where u is the searched functional, f is a function of electromagnetic wave damping, g is a function of electromagnetic wave excitation, f_c is a function of lossy environment, Ω is the defining domain of variables and functions. The distribution of the material in layers is shown in Figure 2.

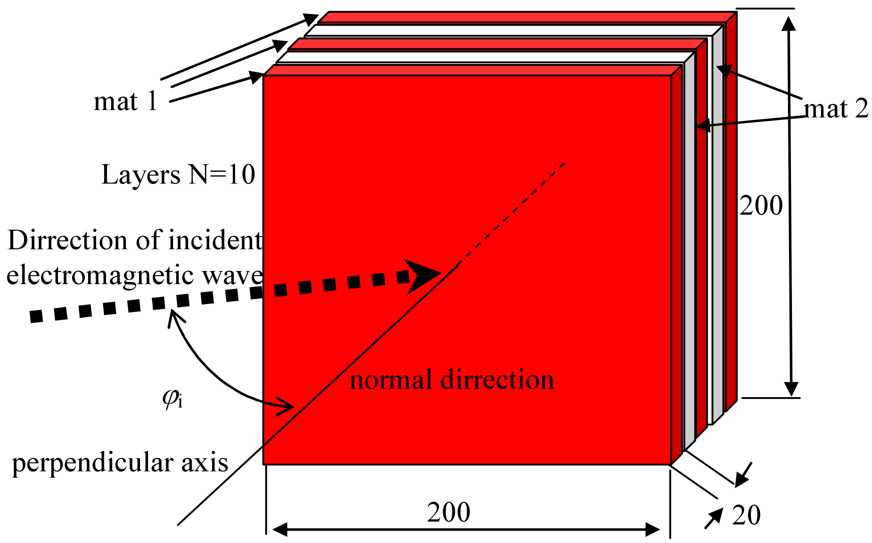

Figure 2. Material and geometrical model, dimensions in mm

The numerical method FEM with defined boundary conditions is applied on equation (5) and there is defined an incident electromagnetic wave also. The distribution of electric field *E* and its phase φ was evaluated within the model analysis. Figures 3a-3d show the distribution of the electric field magnitude E in dependence on the initial angle of electromagnetic wave incidence. For similar incidence angles of electromagnetic wave, the magnitude of electric field and phase of electric field are shown in Figures 4a-4d. The characteristics in Figures 4a-4d correspond to direction of axis perpendicular to layer plane.

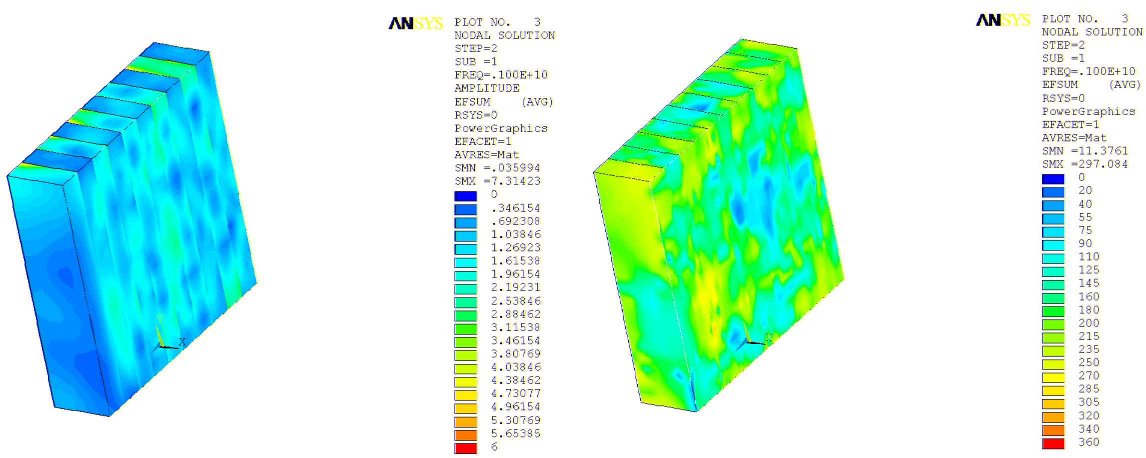

Figure 3a. Distribution of electric field magnitude E (left) and electric field phase (right) for φ_i= 10°

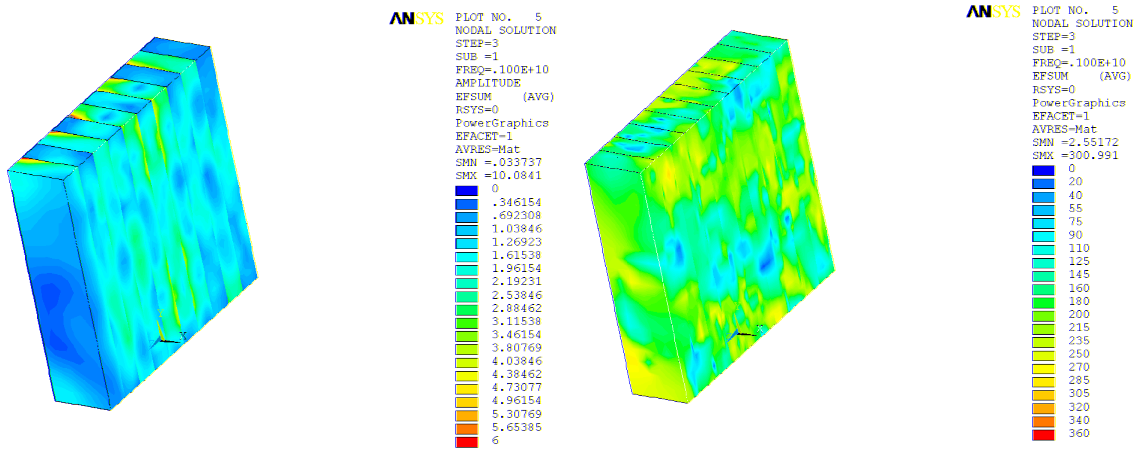

A) B)

Figure 3b. Distribution of electric field magnitude E (A) and electric field phase (B) for φ_i= 20°

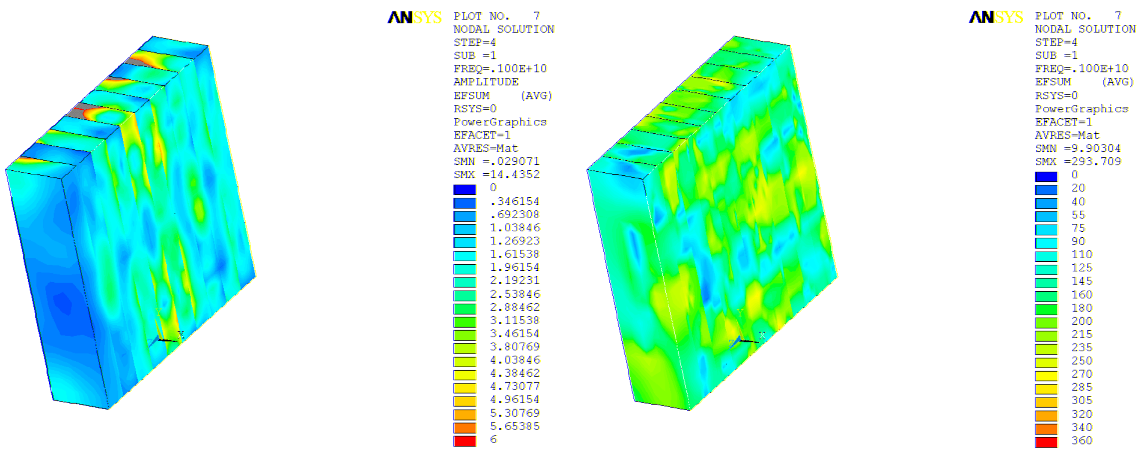

A) B)

Figure 3c. Distribution of electric field magnitude E (A) and electric field phase (B) for φ_i= 30°

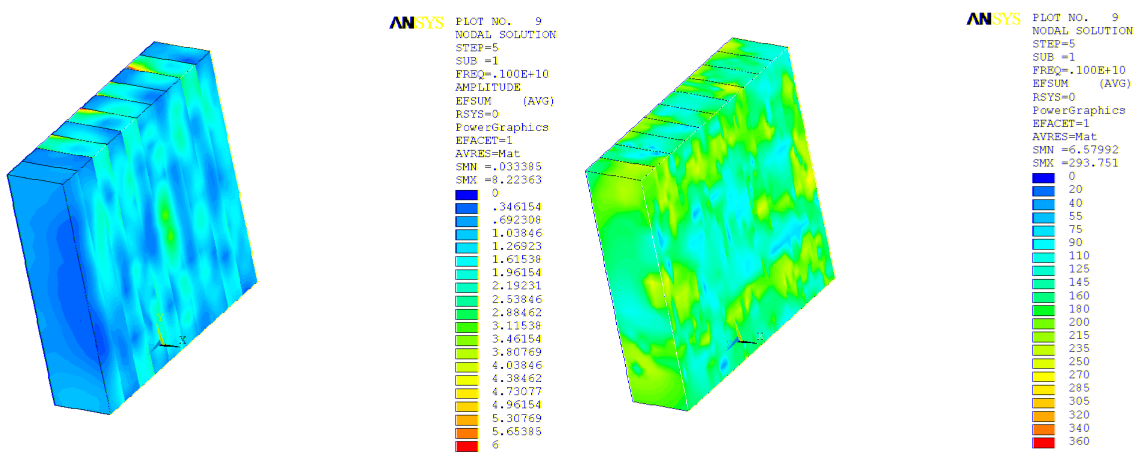

A) B)

Figure 3d. Distribution of electric field magnitude E (A) and electric field phase (B) for φ_i= 40°

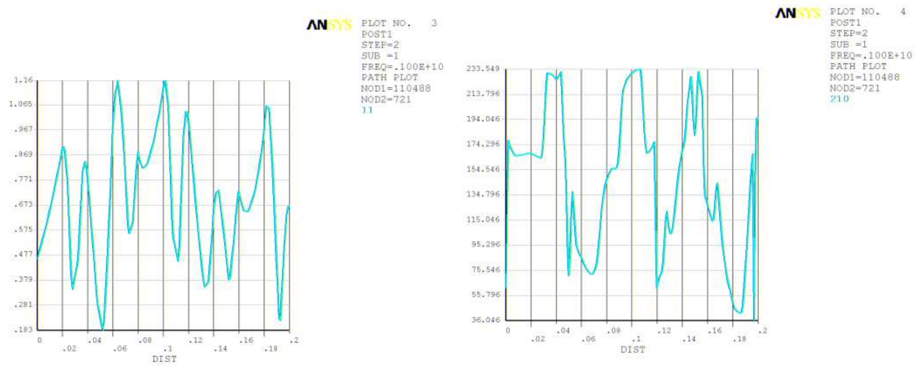

A) B)

Figure 4a. Distribution of electric field magnitude E (A) and electric field phase (B) for φ_l= 10° in direction of axis perpendicular to layer plane

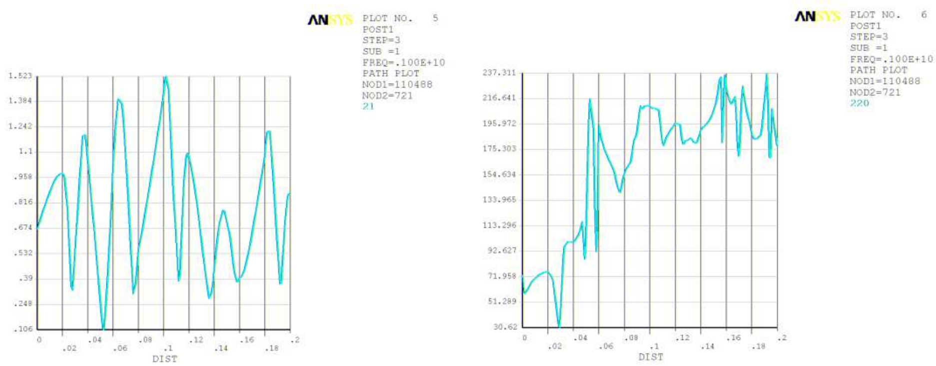

A) B)

Figure 4b. Distribution of electric field magnitude E (A) and electric field phase (B) for φ_l= 20° in direction of axis perpendicular to layer plane

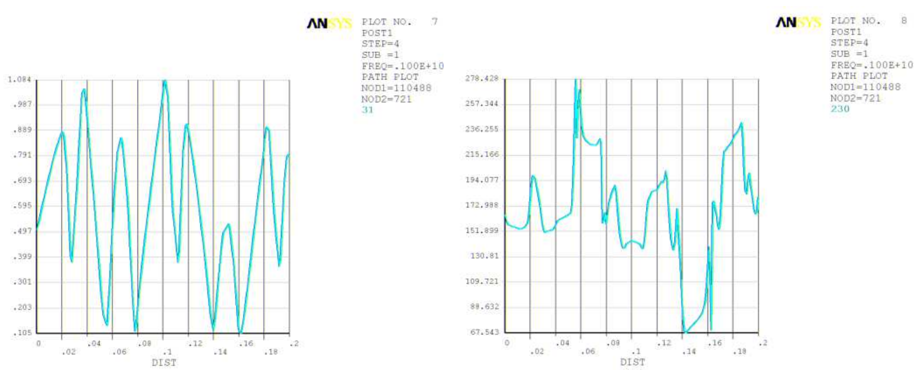

A) B)

Figure 4c. Distribution of electric field magnitude E (A) and electric field phase (B) for φ_l= 30° in direction of axis perpendicular to layer plane

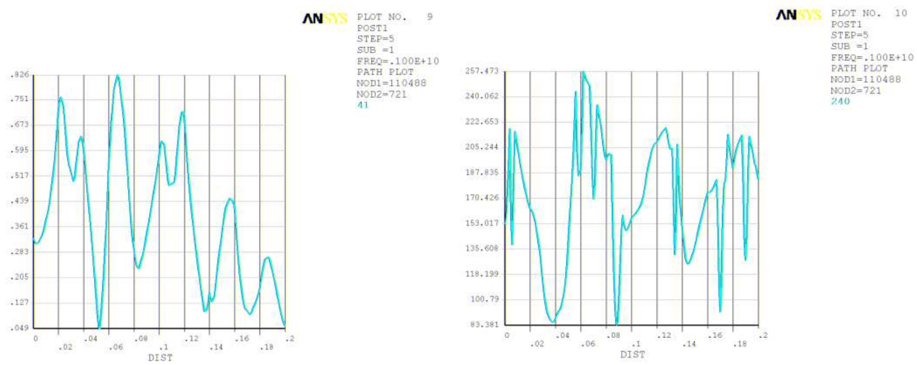

A) B)

Figure 4d. Distribution of electric field magnitude E (A) and electric field phase (B) for φ_i= 40° in direction of axis perpendicular to layer plane

13 Conclusion

Two approaches to analysis of wave propagation in layered material structure has been presented. One of them is based on analytical model of the propagation (3),(4) and has been solved by means of Matlab. The second approach utilizes finite element method applied on relation (5). The finite element method has been enabled by Ansys system. The comparison of the results of both approaches isn't possible to perform directly. Complex form of the angle of reflection and refraction is considered in case of analytical approach, which allows accurate determination of the size and intensity of backward traveling waves. In order to determine the direction of constant phase propagation in lossy medium, there are considered real parts of wave number only

By numerical modeling using the wave equation and ANSYS, the source of electromagnetic waves is continuous. The interference effects arises on materials interface for forward and backward propagating waves. Moreover, into the interference process enters also the time-delayed waves from source and interface reflections. It should be noted that the propagation velocity isn't equal for different layers. Analytical solution and its algorithms process the time-varying phenomena of (pulsed) excitation source. The analytical solution includes the effect of time-dependent propagation of electromagnetic waves in a heterogeneous media and it results the distribution of electromagnetic field at the interfaces in certain time instants.

. Při analytickém řešení časově proměnného (impulzního) zdroje elektromagnetických vln je na rozhraní vrstev heterogenních prostředí fáze intenzity elektromagnetického pole rovnoměrně rozložená.

The results of ANSYS analysis of electromagnetic waves propagation in material in time-domain corresponds to the resulting distribution of superimposed field intensities on individual interfaces of analytical model for frequencies of the excitation signal. In case of evaluation of impulse phenomenon and its instantaneous electromagnetic quantities in heterogenous structures (with mutliple interferences and different wave velocities) the behaviour of phase change is non-uniform. Therefore, it can be concluded that ANSYS method is advantageous for above mentioned analysis. In contrast, the solution of field distribution by means of analytical model gives expectable results, since the behaviour of phase change is uniform.

Methods describe in this paper are suitable for accurate analysis of beam refraction to the other side from the perpendicular line during the passage through the interface. This phenomenon occurs in metamaterials.

Acknowledgements, The funding of the project was supported by Ministry of Education, Youth and Sports of the CR, and by institutional resources from the related Research Design project of the BUT Grant Agency FEKT-S-10-13, GACR 13-09086S and project from Education for Competitiveness Operative Programme CZ.1.07.2.3.00.20.0175 and CZ.1.07/2.3.00/30.0005.

References

Stratton J.A. , 1961, *Theory of electromagnetic field*. SNTL Praha , In Czech.

P.Fiala, M. Friedl, *Stochastic models of electrodynamics*, PIERS 2011, Progress In Electromagnetics Research Symposium Proceedings, Suzhou, China, Sept. 12-16, 2011, pp. 91-96, Suzhou , China, 2011.

Drexler,P. Fiala, P., *Methods for high-power EM pulse measurement*, IEEE SENSORS JOURNAL Volume:7 Issue: 7-8 , 1006-1011, JUL-AUG 2007

MIKULKA, J. „ImageJ Plug- ins for Microscopic Image Processing". In *34th International Conference on Telecommunications and Signal Processing*. 2011. s. 541-543. ISBN: 978-1-4577-1409- 2.

Marcon, P., K. Bartusek, J. Mikulka and M. Cap, koupil, "Magnetic susceptibility measurement using 2D magnetic resonance imaging," *Measurement Science and Technology*, vol. 22(10), 2011.

Orfanidis, S. *Electromagnetic Waves and Antennas*. 2008. 1031 p. Available from WWW: <www.ece.rutgers.edu/~orfanidi/ewa>.

Contact address:
assoc.prof. Ing.Pavel Fiala, Ph.D.,
Ing. Michael Hanzelka, MBA
Ing. Radim Kaldec
Brno university of technology, Faculty of electrical engineering and communication, Department of theoretical and experimental electrical engineering Technicka 12, 616 00 Brno, Czech Republic
fialap@feec.vutbr.cz, michael.hanzelka@daccee.eu, kadlec@feec.vutbr.cz

FAST NPSH3 ANALYSIS USING TBR AND BATCH PROCESSING

TOMÁŠ KRÁTKÝ[A], MILAN SEDLÁŘ[A], LUDĚK BARTONĚK[B]
[A]Centre of Hydraulic Research, [B]Faculty of Science, Palacký University of Olomouc

Abstract: Using ANSYS CFX software, it is possible to model cavitation effects in a pump and evaluate the degradation of the pump performance. The most common task required for hydraulic design is computing the NPSH3 curve. It requires computation of multiple head-drop curves, each of them typically consisting of ten to twenty CFD pump simulations, and thus is very demanding performance-wise. This article shows how to do the NPSH3 computation in an efficient and semi-automated way, using Transient Blade Row and Command Line capabilities of ANSYS.

Keywords: cavitation, CFD, Transient Blade Row

1 Introduction

Cavitation is an important phenomenon influencing pumps. Once the pressure in the blade passage reaches vapour pressure, the fluid vaporizes and cavitation caverns filled only with the vapour are formed. These caverns behave as an obstacle to flow and as a result, head decreases as the suction head decreases. This dependency is shown as a head-drop curve (Image 1 - NPSH is an abbreviation for Net Positive Suction Head).

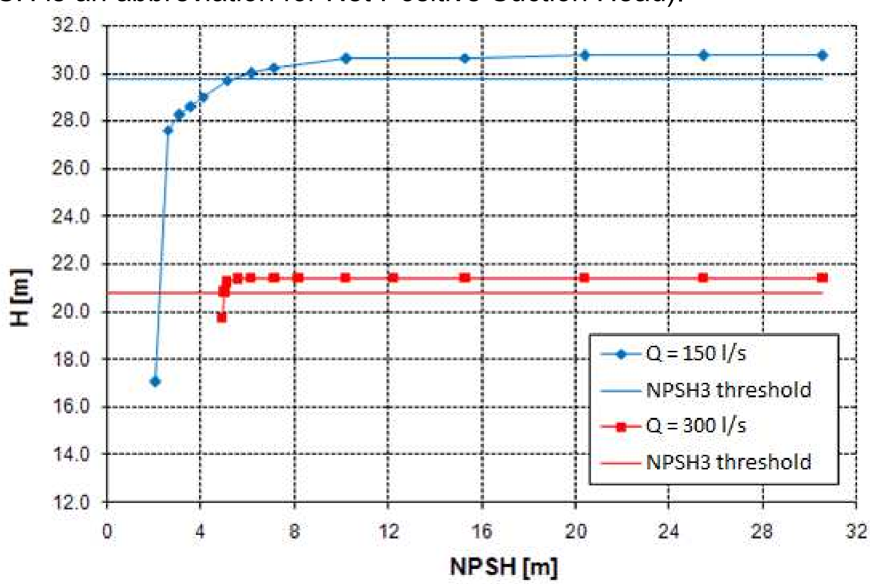

Image 1 – Head-drop curve

The important parameter for hydraulic design is NPSH3 – defined as the NPSH required for 3% drop of the total head of the pump (Gülich, 2010).

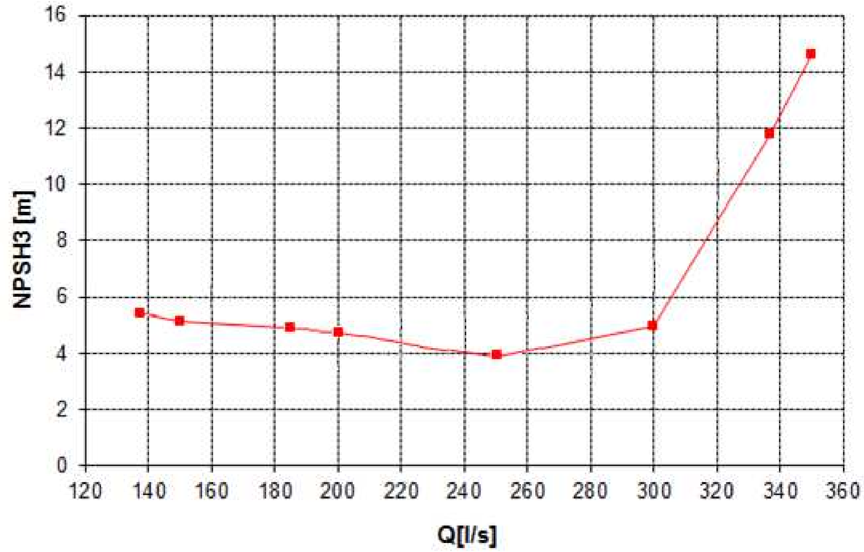

Image2 – NPSH3 curve

For obtaining a NPSH3 curve, multiple head-drop curves need to be computed. Each of them typically requires solving ten to twenty CFD tasks, so the total number of CFD simulations can easily exceed one hundred. That makes the numerical computation of NPSH3 curve very performance demanding, thus doing the single step of CFD simulation as simple as possible is crucial.

2 CFD modelling of cavitation

Employing multiphase models (fluid + vapour) allows modelling of cavitation caverns and the results have proven to be close enough to experimental data over time. The numerical realization does not differ much from "standard" Q-H analysis. The geometry and boundary conditions remain the same, what is new is the vapour fraction.

As an example, a NPSH3 analysis of a diagonal pump with diffuser is shown.

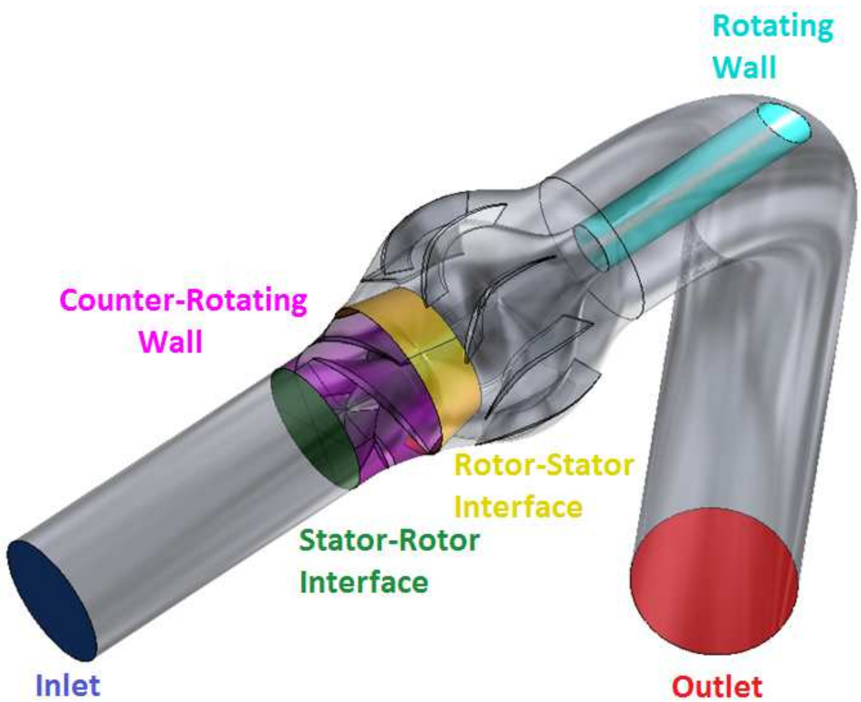

Image 3 – CFD model (full geometry)

The impeller has six blades, the stator includes a diffuser with eleven blades. The mesh was created with ANSYS ICEM software, structured with hexa for impeller and stator and unstructured with tetra/prism for the elbow.

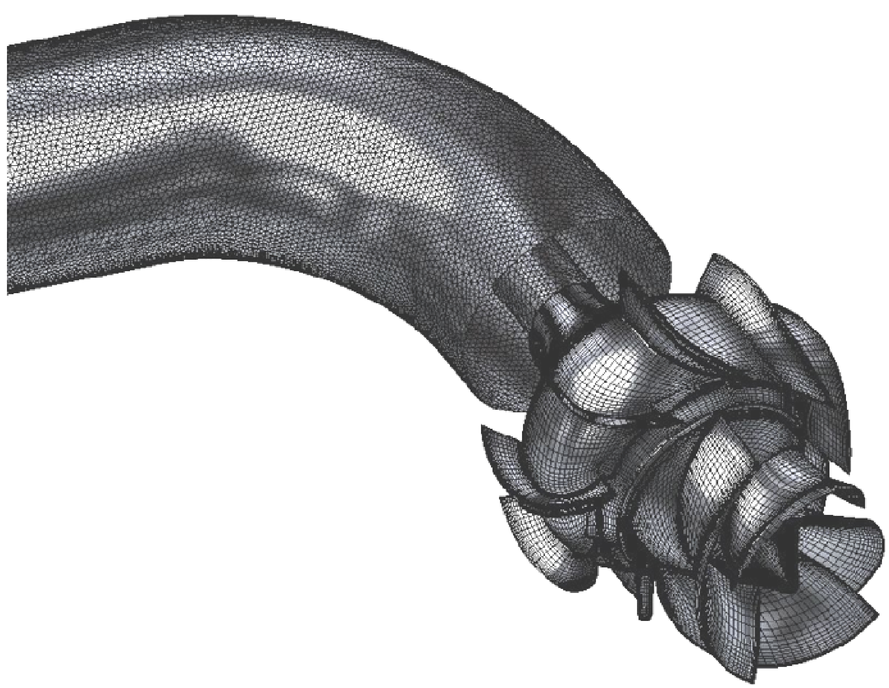

Image 4 – Computational mesh (full geometry)

For dynamic effects of cavitation, the complete geometry is necessary. But if the NPSH3 curve is our only concern, it is possible to use Transient Blade Row (TBR) model offered by CFX. Only the minimal number of blades to match the different numbers in impeller and diffuser is required. In our case, it is one blade of the impeller and two blades of the diffuser.

For proper use of TBR model, the whole model needs to be rotationally symmetric – which is obviously not true for the elbow. Fortunately, thanks to the nature of the cavitation phenomenon, it is usually not a big problem. The cavitation appears first at the leading edge of the impeller and as the NPSH goes down, it fills more and more volume and progresses further into the stator (Brennen, 1994). Thus, the elbow can be replaced by a pipe. The parameters change a bit, but the dependency of head on NPSH remains very similar to the original geometry until the point where the whole pump is filled with cavitation caverns – but the pump cannot work under these conditions anyway.

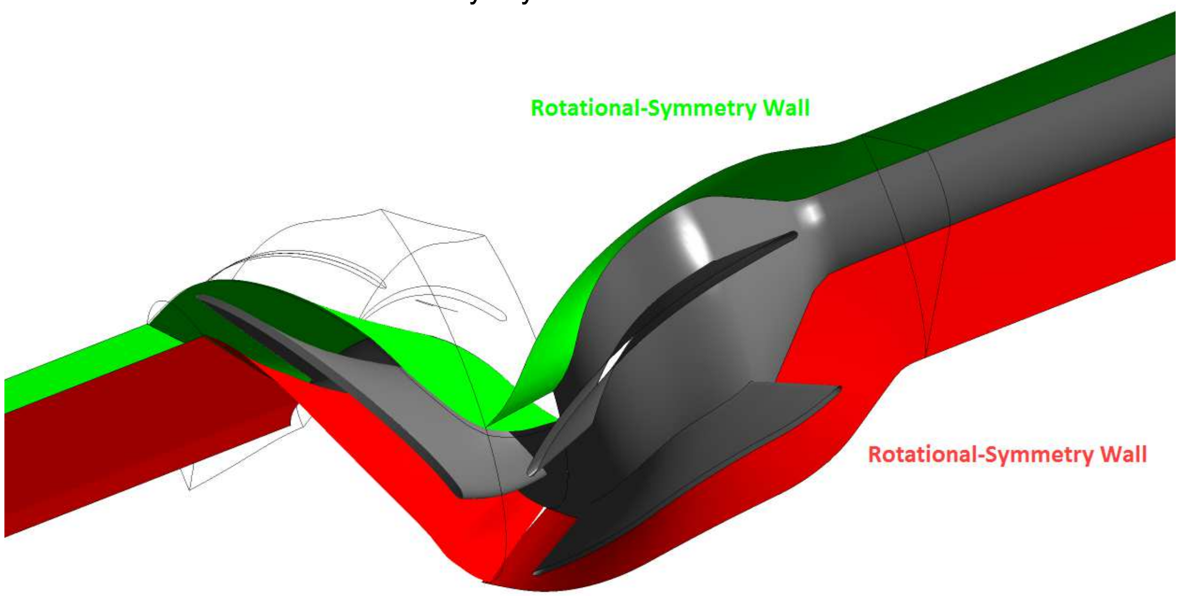

Image 5 – CFD model (TBR)

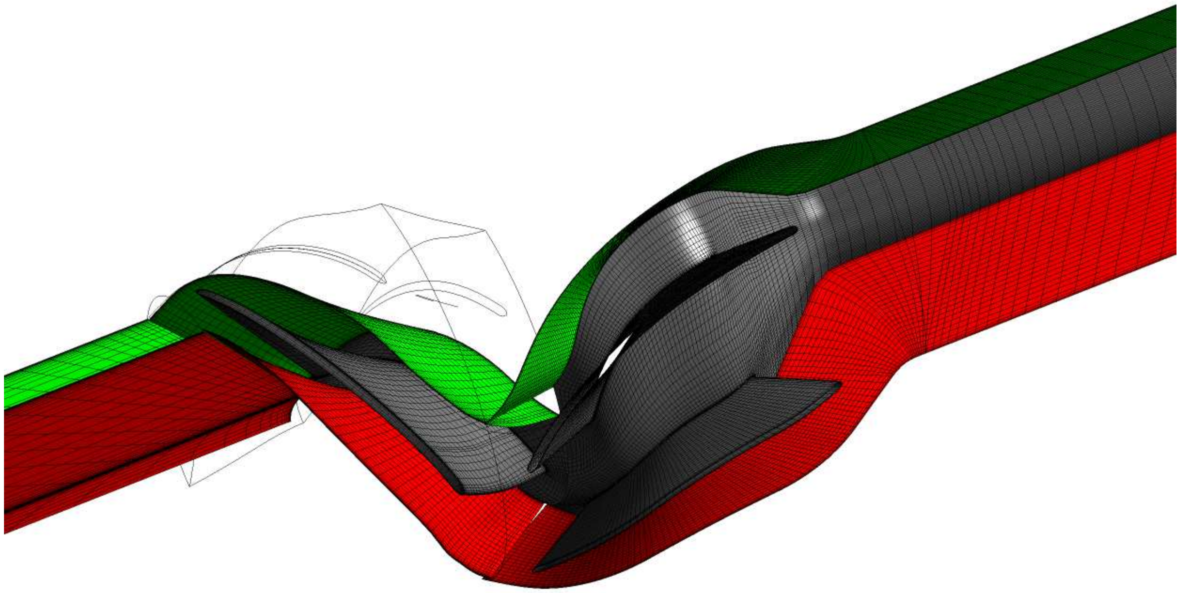

Image 6 – Computational mesh (TBR)

In this sample case, one blade passage in the impeller and two in the diffuser are required. The number of nodes goes down from 1.7 million to 320 thousands and solution time lowered more than five times.

3 Batch processing

Cavitation simulations are numerically very problematic. Due to the nature of the multi-phase model, the solution can easily end up in an "all vapour no fluid" state for low NPSH. To prevent this, the time-proven method is to start at high enough NPSH, lower it slowly and use the previous result file for each step. Too big change in NPSH can once again result in numerical problems and this is the main reason why head-drop curve computation requires relatively many steps.

Thus, computing a NPSH3 curve requires following steps:

- Choosing Q.
- Deciding a fitting starting NPSH - based on expected results and previous experiences with similar pumps.
- Running the task in steady mode and using the result file as the starting one.
- Running the task in TBR mode with the starting result file.
- Lowering NPSH until a point where H drops below the limit.

- Repeating for other Qs.

Geometry and mesh remain the same, only Q and H need to be set for each step. Manual generation of so many files would be too time-consuming, thus a different approach – employing ANSYS command-line capabilities and Excel macros – has been chosen.

Instead of changing the Q and H values one-by-one, an Excel table is given:

Table 6 Q and H values for head-drop curve

Q [l/s]	**H [Pa]**
300	300000
300	250000
300	205000
300	150000
300	100000
300	70000
300	60000
300	52000
300	41000
300	35000
300	31000
300	28000
300	25000

H is set as Inlet pressure, Q remains the same for the whole head-drop curve. In CFX-Pre, a session for changing Q and H and def file generation is recorded, and then this template is substituted with the Excel data using VBA macro. As a result, session files (one for each H) are generated and run through a *cfx5pre –batch [session file name]* command.

This way, the *def* files for ANSYS CFX are generated and subsequently run in batch mode. The batch file has a form

cfx5solve -def [file 1] -ini [results 0] -par-local -partition [number of partitions]

cfx5solve -def [file 2] -ini [results 1] -par-local -partition [number of partitions]

...

Because of the periodic nature of the transient simulation, the last value is not sufficient. Instead, an average of the last period(s) needs to be taken. Unfortunately, CFD-Post cannot load the data for each time-step, only from *trn* files – and storing *trn* files would require too much disc space. Also, processing these files takes too long. This can be solved by setting an average of last *N* time-steps as a variable in CFX-Pre, but since *N* needs to be fixed prior to the computation, it is not really helpful once we decide that the average needs to be taken for different number of periods.

Thus, Excel and batch processing were once again employed. *Cfx5mondata* utility can extract the variables data into a text file

cfx5mondata -res [result file] -output [csv file] -varlist "USER POINT,H"

These text files are loaded into Excel and last *N* values are averaged, using VBA macros. But this time, *N* can be changed anytime.

4 Results and conclusion

The pump was also tested in hydraulic laboratory and the comparison of numerical simulations and experimental results was made.

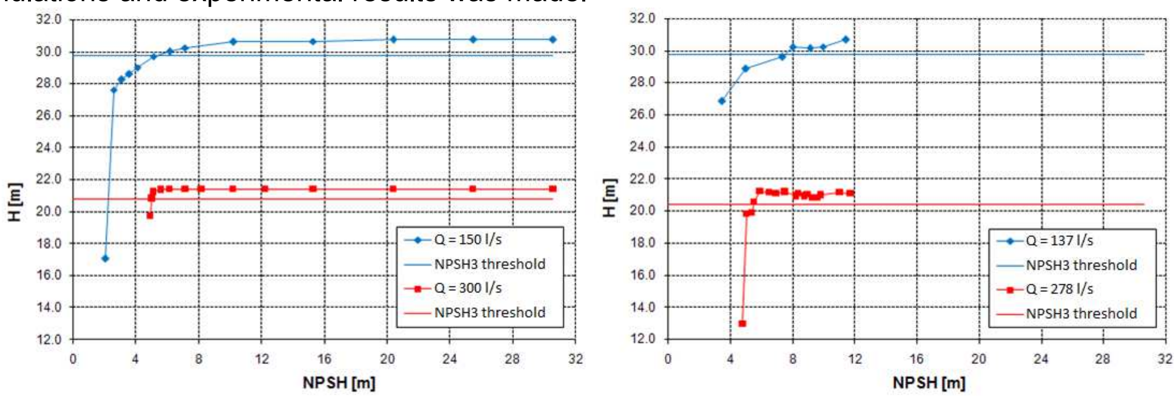

Image 7 – CFD (left) and experiment (right) comparison

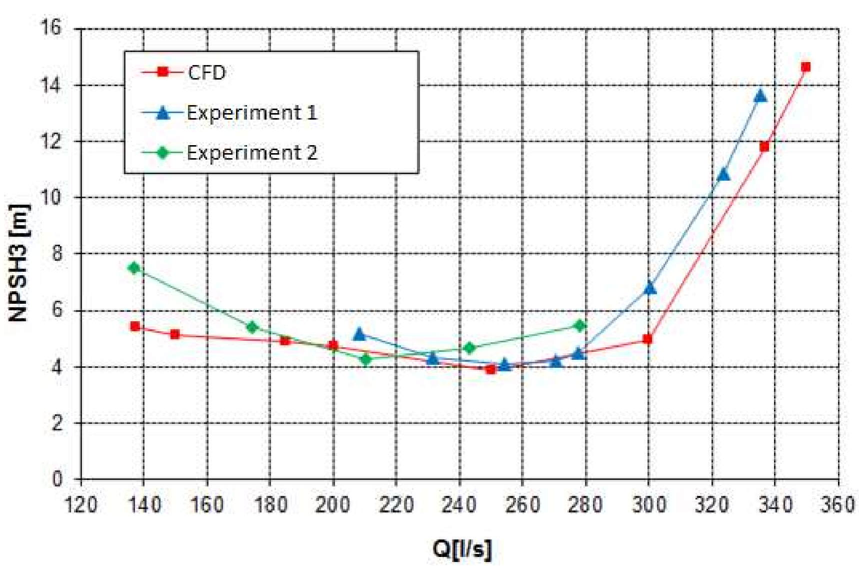

Image 8 – NPSH3 CFD and experiments comparison

Thanks to the cavitation analysis specific nature, employing TBR, batch processing and geometry simplification can save great deal of both computing and assembling time. Further, creating an automatic NPSH decreasing algorithm is a future goal. Another problem worth exploring is the possibility of computing the whole NPSH3 in steady mode. Anyway, even in its current state, this method of NPSH3 analysis has been proven as a fast one – the complete NPSH3 computation usually takes around a week on a four core Xeon processor. Also, the results are in a good agreement with experimental data.

References

BRENNEN C. E., 1994, *Hydrodynamics of Pumps.* Concepts Eti & Oxford University Press.

GÜLICH J. F., 2010, *Centrifugal Pumps.* Springer-Verlag Berlin Heidelberg, 966p. ISBN 978-3-642-12823-3

Acknowledgement
The work was performed with support of TA ČR ALFA project FR-TI1/418 Research and Development of High Speed Pumps with Suppressed Cavitation.

The work was performed with support of AFNet project CZ. 1.07/2.4.00/17. 0014.

Contact address:
Mgr. Tomáš Krátký, RNDr. Sedlář Milan, CSc.
Centre of Hydraulic Research, Jana Sigmunda 190, 783 50 Lutín

Doc. Ing. Luděk Bartoněk Ph.D.
Faculty of Science, Palacký University of Olomouc, 17. listopadu 1192/12, 771 46 Olomouc

FEM MODEL OF SURFACE ACOUSTIC WAVE SENSOR WITH SENSITIVE LAYER

VLADIMÍR KUTIŠ*, GABRIEL GÁLIK*, IVAN RÝGER+, JURAJ PAULECH*,
JUSTÍN MURÍN*, JURAJ HRABOVSKÝ*, TIBOR LALINSKÝ+
*Department of Applied Mechanics and Mechatronics, FEI STU Bratislava, Ilkovičova 3, Bratislava 81219, Slovakia, +Institute of Electrical Engineering SAV, Bratislava, Dubravska cesta 9, Bratislava 84104, Slovakia

Abstract: The paper is focused on modelling and simulation of surface acoustic wave devices using finite element method, especially by code ANSYS. Investigated sensor is made of piezoelectric GaN layer placed on SiC substrate. In the model, there is considered not only sensitive layer made of palladium but also input and output interdigital transducers made of nickel and gold. Only 2D model of sensor is investigated. Two different analyses are performed: modal and full transient. Modal analysis is performed to determine the interdigital transducer eigenfrequency, which is used in next transient analysis as electric frequency of excitation. In transient analysis, the influence of sensitive layer mass density change on output induced electric signal is investigated.

Keywords: MEMS, SAW, Piezoelectric material, Modal Analysis, Transient Analysis, ANSYS

1 Introduction

Surface acoustic wave (SAW) devices typically generate mechanical waves, which propagate on surface of piezoelectric layer. The waves are also called Rayleigh waves (Mayers, 1994). The velocity of waves depends on density and elasticity material properties and the velocity is very sensitive on change of surface layer mechanical parameters (e.g. density), as well. This sensitivity is the reason why SAW devices are so popular as sensor devices (Fraden, 2003), e.g. sensors of concentration of chemical compounds (Nimal, 2006). Rayleigh wave can be generated in piezoelectric material using interdigital transducer - IDT (Datta, 1986). It is basically comb-like structure with fingers connected to electric terminals.

The paper is focused on modelling and simulation of SAW device using finite element method (Burnett, 1987), specially by code ANSYS (ANSYS, 2013). Two different analysis types are investigated - modal and transient. Both analyses are only 2D. Modal analysis, is used to determine the frequency of SAW, which is used in following transient analysis. In transient analysis, wave propagation and the influence of density change of sensitive layer is investigated.

2 SAW piezoelectric sensor

Image 1 shows SAW sensor investigated in this article. SAW sensor is based on GaN piezoelectric layer, that is placed on SiC substrate. Only 2D model is investigated. The thickness of GaN layer is h_{GaN}=2 μm and the thickness of SiC is h_{SiC}=5 μm. The position of IDT and sensitive layer is shown in Image 1 - Top view. The distance between each pair of IDT is half of wave length λ=4 μm, the distance between input IDT and output IDT is 20 μm. The length of sensitive layer is 18 μm. Detail of one IDT pair with materials is shown in Image 2.

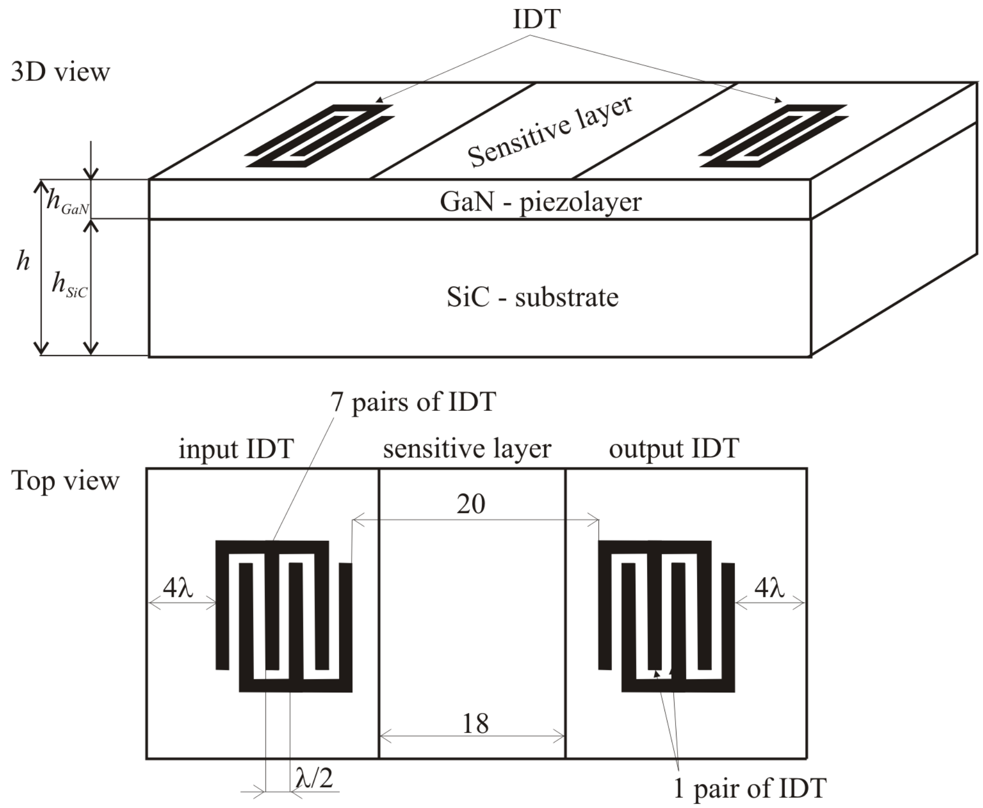

Image 15 – Geometry model of SAW sensor

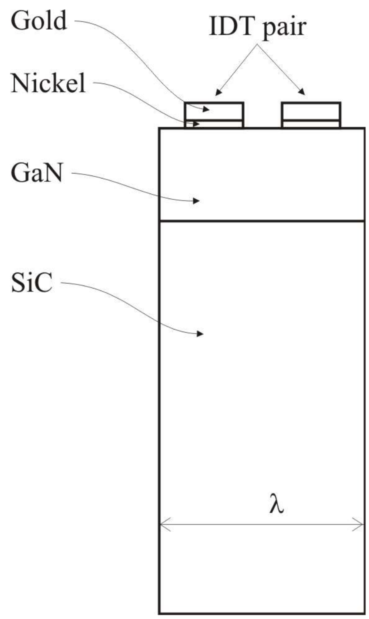

Image 16 – Detail of one IDT pair with materials

Material properties, which have to be considered in piezoelectric analysis of SAW sensor, belong to three categories: mechanical, electrical and piezoelectrical. Mechanical properties have to be defined for all five materials, Gold (electrodes), Nickel (electrodes), Palladium (sensitive layer), GaN (piezolayer) and SiC (substrate), but electrical and piezoelectrical properties have to be defined only for GaN layer. Constitutive law for mechanical behaviour can be written in matrix form as

$$\sigma = C\varepsilon \tag{4}$$

where σ is stress tensor, ε is strain tensor and C is elasticity matrix. Constitutive law for piezoelectric behaviour can be written in matrix form as

$$\begin{aligned} \sigma &= C^E \varepsilon - eE \\ D &= e\varepsilon + e_p^\varepsilon E \end{aligned} \tag{5}$$

where E is vector of electric intensity, D is vector of electric displacement, $e^\varepsilon{}_p$ is permitivity matrix on condition constant strain ε, C^E is elasticity matrix on condition constant electric intensity E and e is matrix of piezoelectric properties. Matrices C, $e^\varepsilon{}_p$ and e for transversally isotropic material with polarization in z direction have following forms

$$C = \begin{bmatrix} c_{11} & c_{12} & c_{13} & 0 & 0 & 0 \\ & c_{11} & c_{13} & 0 & 0 & 0 \\ & & c_{33} & 0 & 0 & 0 \\ & s & & c_{44} & 0 & 0 \\ & & y & & c_{44} & 0 \\ & & & m & & c_{66} \end{bmatrix} \quad e_p^\varepsilon = \begin{bmatrix} e_{p11} & 0 & 0 \\ 0 & e_{p11} & 0 \\ 0 & 0 & e_{p11} \end{bmatrix} \quad e = \begin{bmatrix} 0 & 0 & e_{13} \\ 0 & 0 & e_{13} \\ 0 & 0 & e_{33} \\ 0 & 0 & 0 \\ 0 & e_{15} & 0 \\ e_{15} & 0 & 0 \end{bmatrix} \tag{6}$$

Considered material parameters for GaN and SiC are shown in Table 1. Density of GaN is 6150 kg/m^3 and density of SiC is 2329 kg/m^3. Material properties of other materials used in simulations are: Gold: Young modulus 78 GPa, Poisson ratio 0.44 and density 19300 kg/m^3, Nickel: Young modulus 200 GPa, Poisson ratio 0.31 and density 8600 kg/m^3, Palladium: Young modulus 121 GPa, Poisson ratio 0.39 and density 12023 kg/m^3.

Table 7 Material parameters for GaN and SiC

material	mechanical prop. [GPa]						perm. [-]	piezoelectric prop. [pC/μm^2]			
	c_{11}	c_{12}	c_{13}	c_{33}	c_{44}	c_{66}	e_{p11}	e_{13}	e_{33}	e_{15}
GaN	390	145	103	405	105	123	8.9	-0.51	0.375	0.67
SiC	166	64	c_{12}	c_{11}	79.6	c_{44}	-	-	-	-

3 Modal analysis of SAW sensor

The goal of modal analysis is to determine the eigenfrequency of SAW sensor, that can be used as frequency of input signal in transient analysis. Because the geometry of SAW sensor under IDT is periodic, we can model only 2D small part of SAW device with length equal wave length λ - see Image 2. Boundary conditions have to enable periodic deformation of the model. The conditions are satisfied by coupling of individual degree of freedom on left and right side of the model. Bottom of the model is fixed and the top is free. To perform modal analysis, piezoelectric 2D element PLANE223 and structural 2D element PLANE183 of code ANSYS are used. Block Lanczos method is used to compute eigenfrequencies and eigenmodes of the system. Obtained eigenmode and eigenfrequency of Rayleigh wave are shown in Image 3. Eigenfrequency of the periodic model is f=1.295 GHz.

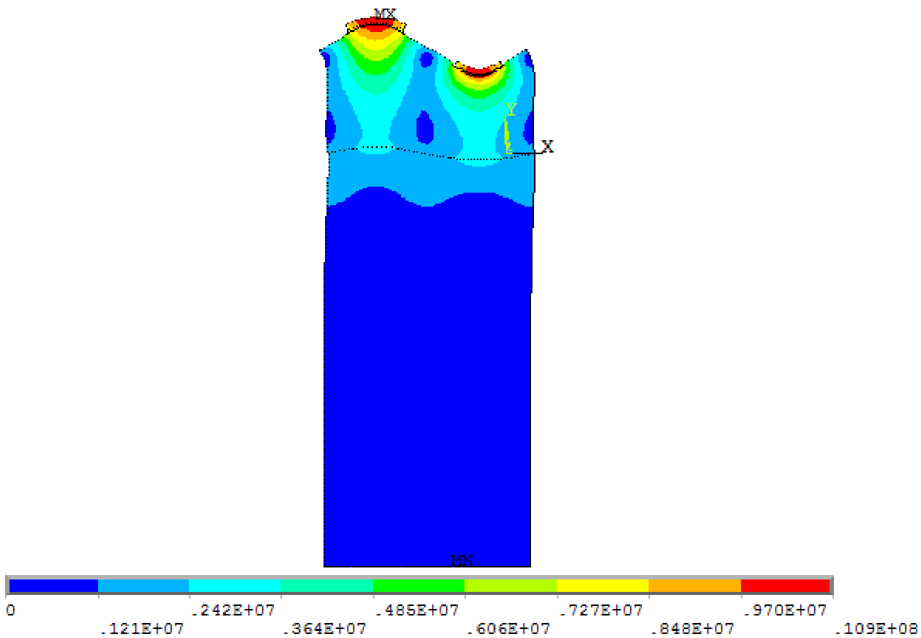

Image 17 – Eigenmode of periodic part of SAW sensor

4 Transient analysis of SAW sensor

Also transient analysis of SAW sensor with sensitive layer is modeled as 2D system. In order to propagated waves do not interfer with reflected waves from the material interface, damping region in GaN and SiC is included in the model - see Image 4.

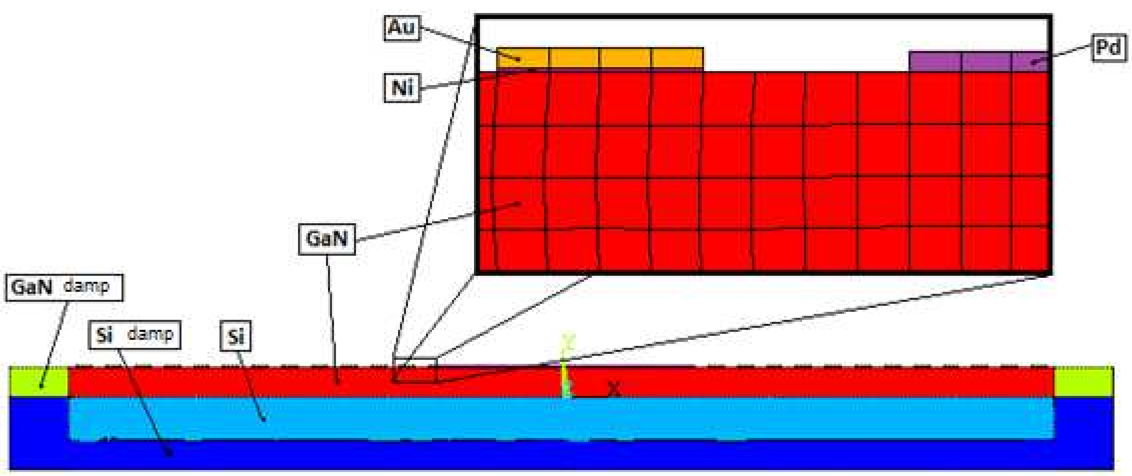

Image 18 – 2D model for transient analysis

Loading of the SAW sensor is harmonic electric voltage on input IDT with amplitude 1 V and with frequency equal to the eigenfrequency computed in modal analysis *f*=1.295 GHz - see Image 7 - blue curve. SAW sensor is fixed at the bottom of substrate. The goal of the simulation is to investigate wave propagation on the surface of SAW sensor as well as induced voltage on output IDT.

The first simulation is performed with original density of sensitive layer. Image 5 shows wave propagation in system at the beginning of simulation - top image, and also at the end of simulation (time 1.5x10^{-8} s) - bottom image. As we can see from both deformations, dominant direction of wave propagation is from input IDT to the output IDT. Detail deformation of the system in vicinity of output IDT is shown in Image 6, at the beginning of simulation - top image, and also at the end of simulation (time 1.5x10^{-8} s) - bottom image.

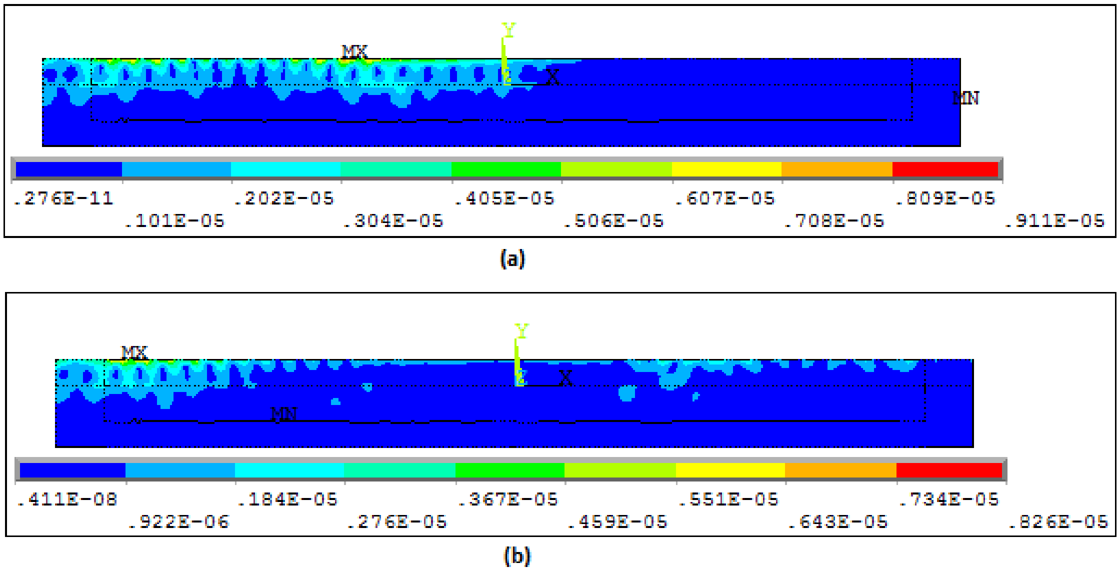

Image 19 – Wave propagation in sensor, top - at the beginning of deformation, bottom - at the end of deformation

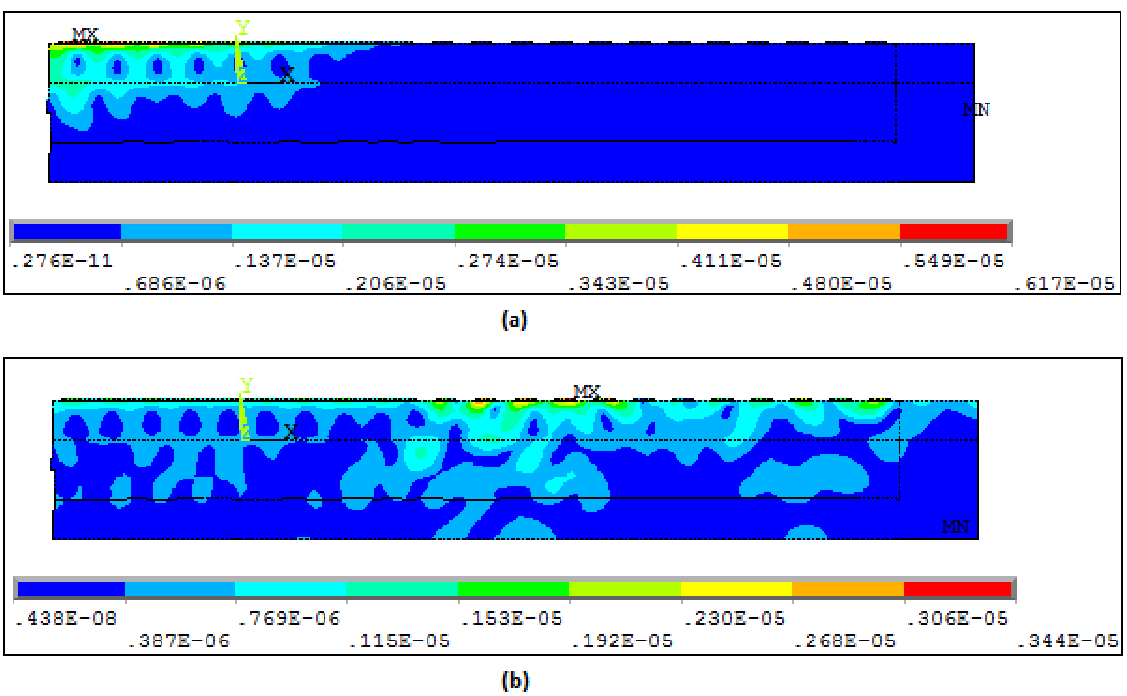

Image 20 – Wave propagation in sensor output part, top - at the beginning of deformation, bottom - at the end of deformation

Input and output electrical signal on IDT is shown in Image 7. As we can see from this figure, wave needs approximately 3.5 ns to propagate form input to the output IDT (red color).

Next analysis was performed with change of sensitive layer density. The change of density is set from 1% to 5% of original density of Palladium and this density change represents the process of chemical absorption in sensitive layer. The shift of wave is shown in Image 8. Detial of the wave shift is shown on the right side in Image 8.

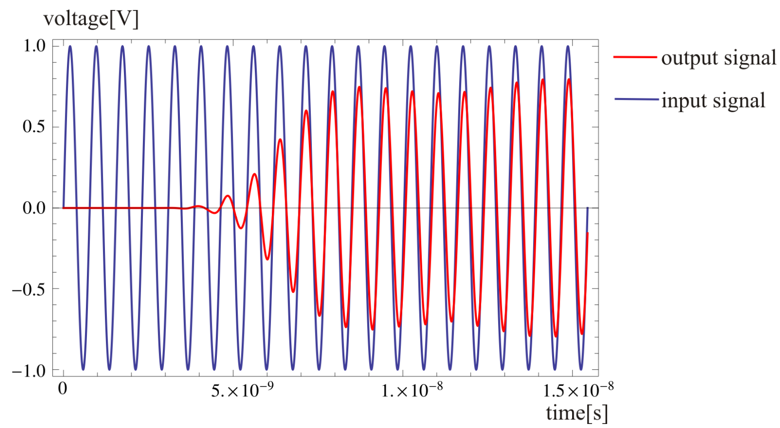

Image 21 – Signal at input and output IDT for original sensitive layer mass density

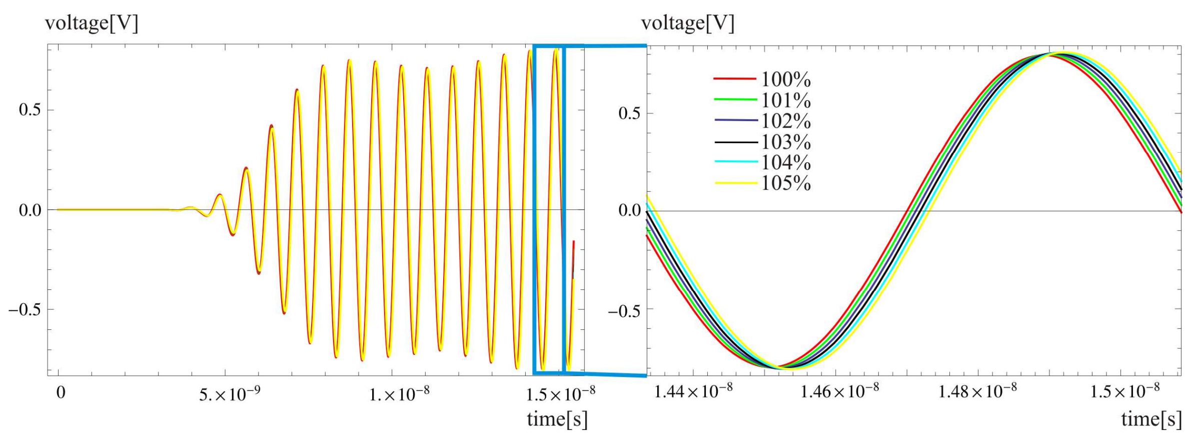

Image 22 – Output signal for different change of sensitive layer mass density

5 Conclusion

The paper deals with modeling and simulation of surface acoustic waves sensor using finite element method - FEM code ANSYS is used. Two different analysis types were performed - modal and transient. Only 2D model was considered in both analyses. Modal analysis is used to determine eigenfrequency of the system. The frequency determined by modal analysis is used as input frequency of electric signal in transient piezoelectric analysis. In transient analysis with harmonic loading wave propagation and the influence of sensitive layer density change is investigated.

References

ANSYS13.0 Help System, 2013.
BURNETT D.S., 1987. *Finite Element Analysis: From Concepts to Applications*, Addison Wesley Publishing Company, 844 pages. ISBN 0201108062.
DATTA S., 1986. *Surface Acoustic Wave Devices*, Prentice-Hall, 208 pages. ISBN 0138779112.
FRADEN J., 2003. *Handbook of modern sensors*, Springer, New York 678 pages. ISBN 1441964657.
MEYERS M.A., 1994. *Dynamic behavior of materials*, John Wiley & Sons. Ltd, Chichester, U. K., 688 pages. ISBN 047158262X.
NIMAL A. T. et al., 2006. A comparative analysis of one-port Colpitt and two-port Pierce SAW oscillators for DMMP vapour sensing. *Sensors and Actuators B Chemical*, 114, 316 316-325 pages. ISSN 0925-4005.

Acknowledgement
This work was supported in part by the following projects: Slovak Research and Development Agency under the contracts APVV-0450-10, Grant Agency KEGA - grant No. 015STU-4/2012 and VEGA No. 1/0534/12.

Contact address:
doc. Ing. Vladimír Kutiš, PhD.
Department of Applied Mechanics and Mechatronics, UEAE, FEI STU Bratislava, Ilkovičova 3, 81219 Bratislava, e-mail: vladimir.kutis@stuba.sk

SOLAR PANEL FOR PARKING SPOT – COUPLED CFD AND STRUCTURAL STUDY

JURAJ PAULECH, JAKUB JAKUBEC, VLADIMÍR KUTIŠ, EMIL MOJTO
Fakulta elektrotechniky a informatiky STU v Bratislave

Abstract: This contribution deals with coupled CFD-structural analysis of solar panel parking spot for electromobiles. Critical states of wind load on the construction will be studied.

Keywords: Solar panel, CFD, Structural analysis, Wind load, ANSYS

1 Introduction

This contribution deals with coupled CFD-structural analysis of solar panel for parking spot primary designed for electromobiles. As Solar panels are outdoor constructions they are extensively loaded by mechanical and thermal forces under various weather conditions. We will deal with critical states of wind load on the construction of solar panel parking spot in this paper.

2 Geometry specifications

Geometry of our model is based on real solar panel parking spot [1], see Image 23. Main dimensions of the parking spot are:

- length: $L = 3.8$ m
- width: $W = 5$ m
- height: $H = 3.2$ m

The parking spot is designed for two cars – especially electromobiles, due to possibility for charging the batteries during parking period.

Image 23 – Solar panel parking spot

Solar panel itself includes 12 solar cell units, its dimensions are length $l = 3.96$ m, width $w = 4.92$ m and thickness $t = 0.1$ m. Inclination of the panel is 18 degrees (detached to the horizontal plane). Solar panel was modeled as one continuous part considering some simplifications. Mechanical material properties of the solar panel were simplified according to fractions of individual components from that the panel consists of (solar cells, steel reinforcement, bottom metal cover and top transparent cover material, air), so artificial Young modulus of the solar panel was $E_{SP} = 3.5$ GPa, Poisson ratio $\nu_{SP} = 0.3$ and artificial density $\rho_{SP} = 350$kgm^{-3}.

Support for the solar panel is ensured by three main legs. These legs are made of thin-walled steel profile with thickness $t_{steel} = 0.01$ m. Mechanical properties of used steel are: Young modulus $E_{steel} = 210$ GPa, Poisson ratio $\nu_{steel} = 0.3$ and $\rho_{steel} = 7850$ kgm^{-3}.

Geometry of the solar panel for parking spot was created in software SolidWorks [2] and is shown in Image 24.

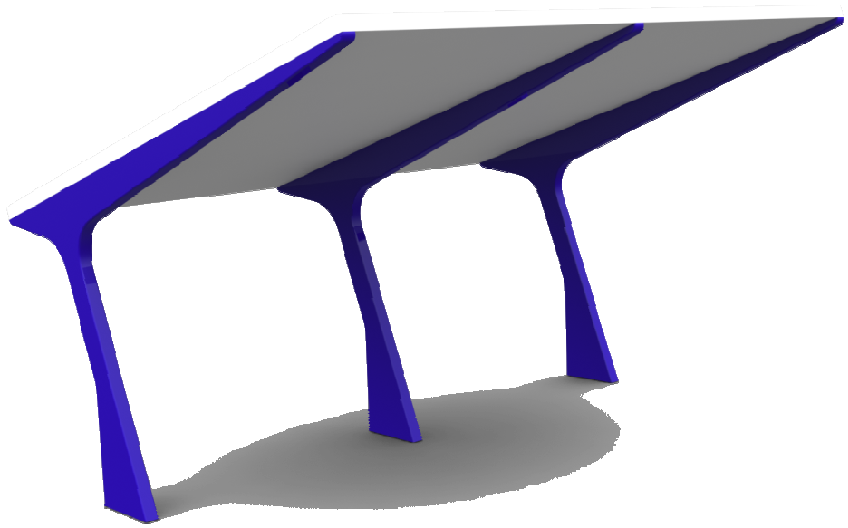

Image 24 – Geometry of the solar parking spot created in SW SolidWorks

3 Finite mesh of the model

We studied influence of direction and strength of the wind on our construction. Under these conditions, coupled CFD – structural analysis is needed. So we needed to create two different finite meshes: for CFD analysis of the air that flow off the solar panel parking spot, and structural mesh for the construction of the parking spot itself.

CFD mesh was created in software ANSYS ICEM CFD [3]. Air region was considered as a box with dimensions 50×25×15 m (length × width × height). As it is in all cases of CFD studies based on Finite Volume Elements (FVM) method, all near-wall regions were modeled in detail. The CFD mesh consists of more than 3.5 million elements. Detail of the mesh is shown in Image 25.

The construction of parking spot was meshed in ANSYS Workbench [3]. High number of solid elements was needed because of thin-walled profile of the construction and because of high demands on mesh quality in the regions where maximum mechanical stress are expected. Total number of solid elements for all three legs is more than 570 000. Detail of the construction's mesh is shown in Image 26.

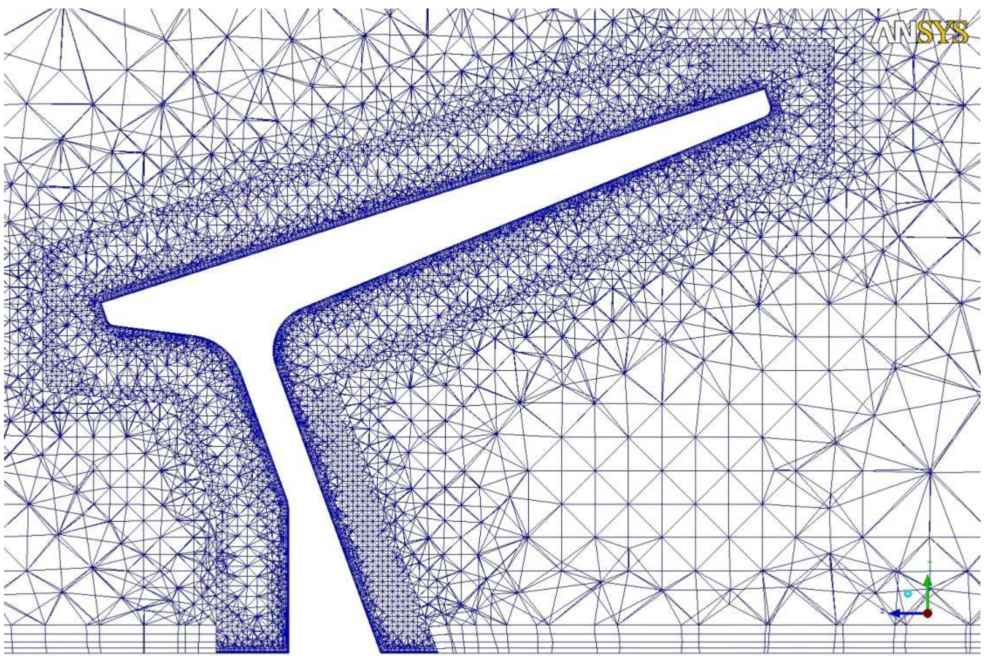

Image 25 – Detail of the mesh in air region

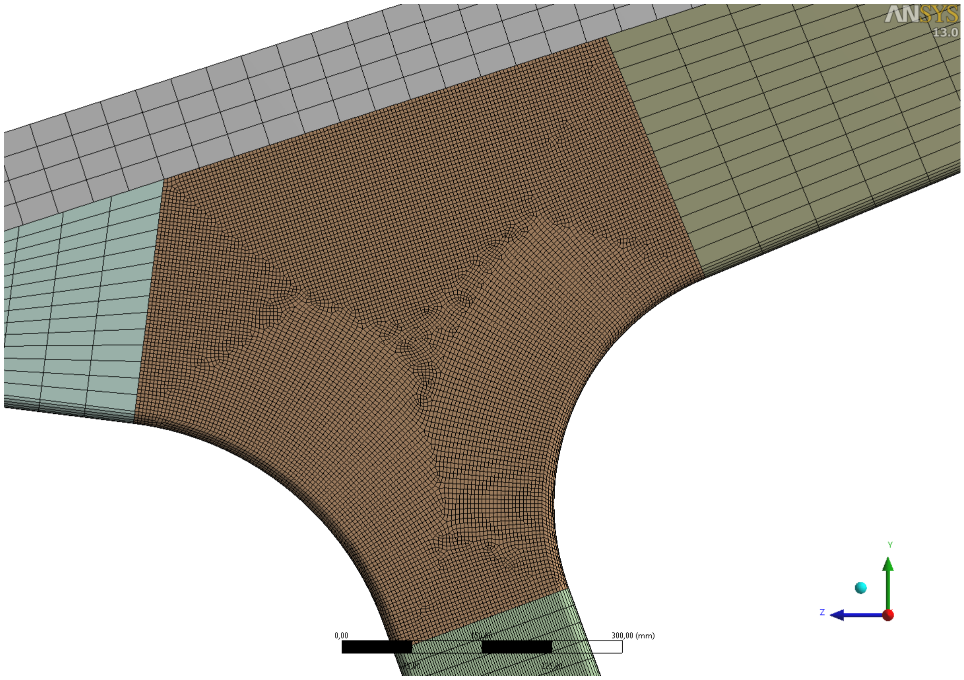

Image 26 – Detail of the construction's mesh

4 Boundary conditions of the model and solution process

The analysis was performed in ANSYS Workbench environment as one-way coupled CFD – structural analysis. The mesh of air region was interconnected with the structural mesh by general connection.

Two horizontal directions of the wind (case "A" and "B", wind direction is changed from inlet to outlet and vice versa, see Image 27) and two wind intensities were considered. So boundary conditions of the model were:

- wind intensity 1: $v_1 = 120$ kmh^{-1}
- wind intensity 2: $v_2 = 150$ kmh^{-1}

The construction was fixed to the ground. Effect of solar panel parking spot self-weight was also considered.

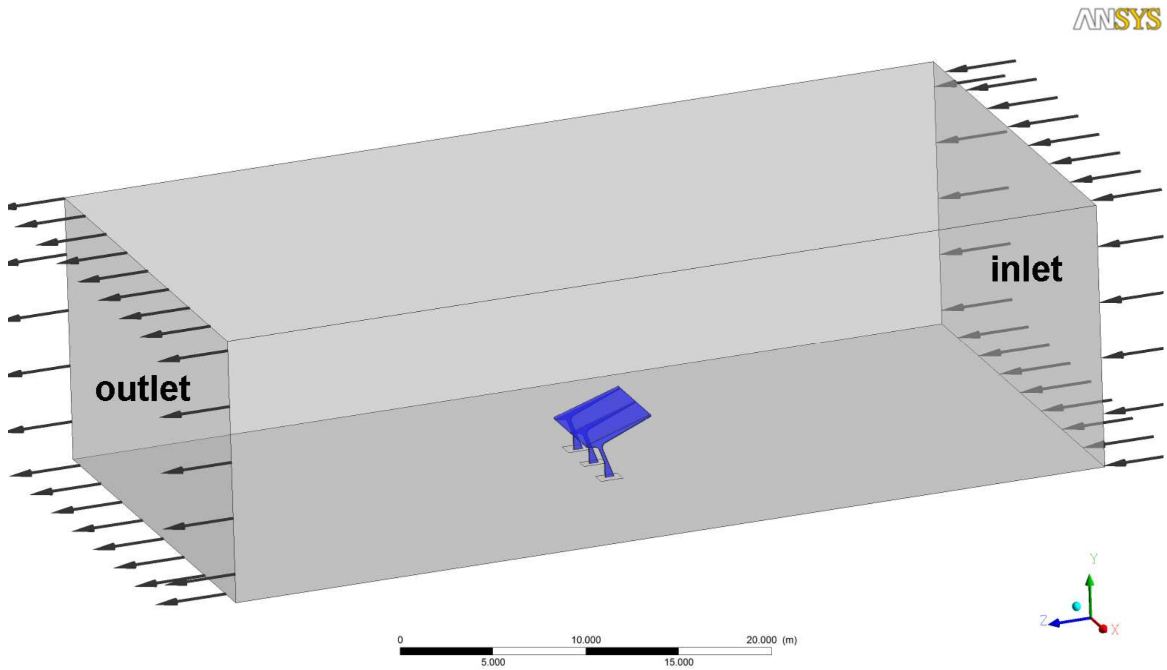

Image 27 – Boundary conditions of the model, case A of the wind direction

The task was solved using cluster computer: 15×CPU@4.0 GHz, 7 GB of RAM occupied, and solution of one case took 10 hours.

5 Obtained results

Results for mechanical deformation for individual load-cases are shown in Image 28. Image 29 shows results for mechanical stresses of the construction. Comparing the obtained results with the critical value for mechanical loading of used type of steel ($\sigma_{crit.} = 150$ MPa), we can see that the solar panel parking spot mechanically resists the applied wind loading. Wind speed around 150 kmh^{-1} can be considered as limiting value under our climatic conditions.

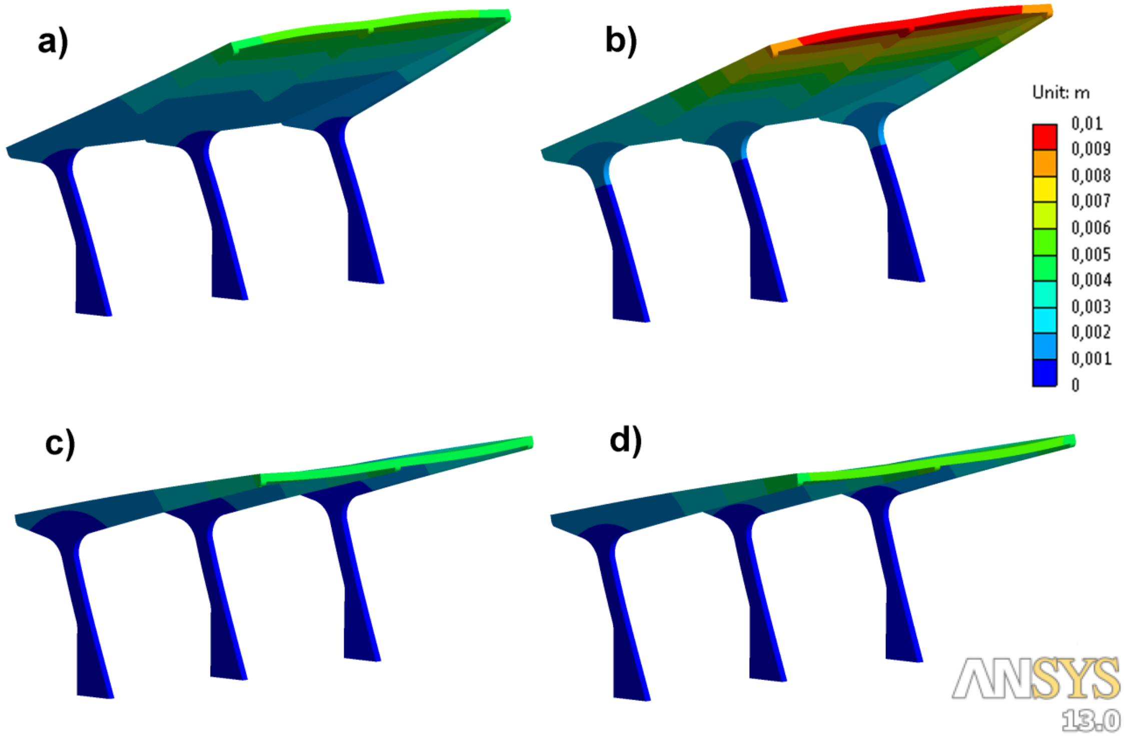

Image 28 – Deformation for a) case A, 120 kmh^{-1} b) case A, 150 kmh^{-1} c) case B, 120 kmh^{-1} d) case B, 150 kmh^{-1}

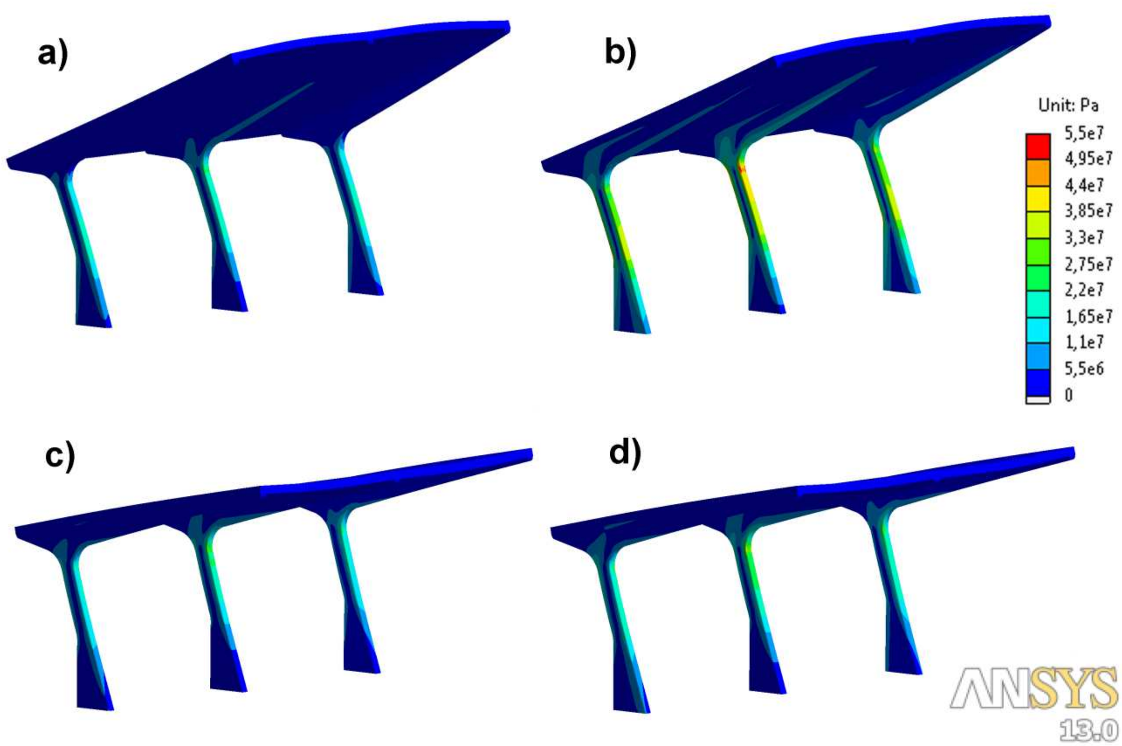

Image 29 – Mechanical stress for a) case A, 120 kmh^{-1} b) case A, 150 kmh^{-1} c) case B, 120 kmh^{-1} d) case B, 150 kmh^{-1}

1 Conclusion

In this paper there was presented one-way coupled CFD – structural computer analysis of the solar panel parking spot under critical wind loading. Direction of the wind and wind intensity were studied. Influence of construction's self-weight was included. Obtained results show that construction of the solar panel parking spot resists the critical wind loading for all considered load cases.

References

[1] Infinite Energy: Electroport, Kinslea Works, Kingston Road, Leatherhead, Surrey. KT22 7LE. UK.

[2] Dassault Systèmes SolidWorks Corp, Waltham, Massachusetts, USA.

[3] ANSYS Swanson Analysis System, Inc., 201 Johnson Road, Houston, PA 15342/1300, USA.

Acknowledgement

- This work was supported by Grant Agency VEGA, project No. 1/0534/12.
- This work was supported by Slovak Research and Development Agency under the contracts APVV-0450-10
- This work was supported by Grant Agency KEGA, project No. 015STU-4/2012.
- This contribution is the result of the project implementation: Finalization of infrastructure of the National Centre for Research and Application of Renewable Energy Sources (ITMS: 26240120028), supported by the Research & Development Operational Programme funded by the ERDF.

Contact address:

Ing. Juraj Paulech
Fakulta elektrotechniky a informatiky STU v Bratislave, Ilkovičova 3, 812 19 Bratislava, Slovakia

Ing. Jakub Jakubec
Fakulta elektrotechniky a informatiky STU v Bratislave, Ilkovičova 3, 812 19 Bratislava, Slovakia

doc. Ing. Vladimír Kutiš, PhD.
Fakulta elektrotechniky a informatiky STU v Bratislave, Ilkovičova 3, 812 19 Bratislava, Slovakia

Ing. Emil Mojto
Fakulta elektrotechniky a informatiky STU v Bratislave, Ilkovičova 3, 812 19 Bratislava, Slovakia

SIMULATION OF MOTORCYCLE HELMET IMPACT BY ECE 22-05

JAN POPL, JAN VYČICHL, MICHAL MICKA, JITKA JÍROVÁ

Czech Technical University in Prague, Faculty of Transport Sciences,
Department of Mechanics and Materials

Abstract: The aim of this work was to develop a numerical model of motorcycle helmet simulating the impact of motorcycle helmet to the planar surce at different angles. A 3D handheld scanner was created to obtain the geometrical model of motorcycle helmet. The MKP model was created from the geometric model in ANSYS ICEM CFD. Material properties to this model were assigned in the LS-PrePost. Simulation of drop test was realised in LS-DYNA solver. The problems of motorcycle helmets testing in Europe is adjusted by the ECE 22-05 standard. The standard primarily determines how to make drop tests. This project was performed within the scope of the institutional research plan, identification code MSM6840770043 and Grant of Czech Technical University, Student's Grant Competition SGS 12/163/OHK2/2T/16.

Keywords: motorcycle helmet, 3D scanner, MKP model, LS-DYNA, droptest, simulation

2 Introduction

Testing of motorcycle helmets by experiments is very expensive. Therefore, in the process of motorcycle helmets development and innovation numerical modeling is suitable. Use the finite element method represents one of the possibilities. Numerical modeling allows tests that cannot be performed by any experiment.

This work is based on creation of a motorcycle helmet geometric model and a head scale model. The model was used at the drop test simulation by help of the LS-Dyna software. In terms of geometry, the model had to match a real motorcycle helmet as perfectly as possible. For maximization the model accuracy t3D scanning by the hand-held 3D scanner was used. The boundary conditions and material properties were assigned to the model by the FEM software. The model was developed and solved in the LS-PREPOST application. The analysis was carried out by the LS-Dyna software.

The aim was to obtain the acceleration of the headform gravity headform. HIC factors were determined by the acceleration values. The simulation drop test was performed in several versions with different angles of the impact pads.

6.7 ECE 22-05 standard

The ECE 22-05 standard is the most widely used standard in the world. Standard does not define any motorcycle helmets production procedure. The standard specifies the test methods and parameters that motorcycle helmets must fulfill. The standard specifies the exact test procedure for the drop test. The helmet is attached to a dummy head. A headform with the attached helmet is inserted into the falling dart. The helmet is dropped on the pad from height of 2.85 meters. The accelerometer measures the resulting acceleration of the headform during impact. The accelerometer must be located in the head gravity center. According to the standard, the resultant acceleration must not exceed the value of 275 G. The drop test simulation was performed according to the criteria specified in the Standard.

6.8 HIC – Head Injury Criteria

Creation of one head injury criterion for different skull and brain dynamic properties is a very difficult job. Brain and skull injuries are very diverse. There are several criteria for a head injury evaluation. For this work there was selected the HIC criterion. The HIC criterion is based on acceleration absorbed by a human head. The HIC criterion seems to be very suitable for evaluating the results of this work.

Calculation of the HIC criteria is performed according to the equation (1). The result is determined by the size acceleration and action duration. The limited value of max HIC=1860 at which fatality most probably occurs was determined on the tests basis.

$$HIC = \left\{(t_2 - t_1)[\frac{1}{(t_2-t_1)}\int_{t_1}^{t_2} a(t)dt]^{2.5}\right\} max, \qquad (1)$$

In Equation (1) t1 indicates the beginning and t2 indicates end of the interval. In this interval, the HIC reaches its maximum. The value of a (t) is the resultant acceleration expressed in "g".

3 Creation of model

The numerical model of the motorcycle helmet drop test consists of three main parts: motorcycle helmet volumetric model , headform model rigid surface model, and impact plate flat rigid surface model. The rigid headform surface model was created from a solid headform model used in previous works. As a template for the helmet model, we used a helmet with the thermoplastic shell whose inner part was made of polystyrene foam (EPS). The helmet geometric model was created by 3D scanning with help of the VIU-scan hand-held scanner. The plate on which the helmet crashed during the tests was created in the LS-PREPOST application.

a. Making headform model

At creation of the headform geometric model we worked with the existing model used by the Department K618. The headform model was made according to the ČSN EN 960 standard addressing the issue of headforms for protective helmets testing. The used headform model and headf size-copy are shown in Fig. 4.

Fig. 4. Geometric headform model and head size-copy

b. Motorcycle helmet modelling

The motorcycle helmets geometric model basis was created by 3D scanning with the handy scanner. The VIU-scan handheld laser scanner was used. This technology allows touchless 3D scanning. This scanner allows relative movement of the scanner and a scanned object during scanning process. Further, the model was modified in several applications up to the final application form.

While scanning, the helmet was covered with positional targets allowing the scanner spatial orientation. The Fig. 2. depicts the motorcycle helmet covered with all targets and the model during scanning.

Fig. 2. Motorcycle helmet, model during scanning process

The scanned model was saved under *.stl file format. Fine errors during scanning were modified in the Blender application. The adjusted geometric model was loaded into the ANSYS ICEM CFD application. ANSYS ICEM CFD is very suitable for creating of FEM mesh models obtained from various CAD software or *.stl files. A network was set up on a geometrical model. We obtained a *.k (k-file) that was opened in the LS-PREPOST application and then it became a part of the source code in the LS-DYNA solver. In the LS-PREPOST, the volumetric FEM helmet model was assigned with material properties of polystyrene foam (Tab. 2). The shell was formed with the thickness of 3 mm on the outer model surface. The material properties of thermoplastic foam (Tab.2) were assigned to the shell. Both parts of helmet are non-contact and form one body. For illustration, they are shown separately in Fig. 3.

Tab. 2. Used materials properties

the inner part of helmet (foam) EPS		outer part of the helmet (shell) ABS	
Yioung's modulus	62,73 MPa	Yioung's modulus	3 Gpa
density	85 kg/m3	density	1040 kg/m3
Poisson's ratio	0,01	Poisson's ratio	0,4
maximum tensile stress	1,3 MPa	Yield stress	60 MPa
Damping coefficient	0,2	ultimate strength	70 MPa

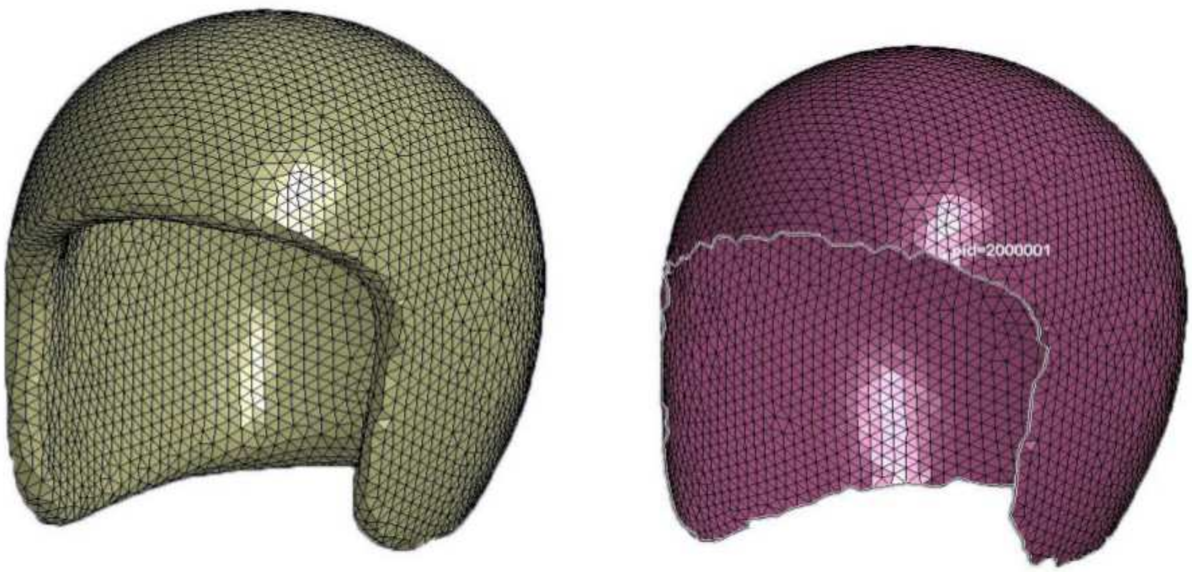

Obr. 3. Outer and inner helmet parts

c. Model compilating in LS-PrePost

For the drop test the non-deformable rigid base in the LS-PREPOST was created. At the rigid plate, all degrees of freedom (rotations and shifts) were fixed. The model was assembled in the LS-PREPOST application. The helmet was mounted on the headform so that it may correspond to reality (Fig.5) The headform with the helmet was placed above the impact pad.

4 Simulation

Fall simulations were carried out in several variants. The impact on the flat surface was simulated as the first. Further, another falls were simulated on the pad turned at the angles of 15 and 30 degrees to the helmet face and of 15 and 30 degrees to the helmet nape (Fig. 6). The last simulated falls were performed on the pad turned by 15 and 30 degrees to one side to the temple (Fig. 7). The rotation was performed only in left side because the model is symmetrical and the results would be identical.

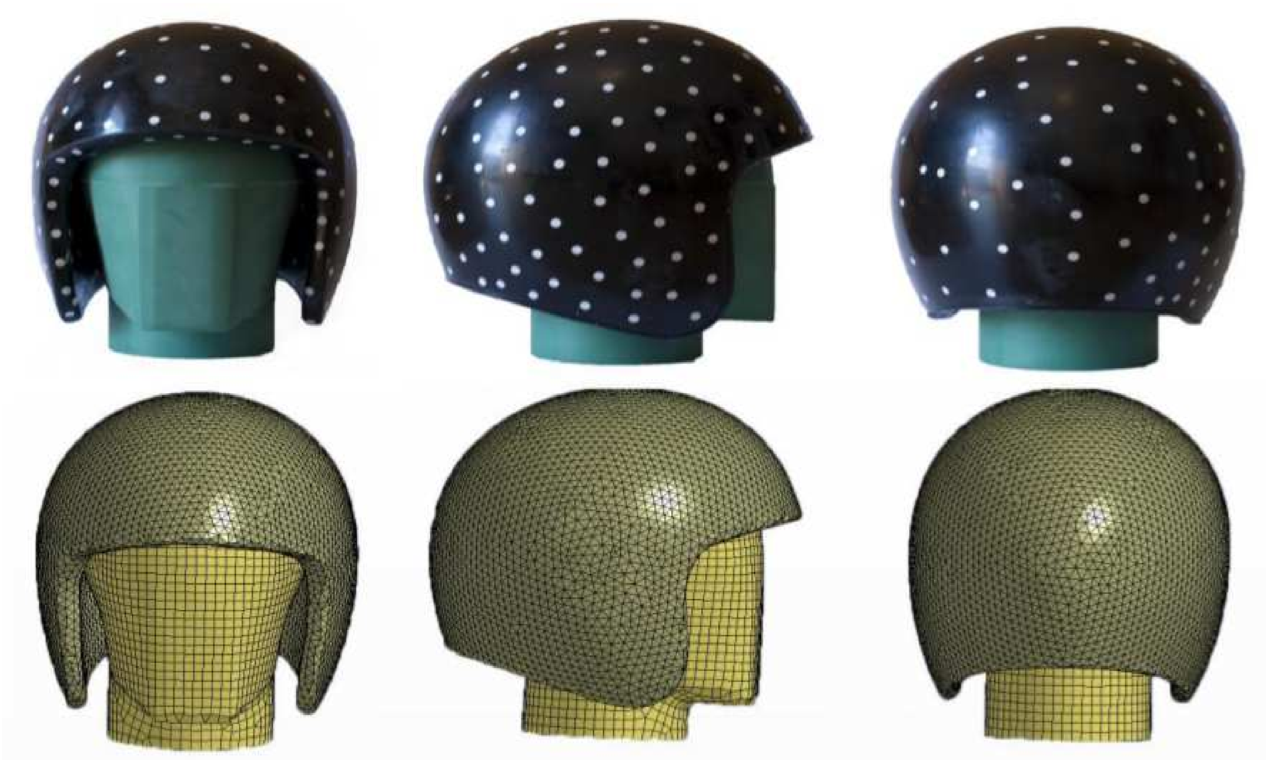

Fig. 5 Set-up model and real situation

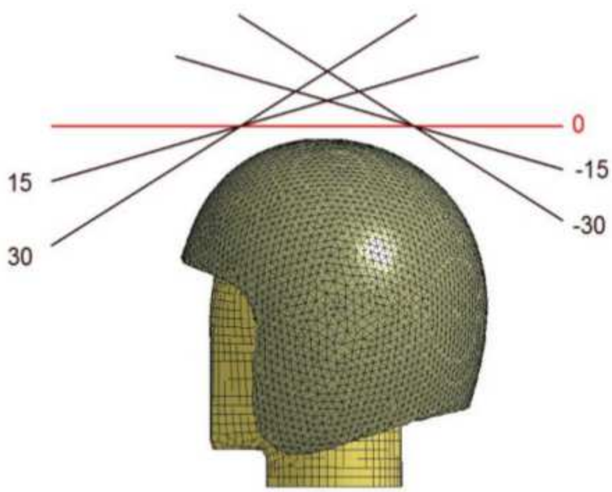

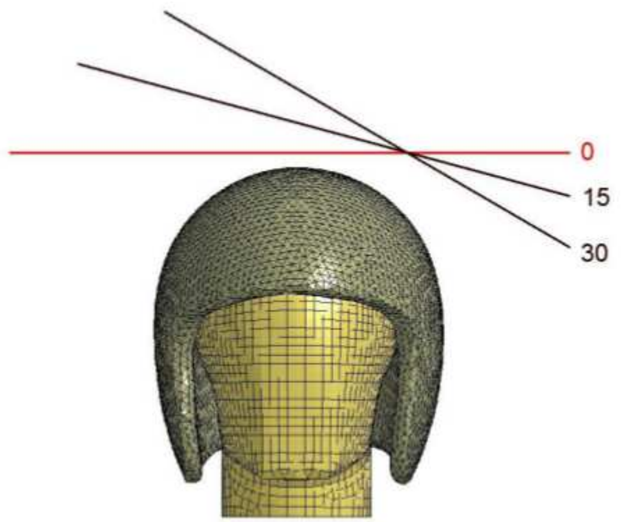

Fig. 6. Impact pad turning angles Fig. 7. Impact pad turning angles

According to the standard, the helmet hits the surface from the height of 2.85 m. From the physical equations the impact velocity of 7.5 m/s was determined. The impact speed was assigned to the headform model and motorcycle helmet model.

The acceleometr is located in the headform gravity center during the drop test. A reference point was created in the model for corresponding with the headform gravity center. The acceleration was measured in the gravity center . This acceleration was measured within the

time periods of 0.001 seconds
General contacts of the Automat c type – Surface to Surface – were defined on the system. The first contact was defined between the headform and helmet while the second one between the helmet and impact plate.

5 Results

The results were obtained after the simulation in solver LS-DYNA. LS-DYNA provides many types of advanced analysis of the results and their software modifications. The helmet fall to the pad was paced at the period of 0.2 ms with total of 42 steps. The picture enclosure 1 shows the loading shells progress. Three selected steps before the point of maximum acceleration condition, maximum acceleration state, and three selected steps after maximum acceleration are shown. The maximum tension is reached at the contact surface between the model helmets and impact plate. The maximum voltage value is 6.04 MPa. On the picture enclosure 2., seven-step course load inside of the helmet are shown. Again, the maximum tension was reached between the model helmets and impact plate. Its value was 2.13 MPa.

a. Impact on horizontal surface

The helmet model hit on the rigid horizontal surface by speed of 7.5 m/s. The velocity and acceleration courses were measured at the headform model gravity center. The HIC factor was determined according to the procedure specified by the manufacturer shown in Graph 1.

Graph 1. HIC 36

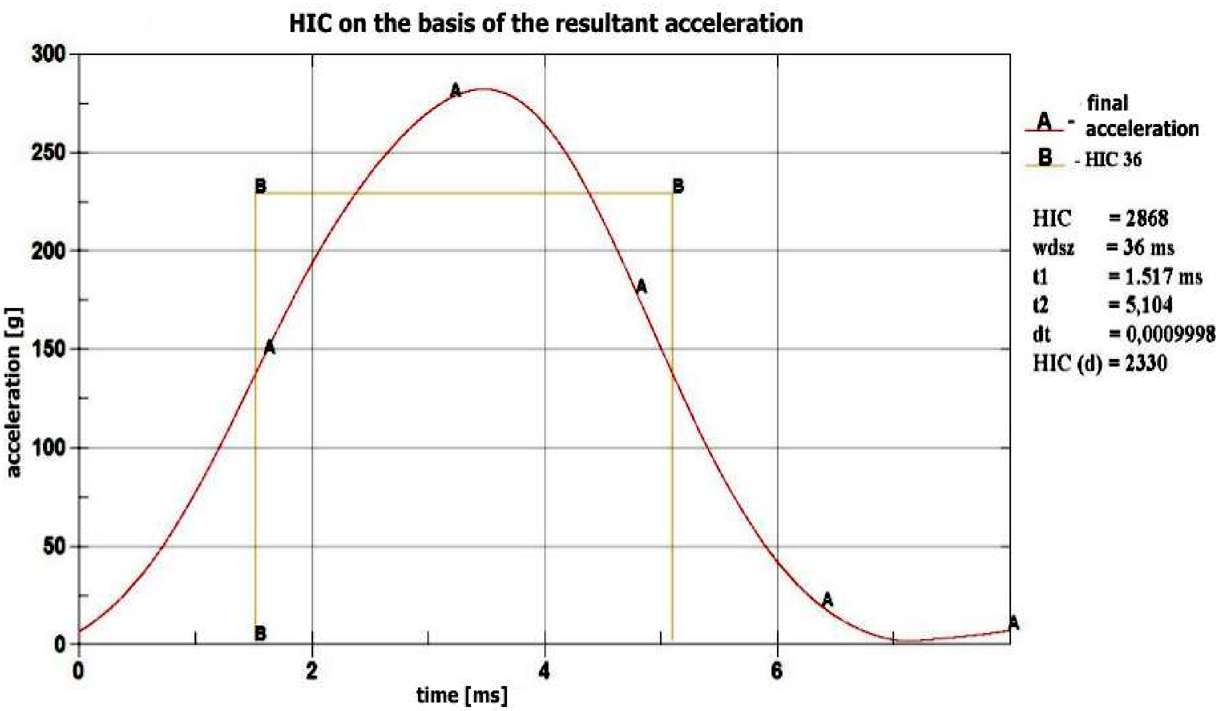

The HIC 36 factor was used. The HIC36 calculation factor is performed in the range of 36 ms. This range is positioned on the time axis so that the HIC may become as high as possible of the whole process. Graph 1., shows the resultant acceleration course and surface representing the resulting HIC 36. The legend contains more important information to the HIC 36 criterion. Maximum stress on shell and on inert part are shown at Fig. 8.

b. Impact to rotated pads

Fall simulations to the turned pad were made similarly as the falls to the horizontal surface. The falls on the turned pad verified different acceleration values acting on the headform at different incidence angles. The supreme acceleration value was achieved at the impact on the horizontal surface. The individual HIC values are shown in Table 3.

Tab. 3. individual HIC values

HIC factors for impact to rotation pad (by Fig. 6.)	
rotation angle [°]	HIC [-]
-30	1440
-15	2018
0	2330
15	2028
30	1443
HIC factors for impact to rotation pad (by Fig. 7.)	
rotation angle [°]	HIC [-]
0	2330
15	2101
30	1553

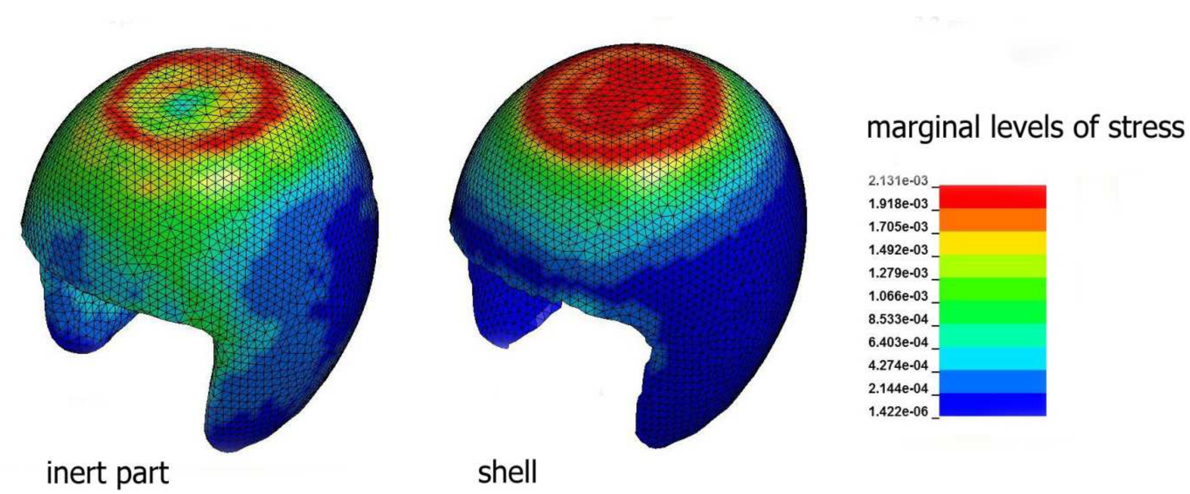

Fig. 8. max. stress on inert part and on shell

1 E

valuation

The work successfully validated the methodology of modeling motorcycle helmets. Procedures for drop test simulations were verified. Value of the resultant acceleration were obtained for several types of impact. Size of criteria HIC were determined from the measured acceleration values. The results show that, the helmet does not comply requirements of the standard. This finding was expected. The construction of helmet is an old type. At the time of manufacture that helmet was different evaluation criteria of safety. To verify the results, would be useful to realized drop test. Continuation of the work is planned. Simulation on new types of helmets will be made. On new types of helmets will be realized drop tests. It is planned to create a proven methodology for testing motorcycle helmets in the future.

References

ČSN EN 960 (2007), Makety hlavy pro zkoušení ochraných přileb
HELMET TEST ECE 25-05 (2005), Motorcycle helmet Safety Standard, U.N. Economic commission for Europe
MICKA M., JÍRA J., JÍROVÁ J., (2010), Modelování pádové zkoušky helmy v ANSYS LS-DYNA, In: ANSYS Users meetinng, 2010
MICKA M., VYČICHL J., (2007), Tvorba modelu přilby z 3D skenování. In: ANSYS Users meetinng, 2007
Tutorial 6. LS-PrePost, Livermore Software Technology Corporation, 2007

Contact address:

Bc. Jan Popl
Czech Technical University in Prague, Faculty of Transport Sciences, Department of Mechanics and Materials, Na Florenci 25, 110 00 Praha 1

ZTRATA STABILITY OCELOVÉ KONSTRUKCE

ZDENĚK PORUBA, JAN SZWEDA
VŠB – Technická univerzita Ostrava

Abstract: The presented contribution deals and describes the possibilities of linear and nonlinear stability loss simulation of steel structure loaded by its weight in addition with bending moment caused by climatic events. The commonly used approach for linear stability loss simulation, i.e. without assumption of initial imperfections, is presented. Subsequently, the simulation of nonlinear stability loss with assumption of imperfections resulting from linear stability loss analysis is introduced. Both presented approaches are compared and their results are presented in the final phase.

Keywords: stability loss, finite element method, bucling, non-linear analysis

1 Úvod

Pří posuzování spolehlivosti a bezpečnosti provozu ocelové konstrukce má posouzení konstrukce na ztrátu stability nezanedbatelný význam. Tento význam je umocněn u vysokých štíhlých konstrukcí, u nichž namáhání vlastní tíhou v kombinaci s přídavným ohybem od klimatických vlivů dává předpoklady pro kolaps konstrukce právě ztrátou stability.

Obvyklým způsobem posouzení konstrukce na ztrátu stability je provedení postupu předepsaného normou. Tento postup předpokládá analýzu ztráty stability s uvážením geometrických a výrobních nepřesností, jejichž zanesení do výpočtového modelu je pro obecně zaměřené výpočtové programy velice komplikované. Předložený příspěvek prezentuje postup posouzení ztráty stability ocelové konstrukce pomocí buckling analyzy pro ideální geometrii a pomocí navazující nelineární analýzy pro výchozí geometrii s uvážením imperfekce v podobě deformace dle výsledků předchozí analýzy buckling.

2 MKP řešení

K řešení úlohy ztráty stability lze z pohledu MKP přistoupit několika způsoby: výchozí geometrie+lineární analýza ztráty stability (linear buckling), výchozí geometrie+nelineární statická analýzá a nebo geometrie upravená o imperfekce+nelineární statická analýza.

2.1 Analýza lineární ztráty stability

Řešení úlohy ztráty stability tvaru vychází z rovnic rovnováhy vnějších a vnitřních sil s uvážením deformací, které tyto silové účinky vyvolají. Za předpokladů malých deformací, lineárního materiálového modelu a absence osttaních zdrojů nelinearit, např. kontaktní páry, vede tato úloha na řešení problému vlastních čísel dle vztahu

$$(\mathbf{K} + \lambda_i \cdot \mathbf{S}) \cdot \psi_i = \mathbf{o}\,, \tag{7}$$

kde **K** značí matici tuhosti, **S** značí matici geometrické tuhosti, ψ_i značí tvar deformace a Λ_i značí násobitel účinků způsobeného geometrickou maticí tuhostí (ANSYS, 2013). Význam veličiny Λ je ovlivněn způsobem, jakým byla získána matice geometrické tuhosti, tzn. je-li matice geometrické tuhosti získána pro návrhové zatížení konstrukce, pak násobitel Λ má význam koeficientu bezpečnosti lineárního vzpěru vůči tomuto zatěžovacímu stavu. Výhodou této analýzy je relativně jednoduchý postup a jednoduchá interpretace výsledků, zatímco nevýhodou je skutečnost, že výsledky jsou získány pro silně idealizovaný modelový stav exploatace konstrukce, tj. obvykle riziko ztráty stability tvaru podhodnocují.

2.2 Nelineární analýza ztráty stability

Nevýhody lineární analýzy ztráty stability jsou přirozeně odstraněny provedením nelineární statické analýzy nastavené tak, aby byla zjištěna maximální přetížení konstrukce, při kterém nastane její selhání. Tato analýza je řešená dle rovnice statické rovnováhy vnitřních a vnějších sil s uvážením nelinearit, zejména geometrické a materiálové, ale případně také nelinerity z titulu kontaktních párů. MKP rovnice řešené úlohy lze zapsat ve tvaru

$$\mathbf{K}(\mathbf{u}) \cdot \mathbf{u} = \mathbf{f}(\mathbf{u})\,, \tag{8}$$

kde $\mathbf{K}(\mathbf{u})$ značí matici tuhosti závislou na hodnotě okamžité deformace, **u** značí vektor deformačních parametrů a $\mathbf{f}(\mathbf{u})$ značí zatěžující účinky obecně závislé na hodnotě okamžité deformace (ANSYS, 2013). Tato analýza zahrnuje vlivy požadovaných nelineárních vlastností chování konstrukce a dovoluje také zahrnout simulaci počátečních imperfekcí, např. úpravou geometrie na základě výsledků předcházející analýzy. Nevýhoda tohoto druhu analýzy je způsob zatěžování konstrukce a způsob následného vyhodnocení ztráty stability. Nabízí se dvě varinaty, a to deformační zatěžování nebo zatěžování silové. U deformačního zatěžování je konstrukci vnucován způsob, tvar kolapsu ovšem okamžik tohoto kolapsu je poměrně dobře zjistitelný např. z průběhu reakční síly. U silového zatěžování je výhodou možnost ovlivnění poměru silových účinků, které kolaps způsobí a současně není ovlivňován tvar kolapsu konstrukce, ovšem podstatnou nevýhodou je fakt, že za okamžik kolapsu je považován stav, kdy Newton-Raphsonův iterční proces řešení nelineární rovnice (2) diverguje.

2.3 Realizovaný MKP postup řešení

Realizována analýza ztráty stability byla provedená etapovitě, kdy jednotlivé etapy na sebe navazovaly sdílením výsledků s cílem ověřit vliv nelineárního chování konstrukce a vliv uvážení počáteční imperfekce geometrie modelu.

Linenární analýza ztráty stability navázaná na statickou analýzu pro plnou kombinaci návrhového zatížení konstrukce. Výsledkem je koeficient bezpečnosti vůči uvažovanému zatížení, ale také tvar ztráty stability.

Nelineární analýza ztráty stability pro výpočtovou geometrii zohledňující imperfekci v podobě výsledku deformace ztráty stability z předchozí analýzy. Zatěžování je provedeno silově s předem zvolenou kombinaci přetížení dílčích zatěžovacích účinků.

Postup realizace a analýza získaných výsledků v prostředí ANSYS Workbench jsou prezentovány v další části příspěvku.

3 Lineární ztráta stability

Tato kapitola popisuje postup výpočtů pro analýzu lineární ztráty stability.

3.1 Výpočtový model

Geometrický model byl vytvořen na základě výkresové dokumentace konstrukce a je vyobrazen na obr. 1. Kromě samotné konstrukce komínu zahrnuje model i část potrubí, které na komín navazuje v jeho dolní části. Důvodem zahrnutí tohoto uzlu je jeho předpokládaný velký vliv na chování konstrukce při analýze ztráty. Vliv zbylé části tohoto potrubí bude nahrazen vhodnou okrajovou podmínkou popsanou v další části příspěvku. Celá geometrie byla vytvořena jako tenkostěnná konstrukce, kdy tloušťka jednotlivých dílů bude ve výpočtu uvažována jako parametr. Geometrie byla doplněna o plochy potřebné pro aplikování okrajových podmínek.

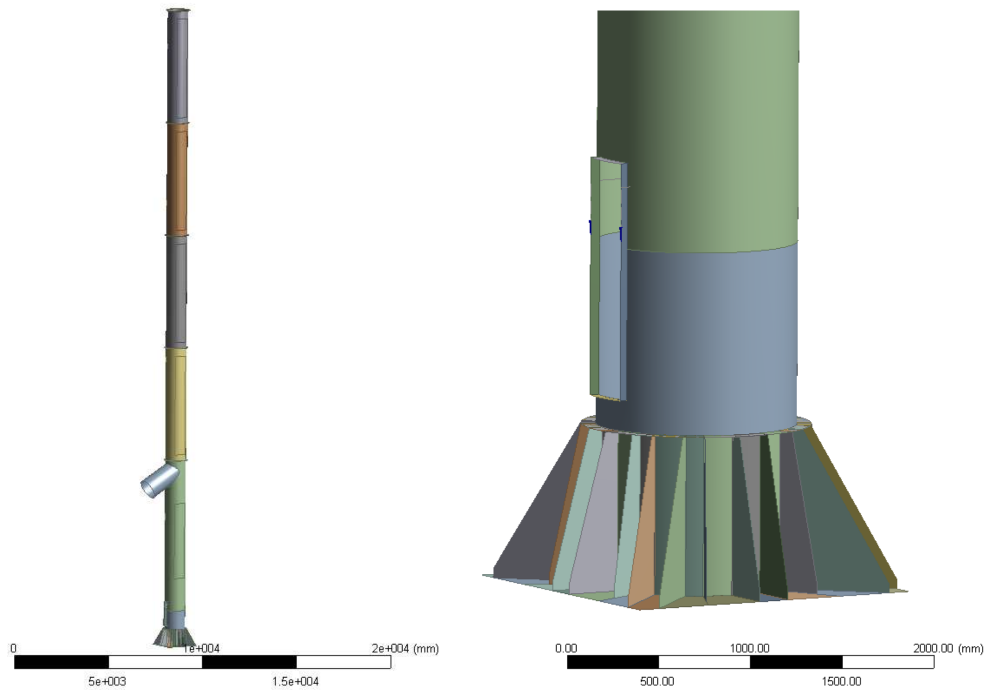

Obrázek 30 – Geometrie konstrukce: celek (vlevo), detail patky (vpravo)

Konečnoprvkový model pro lineární stabilitní výpočet (bez imperfekcí) byl vytvořen z geometrie popsané v předcházejícím kroku. Byla vytvořena konečnoprvková struktura obsahující 27739 uzlů 27484 skořepinových elementů a je vyobrazena na obr. 2.

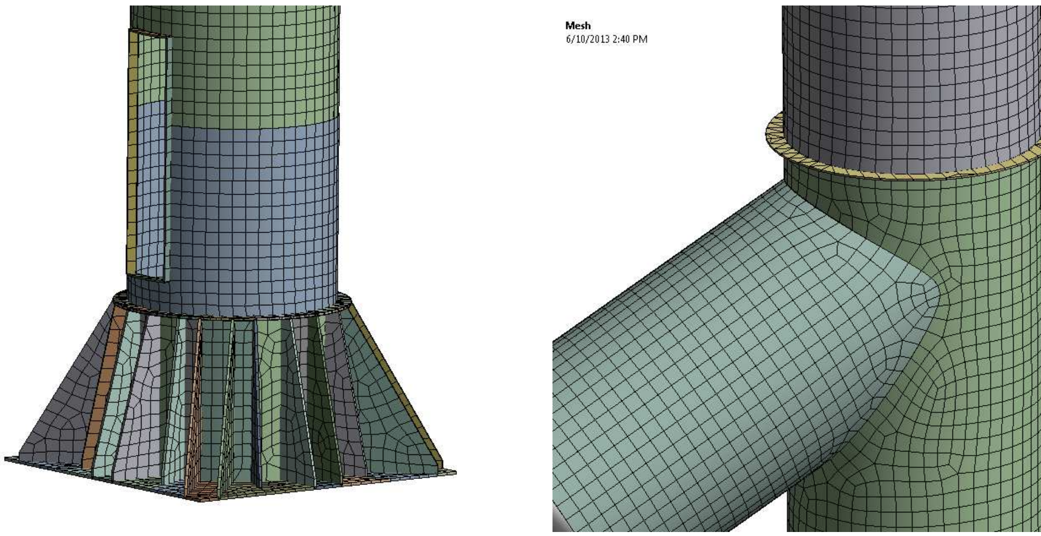

Obrázek 31 – MKP síť: detail patky (vlevo), detail přípoje potrubí (vpravo)

Materiálem uvažované ocelové konstrukce je běžná konstrukční ocel. Byly uvažovány následující (lineární) materiálové vlastnosti: modul pružnosti v tahu $E = 2.1e5$ MPa a Poissonovo číslo $\mu = 0,3$.

3.2 Okrajové podmínky a zatížení

Prvním krokem při výpočtu lineární ztráty stability je lineární statická analýza zatížené konstrukce. Výsledky provedené lineární statické analýzy tvoří vstupní hodnoty (předpětí) pro samotnou analýzu ztráty stability. Oba jmenované typy na sebe bezprostředně navazují a sdílejí tyto okrajové podmínky a zatížení:

Tíhové zrychlení - na celou konstrukci byl aplikován vliv tíhového zrychlení ve svislém směru o velikosti $g = 9,81\ \mathrm{m \cdot s^{-2}}$,

Celá ocelová konstrukce je reálně uchycena šrouby k podložce, v konečnoprvkovém modelu je na spodním okraji konstrukce znemožněn pohyb ve směru všech tří souřadnicových os. Aplikovaná okrajová podmínka je na obr. 3,

Zatížení větrem – hodnoty zatížení větrem jsou specifikovány normou ČSN EN 1991-1-4. Hodnoty zatížení určené dle zmíněné normy byly přepočítány na sílu ve směru větru, která byla dále aplikována na předem vytvořené plochy na jednotlivých segmentech ocelové konstrukce. Hodnoty sil byly určeny takto: segment A: 3000 N, segment B: 2800 N, segment C: 2600 N, segment D: 2300 N. Poslední (nejnižší) segment není větrem zatížen, jelikož je umístěn uvnitř budovy výrobní haly. Zatížení větrem je znázorněno na obr. 4,

Zahrnutí hmotnosti inspekčního žebříku – téměř po celé výšce ocelové konstrukce je na její vnější straně umístěn inspekční žebřík o nezanedbatelné hmotnosti. Jeho vliv je konečnoprvkovém modelu zahrnut umístěním hmotných bodů v místě těžiště žebříku. Jednotlivé hmotné body jsou matematicky svázány s plochami na jednotlivých segmentech, které zároveň slouží k aplikaci sil představujících zatížení větrem. Poloha hmotných bodů je patrná rovněž z obr. 4,

Vliv přívodního potrubí v dolní části konstrukce – v dolní části ocelové konstrukce komínu je nutné uvážit vliv tuhosti přívodního potrubí. Ze známé geometrie přívodního potrubí (světlost, tloušťka stěny, délka, materiálové vlastnosti) byly analyticky dopočteny tuhosti potrubí v radiálním a axiálním směru. V místě ukončení ponechané přívodní části byly následně vytvořeny tři pružiny (2 v radiálním směru a 1 v axiálním směru) o vypočítaných tuhostech. Umístění vytvořených pružin je na obr. 5.

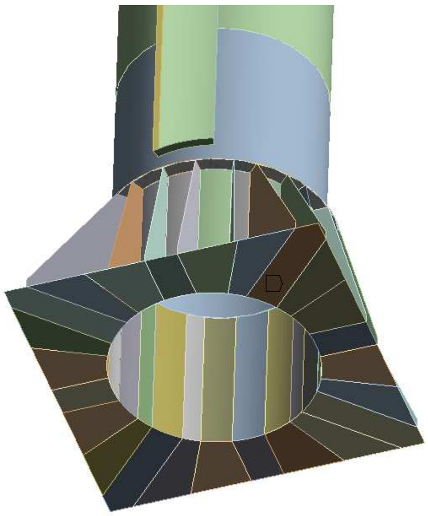

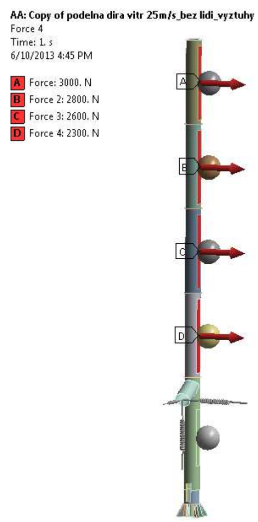

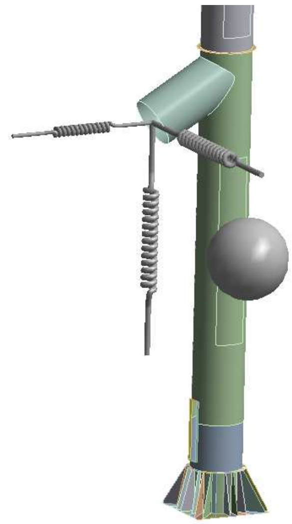

Obrázek 32 – Vetknutí na podstavě Obrázek 33 – Zatížení větrem Obrázek 34 – Vliv potrubí

3.3 Výpočtové analýzy pro simulaci lineární ztráty stability

Jak již bylo zmíněno, je analýza pro simulaci lineární ztráty stability tvaru prováděna ve dvou krocích – lineární statický výpočet (předpětí) a vlastní výpočet lineární ztráty stability tvaru. Lineární statický výpočet byl proveden z důvodů nepřítomností nelinearit proveden v jednom výpočetním kroku. Následná analýza lineární ztráty stability tvaru byla provedena s uvážením výsledků předcházející statické analýzy s cílem zjistit koeficient zatížení pro lineární ztrátu stability tvaru.

Výsledky lineární statické simulace jako vstupních hodnot pro výpočet lineární ztráty stability jsou na obr. 6. Výsledek simulace lineární ztráty stability je na obr. 7. Z vypočtených hodnot je zřejmý součinitel lineární ztráty stability tvaru roven hodnotě 20 a tvar, který u této ztráty stability nastane.

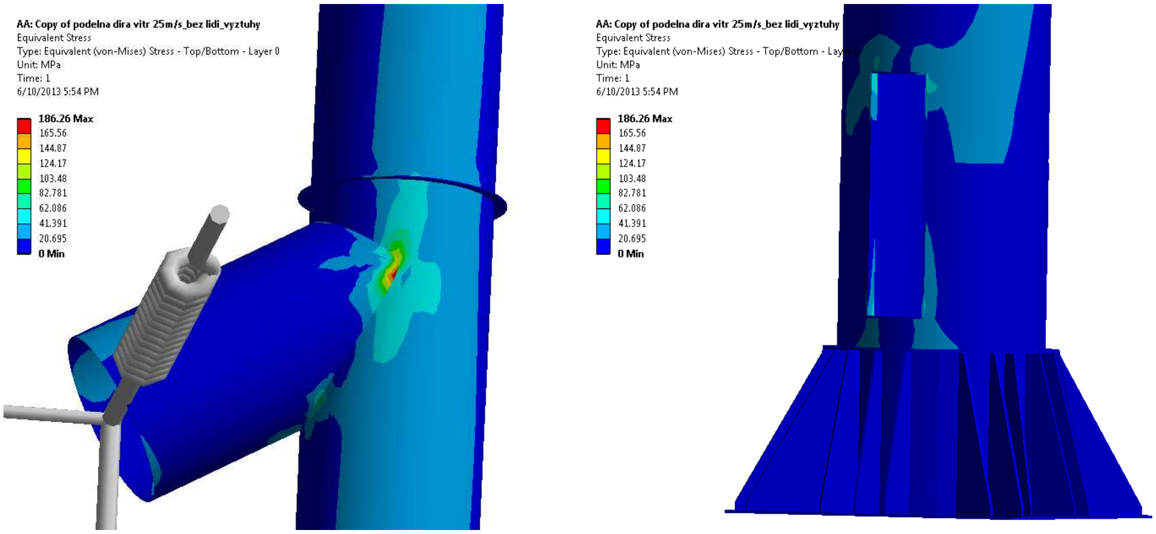

Obrázek 35 - Rozložení redukovaného napětí dle HMH v nejvíce exponovaných místech

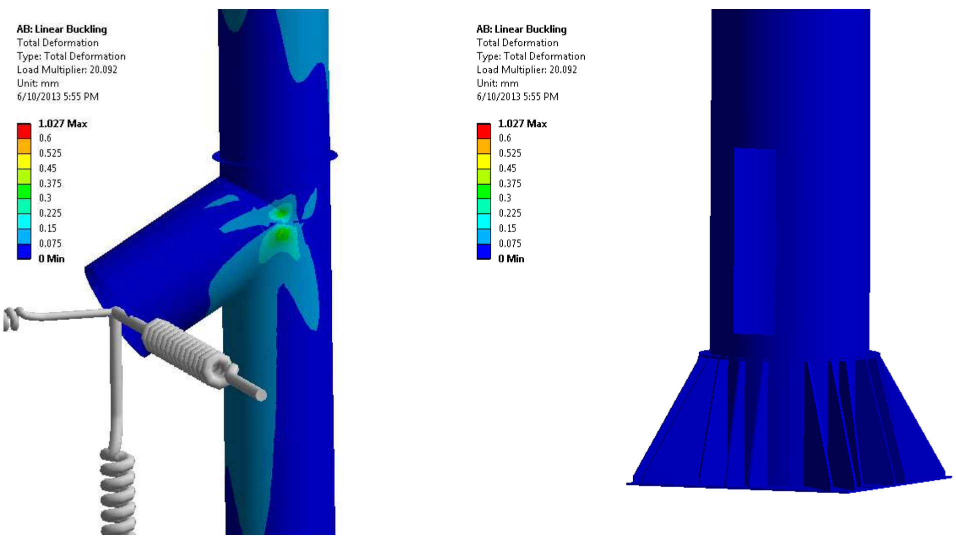

Obrázek 36 - Pole deformací a součinitel zatížení jako výsledek simulace lineární ztráty stability

4 Nelineární ztráta stability

Tato kapitola popisuje postup výpočtů pro řešení nelineární ztráty stability.

4.1 Výpočtový model

Pro případ simulace nelineární ztráty stability tvaru byla geometrie výpočtového modelu upravena na základě výsledků simulace lineární ztráty stability tvaru. V nové statické analýze byla pomocí příkazu „UPGEOM“ vytvořena geometrie reflektující tvar odpovídající lineární ztrátě stability tvaru. Srovnání původní a nově vytvořené geometrie je na obr. 8.

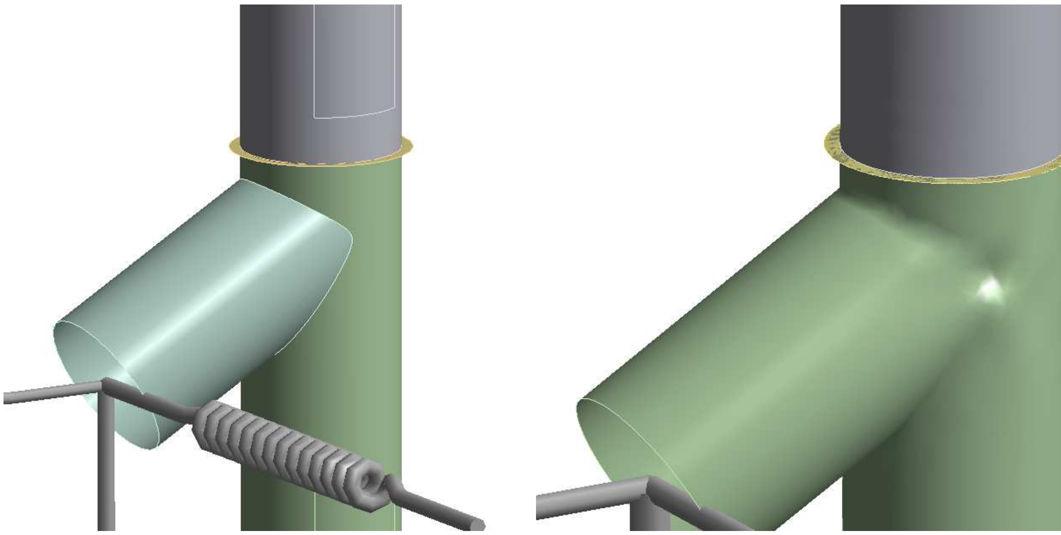

Obrázek 37 - Původní a nově vytvořená geometrie pro výpočet nelineární ztráty stability

Konečnoprvkový model pro lineární stabilitní výpočet (bez imperfekcí) byl vytvořen z geometrie popsané v předcházejícím kroku. Byla vytvořena konečnoprvková struktura obsahující 27739 uzlů 27484 skořepinových elementů a je vyobrazena na obr. 9.

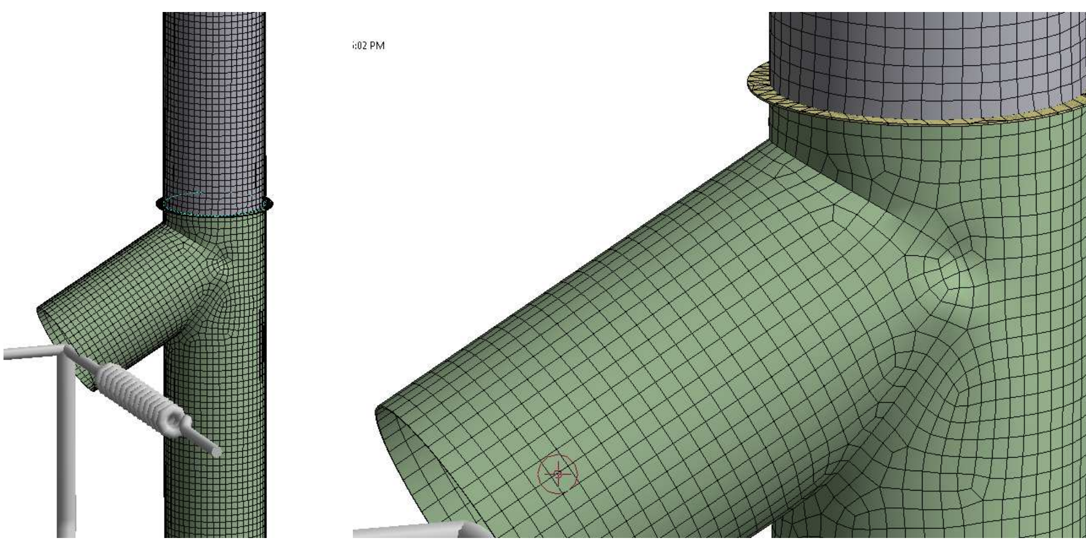

Obrázek 38 - Konečnoprvková síť po úpravě geometrie

Materiálem uvažované ocelové konstrukce je běžná konstrukční ocel. Byly uvažovány následující materiálové vlastnosti: modul pružnosti v tahu E = 2.1e5 MPa a Poissonovo číslo μ = 0,3. a bilineární materiálový model s tečným modulem E_T = 1e4 MPa.

4.2 Okrajové podmínky

V případě simulace nelineární ztráty stability tvaru byly okrajové podmínky obdobné jako v případě lineární ztráty stability tvaru. Na základě výsledků předchozí simulace bylo jako dominantní vyhodnoceno zatížení silou větru. Velikost tohoto zatížení byla pro případ simulace nelineární ztráty stability tvaru vynásobena součinitelem zatížení pro lineární ztrátu stability tvaru, tedy dvacetkrát. Zadané okrajové podmínky jsou následující:

Tíhové zrychlení - na celou konstrukci byl aplikován vliv tíhového zrychlení ve svislém směru o velikosti g = 9,81 $m \cdot s^{-2}$,

Celá ocelová konstrukce je reálně uchycena šrouby k podložce, v konečnoprvkovém modelu je na spodním okraji konstrukce znemožněn pohyb ve směru všech tří souřadnicových os,

Zatížení větrem – hodnoty zatížení větrem jsou specifikovány normou ČSN EN 1991-1-4. Hodnoty zatížení určené dle zmíněné normy byly přepočítány na sílu ve směru větru, která byla dále aplikována na předem vytvořené plochy na jednotlivých segmentech ocelové konstrukce a vynásobena součinitelem zatížení pro lineární ztrátu stability tvaru. Hodnoty sil byly určeny takto: segment A: 60 000 N, segment B: 56 000 N, segment C: 52 000 N, segment D: 46 000 N. Poslední (nejnižší) segment není větrem zatížen, jelikož je umístěn uvnitř budovy výrobní haly,

Zahrnutí hmotnosti inspekčního žebříku – téměř po celé výšce ocelové konstrukce je na její vnější straně umístěn inspekční žebřík o nezanedbatelné hmotnosti. Jeho vliv je konečnoprvkovém modelu zahrnut umístěním hmotných bodů v místě těžiště žebříku. Jednotlivé hmotné body jsou matematicky svázány s plochami na jednotlivých segmentech, které zároveň slouží k aplikaci sil představujících zatížení větrem,

Vliv přívodního potrubí v dolní části konstrukce – v dolní části ocelové konstrukce komínu je nutné uvážit vliv tuhosti přívodního potrubí. Ze známé geometrie přívodního potrubí (světlost, tloušťka stěny, délka, materiálové vlastnosti) byly analyticky dopočteny tuhosti potrubí v radiálním a axiálním směru. V místě ukončení ponechané přívodní části byly následně vytvořeny tři pružiny (2 v radiálním směru a 1 v axiálním směru) o vypočítaných tuhostech.

4.3 Výpočtové analýzy pro simulaci nelineární ztráty stability

Analýza pro simulaci lineární ztráty stability tvaru byla rovněž prováděna jako statická. Na rozdíl od předchozí lineární analýzy byl použit bilineární materiálový model (viz výše) a výpočet s uvážením velkých deformací. Celý výpočtový běh byl rozdělen na 40 kroků – substepů. Okamžik ztráty stability tvaru byl následně uvažován jako moment, kdy dojde k divergenci celé úlohy. Vhodným rozdělením na jednotlivé substepy lze poté snadno určit násobitel původního zatížení pro nelineární ztrátu stability tvaru a srovnat výsledky lineární a nelineární simulace ztráty stability tvaru.

Jako výsledek ztráty stability tvaru byl označen okamžik, kdy dojde k divergenci simulace s uvážením materiálových i geometrických nelinearit, včetně imperfekcí. Jak je patrno z obr. 10, k divergenci úlohy dojde při dosažení 87 % aplikovaného (20 x navýšeného) zatížení. Vzhledem ke způsobu zatěžování v nelineární analýze ztráty stability, tj. přetížení aplikováno pouze na zatížení větrem, lze konstatovat, že při neměnných stálých zatíženích vykazuje konstrukce 17.4 násobnou bezpečnost vůči zatížení větru. Grafické znázornění deformace je patrné z obr. 11 a 12.

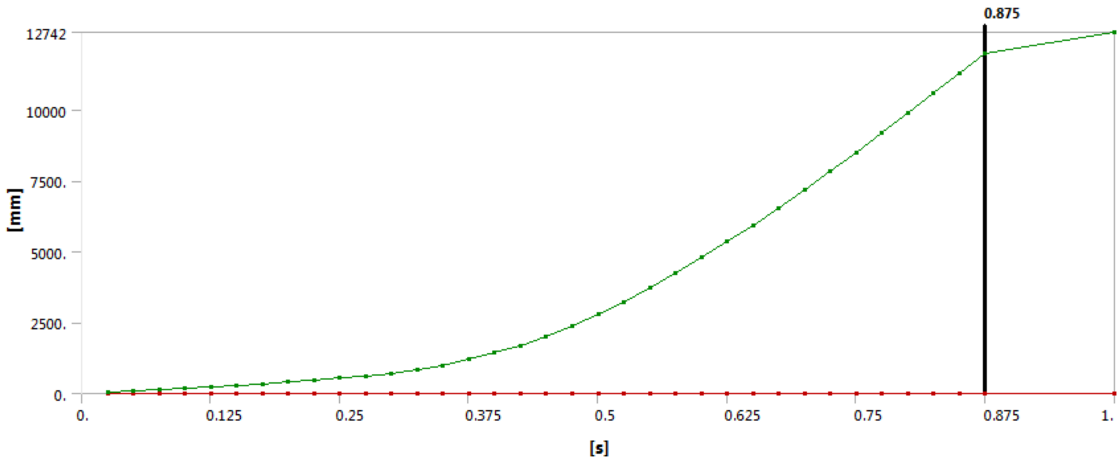

Obrázek 39 - Okamžik divergence úlohy – nelineární ztráta stability

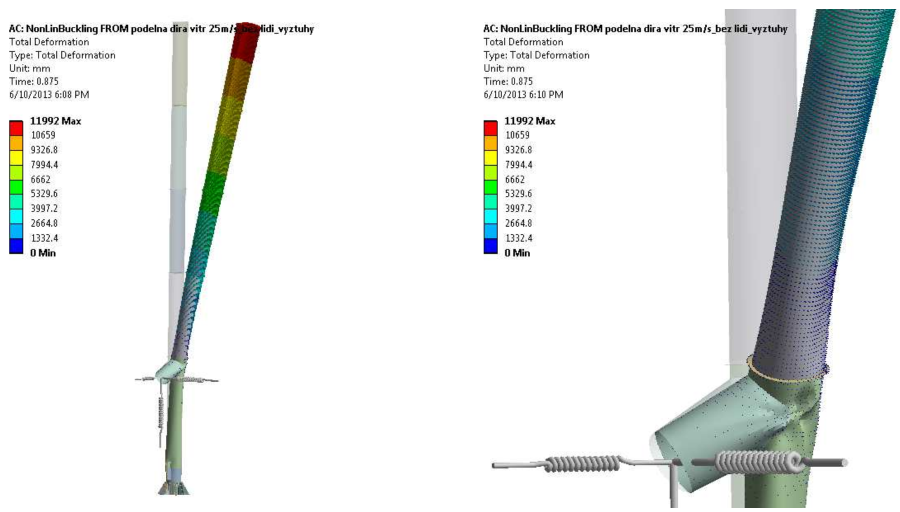

Obrázek 40 - Deformace při ztrátě stability tvaru

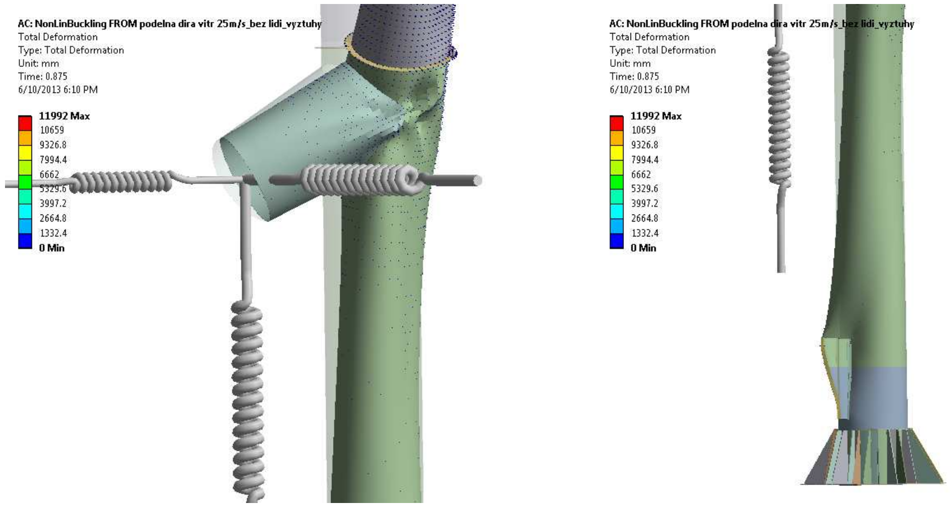

Obrázek 41 - Deformace při ztrátě stability tvaru

5 Závěr

Předložený článek prezentuje dva přístupy k řešení ztráty stability: lineární analýzyu ztráty stability a nelineární statickou analýzu s uvážením imperfekce dle výsledků deformace získané lineární analýzou ztráty stability. Předmětná problematika je řešená na jednoduché válcové ocelové konstrukci, pro níž bylo zatížení stanoveno na základě norem ČSN ISO.

Výsledkem lineární analýzy ztráty stability byla mimo jiné hodnota násobitele zatížení, která pro tuto analýzu činila 20. Navazující nelineární analýza ztráty stability byla realizována pro kombinaci zatížení, kde nejvíce nepříznivé zatížení (zatížení větrem) bylo násobeno získanou hodnotou násobitele zatížení. Následná analýza ukázala, že ke ztrátě stability na nelineárním modelu dojde při 87 % toho zatížení. Získaný výsledek nelineární analýzy je relativně blízko výsledku analýzy lineární, což dovoluje usuzovat na skutečnost, že uvážená imperfekce geometrie a plastické vlastnosti materiálu v tomto případě neovlivňují výrazně odolnost konstrukce na kolaps ztrátou stability.

Literatura

ANSYS, 2012. *ANSYS 14.5 Release Product Decumentation*, SAS IP, Inc.
V elektronické podobě dostupné jako součástí instalace programu ANSYS 14.5

Poděkování

Prezentovaná práce vznikla za finanční podpory Výzkumného záměru CEZ:J17/98:2724019 Ministerstva školství, mládeže a tělovýchovy ČR a výzkumného grantového projektu TA01010705 Technologické agentury ČR, za co srdečně děkujeme.

Kontaktní adresa:
Ing. Zdeněk Poruba, Ph.D., Ing. Jan Szweda, Ph.D.
17. listopadu 2172/15, 708 33 Ostrava-Poruba, Česká republika

ANALÝZA PONORENÝCH PILOT

ĽUBOMÍR PREKOP

Stavebná fakulta STU, Katedra stavebnej mechaniky

Abstract: The subject of this paper is the analysis and modeling of the buried piles. Analytical solution has been briefly described and the created model of the buried pile using the software ANSYS has been presented. The obtained results of displacements and stresses have been compared with the results of an analytical solution.

Keywords: Foundations, Pile, Nonlinear Analysis, FEM, ANSYS

2 Zakladanie na pilotách

Jednou z efektívnych metód zakladania na málo únosných podložiach je zakladanie na pilotách. Pri rýchlom rozvoji vrtnej techniky sa postupne zväčšujú aj priemery pilot, čím sa podstatne zvyšuje ich únosnosť a zároveň hospodárnosť.

Príspevok sa zaoberá výlučne účinkami vodorovne zaťažených pilot. Riešenie je závislé od zvoleného modelu piloty, od modelu podložia a vzájomnej interakcie piloty a podložia. Najčastejšie sa ohybom namáhané piloty vyšetrujú ako pružné prúty, spolupôsobiace s pružným a homogénnym podložím alebo po dĺžke pilot premenným podložím Winklerovho typu pri obojstrannej väzbe piloty a podložia. Winklerov model pomerne dobre popisuje prácu nesúdržných podloží. Neumožňuje však roznos zaťaženia v pôdnom masíve a vyšetrovanie tej istej piloty od iných účinkov. Iné účinky sú reprezentované najmä pôsobením zvislého zaťaženia, centricky pôsobiacimi silami alebo priťažením povrchu podložia v okolí piloty.

Aby sa odstránili nedostatky doteraz používaných modelov podložia a bolo možné vyšetrovať piloty od všetkých účinkov jednotným spôsobom, zaviedol sa model pružného polpriestoru. Použitie pružného polpriestoru pre ohybom namáhané piloty je možné v podstate dvomi spôsobmi:

- podložie sa chápe ako pružné a homogénne prostredie a pri vzájomnom účinku piloty a podložia sa vychýdza zo vzorcov *R.Mindlina*,
- použije sa model nehomogénneho podložia a kontaktná úloha piloty a podložia sa rieši pomocou metódy konečných prvkov.

V obidvoch prípadoch sa analýza vykonáva diskrétnymi metódami.

5.1 Ponorené piloty

Často používaným kotevným systémom pri zakladaní stavieb sú ponorené piloty. Tieto pomáhajú prenášať zemný tlak pôsobiaci na paženie do základovej pôdy. Uplatňujú sa hlavne pri kotvení štetovnicových, pilotových a podzemných stien do okolitého zemného masívu.

Ďalšími možnosťami použitia sú oporné a nábrežné múry, ochranné steny proti podomletiu, brehové opevnenia, vzdúvacie zariadenia lodných kotvíšť a podobne. Kotevný systém tvorí ťahadlo, ktoré je jedným koncom pripevnené o paženie a druhým koncom o kotviacu pilotu. Kotviaca pilota ponorená do podložia je v ľubovoľnom bode drieku namáhaná sústredenou silou (obrázok 1).

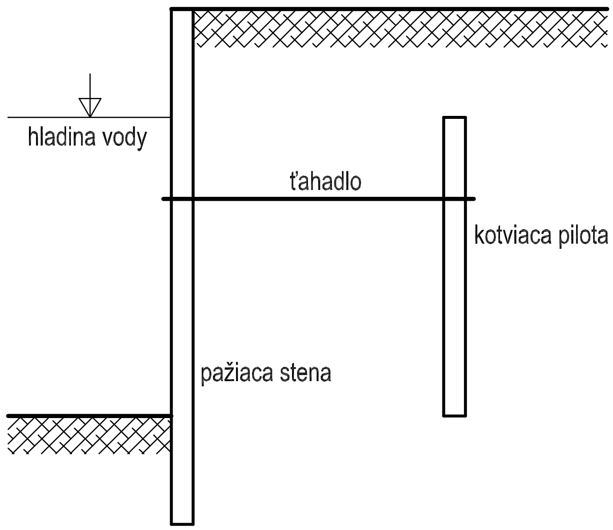

Obrázok 42 – Kotevný systém nábrežného paženia a ponorenej piloty

Úlohou je nájsť veľkosť a spôsob rozdelenia napätí na dotyku piloty a podložia tak, aby boli pod kontrolou dodatočné pretvorenia a vnútorné sily v pilote. Hlava ponorených pilot je zvyčajne voľná a päta môže byť podľa spôsobu uloženia voľná, kĺbovo podopretá alebo dokonale votknutá. Otázkam ponorených pilot je v literatúre venovaná pomerne malá pozornosť. Ideový postup riešenia vypracoval *B.N.Žemočkin* a prvé konkrétnme riešenie podzemných kotiev situovaných horizontálne s rovinou ohraničujúcou polpriestor pochádza od *D.J.Douglasa* a *E.H.Davisa*.

Príspevok sa pridržiava upraveného Žemočkinovho postupu. Pritom sa predpokladá, že podložie predstavuje prostredie, ktoré opisujú rovnice pre Boussinesquov polpriestor.

5.2 Pilota v hlave aj v päte voľná

Hlava piloty ponorenej v polpriestore, ktorá je v hlave aj v päte úplne voľná, sa nachádza v hĺbke h pod rovinou, ohraničujúcou okraj polpriestoru. Pilota je v ľubovoľnom bode drieku zaťažená sústredenou silou P. Neznáme dotykové napätia sa určia z podmienok rovnováhy piloty ako celku a z deformačnej podmienky piloty a podložia. Podrobný popis analytického riešenia je uvedený v (Kollár P., Mistríková Z., 1987).

3 Model ponorenej piloty

Model ponorenej piloty namáhanej ohybom bol vytvorený v programe ANSYS a následne boli dosiahnuté výsledky porovnané s analytickým riešením. Riešenie bolo vykonané na pilote s dĺžkou l=6,0 m. Pilota mala priemer $\varnothing$=370 mm, Youngov modul pružnosti $E_p = 2{,}1.10^7$ kPa a bola ponorená pod povrchom terénu do hĺbky h=2,0 m. Sústredená sila, reprezentujúca silu v ťahadle pôsobila vo vzdialenosti 2,0 m od hlavy piloty. Vo výpočte boli použité tri rôzne druhy podložia s nasledujúcimi deformačnými modulmi E_z = 1000 kPa (model

A), E_z = 5000 kPa (model B) a E_z = 50 000 kPa (model C), Poissonovo číslo μ_z = 0,35. Zaťažovacia schéma a rozmery modelovanej piloty sú na obrázku 2.

Bol vytvorený priestorový model ponorenej piloty. Na modelovanie piloty bol použitý prvok SOLID65, okolitý zemný masív bol vytvorený pomocou prvkov SOLID45 a kontakt typu plocha–plocha pomocou kontaktných prvkov TARGE170 a CONTA173.

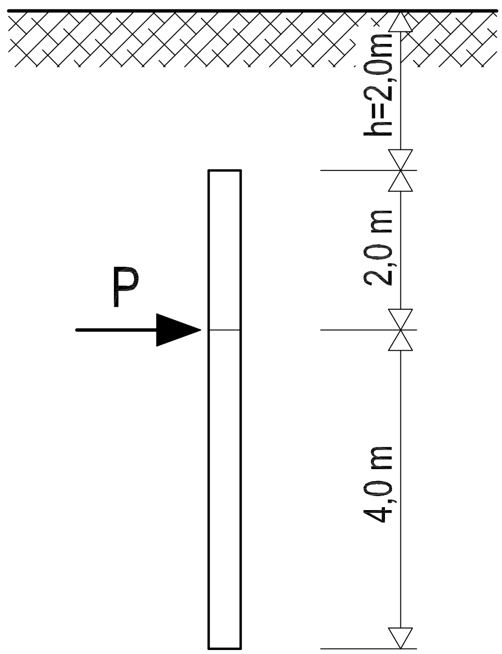

Obrázok 2 – Ponorená pilota, rozmery a zaťaženie

Priebeh priehybov po výške piloty je znázornený na nasledujúcich obrázkoch.

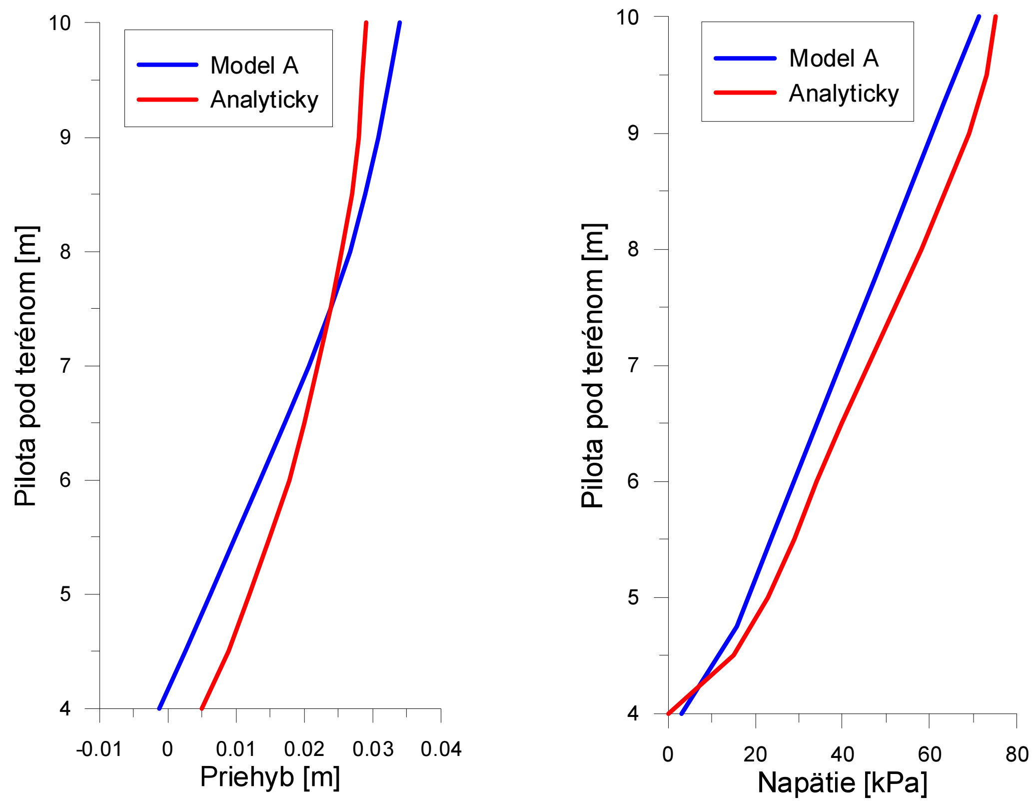

Obrázok 3 – Model A – priehyby a kontaktné napätia

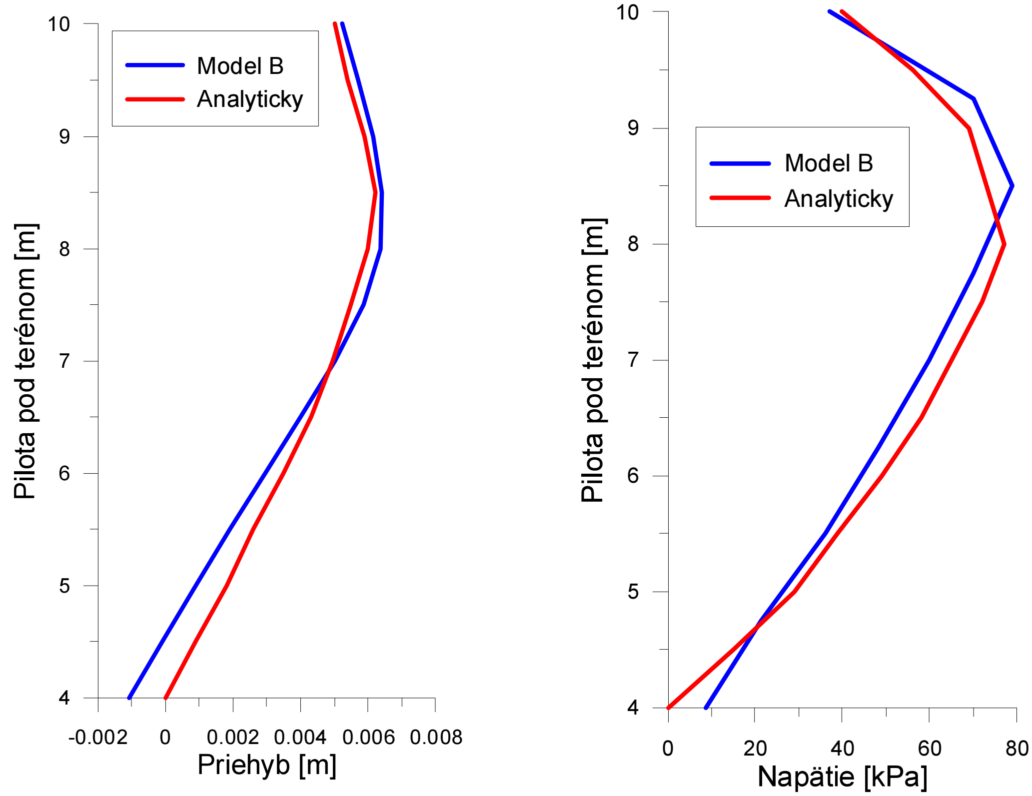

Obrázok 4 – Model B – priehyby a kontaktné napätia

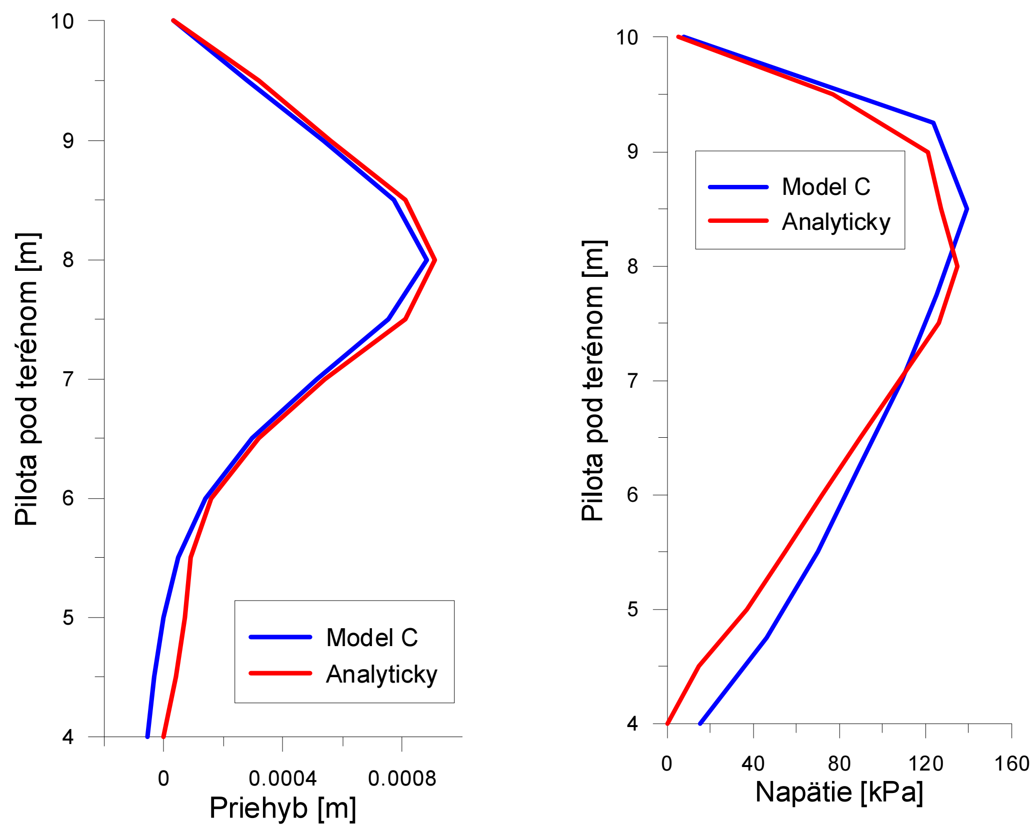

Obrázok 5 – Model C – priehyby a kontaktné napätia

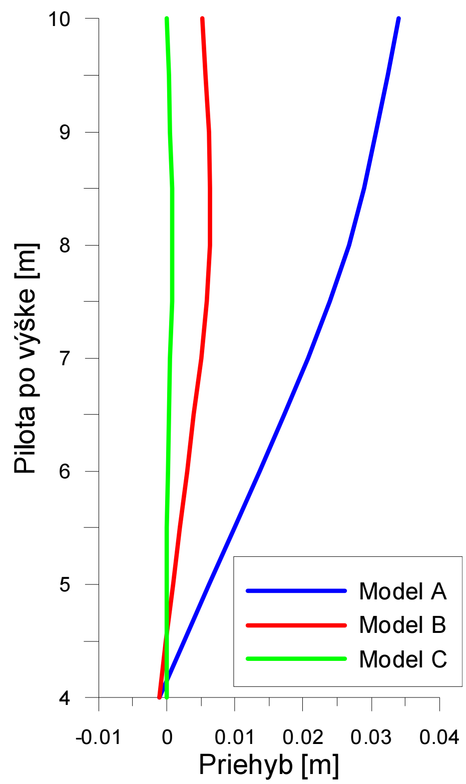

Obrázok 6 – Porovnanie priehybov pre všetky modely

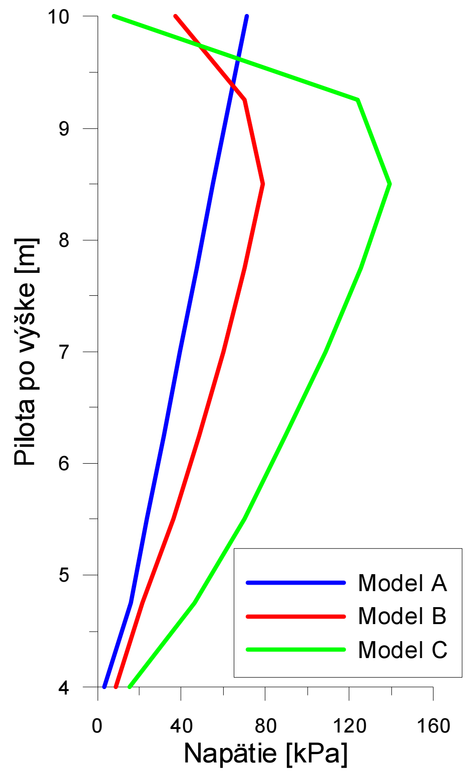

Obrázok 7 – Porovnanie kontaktných napätí pre všetky modely

Z výsledkov porovnania pre všetky modely konštrukcie je zrejmé, že vlastnosti podložia v podstatnej miere ovplyvňujú rozdelenie napätí a hodnoty priehybov po výške piloty a v podstatne menšej miere ovplyvňujú vnútorné sily (ohybové momenty a priečne sily). Na záver je možné konštatovať, že použitý spôsob modelovania kontaktu ponorenej piloty s okolitým zemným masívom veľmi dobre popisuje správanie sa konštrukcie od zaťaženia a je možné ho použiť pri ďalších výpočtoch tohto typu konštrukcie.

Literatúra

ANSYS ® User’s Manual for Revision 12, Swanson Analysis Systems, Inc.

KOLLÁR P., MISTRÍKOVÁ Z., 1985. Spolupôsobenie ohybom namáhaných pilot s pružným polpriestorom – polity v hlave voľné. *Inžený rske stavby,* 1985, číslo 1, stránky 29–39.

KOLLÁR P., MISTRÍKOVÁ Z., 1987. Ponorené piloty ako korene zemných kotiev namáhané ohybom. *Inženýrske stavby,* 1987, číslo 5, stránky 232–242.

PREKOP Ľ., 2012. Modelovanie kontaktu pilota – zemný masív. In.: *20th SVSFEM ANSYS Users' Group Meeting and Conference 2012*, Přerov, 17.–19.10.2012. Brno: SVSFEM s.r.o., 6pp. ISBN **978-80-260-2722-5**.

PREKOP Ľ., 2012. Interakcia piloty namáhanej ohybom s podložím. In: *10th International Conference on New Trends in Statics and Dynamics of Buildings*, Bratislava, 3.–5.10. 2012, pp. 211-214. **ISBN 978-80-227-3786-9.**

Poďakovanie
Tento príspevok bol vypracovaný v rámci grantového projektu VEGA č.1/0629/12.

Kontaktná adresa:
Ing. Ľubomír Prekop, PhD., lubomir.prekop@stuba.sk
Katedra stavebnej mechaniky, Stavebná fakulta STU, Radlinského 11, 813 68 Bratislava

DESIGN OPTIMIZATION OF RECIPROCATING COMPRESSOR PULSATION SUPPRESION DEVICE IN ACCORDANCE WITH API 618

KIRILL SOLODYANKIN*, JIŘÍ BĚHAL
ČKD KOMPRESORY a.s.

Abstract: Industrial reciprocating compressors are provided with pulsation suppression devices. Its design optimization is presented. Submitted modification was aimed at a mechanical stress reduction in the support system elements and it was done in accordance with API 618. Finite element analysis of complex structure dynamic behaviour and mathematical modelling were applied. An improved structural geometry is the result of analysis. The new design has been validated in the course of performed modification of an operated machine.

Keywords: Reciprocating compressor, Dynamic analysis, Pulsation suppression device, API 618

1 Introduction

Reciprocating compressors are widely used equipment in petroleum, chemical and gas industry services. In most cases, they must satisfy the requirements of commonly used API 618 practice. This study shows which type of technical problems can be met in some set of circumstances, in spite of the fact that original equipment design had passed all standard specifications.

A support structure is necessary in some cases of pulsation suppression devices. Static loading, acoustic shaking forces and mechanical responses shall be considered in support elements design. Several criteria related to dynamic or vibration limitation are applied to a compressor, pulsation suppression devices and piping system [1]. All of these requirements were granted in the design of 3 MW compressor. Nevertheless, fatigue cracks were detected on support system elements approximately after a year of routine operation.

Some modification of piping system configuration was done after compressor equipment installation. Understanding of structural modifications or boundary conditions which caused the system dynamic behaviour changes was crucial. The dynamic response of suction pulsation suppression device on the first compressor stage has been identified as the piping system reconfiguration consequence. Modal and harmonic analyses were done for the purpose of failure process simulation and design of safety measures.

2 Methods

An industrial compressor of a new design was installed in the difficultly accessible location. The customer asked the compressor manufacturer for safe operation guarantee.

Because of the remote operator destination, well prepared intervention was the must. The task of object optimisation was defined. According to available tools, a workflow proposal was developed consisting of consequent sessions:

a. vibration amplitudes measured on real structure in the course of its operation;
b. simulation of the structure behaviour using technical drawings and FEM;
c. identification of possible sources of the energy input;
d. calculation of the structure response to the nominal input for individual source;
e. variation of the input amplitudes for the best fitting of the measured vibration amplitudes;
f. analysis of the energy transmission path from the source to the high vibrating areas;
g. design of alternative structural modifications of the elements along the paths with respect to stress distribution/concentration and desired toughness shift;
h. simulation of the modified structure behaviour using FEM and the same combination of inputs;
i. evaluation of the alternative modifications for the critical area stress reduction;
j. manufacture of the modified parts for the best design;
k. measurement of the vibration amplitudes in the course of mounted new parts;
l. evaluation of the confidence of the simulated data and the ones measured on the modified structure.

The measurement in-situ was done by an external local organisation. Chosen locations were investigated in multi-axis directions. The analyser allowed measurement of the single channel in a time providing the maximal amplitude.

The drawings were available from the machine production in past. An ANSYS system was used for the FEM analysis. The possible energy inputs were proposed according to machine architecture and operation concept.

A spreadsheet processor was used for the evaluation of the best-fitting input combination. Harmonic oscillation of the input amplitude was supposed. Both vibration amplitudes and time phases in all measured locations were considered simultaneously. Logical input channel relatives were implemented in the mathematical model such as phase of the pistons connected to the common crank shaft.

3 Numerical Dynamic Simulation

First of all, the modal analysis of assembly was done. The simulation model of the first stage section is in Figure 19. There are three cylinders with piston-rod guides, discharge and suction pulsation suppression devices with supporting system, and first stage suction pipeline. Fixed support boundary condition was applied to marked surfaces. Appropriate material properties were defined for the each model part.

The modal analysis identified the suction suppression device natural frequency located nearby the 3x rate speed of compressor shaft. The related mode shape is illustrated in Figure 20. The suction pulsation suppression device oscillation can be observed. Suction pipeline isn't shown in the figure. There is only 7 % separation margin between 3x rate speed and natural frequency of the device. This value of separation margin does not satisfy the requirement of the standard. In accordance to standard, the predicted mechanical natural frequency shall be designed to be separated from significant excitation frequencies by at least 10 %.

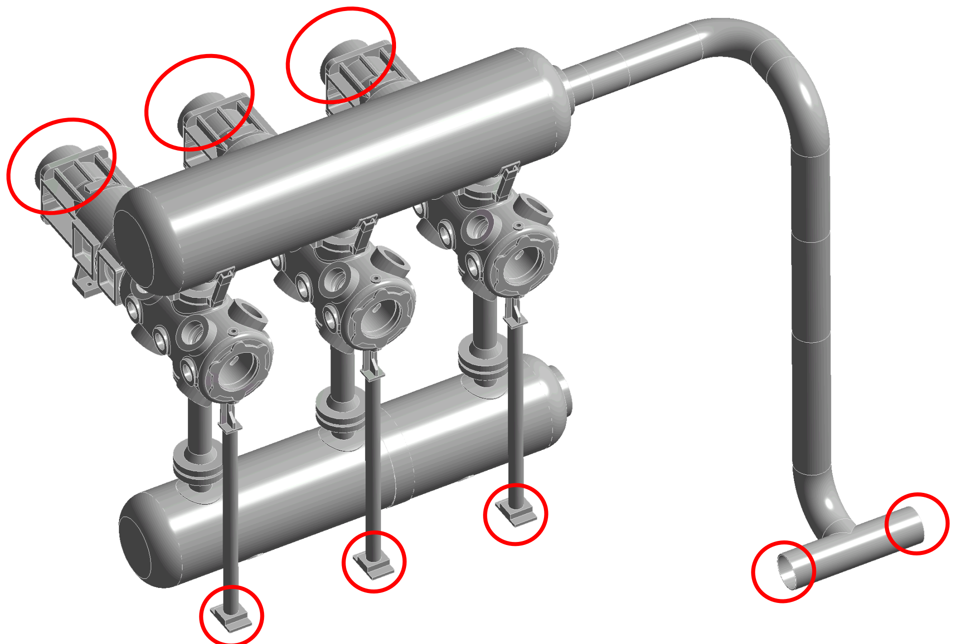

Figure 19 Simulation model

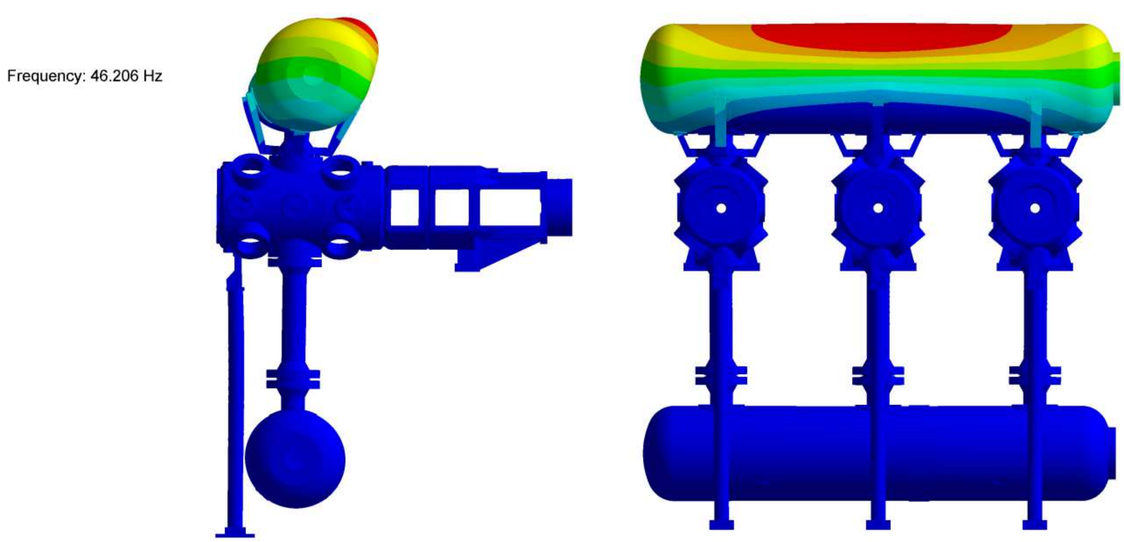

Figure 20 Mode shape of the original structure

4 Harmonic Analysis

The second step was a harmonic analysis of the dynamic system. The previous calculating model was complemented by exciting forces. The exciting forces were applied to the free end of each cylinder and suction device flange. Applied forces simulated oscillating pressure in cylinders under operating conditions. The values of exciting forces weren't essential in this phase of analysis. The forces values calibration will be shown further. The calculating model for harmonic analysis is represented in the Figure 21. Suction pipeline isn't shown in this figure. Amplitude frequency response of a suction device shell is illustrated in Figure 22. The 1x, 2x and 3x rate shaft speed with 10 % separation margins are also shown in the figure.

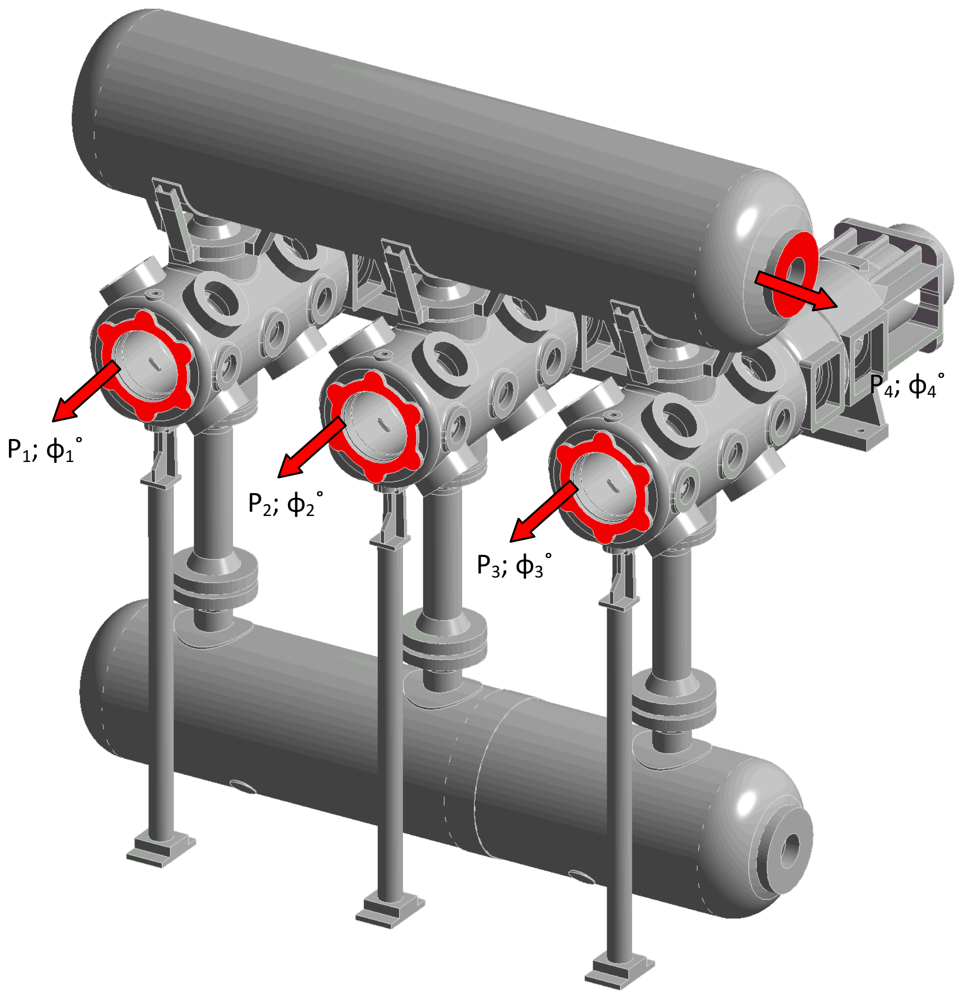

Figure 21 Calculating model for harmonic analysis

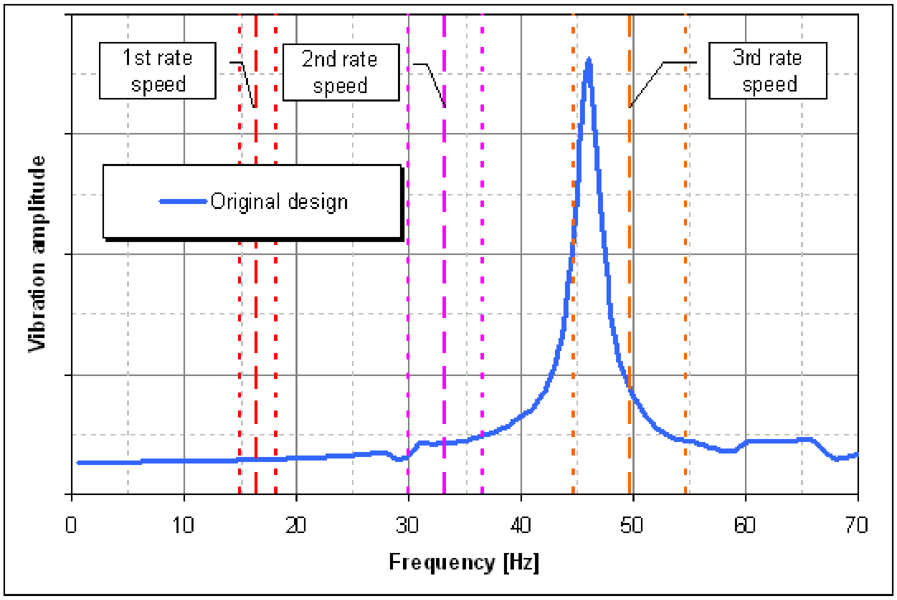

Figure 22 Amplitude frequency response of suction device shell with original design support

Quantification of the exciting forces values was provided in the next step of the analysis. Calibration was based on experimentally measured two axes directional displacement values in horizontal plane in 10 points on compressor cylinders, supporting system parts and suction suppression device flange. Scheme of measuring points is illustrated in Figure 23. Maximum likelihood estimation method was used for an appropriate exciting forces simulation. Description of mathematical modelling exceeds this paper scope. Quantified excitation was added to FEM model. Calculated results of tracking directional displacement points were compared with measured values. Figure 24 shows a comparative graph of calculated and measured values in measured points.

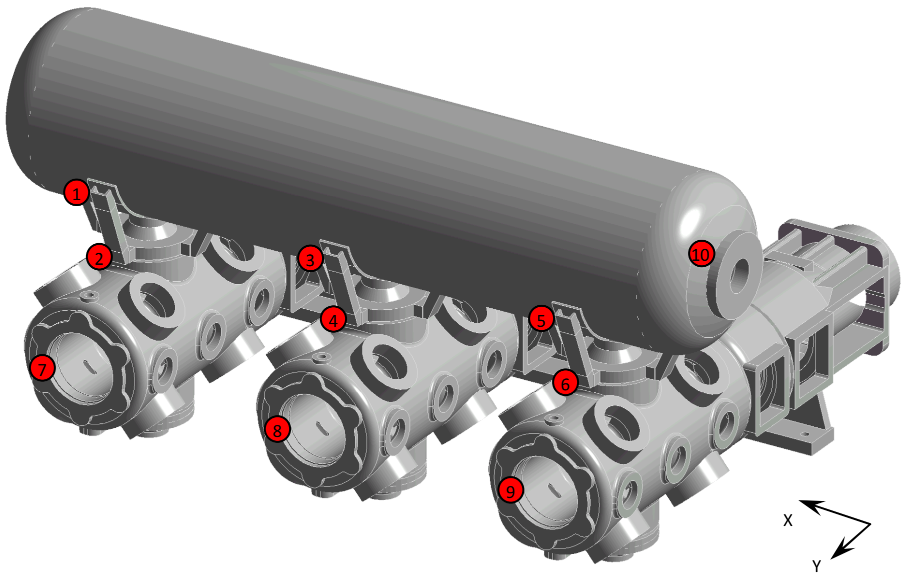

Figure 23 Scheme of measuring points

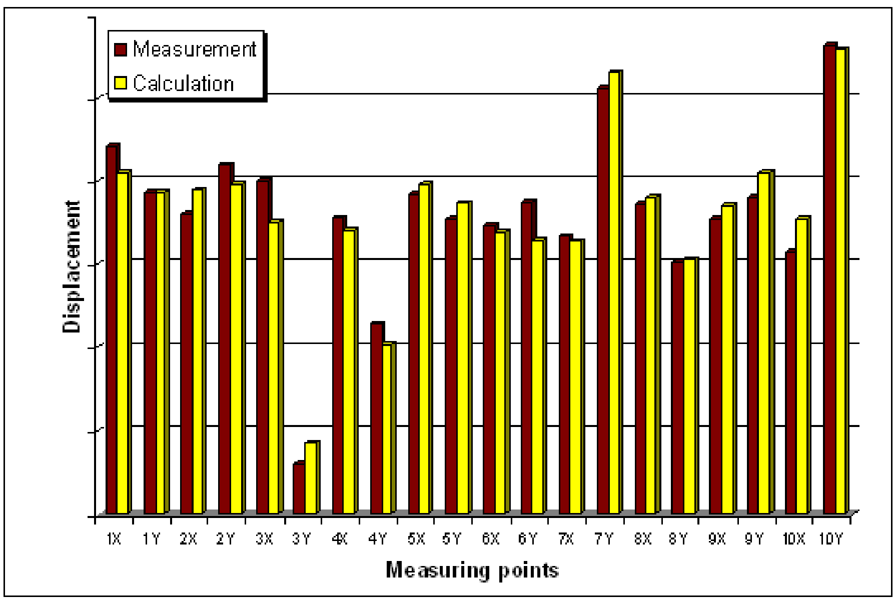

Figure 24 Comparison of measured and calculated displacement values

Equivalent stress distribution in the course of dynamic operation loading was obtained. The stress levels in device support system are illustrated in Figure 25 and Figure 26. The location of maximum stress areas is compared with observed cracking in Figure 27 and Figure 28.

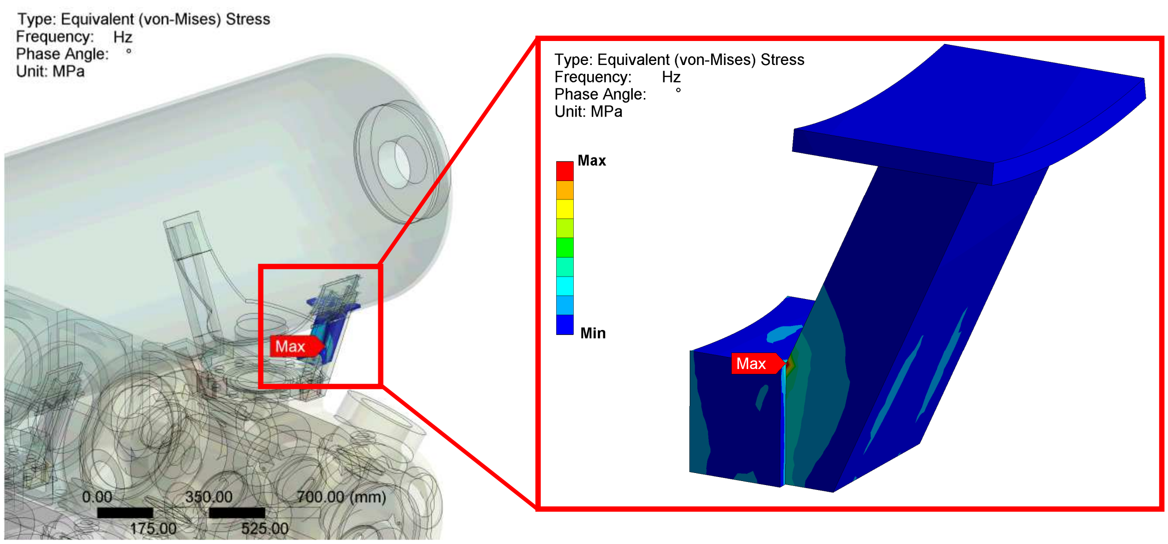

Figure 25 Equivalent stress distribution in axial support part

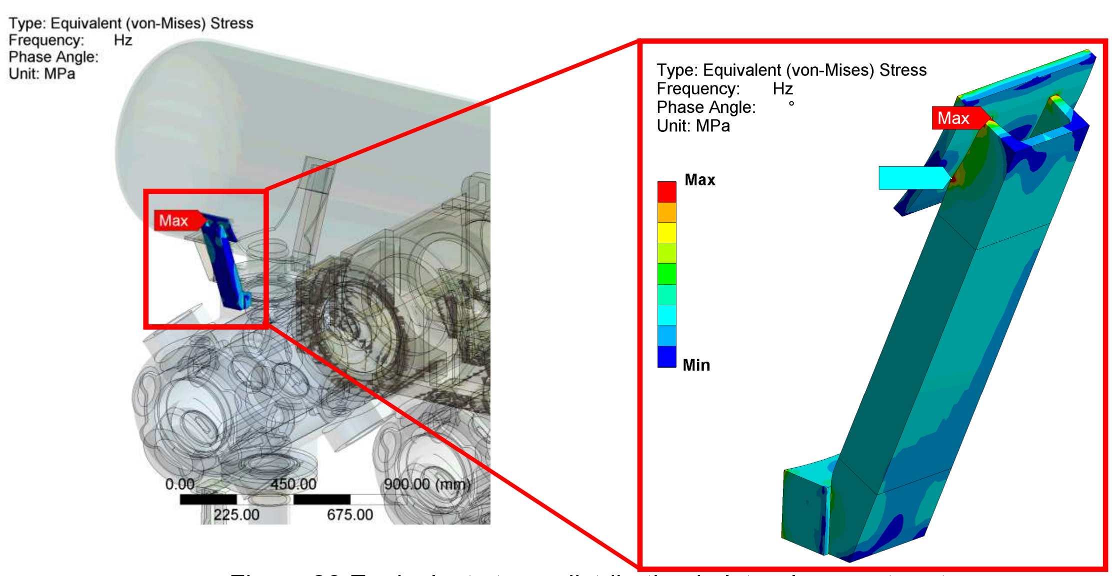

Figure 26 Equivalent stress distribution in lateral support part

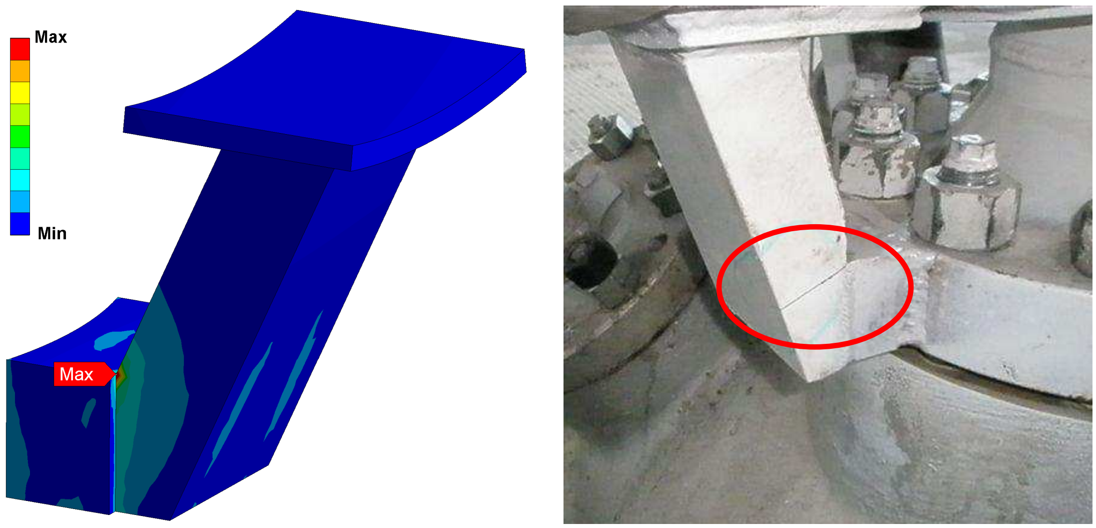

Figure 27 Stress distribution and crack comparison in axial support part

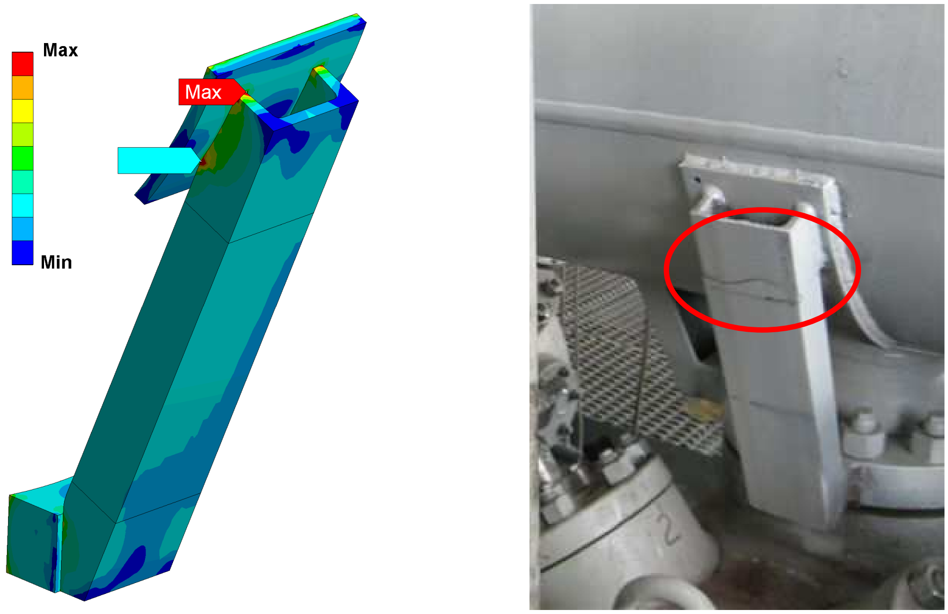

Figure 28 Stress distribution and crack comparison in lateral support part

5 Structural Modification Design

Fatigue cracking of support system parts appeared namely due to:

- the support system was cyclically loaded with pressure suppression device oscillation due to nearly resonance state of dynamic system;
- the beams are too stiff to carry suppression device wall displacements resulting in high stress levels;
- the critical areas appeared in the rough weld seams with large stress concentrations.

These factors were considered in the new support system parts design. The new geometry is illustrated in Figure 29.

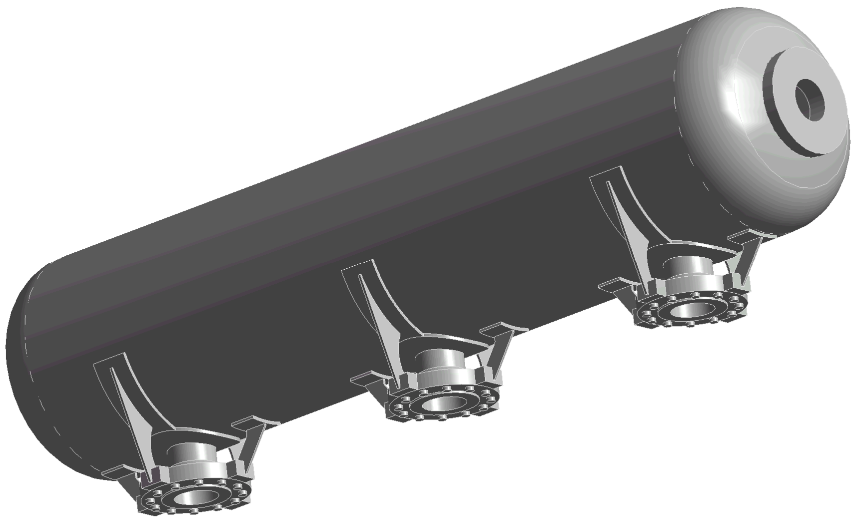

Figure 29 New support system design

The natural frequency of followed mode shapes shifted from 46.2 Hz to 39.7 Hz. The new separation margin is 19 % between followed frequency on 2x rate shaft speed, and 20 % on 3x rate shaft speed respectively. These values fully satisfy the standard requirements. Related mode shape is shown in Figure 30.

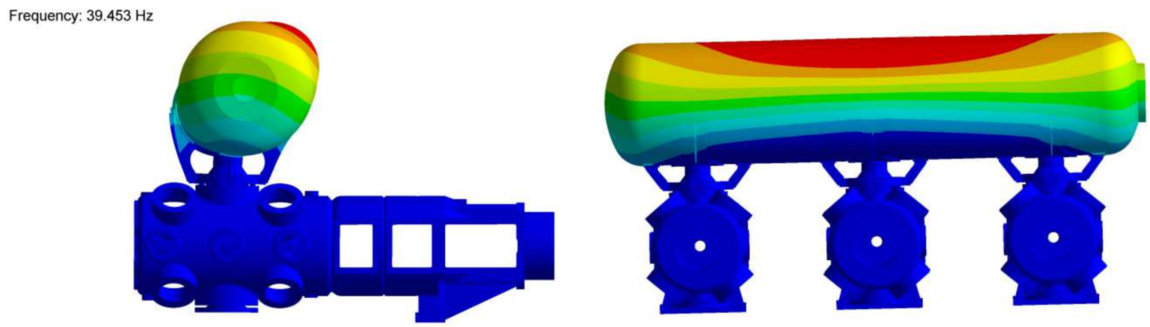

Figure 30 Mode shape of the new structure

It was supposed that values of exciting forces were not affected by supporting system stiffness changes. New model of dynamic system for harmonic analysis was loaded with the same excitation forces. Equivalent stress distribution and amplitude frequency response were obtained and optimised. Equivalent stress distribution in the new support design is illustrated in Figure 31. The maximum equivalent stress level decreases nearly 50 % compared to the original one. Amplitude frequency response analysis of modified structure is illustrated in Figure 32.

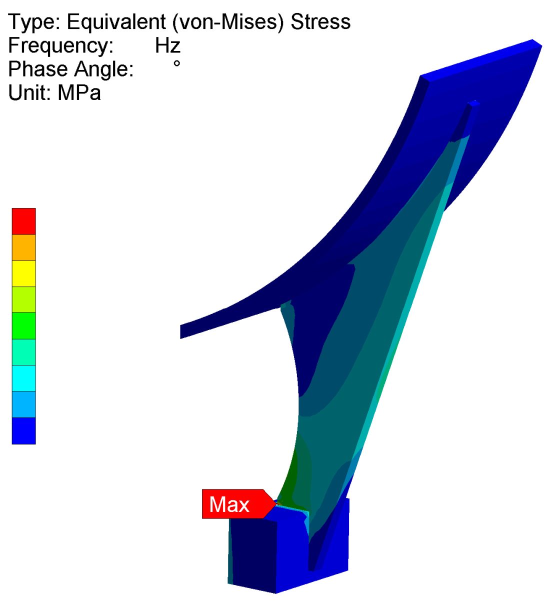

Figure 31 Equivalent stress distribution in the new design support part

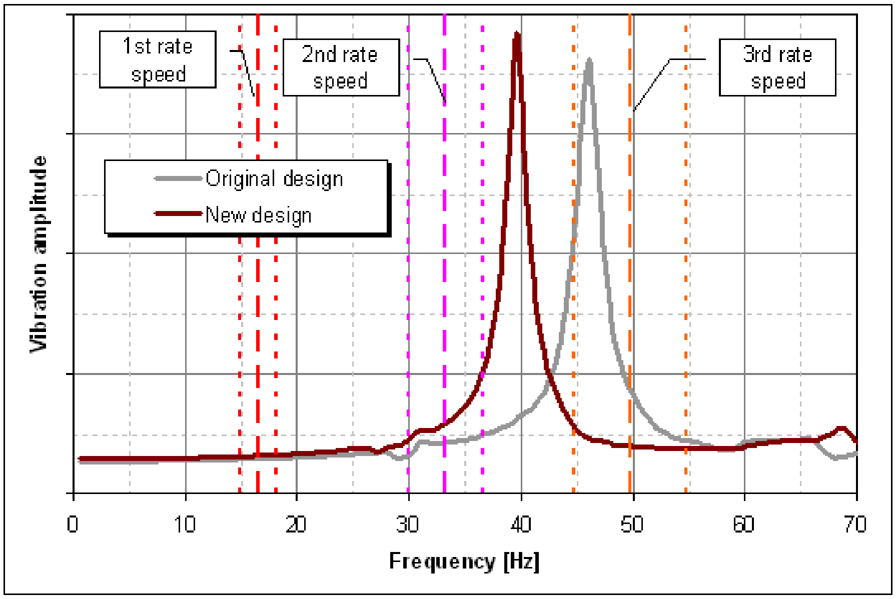

Figure 32 Amplitude frequency response of suction device shell with new design support

6 Modification Performance

The submitted modification has been applied on an operator site. Repetitive vibration measurements were done in the same points as in case of the original structure. The reduction of vibrations has been confirmed by an experiment. Figure 33 illustrates the comparison of measured displacement values in followed measuring points of structure with the new and the original supporting system design.

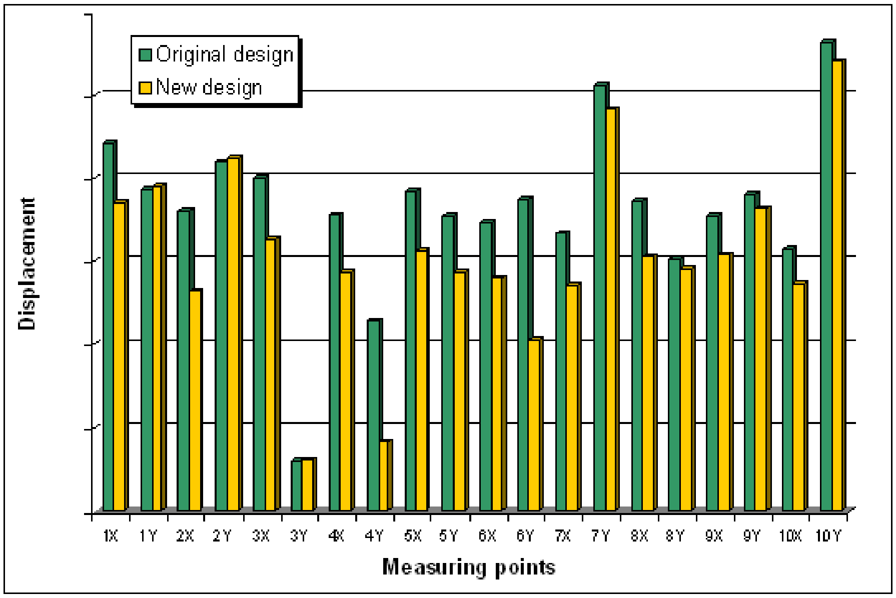

Figure 33 Displacement comparison of structure with the new and the original support

7 Conclusion

Case study of a structural geometry optimisation is presented. The structure of reciprocating compressor machine is loaded by high frequencies and the mechanical vibrations have been investigated. 3D object properties, assembly behaviour and the system response have been simulated by a finite element method.

The new optimized pressure suppression device support system of reciprocating compressor is the result of performed analysis. Standard requirements of API 618 are met in the new design. Design optimization was done in several steps, including amplitude vibration measurement in-situ. Efficiency of optimized design has been confirmed in the course of practical application.

References

[1] API 618, Fifth edition, December 2007. Reciprocating Compressors for Petroleum, Chemical, and Gas Industry Services. Washington, DC, USA.

Contact address:

Ing. Kirill Solodyankin
ČKD KOMPRESORY a.s.
Klečákova 347
190 02 Prague 9
Czech Republic
E-mail: kirill.solodyankin@ckdkompresory.cz

Jiří Běhal Ph.D.

ČKD KOMPRESORY a.s.
Klečákova 347
190 02 Prague 9
Czech Republic
E-mail: jiri.behal@ckdkompresory.cz

ANALYSIS THE CEILING PLATE COBIAX

KATARÍNA TVRDÁ
Slovak University of Technology Bratislava, Department of Structural Mechanics

Abstract: This paper deals with static and probability analysis of the ceiling boards, made of the Cobiax-system. The ceiling plate Cobiax is made of cobiax balls with a diameter of 27cm, where place around columns are not located at the site of cobiax balls, but the full-system. Probability analysis of Monte-Carlo method in software Ansys is presented. Input parameters are changing according to Gauss or triangular distribution.

Keywords: probability, static analysis, finite element method, Monte Carlo

1 Introduction

One of the possible solutions of static analysis and expertise is also an assessment of the reliability of structures. Ansys software allows to assess the structure of a safety or a failure based on probability analysis using Monte Carlo methods. A number of papers dealing with probability analysis may be found in works of authors (Marek, 2003), (Králik, 2009), (Kormaníková, 2010), (Frydrýšek, 2010). Such calculations can better contribute to the safety of the structures.

2 Spot ceiling plate supported

2.1 Static analysis of the plate

We will deal with the static analysis of the ceiling plate loaded by uniformly distributed load $q = 6.5\ kN/m^2$ (Image 1). The plate is made of concrete B30/37 class with a modulus of elasticity $E = 33$ GPa. The thickness of this plate is $h = 0.4$ m.

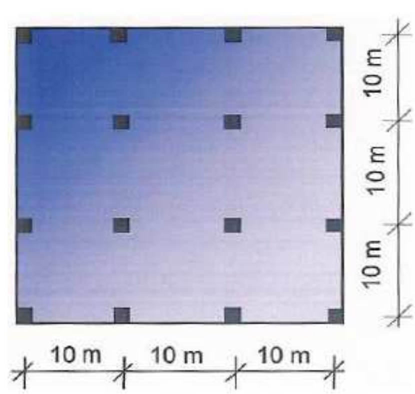

Image 43 – Spot ceiling plate cobiax supported

Results of the static analysis, displacements, as well as internal forces of the plate are shown in the following Figures (Images 2-3).

From the next figure, it is clear that the maximum deflection is in the outer fields and its value is 2,196 mm. This plate was calculated without dead load.

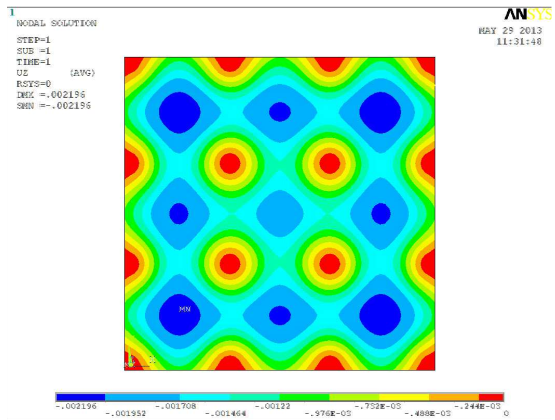

Image 2 – Displacement of the plate

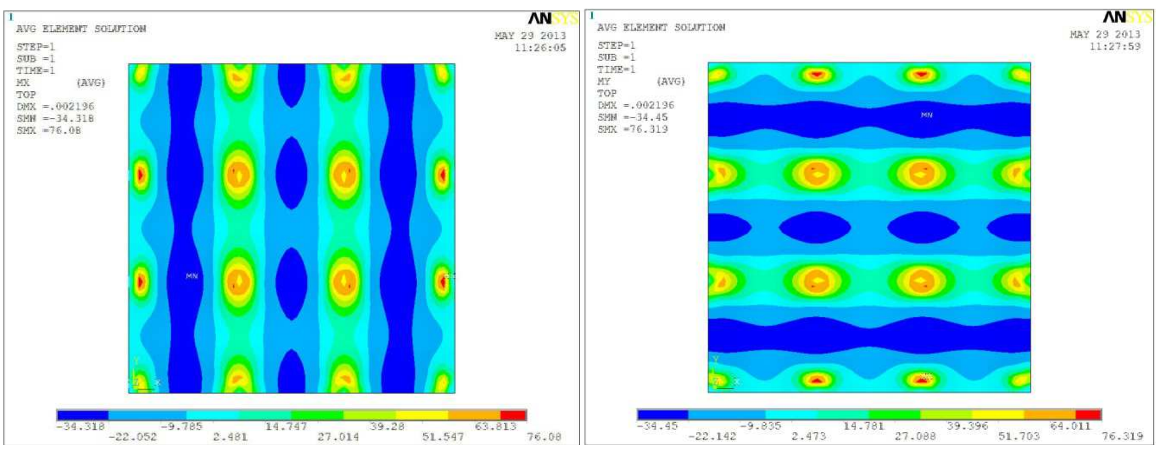

Image 3 – Specific moments mx and my

2.2 Static analysis of the cobiax plate

Ceiling plate is made of the same materials as referred to in paragraph 2.1, of the same thickness (h = 0.4 m) and of the same concrete B30/37 class with a modulus of elasticity E = 33 GPa. In this case we are considering (Fig. 4) with dead load as well. Random load is 1.5 kN/m^2, still load 5 kN/m^2. Dead load of 0.4*25 kN/m^3 = 10 kN/m^2 was in columns location compared with dead load 0.4*25 kN/m^3- 2.86 = 7.14 kN/m^2 at location of balls with a diameter of 27cm. Manufacturer of the Cobiax prescribed in this case to reduce the flexibility of the modulus on E_b = 0.92 * 33 GPa = 30.366 GPa. The static scheme is in Image 5.

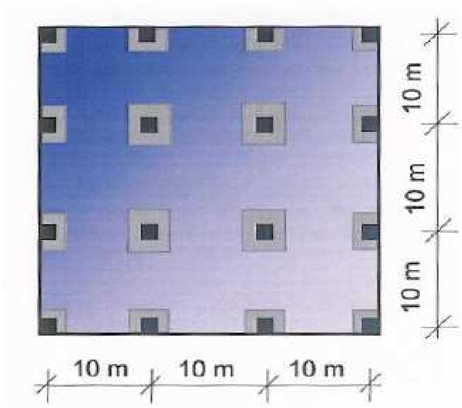

Image 4 – Spot ceiling plate supported

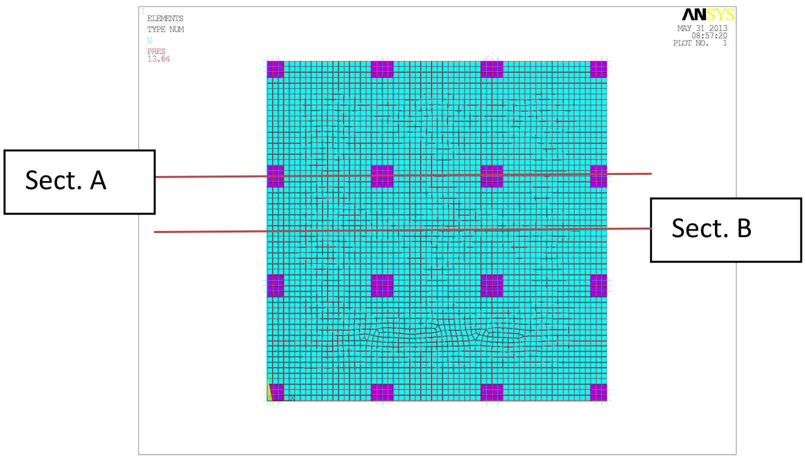

Image 5 – Static scheme

The following figures referre to the resulting stress, strain and internal forces of the ceiling plate Cobiax.

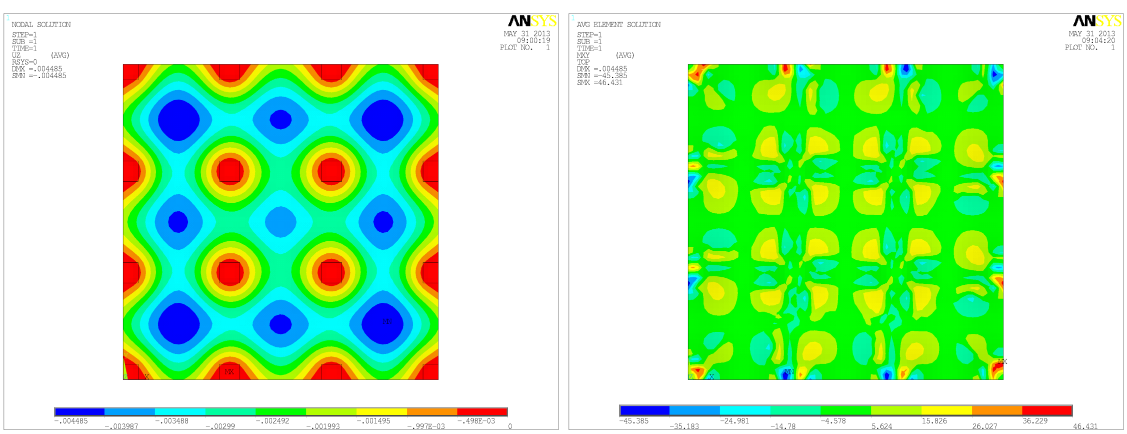

Image 6 – Deformation and specific moment mxy

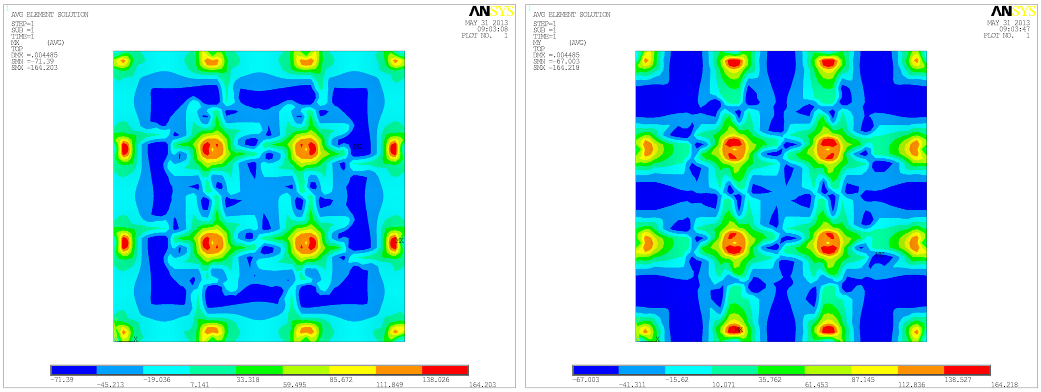

Image 7 – Specific moments mx and my

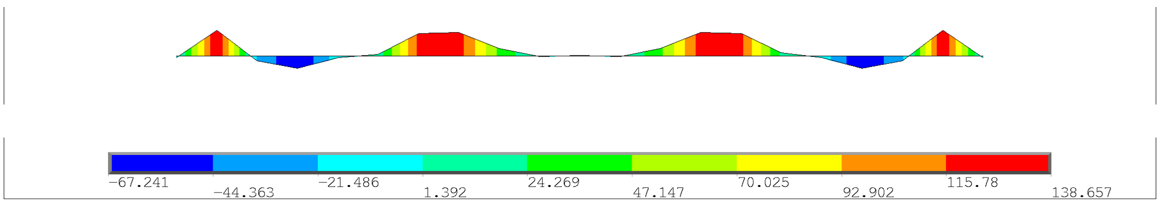

Image 8 – Specific moments mx at path A

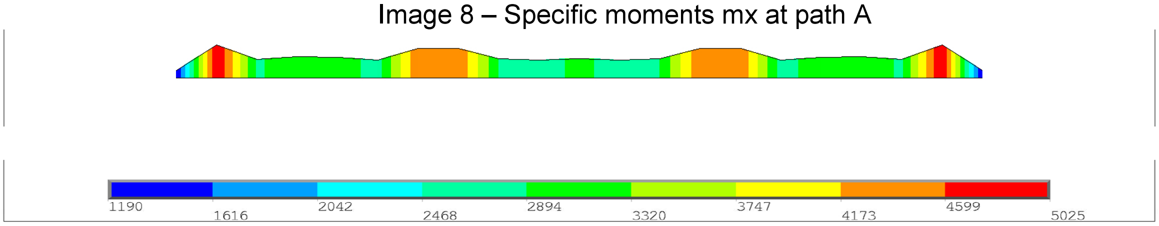

Image 9 – Stress along the section A

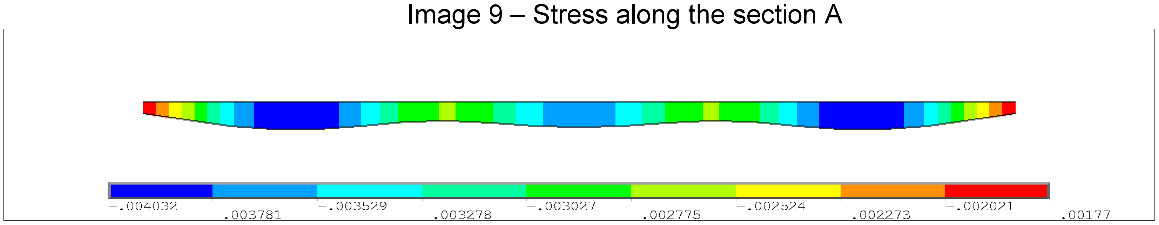

Image 10 – Specific moments mx along the section B

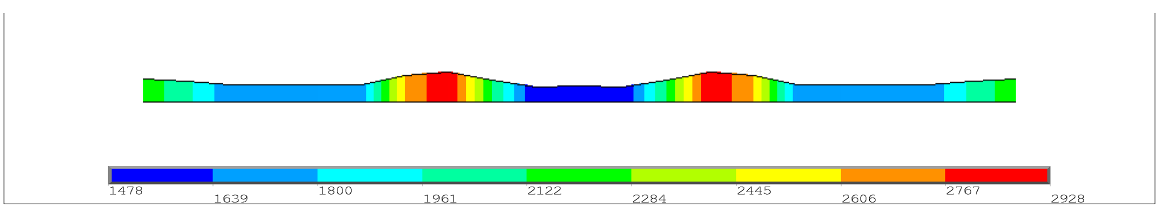

Image 11 – Stress along the section B

3 Probability analysis

As we know, any building structure is subjected to certain specified tolerances in the manufacture of the construction of dimension proportions. We can also specify the load, modulus, which may be randomly changed. This analysis, which deals with all these uncertainties and the variation, is called the probability analysis.

The method used for this purpose was the Monte Carlo method with a direct sampling and number of cycles was set to 10000. In this case it was set 5-output parameters as the maximum deflection (PRIEH), maximum specific moment mx (MAX_MX), maximum specific force (MAX_Vxz), Misses stress (NAP), reliability (CO), which varied depending on the four input parameter. The input parameters were: modulus of elasticity for the Cobiax plate (E_kob), for full plate (E_), uniformly distrebuted load (q_), and the thickness of the plate (h_).

Type and distribution of some inputs are given in the following Table 1 and Images. 12, 13. From Image 12 it is clear, that input variable E_kob has a Gauss distribution, and input variable H_ has triangular distribution.

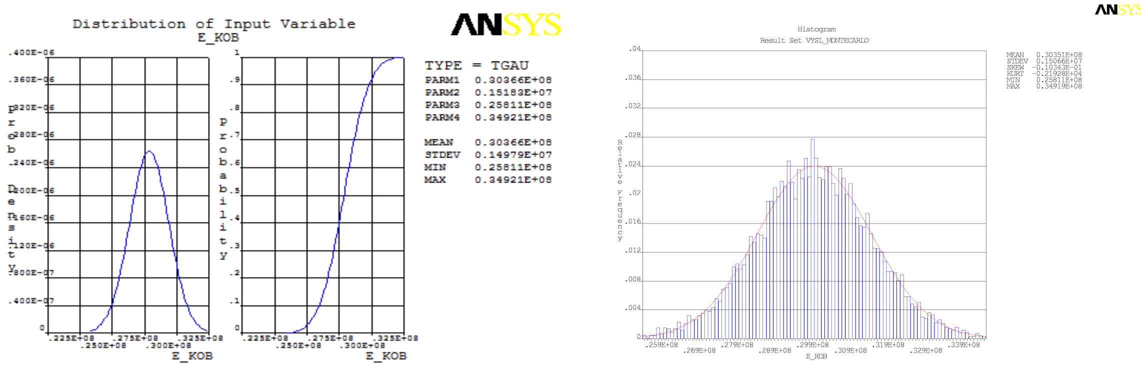

Image 12 – Distribution and histogram of input variable E_kob

Table 8 Table of Input Variables

Variable	Distribution	Min	Max
E_kob	TGAU	0.05*30366e3	0.85*30366e3
E_	TGAU	0.05*33e6	0.85*33e6
q_,	TGAU	0.05*13.64	0.85*13.64
h_,	TRIA	0.35	0.45

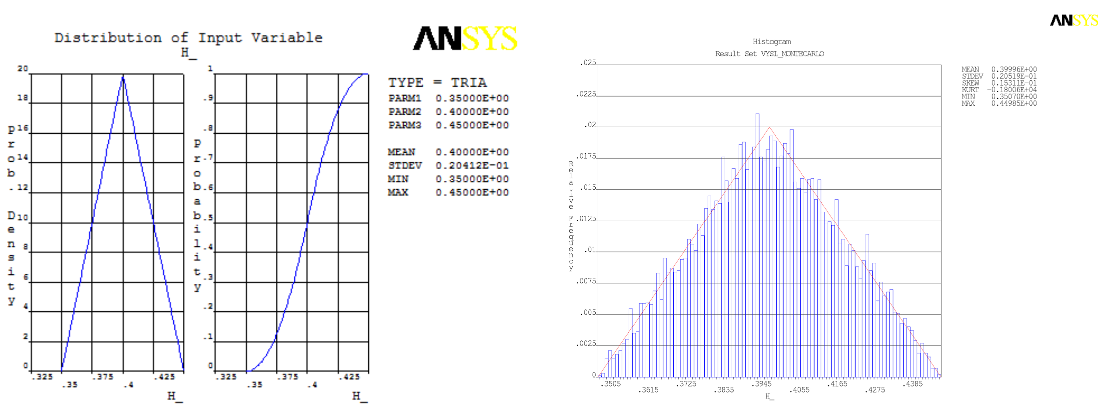

Image 13 – Distribution and histogram of input variable H_

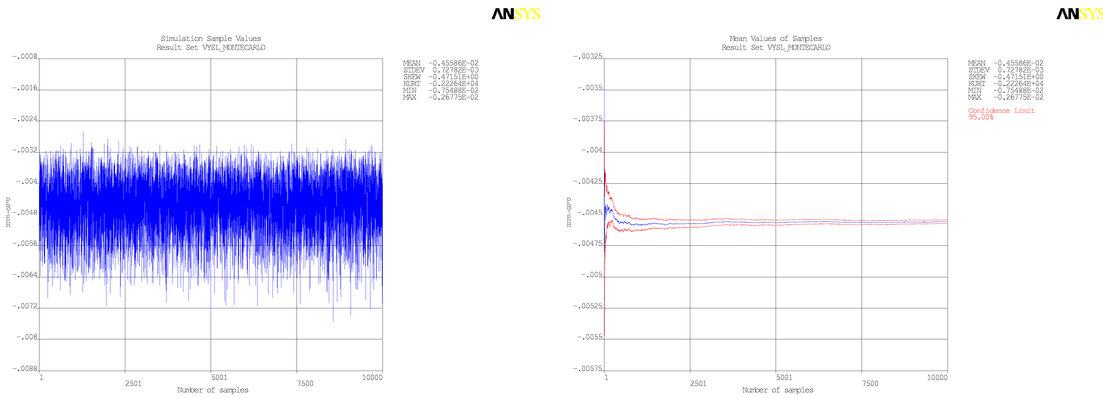

Image 14 – Simulation sample values max displacement and history of mean values of max PRIEH

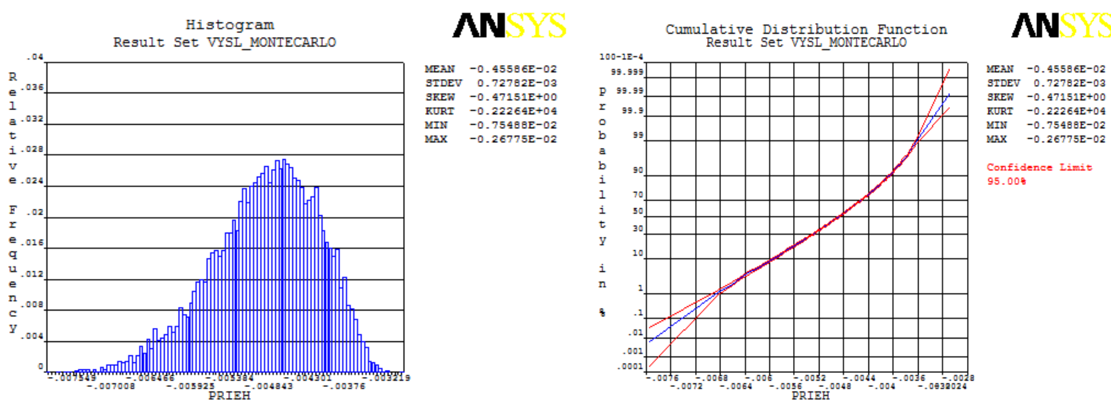

Image 15 – Histogram of output variable PRIEH and CDF max. deflection PRIEH

Simulation sample values maximum displacement (PRIEH) and history of mean values of maximum displacement (PRIEH) are given in Image 14. The blue curve (medium) in Image 14 converges, implying that number of cycles was sufficient and the maximum deflection is moved in the range of -0.007548 to -0.0026775.

According to the CDF (cumulative distribution function, Image 15) we can determine probability of the corresponding parameter PRIEH (the maximum value of deflection).

```
Probability Result of Response Parameter PRIEH
==============================================

Solution Set Label    = VYSL_MONTECARLO
Simulation Method     = Monte Carlo with Direct Sampling
Number of Samples     = 10000
Mean (Average) Value  = -4.5585664e-003
Standard Deviation    =  7.2781813e-004
Skewness Coefficient  = -4.7150649e-001
Kurtosis Coefficient  = -2.2264086e+003
Minimum Sample Value  = -7.5488392e-003
Maximum Sample Value  = -2.6775103e-003

The probability that PRIEH is smaller than -7.0000000e-003 is:

 Probability  [  Lower Bound,  Upper Bound]
1.50635e-003  [ 8.69488e-004, 2.39734e-003]

NOTE: The confidence bounds are evaluated with a confidence level of  95.000%.

The probability is interpolated between:
PRIEH=-7.0051668e-003 which has rank 15 out of 10000 samples
PRIEH=-6.9921200e-003 which has rank 16 out of 10000 samples
```

The output shows the probability that max deflection is less than -0.007 m, representing that the design is at 0.15% is unreliable.

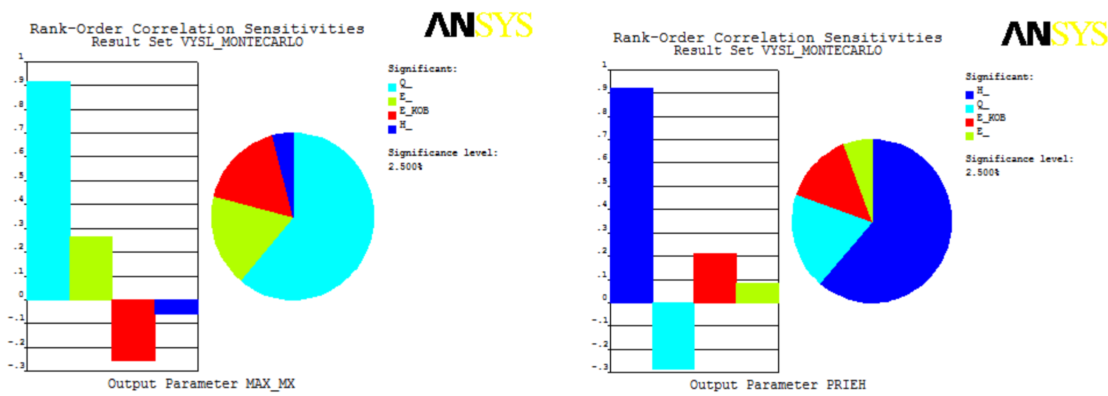

Image 16 – Rank-order correlation sensitivities of output variable MaX_MX and PRIEH

Sensitivity analysis in Image 16 showed that the input parameter E_ module of elasticity most affects on the output PRIEH-deflection of the plates or parameter Q_ uniformly distributed load on the output parameter Max_Mx – specific bending moment.

4 Conclution

The aim of this analysis was to determine the probability of failure of structures, and then to determine its reliability depending on the input parameters. In our case, there has been a failure (0,15 %), if we have exceeded the limit deflection -0.007 m.

References

Marek, P., Brozzetti, J., Guštar M., 2003. *Probabilistic Assessment of Structures Using Monte Carlo Simulation Background, Exercises and Software*, ITAM CAS, Prague, Czech Republic, pp.471. ISBN 80-86246-19-1

Králik, J., 2009. *Reliability analysis of structures using stochastic finite element method*. Edícia vedeckých prác, zošit č.77. STU v Bratislave, 138 s. ISBN 978-80-227-3130-0

Kormaníková, E., 2010. *Optimization of laminate plate subjected to maximum strain criterion*, on *CD-ROM,* In: Modelování v mechanice 2010: sborník příspěvků vědecké konference: Ostrava, VŠB-TU, P.1-7. ISBN 978-80-248-2234-1.

Frydrýšek, K., 2010. *Pravdepodobnostní výpočty v mechanice 1*, VŠB TU, Ostrava. ISBN 978-80-248-2314-0. (in Czech)

Acknowledgement
The work has been supported by the grant from Grant Agency of VEGA in Slovak republic No. 1/0480/13, No. 1/1186/12.

Contact address:
Ing. Katarína Tvrdá, PhD., katarina.tvrda@stuba.sk, Slovak University of Technology, Faculty of Civil Engineering, Department of Structural Mechanics, Radlinského 11, 813 68 Bratislava, Slovakia

NUMERICAL MODELING OF THE BEHAVIOUR OF A FLEXIBLE CLAMP AT GRIPPING OF A RAIL

TADEÁŠ VOLF, JAN VYČICHL

Czech Technical University in Prague, Faculty of Transport Sciences,

Department of Mechanics and Materials

Abstract: This work is focused on the elastic fastening rail to the sleeper, the definitions of used types, their usage in the Czech republic, main advantages and disadvantages, the comparison of the most popular systems on the SZDC site and the summary of the requirements for the fastening. The practical part of the work is focused on the creation on a model in the ANSYS Workbench software. There are four simulations of the load, which correspond with the real situations. The results from each situation have been analyzated (the equivalent stress, the total deformation) and have been compared among themselves. The other parts of the rail truck were analysed too.

Keywords: rail fastening, tension clamp, Vossloh W 14, finite element method, ANSYS Workbench

1 Introduction

The fixation between rail and sleeper is a very important parametr of the whole rail track construction. The suitable type of the fastening can reduce costs of the rail-track servicing, the trains operate more quietly and more comfortably, the vibration and noise is lower. Nowadays almost exclusively,it is used the flexbile fastening systems, where the tension clamp causes the elastic characteristic.

This article describes the stress analysis of the rail fastening. It was created the system Vossloh W 14 with the tension clamp Skl 14, because it is the most commonly used system in the Czech Republic. The model was designed in the ANSYS Workbench software. The type of the rail sleeper is B91/S, the rail UIC 60, the rubber pad under the rail is WU-7 and the angled guide plate Wfp 14. These parts can be used in the rail tracks in the Czech republic.

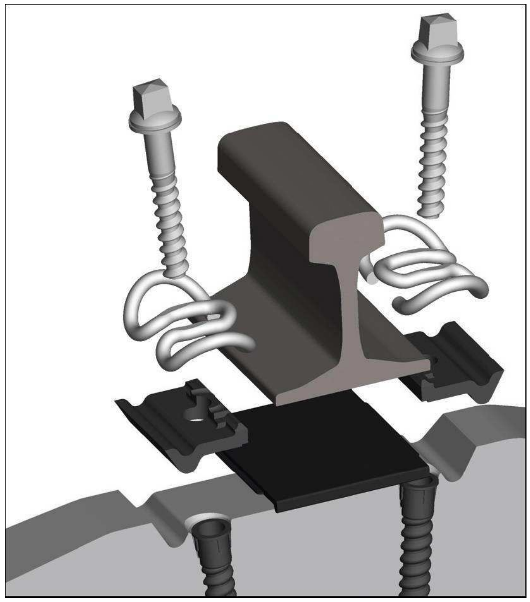

Image 44 - The Vossloh W 14 System

2 Virtual model

a. Geometrical model

The geometrical model corresponds to a real situation. The model was simplified in not importing parts (the sleeper, the rubber pad), this simplification is not very important for getting the good results. The tension clamp was created in the software Autodesk Inventor, because Autodesk Inventor is more suitable for designing the complicated geometrical parts. Then it was imported to the ANSYS Workbench. It was possible to create only a quarter of the whole model, the rest of the model was achieved with mirroring. The length of the rail in the model is 600 mm. It's half of the length between two sleepers. The geometrical model is in the next picture, but there is showed the whole model, for better understanding.

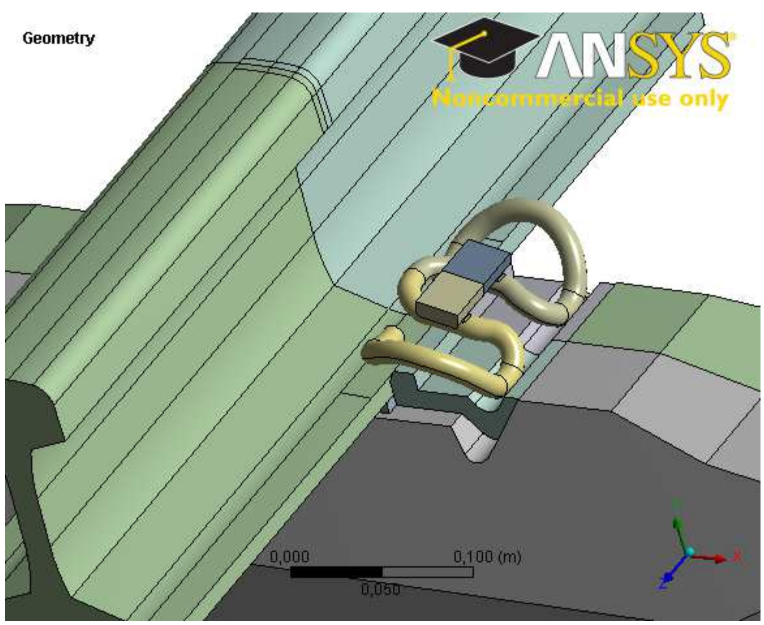

Image 45 - The geometrical model

b. Finite-element model

It was necessery to modify the finite element mesh. We need the most fine mesh for the good results, but on the other hand, the computer hardward and the ANSYS license were limited. . I used the face sizing, contact sizing and body sizing of the mesh in my model.The finest mesh is located in the contact areas, especially between the tension clamp and the angled guide plate or rail. These parts are very important in this model. The largest element size is on the sleeper, but not in the contact areas. The model contains 36 266 elements and 135 407 nodes.

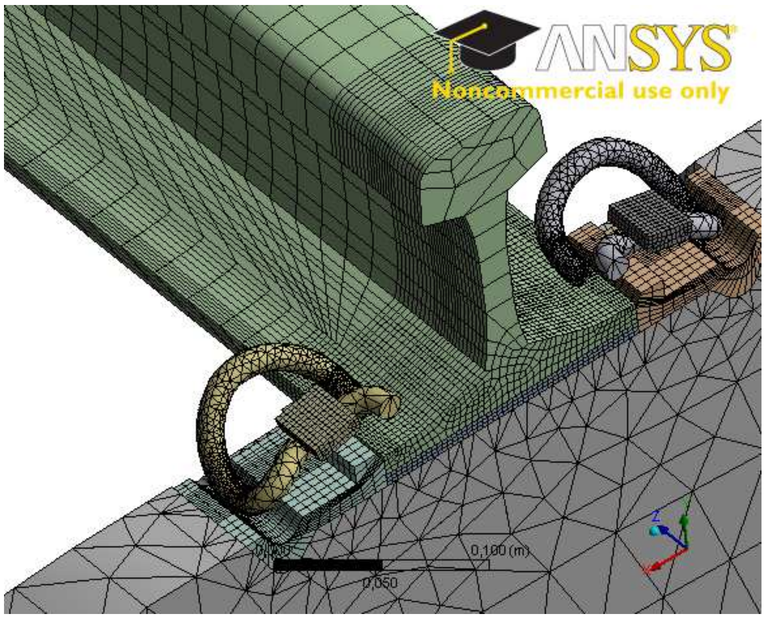

Image 46 - The Finite-elements Model

c. Initial conditions

The lower part of the sleeper is supposed to be fixed supported, there are removed 6 degress of freedom in the 3D space. The moving of the free end rail is allowed only in the one, vertical direction. It was used two symetry regions because of the reduction counts of the elements. The contact areas are defined in the next table:

Table 3 – Type of elements

Part no.1	Part no.2	Type of the contact	COF	Max. size of elements
rail	rubber pad	frictional	0,8	3,0 mm
rail	angled guide plate	frictional	0,1	2,0 mm
temsion clamp	angled guide plate	frictional	0,1	1,5 mm
rail	tension clamp	frictional	0,2	1,5 mm
rubber pad	angled guide plate	frictional	0,1	3,0 mm

rubber pad	sleeper	bounded		8,0 mm (on the sleeper)
angled guide plate	sleeper	bounded		8,0 mm (on the sleeper)

All contacts have the behaviour type Adjust to touch. The other possibilities of behaviour have the default settings. I used the standard earth gravity in the whole model.

d. Material properties

The materials in the model corresponds to the real situation. But it was not able to find the material properties of some parts, so I used the most similiar material. All used materials are from the basic material library in ANSYS Workbench and all materials are linear and isotropical. The basic properties are in the next table:

Table 4 . Material propeties

Part	Young's modulus [MPa]	Poisson's ratio	Density [kg.m^{-3}]
rail	210 000	0,30	7 580
concrete sleeper	32 000	0,18	2 300
angled guide plate	2 500	0,39	1 140
rubber pad	2,15	0,48	2 000
tension clamp	210 000	0,30	7 580
bolt	210 000	0,30	7 580

3 The solving cases

The calculation of the model runs in the five steps each in one second. The prestression grows up linerarly. The deformation of the clamp is big and the results needn't be correct in only one step.

3.1 The unloaded railway – Situation no.1

The tension clamp is tightened by the prescribed torque. The clamp is deformated elastically and both endings press the rail with the required force to the sleepers. The nose of the tension clamp has to touch the part of the angled guide plate, but the nose must not touch the rail. This behaviour of the tension clamp is supposed in all solved situations, too.

3.2 Loaded rail in the straight line – Situation no.2

The railway is located in the straight direction, without curves. The rail is loaded by the force of the rail wheel in the vertcal direction. The typical locomotives weight ca. 88 tons, so it is 11 tons for one wheel. This force loads the railway over the sleeper. The contact area between wheel and rail is 1 mm^2.

3.3 The loaded canted railway in the curved track with cant deficiency – Situation no.3

The size of the transverze force can be eliminated by the cant in the railway. But it isn't possible to design the theroretical size of the cant, because the trains have different speed. So we designed the recommended size of the cant.

In this situation the train has a higher speed in the curve and the train has the cant deficiency. The centrifugal force has effect for the train. The size of the centrifugal force is 65 kN for one wheel. This force is the maximal size of the centrigugal forces according to the UIC law. This force loads the railway over the sleeper.

3.4 The loaded canted railway in the curved track with excess of cant – Situation no. 4

The slow ride of the trains in the curve causes the big weight on the inside rail. The maximal size is 145 kN for one wheel, this size is in the UIC (518) law. So I used this force as a wheel force, the centrifugal force is 6 kN for one wheel.

4 Results

4.1 Equivalent stress in clamps

It was found out the values of the equivalent stress and its grafical representation on the parts of the model. The grafical results look for examlpe like this:

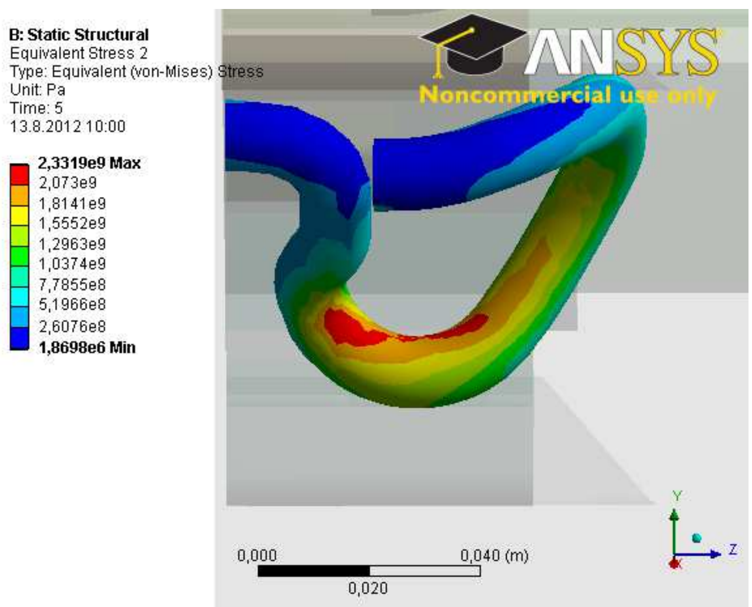

Image 47 – An equivalent stress in the clamp

There are shown the results for each simulation in the next table. The values are the maximum equivalent stress in every situation.

Table 5 – The results of the equivalent stress in clamps

Tension clamp	Situation no.1 [.10^9 Pa]	Situation no.2 [.10^9 Pa]	Situation no.3 [.10^9 Pa]	Situation no.4 [.10^9 Pa]

inside	2,3319	2,2808	2,3361	2,2210
outside	2,3223	2,2915	2,2666	2,2120

It's obvious, that the max. value is in the Situation no.3 - The loaded canted railway in the curved track with cant deficiency. The train in the curve causes the big force on the outside rail. The inside clamp forestalls the moving or rotating of the rail. On the other hand, the smallest values we can find in the situation no.4. It's because the big vertical force presses the rail down and the stress in the clamps is reduced.

4.2 The analysis of the rubber pad

The rubber pads under the rail is weighed by a big force from the trains. The rubber pad is easy to misshape, because it's made from a very elastic material. This deformation is possible to see in a real scale, but I choose 5,5x bigger scale for a better presentation of the deformation. The next picture shows the model from the 4th situation, because there are big vertical forces on the rail.

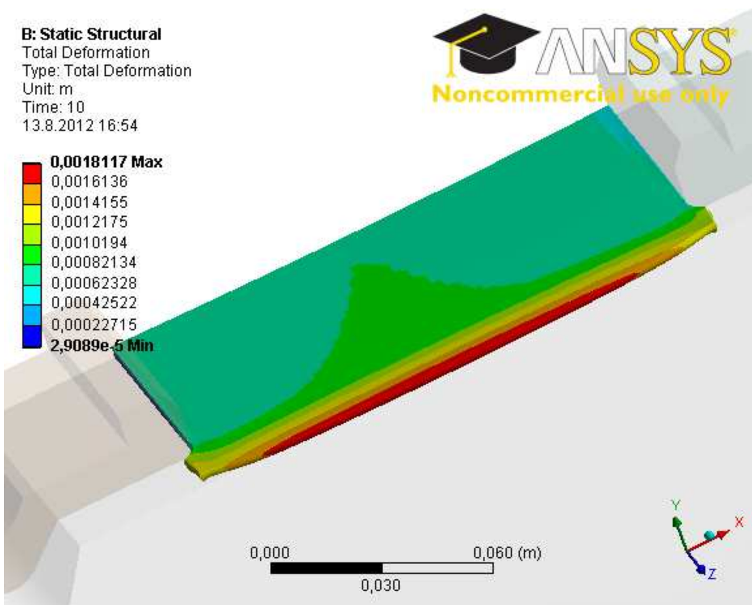

Image 48- A deformation of the the rubber pad

The equivalent stress in the rubber pad is the biggest on the lower edge, the value of the maximum equivalent stress is 9,753 MPa. For comparison, the biggest equivalent stress in the 4th situation is 5,6034 MPa.

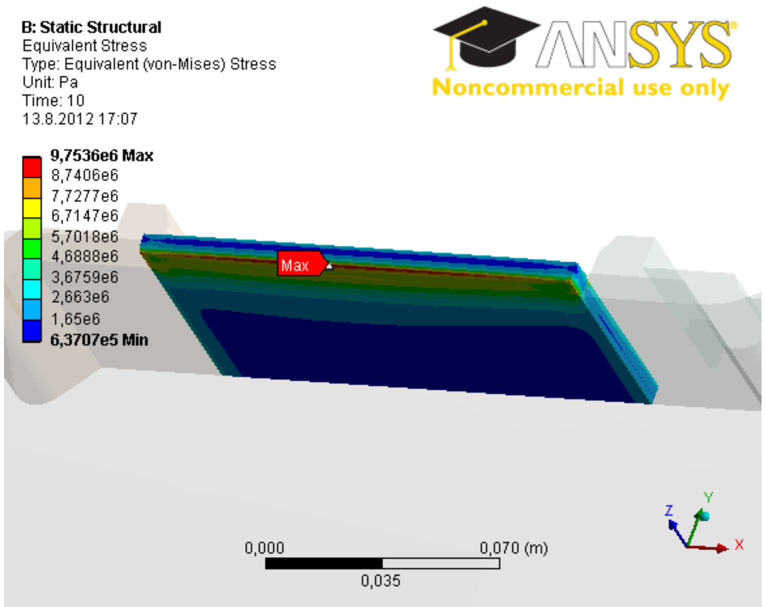

Image 49 - An equivalent stress in the rubber pad

5 Conclusion

The aim of the project was finding the stress results in the tension clamps, because the clamps are very important for the rail fastening. The biggest stress values were found in the 3rd situation (trains in the curve with cant deficiency). That was suggested before the simulation. But the diferences between the situations aren't very high. So the values of the average loads haven't big influences on the clamps.

The rubber pad under the rail was analysed too. The deformation of the rubber pad is obvious in the real scale, the values of the deformation is high. The equivalent stress in the pad is different too, the maximum value is in the 4th situation.

.

References

KUBÁT, Bohumil. TÝFA, Lukáš. *Železniční tratě a stanice.* Praha : ČVUT, 2003. 80-01-02782-1.

ČD. Předpis S3. *Železniční svršek.* 2003.

PLÁŠEK, Otto a kol. *Železniční stavby - Železniční spodek a svršek.* Brno : Akademické nakladatelství CERM, 2004. 80-214-2621-7

PAZDERA, Luboš, SMUTNÝ, Jaroslav, TOMANDL, Vladimír. Dynamická a akustická analýza pružného upevnění kolejnic bez podkladnic. *Stavební obzor.* 08 2009.

PAZDERA, Luboš, SMUTNÝ, Jaroslav, TOMANDL, Vladimír. Dynamická a akustická analýza pružného upevnění kolejnic bez podkladnic. *Stavební obzor.* 08 2009.

KREJČIŘÍKOVÁ, Hana. *Modelové výpočty v železničním stavitelství.* Praha : ČVUT, 1997. 80-01-01612-9.

Acknowledgement

This project was done within the framework of the institutional research plan, identification code MSM6840770043 and Grant of Czech Technical University, Student's Grant Competition SGS 12/163/OHK2/2T/16

Contact adress

Bc. Tadeáš Volf

Czech Technical University in Prague, Faculty of Transportation Sciences, Department of Mechanics and Materials

Na Florenci 25, 110 00, Praha 1

THE OBTAINING OF BICYCLE HELMET'S MODEL FOR NUMERICAL ANALYSIS

JAN VYČICHL, ONDŘEJ KRUPIČKA, MARTIN ŠUDŘICH

Czech Technical University in Prague, Faculty of Transportation Sciences, Konviktská 20,

110 00 Prague 1

Department of Mechanics and Materials

Abstract: The main aim of this study is to obtain a new virtual model of a bicycle helmet, using reverse engineering. The real bicycle helmet was transferred to the virtual model using 3D scanning equipment. The virtual surface model was subsequently modified in several software products, which supports application of reverse engineering. Using multiple editing software aims to determine the most appropriate option obtaining accurate computer models for the future. The resulting model will be applied to optimize the drop test in LS-DYNA. The numerical calculation will be compared with the measured data obtained from the real tests. This project was done within the framework of the institutional researchplan, identification code MSM6840770043 and Czech Technical University Student's Grant Competition, identification code SGS12/163/OHK2/2T/16.

Keywords: 3D-scanner, Helmet, Reverse ingeneering

1 Úvod

Cílem studie bylo zavedení a vyzkoušení postupu zpětného inženýrství pro získávání virtuálních modelů vhodných k výpočtovým zkouškám ve FEM software LS-DYNA, tak aby mohly být porovnány výsledky reálných pádových zkoušek cyklistických přileb s výpočtovými. Postup by měl být co nejuniverzálnější a aplikovatelný na všechny typy testovaných přileb na padostroji.

Postup spočívá v přípravě předlohové přilby před snímáním, 3D skenováním tělesa a v následné úpravě v software, vhodném pro zpracování povrchů. Nakonec je z výsledného virtuálního modelu vytvořena konečně-prvková síť vhodná pro import do LS-DYNA.

2 Příprava přilby před skenováním

Jako model byla vybrána cyklistická přilba značky Giro. Před vlastním skenováním povrchu skutečné přilby bylo potřeba udělat některé úpravy. Nejdříve bylo nutné odstranit vnitřní výstelky a zařízení sloužící k doladění velikosti přilby na jednotlivce. Následovalo odstranění čelního štítku. Úpravy byly prováděny tak, aby bylo možné později na reálnou pádovou zkoušku opět uvést přilbu do původního stavu. Z tohoto důvodu nebyly odstraněny řemínky se zapínáním pod bradou uchycovacího systému, protože by při demontáži již nemohla být zaručena jejich funkčnost. Poutací řemínky výsledný virtuální model nijak neovlivnily a nejsou ani jeho součástí.

Další úprava se týká povrchu přilby, hlavně polymerové skořepiny. Samotná polystyrenová pěna, tvořící u většiny dnešních přileb více jak polovinu celého povrchu, má strukturu svého povrchu téměř ideální pro snímání 3D skenovacím zařízením. Polymerová skořepina je však u mnoha přileb v lesklém módním provedení, které je pro aplikaci skenování naprosto nevhodná. V případě zkoumané přilby byl povrch v matové úpravě s drsnějším povrchem. Přesto však po konzultaci s operátorem skenovacího zařízení, byla tato část povrchu přelakována matným lakem za využití techniky airbrush. Byl použit japonský lak od firmy Gunze Sangyo, nanesený ve dvou rovnoměrných tenkých vrstvách.

9.1 Referenční body na povrchu přilby

Pro orientaci 3D skenovacího zařízení bylo nutné po celém povrchu, jak vnitřním tak vnějším, umístit referenční bílé terčíky. Kladení referenčních terčíků má svá pravidla. Nemají se umísťovat do blízkosti, či přímo na hrany povrchu. Dále není vhodné symetrické rozložení po dvou stranách zpracovávaného objektu. Pro dosažení co nejvyšší přesnosti získaného modelu je vhodné klást terčíky na místa s co nejmenší křivostí povrchu. Bohužel, u skenované cyklistické přilby, není veliká možnost k vybrání vhodných nesymetrických a plochých míst. Po skenování virtuální model obsahoval patrné stopy, které naznačují, kde se referenční body při skenování nacházely a bylo nutné je v dalších softwarech odstranit.

Pro značnou složitost povrchu snímaného objektu, byl umístěn poměrně velký počet referenčních bodů. Je vhodné umístit co nejvíce bodů ke spodní části přilby, aby skener zaznamenával při přechodu z vnějšího povrchu do vnitřního a naopak jejich dostatečný počet. Toto opatření není nutné v případě, že je skenována vnitřní část přilby a vnější část přilby zvlášť ve dvou samostatných souborech. Objekt před snímáním je patrný na Obr. 1.

Obrázek 50 – Cyklistická přilba připravená pro snímání 3D ručním skenerem

3 Snímání povrchu laserovým skenerem

Příprava před měřením začíná vytvořením bodového pole tak, abychom určili body v prostoru. Následuje vlastní skenování, které probíhá automaticky bez zásahu lidského faktoru. Principem tohoto druhu skenování je využití laserového paprsku, který je vyslán kolmo proti skenovanému předmětu, odrazí se od něj a vrátí se zpět do skenovacího zařízení. Rozhodující je časový úsek, který uplyne od vyslání do navrácení paprsku. Tak je získána informace o rozměru předmětu ve směru letu paprsku. Informaci o zakřivení povrchu je obdržena z úhlu, pod jakým se paprsek vrací zpět do zařízení. Spojením těchto dvou základních informací skener obdrží přesnou polohu bodu, kterou odešle do počítače.

Výstupem je mračno bodů. Toto mračno je zpracováváno softwarem tak, že jsou odstraněny zbytečné body a minimalizovány odchylky. Dále jsou jednotlivá části mračna nahrazena polygony, které definují geometrii povrchu tělesa. Tímto způsobem je vytvořen 3D model, který může být importován do CAD systémů.

Kvalita výsledného modelu je dána hustotou, s jakou laserový paprsek pokryl plochu reálného objektu. Součástí zařízení bývá i barevná kamera, která při samotném skenování snímá barevnou informaci. Kamera pracuje na stejném principu jako optické skenery. Díky ní může mít virtuální plošný model i stejnou barvu povrchu jako snímaný objekt.

Laserové skenery jsou výhodné díky jejich vysoké přesnosti a nenáročnosti na obsluhu během skenování. Mají nejlepší předpoklady pro široké využití v praxi. Jejich používání je rychlé a výstupy jsou kvalitní. Nevýhodou může být jejich cena, která je v porovnání s ostatními skenery mnohonásobně vyšší.

Laserové 3D skenování je zastoupeno nejvíce a využívá se v mnoha oblastech. Jednou z nich je stavebnictví, kde je tento způsob tvoření 3D modelů nejvíce využívaný. Je vhodný pro zaměřování skutečného stavu budov, složitých konstrukcí, mostů, podjezdů, hrází nebo pro získání podkladů pro stavbu zaměřením profilu terénu a následným vytvořením 3D modelu. Dobrým pomocníkem je i v případech měření těžko dostupných míst jako jsou kamenolomy, jeskyně, doly a potrubní systémy. Tohoto způsobu převádění reálných těles do trojrozměrných modelů využívají také památkáři při rekonstrukci a dokumentaci památek.

10.1 Použité skenovací zařízení

ČVUT Fakulta dopravní vlastní laserové skenovací zařízení Handyscan 3D. Tento skener byl využit pro získávání virtuálního modelu cyklistické přilby. Jedná se o ruční skener, který patří do skupiny laserových zařízení, je samo polohovací a bezkontaktní. Na základě reflexních značek umí zjistit změnu polohy snímaného objektu a automaticky tak navázat polygonovou síť na správném místě.

Na rozdíl od tradičních skenerů tento bezkontaktní ruční laserový skener nepotřebuje žádné další zařízení pro určení polohy vůči snímanému objektu, jako jsou například externí sledovací zařízení CMM nebo pohyblivá ramena k určení vlastní polohy nebo polohy snímaného objektu. Není tedy nutné skenovaný předmět vůči skeneru fixovat.

Pomocí dvou zabudovaných kamer skener snímá laserový kříž na tělese. Během snímání se v reálném čase na obrazovce počítače zobrazuje obraz snímání. Díky této schopnosti může uživatel vidět, jakou část má již nasnímanou, a zda je třeba v některém místě získat více informací.

Ke skeneru byl pořízen i ovládací software VxElements, který byl vyvinutý přímo pro tento ruční skener. Tento program je kompatibilní s OS Microsoft Windows, je velmi intuitivní, během skenování zobrazuje aktuálně nasnímanou síť a obsahuje algoritmus na optimalizaci výsledné sítě. VxElements automaticky vytváří z nasnímaných dat (mraku bodů) přímo polygonovou síť. Umožňuje vysoce výkonné snímání s různým rozlišením povrchu i snímání textury. Software umožňuje export objektů ve formátu STL, čehož bylo v tomto případě využito.

10.2 Proces snímání reálné přilby

Před prvním skenovacím procesem byla provedena kalibrace zařízení. Následovala konfigurace na jednotlivé povrchy. Jak pro polystyrenovou pěnu, tak pro polymerovou skořápku přilby byla nastavena jiná hodnota závěrky. Pro vnější povrch bylo zvoleno 10,5 ms a pro vnitřní 33,3 ms.

Rozlišení povrchu bylo nastaveno na 0,5 mm. I když skener nabízí možnost nastavení i většího rozlišení povrchu (až 0,2 mm), zvolená hodnota se zdála optimální.

V průběhu skenování byly získány dva základní modely. Nejdříve skenování probíhalo z vnitřního povrchu a následně skener snímal vnější povrch. V tomto případě byl však značný rozdíl v počtu chybných míst. Pokud skenovací proces byl započat na vnitřním povrchu přilby, byla tato část modelu bez výrazných chybných míst, avšak vnější povrch obsahoval větší počet otvorů. Pokud se skenovací proces obrátil, byl vnější povrch mnohem kvalitnější na úkor vnitřního povrchu. Výsledek snímání je patrný na Obr. 2, kde je možné vidět i některá špatně oskenovaná místa (otvory šedé barvy).

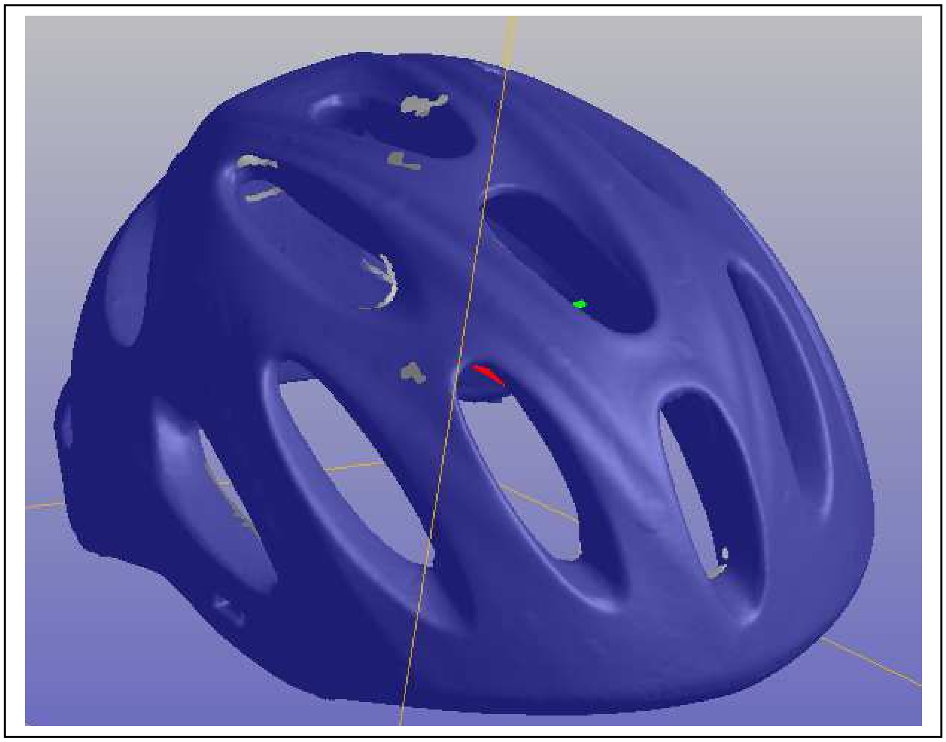

Obrázek 2 – Výsledný model přilby v software Geomagic Studio 2012

Výsledek byl exportován v STL formátu ze software VxElements. Před exportem proběhlo ještě nastavení počátku souřadného systému do těžiště modelu. Kladná část osy x směřuje do přední části, osa y míří do boku a osa z k vrchní části přilby.

4 Úpravy modelu po nasnímání

Po nasnímání bylo nutné povrchový model ve formátu STL upravit, protože povrch nebyl, vzhledem ke svému tvaru, nasnímán kompletně. Byly použity dva počítačové programy: Dassault CATIA V5R18, Geomagic Studio 2012. Úpravy ve vyjmenovaných programech probíhali paralelně, s cílem dosáhnout optimálního postupu.

Každý z těchto programů je specifický a má odlišné ovládání a funkce. Pro potřeby úpravy STL modelu do podoby „vodotěsného“ (watertight) povrchu poslouží oba uvedené.

10.3 Využití software Dassault CATIA

Práce se soubory STL v software CATIA V5R18 byla prováděna v modulu Digitized Shape Editor, který je vhodný pro úpravy plošných modelů a má mnoho užitečných funkcí.

Nejdříve byl model celé přilby načten pomocí funkce Import STL. Pro zjednodušení budoucího výpočetního modelu byly funkcí Remove vyřezány montážní a upevňovací otvory, sloužící na původní přilbě k upevnění čelního štítku a vnitřního vybavení.

Obrázek 3 – Výsledný model přilby v software CATIA V5R18

Následně bylo potřeba zacelit chyby povrchu vzniklé snímáním a výřezem. Za několikanásobného využití funkce Fill Holes se povedlo zacelit celý povrch. Nově vytvořené plochy jsou však skládány z větších trojúhelníků než původní a nanavazují na původní povrch se stejnou křivostí. Pro kontrolu je možné využít funkci Mesh Cleaner. Tato funkce analyzuje celý povrch vybraného modelu a určí počet poškozených, duplikovaných a inkonzistentních trojúhelníků, základních prvků povrchu. Dokáže také odhalit trojúhelníky povrchu s atypicky dlouhou hranou a tzv. Non-manifold trojúhelníky. Po kontrole bylo znovu potřeba zaplnit nově vzniklé otvory v povrchu. Procedura byla několikrát opakována dokud nebylo dosaženo modelu, jehož povrch byl bezchybný.

Následovalo vyhlazení přilby Mesh Smoothing s nastavením koeficientu 1 a maximální odchylkou změny povrchu do 2 mm. Následně proběhlo porovnání importováno STL modelu s přilbou po úpravách, v CATII toto lze provést pomocí funkce Deviation Analysis. Rozdíly samozřejmě byly patrné v místech kde došlo k odstranění montážních otvorů a v místech kde nebylo možné povrch správně nasnímat. Maximálně však byla zaznamenána odchylka o velikosti 1,1 mm, a průměrná odchylka o velikosti 0,37 mm, což je poměrově k velikosti celé přilby zanedbatelná hodnota. Výsledný model je znázorněn na Obr. 3.

10.4 Využití software Geomagic Studio

Gemagic Studio je sofware přímo navržený pro potřeby reversního inženýrství. Je velice snadno ovladatelné a intuitivnější než výše zmíněná CATIA.

Po načtení STL modelu vzniklého ze snímání byl povrch nejdříve zkontrolován funkcí Oprava Polygonů. Byly tak odebrány hroty, vysoce složené okraje, nerozložené hrany, průsečíky protínající sama sebe a malé otvory. Pomocí funkce Výběr uživatelské oblasti byly označeny montážní a upevňovací otvory. Následně byly tyto vybrané oblasti odstraněny.

Další úpravy zahrnovali zaplnění všech otvorů funkcí Vyplnit vše, přičemž byl nastaven parametr, kdy se nově tvořený povrch navazuje na stávající stejnou křivostí. Tako funkce je zřejmě nejlepší ze všech tří použitých programů, na modelu vytváří vyplnění otvorů, které je pohledově velmi přirozené. Je také možné volit napojení nových povrchů jako tečné, avšak výsledek nebyl přesvědčivý. Následovala samostatná funkce odstranění hrotů, čímž byly body určující vrcholy trojúhelníků posunuty do statisticky vhodnějších oblastí. Nakonec přišlo vyhlazení celého povrchu s důrazem na zachování tvaru, kdy maximální odchylka po vyhlazení nepřesahovala 1,5 mm. Výsledný model je vyobrazen na Obr. 4.

I zde byla provedena analýza odchylky importovaného souboru a výsledného. Průměrná odchylka byla zjištěna na 0,36 mm. Maximální odchylka byla řádově větší, 5y7 mm, avšak byla na místě zaceleného montážního otvoru. Zajímavostí je že CATIA tento rozdíl vůbec nezaznamenala, ač se u obou programů vycházelo ze stejného základního modelu získaného ze snímání.

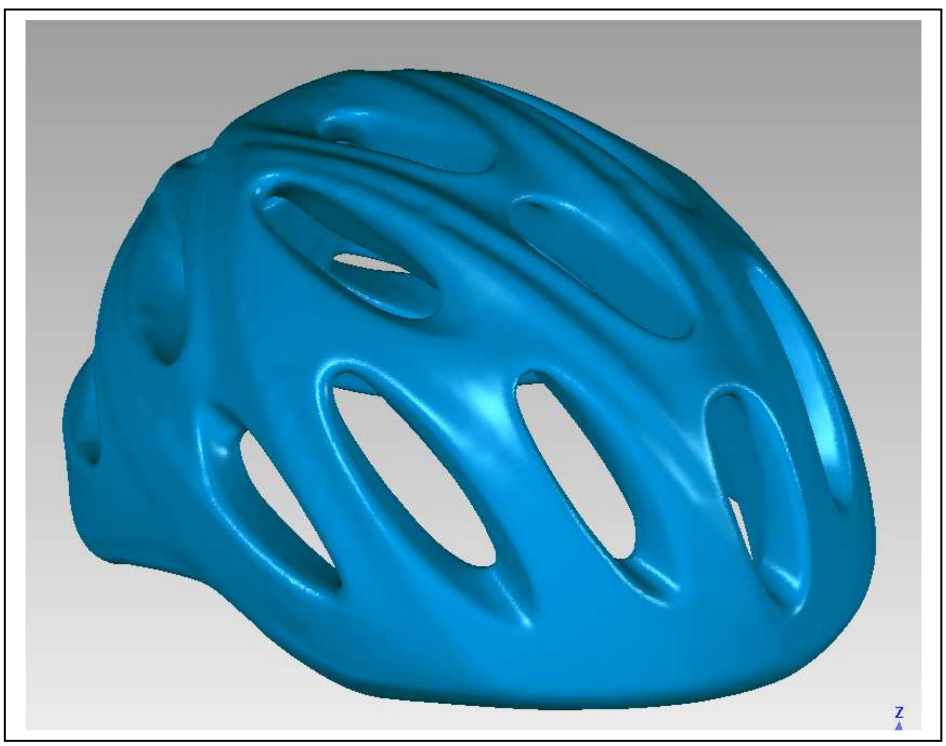

Obrázek 4 – Výsledný model přilby v software Geomagic Studio 2012

Oba výsledné modely byly následně v programu Geomagic Studio porovnány. Průměrná odchylka mezi modely byla 0,06 mm, maximální pak 1,2 mm. Maximální odchylka byly naměřena v místě hrany větracího otvoru, kde informace o povrchu ze skeneru úplně chyběla a povrch byl dotvářen nově programy. Celkově však byl rozdíl úpravených modelů minimální. Nelze tedy s jistotou říci, který z obou programů je pro takto specifickou funkci vhodnější. Dále bylo pracováno s modelem vycházejícím z Geomagic Studio.

5 Vytvoření sítě elementů

Upravený model přilby byl importován do prostředí ICEM CFD 14.5, který je součástí balíku ANSYS. Zde byla vytvořena konečně-prvková síť elementů, kterou lze bez obtíží importovat do programu LS-PrePost. Přilbu tak bude možné zaměnit za aktuálně testovaný typ.

Pomocí funkce Global Mesh Setup byla vytvořena síť elementů. Typ byl nastaven na Cartesian metodou Body-Fitted. Vzniklo tak 152 112 uzlových bodů a 179 123 elementů. Výsledek je zobrazen na Obr. 5. Nakonec byla síť exportována pomocí funkce Export Mesh To LS-DYNA.

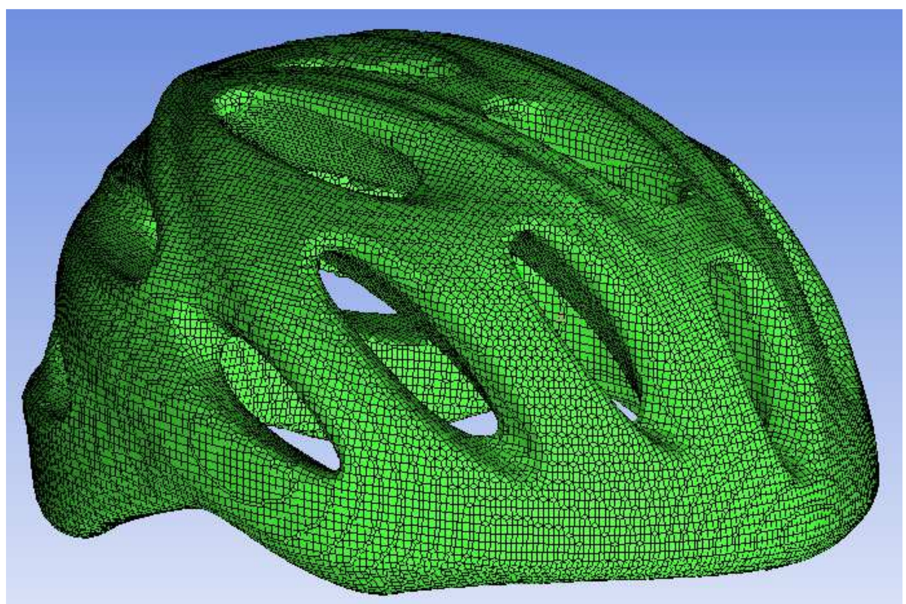

Obrázek 5 – FEM model cyklistické přilby

1 Závěr

Byl prověřen postup získávání modelů pro výpočtové simulace. Do budoucna řešitelský tým počítá s testováním rozličných cyklistický přileb a proběhlo tak ověření, že k reálným testům nebude problém vytvořit geometricky velice přesný virtuální obraz. Po odladění výpočtu pádové zkoušky bude možné poměrně snadně vyměňovat jednotlivé typy testovaných přileb dle potřeby.

Literatura

MICKA M., VYČICHL J.,(2007). Tvorba modelu přilby z 3D skenování. In: ANSYS Users meeting, 2007.

MARCIÁN P., FLORIAN Z., MRÁZEK M., (2010). Práce se soubory STL v software CATIA. V rámci grantového projektu FRVŠ 1402/2010/G1.

Poděkování
Tento projekt byl řešen v rámci výzkumného záměru MSM6840770043 a Studentské grantové soutěže na ČVUT s číslem uděleného grantu SGS12/163/OHK2/2T/16.

Kontaktní adresa:
Bc. Ondřej Krupička
České vysoké učení technické v Praze, Fakulta dopravní, Ústav mechaniky a materiálů,
Na Florenci 25, 110 00 Praha 1

INVESTIGATION OF HYDRODYNAMIC PUMP PARAMETERS WITH APPLICATION OF THE PARTIAL WETTABILITY BOUNDARY CONDITION

LUKÁŠ ZAVADIL, SYLVA DRÁBKOVÁ

Abstract: The influence of the partial surface wetting on the flow field in the hydrodynamic pump was investigated using numerical modeling. Wall boundary conditions were modified to account for partial wettability based on the theoretical assumptions proposed by Pochylý for the general curved surface (Pochylý, 2006). ANSYS FLUENT software was used for modeling of flow in the interior of the hydrodynamic pump. The results obtained by numerical modeling in which modified boundary conditions were used, are compared with the results with no slip boundary condition.

Keywords: pump, CFD, wetting, parameters

12 Introduction

Probably all branches of industry are aimed for reduction of power consumption and increasing the energy efficiency. For pumps, which take the second place in energy consumption, just behind the electric motors, the efficiency is really important. One way how to improve the efficiency of a pump is to optimize the shape of hydraulic surfaces. Another way leads to improvement of properties of the materials used for manufacturing of surfaces inside the pump, which are in contact with a delivered liquid. The specific properties of materials may serve for innovations in the design and production of the pumps. One of these properties is a partial wettability which causes that the liquid which is in contact with the inner surface "slips" on this surface.

13 Theoretical approach

The definition of boundary condition for the generally curved surface, which is partially wettable, applies following assumptions: if the fluid is slipping on the surface with the velocity $\boldsymbol{c}$, the adhesive shear stress vector σ_A lays in the plane defined by the outer normal vector $\boldsymbol{n}$ to the surface and the velocity vector $\boldsymbol{c}$ (Image 1). The adhesive shear stress vector σ_A tangentional to the surface can be defined as follows:

$$\boldsymbol{\sigma}_\mathbf{A} = (\boldsymbol{\sigma} \times \mathbf{n}) \times \mathbf{n} = -k \cdot \mathbf{c} \tag{1}$$

where k is adhesive coefficient (Pa·s·m^{-1}).

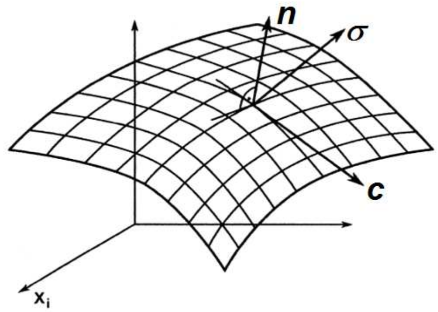

Image 51 – Shear stress on general curved surface

The theory of mathematical definition of partially wettable surface by means of adhesion coefficient *k* was introduced by Pochylý (Pochylý, 2006). This approach will be further applied on the selected surfaces in the interior of a hydrodynamic pump. But at first the modified boundary condition was used for steady laminar isothermal flow of incompressible fluid in a tube with circular cross section. In that case, the theory with no slip condition on the walls is well known and the results for the no slip case and the partially wettable case can be compared.

13.1 Theoretical assumptions for laminar flow in pipe with circular cross section

The shear stress is proportional to the rate of the shear strain according to the Newton's law of viscosity:

$$\tau = \eta \frac{dc}{dr} \tag{2}$$

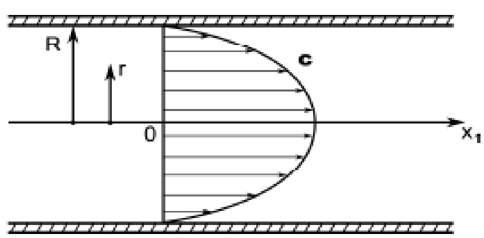

Image 2 – Straight pipe section with velocity distribution in case of fully wettable wall (no slip)

The velocity distribution in the cylindrical coordinate system can be defined as a function of the distance from the center of the pipe:

$$c = \frac{\Delta p}{4\eta l}\left(R^2 - r^2\right) \tag{3}$$

The pressure drop in a fluid flowing through a long cylindrical pipe can be calculated from the Hagen–Poiseuille law:

$$\Delta p = \frac{8\eta l Q}{\pi R^4} \tag{4}$$

Now let's account for a slip of the fluid on the wall. In this case the outer surface of the control volume moves with the slip velocity defined as:

$$c_0 = \frac{\Delta p R}{2lk} \tag{5}$$

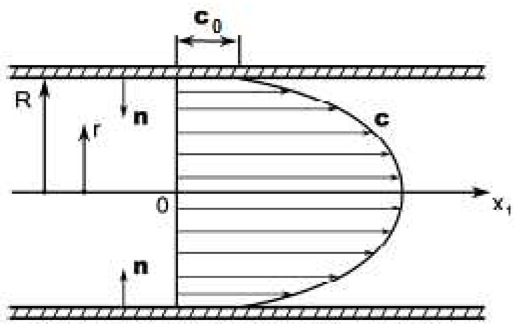

Image 3 – Velocity profile for partially wettable surface of the tube

The velocity profile is modified according to the following formula:

$$c = \frac{\Delta p}{4\eta l}\left(R^2 - r^2\right) + \frac{\Delta p R}{2lk} = \frac{\Delta p}{2l}\left(\frac{R^2}{2\eta} + \frac{R}{k} - \frac{r^2}{2\eta}\right) \tag{6}$$

The pressure drop Δp can be again calculated based on the flow rate Q:

$$\Delta p = \frac{8l\eta Q}{\pi R^4\left(1 + \dfrac{4\eta}{Rk}\right)} \tag{7}$$

13.2 Comparison of theoretical assumptions with CFD results

Standard fully wettable surfaces exhibit zero velocity, which is connected with the noslip boundary condition on the wall. In Fluent the no-slip condition is applied by default, but it is possible to define a tangential velocity component in terms of the translational or rotational motion of the wall boundary, or to model a "slip" wall by specifying a certain value of shear. Such definition may cause a problem in a complex geometry where the velocity may differ in various parts in which the flow is modelled. That is why a different approach was applied based on (Pochylý, 2006) and the UDF (User Defined Function) was assembled, that enables to define the wall shear stress according to (1). The fluid flow was solved as a 2D axisymmetric problem as well as in full 3D geometry. Results shown in following Images were obtained from 3D solution.

This approach is more precisely defined in (Zavadil, 2011). The results shown and described in this article are aimed to demonstrate only how the created UDF can modify parameters of the flow.

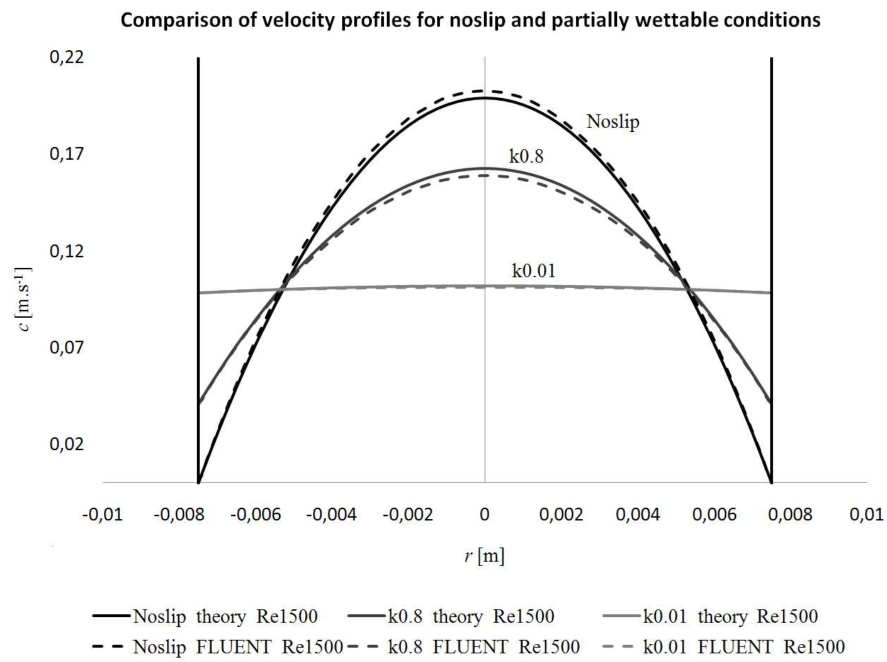

Image 4 – Comparison of velocity profiles obtained from theory and FLUENT simulation

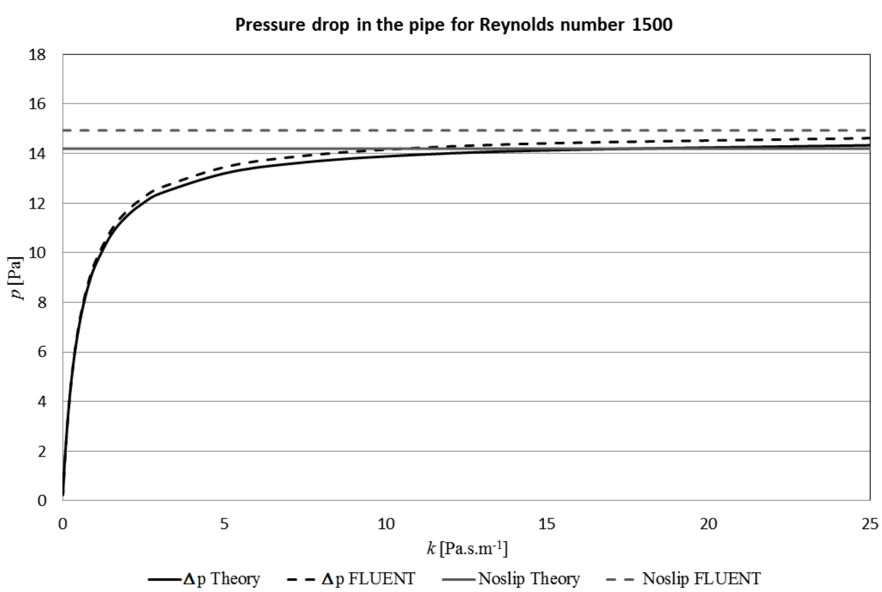

Image 5 – Comparison of pressure drop for wettable (no slip) and partially wettable (slip) boundary conditions on the pipe wall for *Re* = 1500

The first Image (Image 4) shows changes of velocity profile for different values of adhession coefficient k. Results from the numerical solution are in a good agreement with the result given by theory.

In Image 5 we can observe the exponential dependency of the pressure drop on the adhesion coefficient *k*. The adhesion coefficient should theoretically vary from near zero to infinity. But it can be seen, that only a small range of *k* brings significantly lower value of the pressure drop. When a certain limit of *k* is reached, the pressure drop is approaching the value of the no slip condition. The difference between the theoretical and numerical predictions is within 5%.

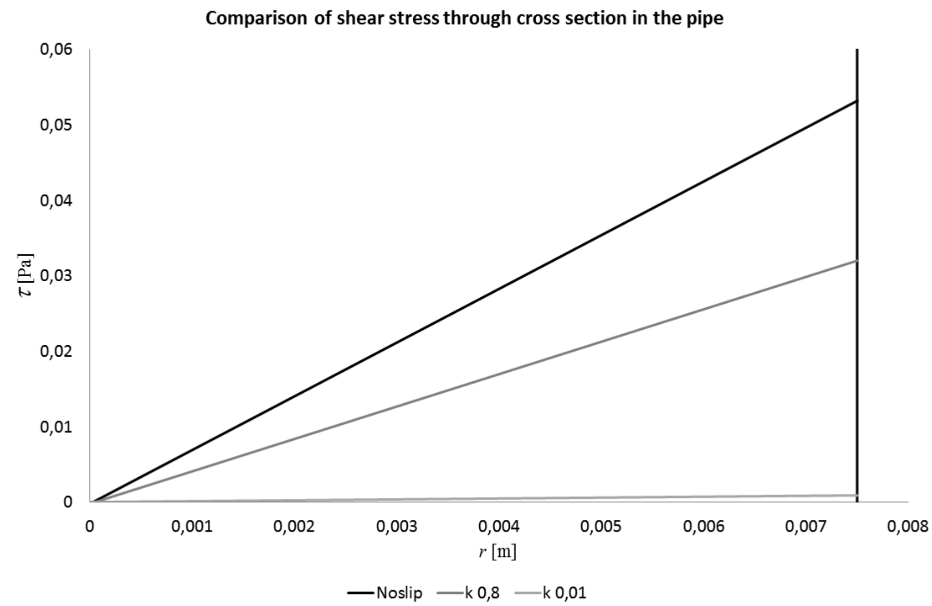

Image 6 – Shear stress profile in dependence on *k*

Last Image 6 ilustrates how the created UDF modified a value of the shear stress through the cross section in the pipe at laminar flow.

14 Numerical modeling of flow in centrifugal pump

The viscous fluid flow can be described by the partial differential equations that must be solved by numerical methods. Using this approach, it is possible to solve in an appropriate manner the 3D Navier-Stokes equations in complex geometries.

ANSYS FLUENT release 13 was applied to model numerically the flow through a volute pump. The incompressible steady flow was modeled in a complex 3D geometry. The problem involves multiple moving parts as well as stationary surfaces. In Fluent, two approaches can be applied for the modeling of such cases:

- Multiple Rotating Reference Frames
  - *Multiple Reference Frame model (*MRF*)*
  - *Mixing Plane Model (*MPM*)*

Both the MRF and MPM approaches are steady-state approximations, and differ primarily in the manner in which conditions at the interfaces are treated. In this case results are given for one position of blades of the impeller against the volute. Such simulations are less time demanding but the dynamic effects of flow are neglected in this approach.

The turbulence model k-ω SST was applied as it is recommended for the modeling of flow in rotating geometries. This model employs the k-ε model in the core flow, the k-ω model near the wall and it modifies the relation for the eddy viscosity.

Using numerical methods (mostly finite volume method), the partial differential equations are converted into algebraic equations and solved by different algorithms which differ in convergence, accuracy and time of computation. The convergence of the steady solution can be observed by evaluation of residuals and also by monitoring the value of the outlet pressure.

14.1 Design paramegters of modeled centrifugal pump

Numerical modeling has been used to investigate the flow in a single-stage centrifugal pump with horizontally mounted shaft and twisted blades. The design parameters are specified in table1.

Table 9 Design parameters of modeled centrifugal pump

Head	H =	80.9	[m]	Outlet diameter	D_2 =	244	[mm]
Flow rate	Q =	7	[$dm^3 \cdot s^{-1}$]	Number of blades	z =	5	
Rotational speed	n =	2900	[min^{-1}]				

As can be seen from design parameters, the pump provides high head and low flow rate, which yields a low value of non-dimensional specific speed.

$$n_b = n\frac{Q^{0.5}}{Y^{0.75}} = \frac{2900}{60} \cdot \frac{0.007^{0.5}}{(80.9 \cdot 9.81)^{0.75}} = 0.0263 \tag{8}$$

where n_b is specific speed (1), n is rotational speed (s^{-1}), Q_V is flow rate ($m^3 \cdot s^{-1}$), Y is specific energy ($J \cdot kg^{-1}$).

The obtained value of specific speed is very low and it is below the specific speed range considered for the radial type of impeller. It is caused by the high values of the head in connection with the low values of the flow rate. Such parameters can be reached by twisting the blades of the impeller, as it was designed at the Victor Kaplan Department of Fluid Engineering, Energy Institute, Brno University of Technology.

14.2 Definition of the computational geometry

At the beginning of the numerical modelling, a 3-dimensional geometric model of the pump components must be created which describes the calculation domain by coordinates. This calculation domain is then subdivided into a large number of cells, i.e. a grid is generated, the quality of which is essential for the reliable numerical solution. Large number of cells brings better accuracy but also higher demands on computational time. Geometry is presented in Image 7.

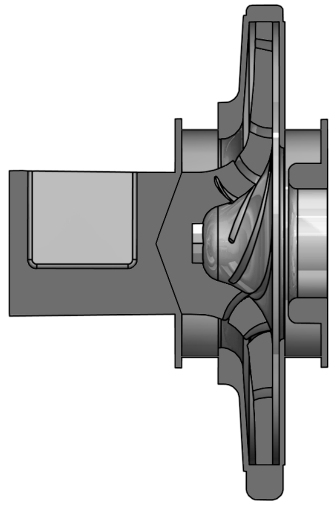

Image 7 – *Geometry with impeller casing*

The geometry (Image 7) was divided into six volumes (inlet part, impeller, volute with impeller sidewall gaps, clearances between impeller and casing on the front and rear side and the space behind the rear shroud under the annular seal. The number of cells in created mesh was about 4.3 mil.

14.3 Application of the partial wettability boundary condition on selected surfeces of the pump

For application of partial wettability boundary condition the volute surface and surfaces on impeller discs were selected. The fluid which is closed between rotating discs and stationary parts of the pump increases the amount of torgue which is acting on the rotor. It is caused by the shear between the fluid and the rotating impeller. But if the outer surfaces of the impeller will be partial wettable, the fluid will slip on the surface and the amount of torgue will be lower. The amount of shear depends on the adhession coefficient *k*. Application of a wettable coating on the inner surface of volute can lower losses caused by the friction of fluid on this surface. Surfaces for which the partial wettability boundary condition was used are shown in Image 8.

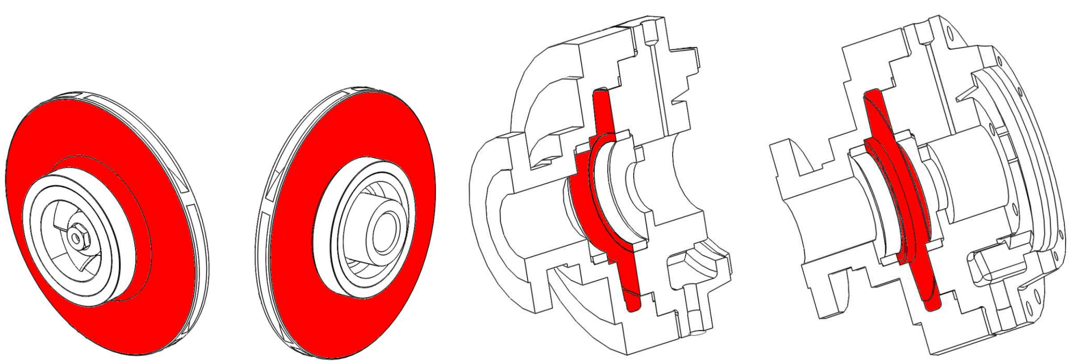

Image 8 – *Surfaces which were selected as partial wettable (Impeller casing, volute)*

Finally four studies were solved. In the first one the noslip condition was selected for all surfaces. The second applied wettable surfaces for the discs of the impeller. In third case the impeller discs and the volute surfaces were solved as partial wettable. In the last case the partial wettability was set only for the volute surfaces.

14.4 Q-H curve of the pump with partial wettability boundary condition

Using numerical methods, the basic power curves were set. One of them is the Q-H curve, which represents the dependency between the flow rate through a pump and the delivery head. The partial wettability can significantly improve the Q-H curve, but the improvement depends directly on the value of adhesion coefficient *k* of coating, which is used. Higher values of adhesion coefficient *k* mean, that the resulted head will be closer to results obtained with the noslip boundary condition.

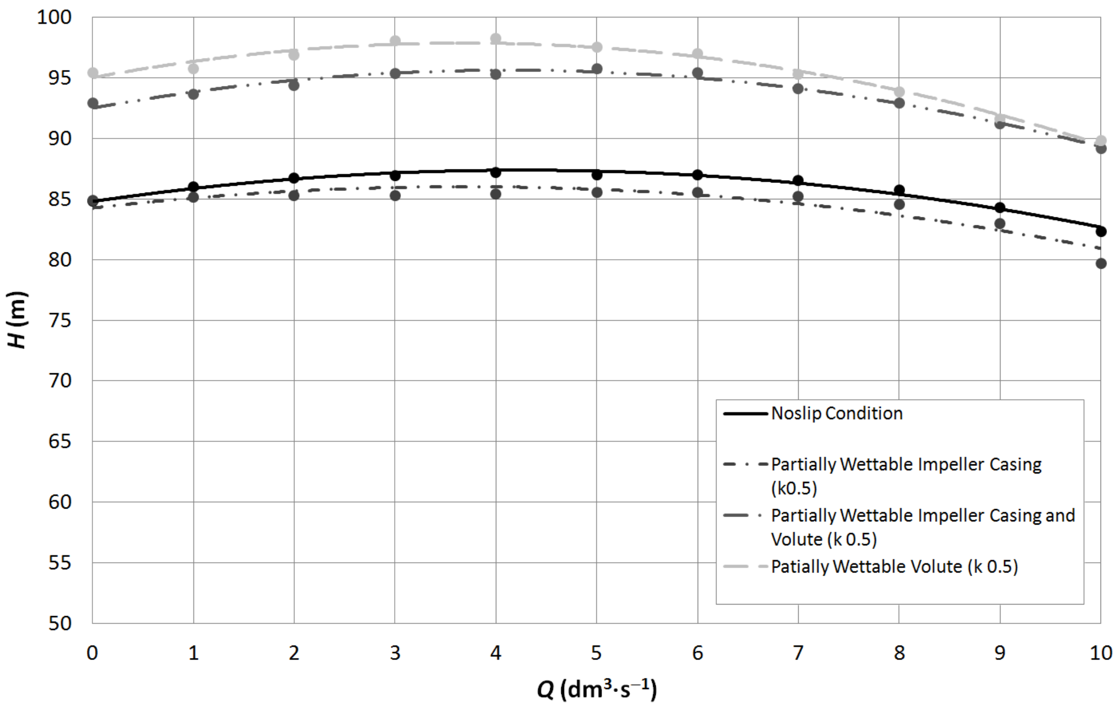

Image 9 – *Q-H curves for computed cases*

14.5 Q-P curve of the pump with partial wettability boundary condition

The power input of a pump is directly proportional to the torgue, which is acting on the rotor of the pump. This torgue is caused by the pressure which is acting on the blades and by the shear of fluid on the impeller surface. The amount of torgue which is caused by the shear of fluid on discs of impeller can be reduced with using a partial wettable coating. In Image 10 we can see how the adhession coefficient influence the amount of shear torgue.

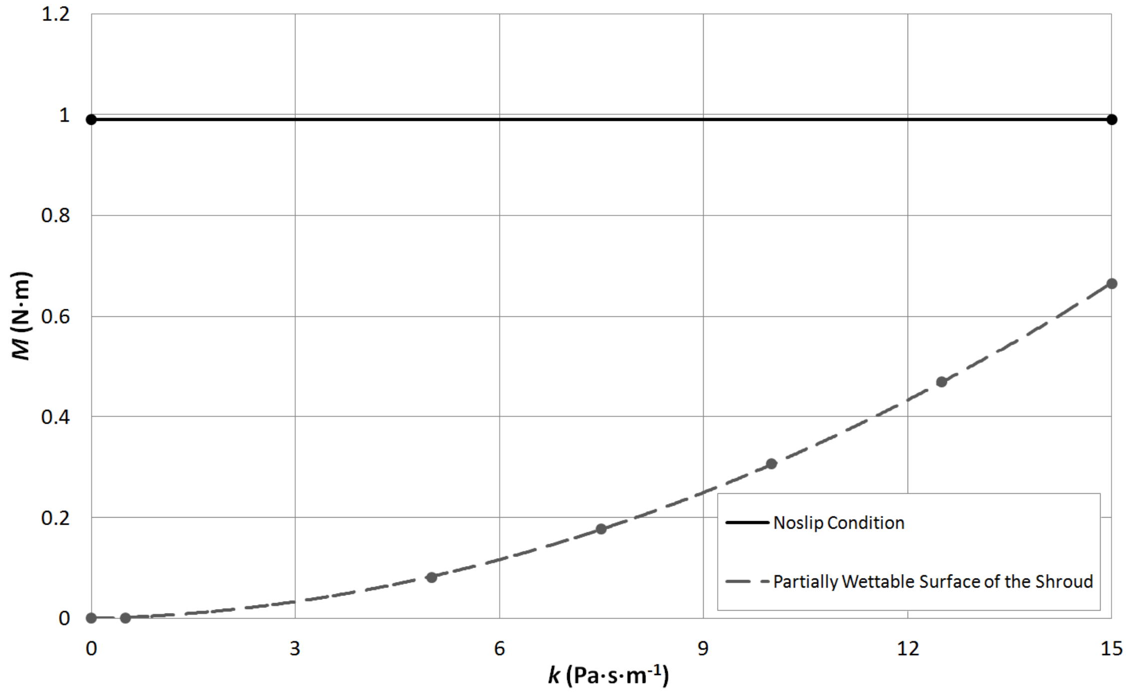

Image 10 – *Amount of shear torgue on Shroud of the Impeller casing for different values k*

Predicted Q-P curves for all computed cases are shown on Image 11. In all cases where the partiall wettability was set, the power consumption is lower then in the case with noslip condition. Best results were obtained when the volute and the impeller casing are partiall wettable.

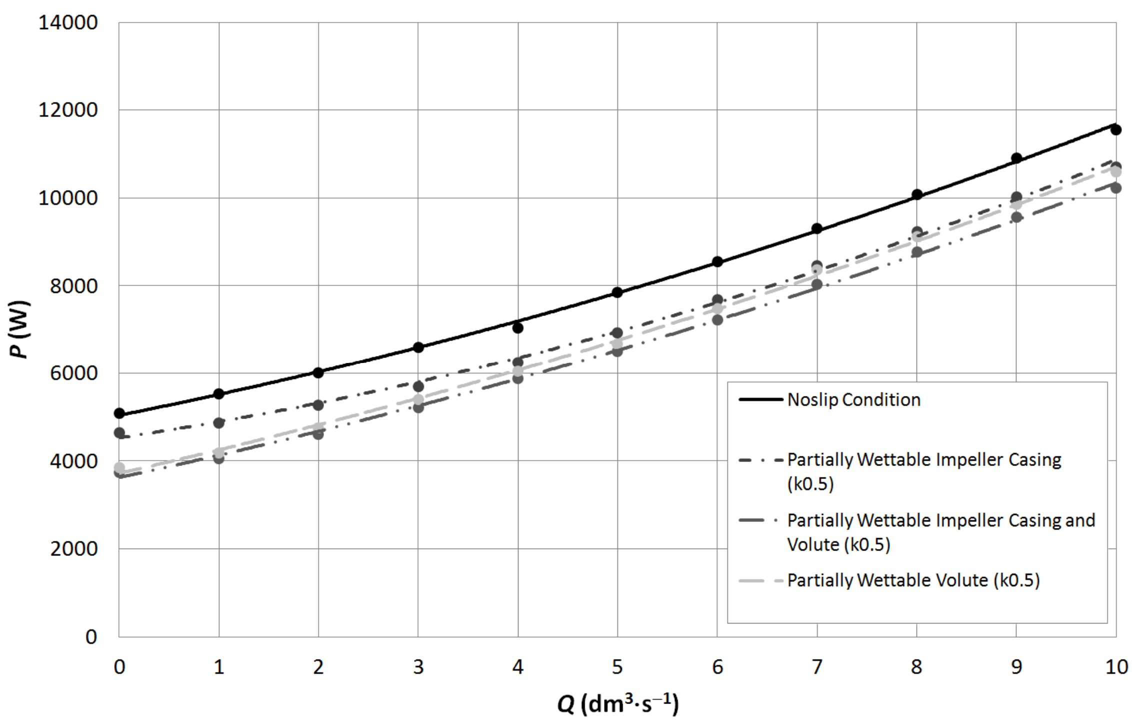

Image 11 – *Q-P Curves for Computed Cases*

14.6 Q-η curve of the pump with partial wettability boundary condition

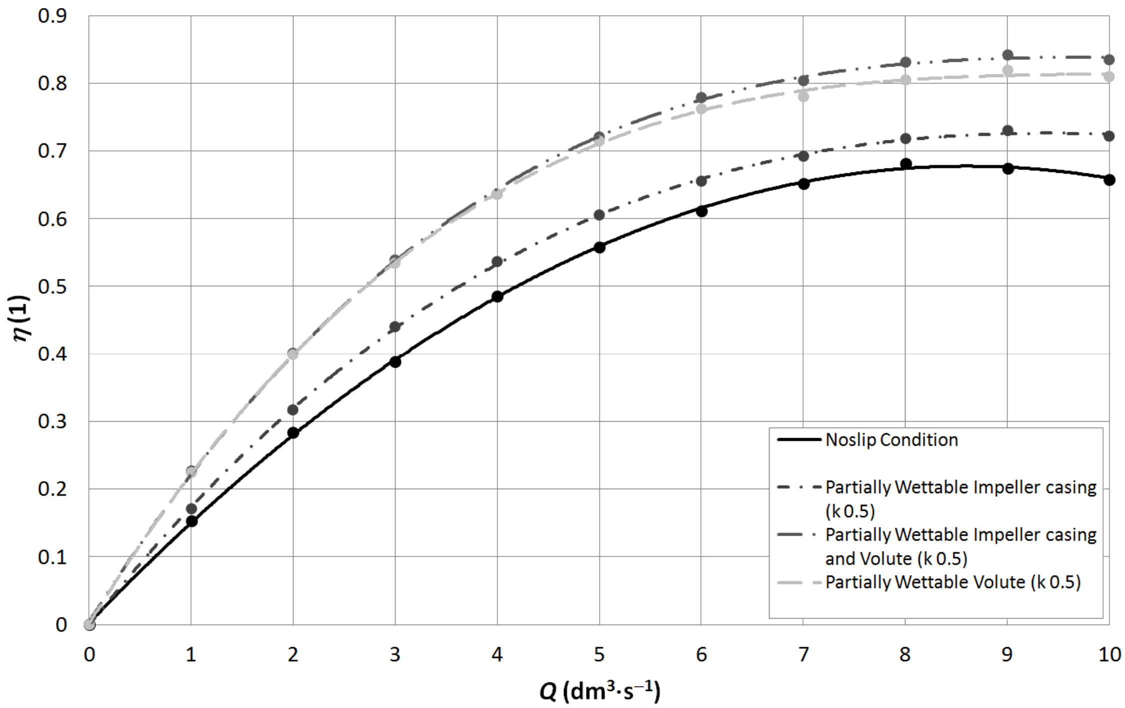

Image 12 – *Q-η Curves for Computed Cases*

Efficiency of the pump can be significantly improved using partial wettable materials. The efficiency is higher in all range of the flow rate for cases with partiall wettability boundary condition. Again the best results were obtained when the volute and the impeller casing are partiall wettable.

15 Conclusion

Data which were obtained by numerical modelling show that the partially wettable materials or coatings can significantly influence parameters of the hydrodynamic pump. Nevertheless the results depend on the value of the adhesion coefficient *k*. There are many hydrophobic materials but these materials must be suitable for application in interiors of hydrodynamic pumps. It means that this materials need to have a good abrasion resistance and must be acid resistant to guarantee a long working life.

References

POCHYLÝ F., HABÁN V., JURAČKA, J. 2006. Smáčivost kapalin vůči pevným povrchům. *Zborník abstraktov a príspevkov z mezinárodnej konferencie "Strojné inženierstvo 2006"*, ISBN 80-227-2513-7

POCHYLÝ F., HABÁN V., 2006. Smáčivost kapalin vůči pevným povrchům, *Výzkumná zpráva VUT-EU13303-QR-14-06*.

POCHYLÝ F., RINKA L., 2007, Povrchová energie v hraniční vrstvě kapky vody a tuhého povrchu, *Výzkumná zpráva VUT-EU13303-QR-34-07*.

ZAVADIL L., DRÁBKOVÁ S., KOZUBKOVÁ M., FRODLOVÁ B., 2011. The Influence of the Partial Surface Wetting on the Flow Field in a Pipe with Circular Cross-Section. *Transactions of the VŠB – Technical University of Ostrava, Mechanical series*, vol. 57, pages 267-274, ISSN 1804-0993

ZAVADIL L., KOZUBKOVÁ M., POCHYLÝ F., DRÁBKOVÁ S., 2011, The Influence of the Partial Surface Wetting on the Flow Field Between the Two Coaxial Cylinders, *Transactions of the VŠB – Technical University of Ostrava, Mechanical series*, vol. 57, pages 275-282, ISSN 1804-0993

Contact address:
Ing. Lukáš Zavadil, Ph.D.
Centre of Hydraulic Research, Jana Sigmunda 190, Lutín

doc. Ing. Sylva Drábková, Ph.D.
VŠB-TU Ostrava, Faculty of Mechanical Engineering, Department of Hydromechanics and Hydraulic Equipment, 17. listopadu 15, Ostrava-Poruba